IntechOpen

Gas Turbines

Materials, Modeling and Performance

Edited by Gurrappa Injeti

GAS TURBINES - MATERIALS, MODELING AND PERFORMANCE

Edited by **Gurrappa Injeti**

Gas Turbines - Materials, Modeling and Performance
http://dx.doi.org/10.5772/58504
Edited by Gurrappa Injeti

Contributors

Ene C. Barbu, Valeriu Vilag, Jeni Alina Popescu, Bogdan Gherman, Andreea Petcu, Romulus Petcu, Valentin Silivestru, Tudor Prisecaru, Mihaiella Cretu, Daniel Olaru, Kazuhiro Ogawa, Edgardo Javier Roldan-Villasana, Yadira Mendoza-Alegria, Ezenwa Alfred Ogbonnaya, Gurrappa Injeti

Notice

First published in Croatia, 2015 by INTECH d.o.o.
eBook (PDF) Published by IN TECH d.o.o.
Place and year of publication of eBook (PDF): Rijeka, 2019.
IntechOpen is the global imprint of IN TECH d.o.o.
Printed in Croatia

Legal deposit, Croatia: National and University Library in Zagreb

Additional hard and PDF copies can be obtained from orders@intechopen.com

Gas Turbines - Materials, Modeling and Performance
Edited by Gurrappa Injeti

p. cm.

ISBN 978-953-51-1743-8

eBook (PDF) ISBN 978-953-51-6371-8

Meet the editor

Prof. Dr. Gurrappa is a Senior Scientist in Defence Metallurgical Research Laboratory (DMRL), Hyderabad, India, working in the field of Gas Turbine Engine Materials for about three decades. In addition to defense systems, he has been helping different industries in solving the corrosion problems and stressing the need of prevention of corrosion by using different advanced protective techniques. He has been recognized globally. He is the recipient of Prestigious Fellowships.He is also the recipient of "Corrosion Awareness Award" and "Meritorious Contribution Award" from NACE International India section in 2004 and 2010 respectively. He has received a number of best paper awards and delivered a number of invited lectures / talks, keynote addresses in various international / national symposia and chaired the technical sessions. He authored 200 publications, 9 books / book chapters and edited two books on Gas Turbines. He is an elected Fellow of Royal Society of chemistry, London and Andhra Pradesh Akademi of Sciences, India.

Contents

Preface

Modern aero, marine and industrial gas turbines essentially need to exhibit outstanding performance, reliability and efficiency. This is possible only by selecting advanced materials, coatings and excellent designing. For this, the gas turbine manufactures should adopt modern technologies / techniques. This book presents current research in the area of gas turbines. It is a useful book providing a variety of topics ranging from basic understanding about the materials and coatings selection, designing and modeling of gas turbines to advanced technologies for their ever increasing efficiency which is the need of the hour for modern industries.

Chapter 1 presents a work that has been carried out on the modelling of dynamic response of marine GT rotor shaft systems. It is shown that when a system is subjected to force harmonic excitation, its vibration response takes place at the same frequency as that of the excitation. To determine the response of the shaft under vibration, readings were collected from bearings 1, 2, and 3 of GT 17 in Afam thermal station. The engine characteristic obtained in GT 17 is shown. Equation 40 was developed to determine the response of the system under vibration. This mathematical equation is used to run a computer programme with a code in C++programming language. The recommendations are 1. More attention should be paid to shaft vibrations as is the case with vibration on bearing. 2. Some factors which affect the performance of gas turbines on industrial duty should be considered while carrying out vibration based simulation of GT rotor shafts. 3. Errors and extraneous environmental factors should be put into consideration when modelling the response of rotor shaft under vibration. 4. GT rotor shaft systems should be provided with more supports to prevent adverse effects of eccentricity which leads to bow and whirl.

Chapter 2 describes 1. The selection of a location for a gas turbine cogenerative plant imposes climatic conditions and demands adequate technical solutions to meet performance requirements, especially during summer season when inlet air temperature rises, leading to a decrease in power output and efficiency. 2. Water content modifies thermodynamic properties of intake air (density, specific heat) affecting power output and heat mass flow resulted from the gas turbine. If in the past air humidity was neglected, in present day cogenerative gas turbine power increase, but also water/steam injection impose the need for it to be taken into account. 3. The main research directions in the area of cogenerative groups with gas turbines efficiency are: combustion temperature increase; compression ratio increase; improvement of design methods, combustion technology and advanced materials; technological transfer for aviation domain to industrial turbines domain; integrated systems (combined cycles, intake air cooling, exhaust turbine gases heat recovery, afterburning, etc.). 4. Determinant factors concerning the overall efficiency of the cogenerative group are: gas turbine exit temperature, temperature at the heat recovery steam generator stack; ambient

environment temperature. For these the most influential factor upon the increase of the overall efficiency is the temperature at the heat recovery steam generator stack. 5. Operating flexibility of equipment has become a major subject. Gas turbines are designed to function generally at nominal regime, in maximum efficiency conditions and minimum pollutants. At cogenerative groups with heat recovery steam generator, for producing technological steam, is preferable that the flexibility to the process demands to be achieved using afterburning installation. 6. Theoretical and experimental research conducted at INCDT COMOTI Bucharest, revealed that, in the case of a gas turbine with intercooling, the performances variation is approximately linear for a compression ratio between 10.2 - 16, with a power decrease of 2.5 % for each 5 degrees increase of the environment temperature; to be obtained a afterburning module with a 30 % reduction of the NOx reduction (at partial load) in comparison with the existing cogenerative power plant 2xST 18 – Suplacu de Barcau; to demonstrate the power increase and NOx emissions reduction when injecting water in the intake device of TA2 gas turbine.

Chapter 3 highlights the importance of high temperature corrosion i.e. oxidation, type I and II hot corrosion which are catastrophic for the gas turbines. Hot corrosion is a major problem for the gas turbines engines due to which failures take place during service. Though advanced superalloys comprising new alloying elements such as rhenium, ruthenium and iridium (4th and 5th generation) that have been developed recently, exhibit considerably improved high temperature strength properties, their hot corrosion resistance is found be very poor. Therefore, there is a need to apply appropriate hot corrosion resistant coatings on the superalloys as the gas turbine engine components should exhibit both high temperature strength as well as hot corrosion resistance. Considerable amount of research has been carried out in the coatings area. As a result, new compositions, graded coatings have been emerged and efforts have also been made to predict their lives. However, no work was reported to predict the lives of coatings under hot corrosion conditions. Recently, smart coatings with varied techniques and compositions have been reported, which provides total protection to the superalloy components against high temperature oxidation, type I and II hot corrosion with their intelligent behaviour which in turn enhances the efficiency of gas turbines by eliminating failures during service. Therefore, it is recommended to apply smart coatings for the advanced superalloys as bond coatings used in all types of modern gas turbines i.e. aero, industrial, and marine in order to obtain ever greater efficiency, which is essential in the present world. The chapter also presents the future research trends in the field.

Chapter 4 describes the formation and growth behaviour of thermally grown oxide (TGO) at the interface between ceramic thermal barrier coating and metallic bond coating. During thermal aging, a TGO is formed at the TBC/MCrAlY interface. SEM and EDX analysis show that the TGO contains two different oxides. One is alumina closer to the MCrAlY, and the other is mixed oxide closer to the TBC. Thickness of both alumina and mixed oxide increased with aging time. In the case of aged specimen for a long time, the macro-crack was identified everywhere in the TGO. This reason indicates that thermal expansion mismatch accompanied by formation and growth of alumina is one of the driving forces of macrocracks formation. However, the driving force is not only thermal stress but also decrease in adhesive force or formation of stress concentration site caused by formation of porosity or micro-crack. Almost all macro-cracks passed through the porosity in mixed oxide or microcrack in YSZ layer. It is thought that the delamination or the spalling is initiated and propagated due to an interaction of these degradation factors such as thermal stress, initiation of

stress concentration sites, and decreasing adhesive force due to formation and growth of alumina, porosities and microcracks. It has been made clear from kinetics of TGO growth that oxidation behaviour of the mixed oxide layer obeys parabolic law. On the other hand, it is thought that the oxidation rate constant of the alumina is a function of thickness of mixed oxide. Consequently, the alumina thickness obeys anomalous parabolic law. Furthermore, improvement technique for bonding strength between TBC and bond coat was suggested. By adding Ce and Si to conventional CoNiCrAlY, morphologies of the thermally grown oxide changed drastically. Furthermore, the influence became more pronounced when the amount of Ce increased. Ce addition to the bond-coat made the wedge-like oxide. The wedge-like oxide can improve the bonding strength. From these results, if we can control the morphology of the TGO, we can control the bonding strength between TBC and bond coat.

Chapter 5 covers needs of the GSACS. A generic model of such a combustion process designed to work in any operators' training simulator. Validation of the model has been intrinsically demonstrated with the inclusion of the model in a gas turbine and a combined cycle power plants simulators for operators' training. In the proper date, CENAC endorsed and accepted as correct the results of the tests in accordance with the testing acceptance procedures and the ANSI norm. Some other off-line examples have been presented with the objective to explain the model principles and potential. Consequently, the future work is discussed.

I believe that this book will be highly useful to materials scientists, gas turbine engine design engineers, manufacturers, mechanical engineers, undergraduate, post graduate students and academic researchers.

Injeti Gurrappa
Defence Metallurgical Research Laboratory
Hyderabad, India

Chapter 1

Analysis of Gas Turbine Blade Vibration Due to Random Excitation

E.A. Ogbonnaya, R. Poku, H.U. Ugwu, K.T. Johnson,
J.C. Orji and N. Samson

Additional information is available at the end of the chapter

http://dx.doi.org/10.5772/58829

1. Introduction

In recent times, a considerable impact has been made on the modeling of dynamic characteristics of rotating structures. Some of the dynamic characteristics of interest are critical speed, systems stability and response to unbalance excitation. In the case of Gas Turbines (GT), the successful operation of the engine depends largely on the structural integrity of its rotor shaft (Surial and Kaushal, 2008).

The structural integrity in turn depends upon the ability to predict the dynamic behavior or characteristic accurately and meet the design requirement to withstand steady and vibratory stresses. An accurate and reliable analysis of the rotor shaft behavior is therefore essential and requires complex and sophisticated modeling of the engine spools rotating at different speeds, static structure like casing, frames and elastic connections simulating bearing (Zhu and Andres, 2007). In this work, GT rotor shaft dynamic modeling will be based on the speed and the force response due to unbalance. During the design stage of GT rotor shaft, the dynamic model is used to ensure that any potential harmful resources are outside the engine operating speed.

Engine vibration tests are part of the more comprehensive engine test program conducted on all development and production engines (Surial and Kaushal, 2008). In the design and retrofit process, it is frequently desirable and often necessary to adjust some system parameters in order to obtain a more favourable design or to meet the new operating requirement Kris, et al (2010). Rotor shaft unbalance is the most common reason in machine vibration (Ogbonnaya 2004).

Most of the rotating machinery problem can be solved by using the rotor balancing misalignment. Mass unbalance in a rotating system often produces excessive synchronous forces that reduce the life span of various mechanical elements (Hariliaran and Srinivasan, 2010). A very small amount of unbalance may cause severe problem in high speed rotating machines. Overhung rotors are used in many engines ring applications like pumps, fans, propellers and turbo machinery. Hence, the need to consider these problems, even at design stages.

The vibration signature of the overhung rotor is totally different from the center hung rotors. The vibration caused by unbalance may destroy critical parts of the machine, such as bearings, seals, gears and couplings. In practice, rotor shaft can never be perfectly balanced because of manufacturing errors, such as porosity in casting, and non-uniform density of materials during operation (Eshleman and Eubanks (2007), Mitchell and Melleu (2005), Lee and Ha (2003)).

1.1. Damped unbalance response analysis

The second part in the rotor shaft dynamic analysis is conducting the damped unbalance response analysis. The objective of this analysis is to accruably determine the critical speeds and the vibration response (amplitude and phase angle) below the trip speed. API 617 (2002) requires that damped unbalance response analysis be conducted for each critical speed within the speed range of 0%-125% of trip speed. The standard requires calculating the amplification factors using the half power method described in figure 1. This helps to determine the required separation margin between the critical speed and the running speed.

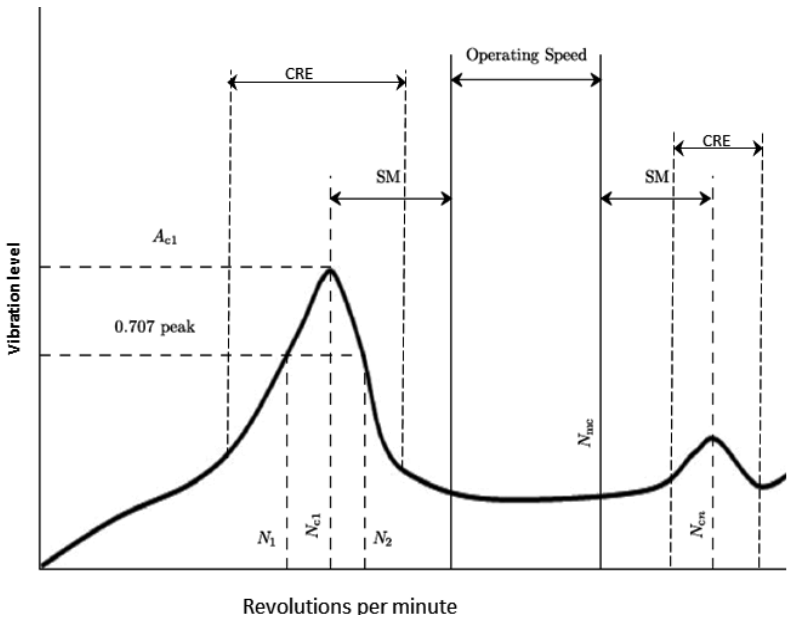

Figure 1. Amplification factor calculation from API 617 (2002)

The Legends in figure 1 are as follows:

http://dx.doi.org/10.5772/58829

N_{C1}=*Rotorfirstcritical,centerfrequency,cyclesperminute*

N_{Cs}=*Criticalspeed,*

N_{mc}=*Maximumcontinuousspeed,105%*

N_1=*Initial(lesser)speedat0.707xpeakamplitude(critical)*

N_2=*Final(greater)speedat0.707xpeakamplitude(critical)*

N_2-N_1=*Peakwidthattheball-powerpoint*

A_f=*Amplificationfactor*

$$= \frac{N_{C1}}{N_2 - N_1}$$

SM=Separationmargin

CRE=Criticalresponseenvelope

A_{c1}=*AmplificationatN*$_{c1}$.

A_{c2}=*AmplificationatN*$_{c2}$

As the amplification factor increases, the required speed increase up to a certain limit. A high amplification factor (AF>10) indicates that the rotor vibration during operation near a critical speed could be considerable and that critical clearance component may rub stationary elements during periods of high vibration.

From the figure 1, a low amplification factor (AF<5) indicates that the system is not sensitive to unbalance when operating in the vicinity of the associated critical speed. To ensure that a high amplification factor will not result in rubbing the standard requires that the predicted major axis peak to peak unbalance response at any speed from zero to trip speed does not exceed 75% of the minimum design diametric running clearances through the compressor.

This calculation is be performed for different bearing clearance and lubricating oil temperatures to determine the effect of the rotor stiffness and damping variation on the rotor shaft response. Also, the standard requires an unbalance response verification test for rotor shaft operating above the critical speeds.

The test results are used to verify the accuracy of the damped unbalance response analysis in terms of the critical speed location and the major axis amplitude of peak response. The actual critical speeds shall not deviate by more than 5% from the predicted, as the actual vibration amplitude shall not be higher than the predicted value (Bader, 2010).

The purpose of this study is therefore to show the dynamic response of a GT rotor shaft using a mathematical model. In the course of this work, it was noted that the rotor shaft can never be perfectly balanced because of manufacture errors. Hence the model involved the following:

a. The working principle of GT rotor shaft

b. Causes of unbalancing on a rotor shaft

c. The response of the system to the critical speed

The objectives and contributions to learning through this work are also as follows:

a. To model the dynamic response of a GT turbine system

b. To consider defects of the rotor shaft on the components of the GT system.

c. The result of this research could thereafter be extended to solve problems on other rotor dynamic engines.

d. To propound a viable proactive integrated and computerized vibration-based maintenance technique that could prevent sudden catastrophic failures in GT engines from rotor shaft.

2. Rotor shaft system and unbalance response

The rotor shaft system of modern rotating machines constitutes a complex dynamic system. The challenging nature of rotor dynamic problem has attracted many scientists, Engineers to investigations that have contributed to the impressive progress in the study of rotating systems.

According to Ogbonnaya (2004), the study of the unbalance responses of GT rotor shaft is of paramount importance in rotor dynamics. He further stated that the GT rotor shaft is a continuous structure and cannot therefore be considered as an idealized lumped parameter beam. Hariliarau and Srinivasan (2010) gave detailed model of rotor shaft coupling. They reviewed the rotor shaft and coupling modeled using Professional Engineer wildfire with the exact dimension as used in experimental setup. A number of analytical methods have been applied to unbalance response such as the transfer matrix method, the finite element method (Lee and Ha, 2003) and the component model synthesis method (Rao, et al 2007; Ogbonnaya, et al 2010).

Unbalance response investigations of geared rotor bearing systems, based on the finite element modeling was carried out by Neriya, et al (2009) and Kahraman, et al (2009) utilizing the model analysis technique. Besides, based on the transfer matrix modeling, Lida et al (2009) and Iwatsubo et al (2009) reported on studies utilizing the usual procedure of solving simultaneous equations while Choi and Mau, (2009) utilized the frequency branching technique to carry out the same analysis.

Further concerning unbalance response investigations of dual shaft rotor-bearing system coupled by bearing, (Hibner, 2007 and Gupta et al., 2003) carried out investigation utilizing the usual procedure of solving simultaneous equations based on transfer matrix modeling. However, all of the above investigations resulted in full numerical solutions of the unbalance response of coupled two shaft rotor bearing systems. On the other hand, Rao (2006) suggested analytical closed-form expressions for the major and minor axis radii of the unbalance response or bit for one-shaft rotor bearing.

http://dx.doi.org/10.5772/58829

2.1. Active balancing and vibration control of rotor system

It is well established that the vibration of rotating machinery can be reduced by introducing passive devices into the system (Gupta, *et al*, 2003). Although an active control system is usually more complicated than a passive vibration control scheme, an active vibration control technique has many age advantages over a passive vibration control technique.

First, active vibration control is more effective than passive vibration control in general (Shiyu, and Jianjun 2001). Second, the passive vibration control is of limited use if several vibration modes are excited. Finally, because the active actuation device can be adjusted according to the vibration characteristics during the operation, the active vibration technique is much more flexible than passive vibration control.

2.1.1. Active balancing techniques

A rough classification of the various balancing methods is shown in figure 2. The most recent development in active balancing is summarized in the dashed-lines shown in figure 2.

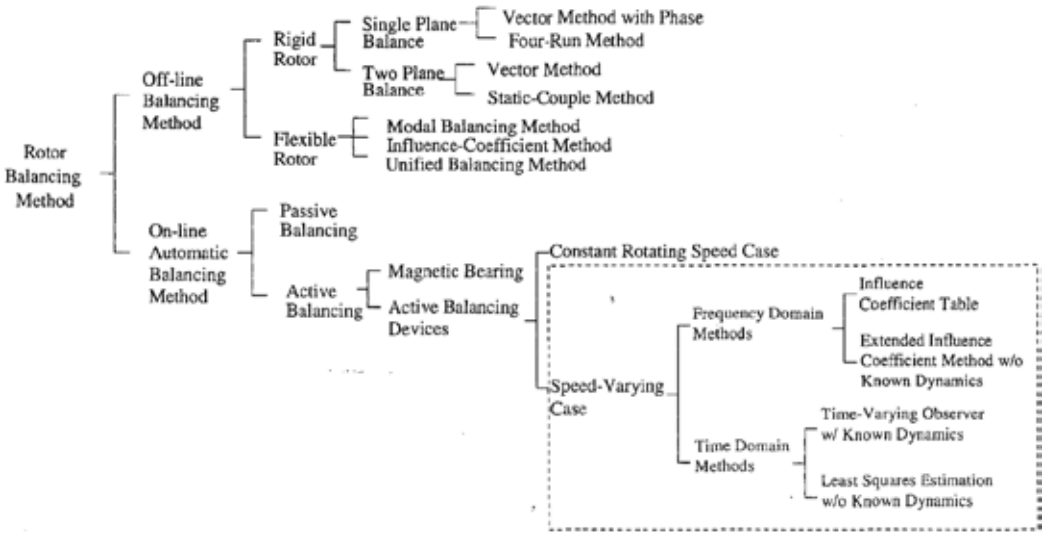

Figure 2. Classification of balancing methods; *Source:ShiyuandJianjun* (2001)

The rotor balancing techniques can be classified as offline balancing methods and real-time active balancing methods. Since active balancing methods are extensions of off-line balancing methods, a review of off-line methods thus is provided (Shiyu and Jianjun, 2001).

2.1.2. Off-line balancing methods

The off-line rigid rotor balancing method is very common in industrial applications. In this method, the rotor is modeled as a rigid shaft that cannot have elastic deformation during operation. Theoretically, any imbalance distribution in a rigid rotor can be balanced in two different planes. Methods for rigid rotors are easy to implement but can only be applied to low-speed rotors, where the rigid rotor assumption is valid. A simple rule of thumb is that rotors operating under 5000 rpm can be considered rigid rotors. It is well known that rigid rotor balancing methods cannot be applied to flexible rotor balancing. Therefore, researchers developed modal balancing and influence coefficient methods to off-line balance flexible rotors.

Modal balancing procedures are characterized by the use of the modal nature of the rotor response. In this method, each mode is balanced with a set of masses specifically selected so as not to disturb previously balanced, lower modes. There are two important assumptions: (1) the damping of the rotor system is so small that it can be neglected and (2) the mode shapes are planar and orthogonal. The first balancing technique similar to modal balancing was proposed by Hibner (2007). This method was refined in both theoretical and practical aspects in Ogbonnaya (2004).

Many other researchers also published works on the modal balancing method, including Rao (2006). Their work resolved many problems with the modal balancing method such as how to balance the rotor system when the resonant mode is not separated enough, how to balance the rotor system with residual bow, how to deal with the residual vibration of higher modes, and how to deal with the gravity sag. An excellent review of this method can be found in Rao (2006). Most applications of modal balancing use analytical procedures for selecting correction masses. Therefore, an accurate dynamic model of the rotor system is required. Generally, it is difficult to extend the modal balancing method to automatic balancing algorithms.

2.2. Self-excitation and stability analysis

The forces acting on a rotor shaft system are usually external to it and independent of the motion. However, there are systems for which the exciting force is a function of the motion parameters of the system, such as displacement, velocity, or acceleration (Ogbonnaya, 2004). Such systems are called self-excited vibrating systems since the motion itself produces the exciting force. The instability of rotating shafts, the flutter of turbine blades, the flow induced vibration of pipes and aerodynamically induced motion of bridges are typical examples of the self-excited vibration (Rao, 2006).

2.3. Dynamic stability analysis

A system is dynamically stable if the motion or displacement coverage or remains steady with time. On the other hand, if the amplitude of displacement increases continuously (diverges) with time, it is said to be dynamically unstable (Ogbonnaya, 2004). The motion diverges and the system becomes unstable if energy is fed into the system through self-excitation. To see the

http://dx.doi.org/10.5772/58829

circumstances that lead to instability, we consider the equation of motion of a single degree of freedom system as shown in equation 1:

$$M\ddot{x} + C\ddot{x} + kx = 0 \tag{1}$$

If solution of the form $x(+)C_e^{st}$ when C is a constant, assuming the equation 1 lead to characteristic equation

$$S^2 + \frac{C}{m}s + \frac{k}{m} = 0 \tag{2}$$

The root of this equation is as shown in equation 3:

$$S_{12} = \frac{C}{2m} + \frac{1}{2}\left[\left(\frac{C}{m}\right)^2 - 4\left(\frac{K}{m}\right)\right]^{1/2} \tag{3}$$

Since the solution is assumed to be $x(+)C_e^{st}$, the motion will be diverging and a periodic, if the roots S_1 and S_2 are complex conjugates with positive real parts. Analyzing the situation, let the roots S_1 and S_2 of equation 2 be expressed as:

$$S_1 = P + iq, \quad S_2 = P + iq \tag{4}$$

Where p and q are real numbers so that:

$$\begin{aligned}\left(S - S_1\right)\left(S - S_2\right) &= S^2 - \left(S_1 S - S_2 S + S_1 S_2\right) = m + \frac{k}{m} \\ &= S^2 + \frac{C}{m}S + \frac{k}{m} = 0\end{aligned} \tag{5}$$

Equations 4 and 5 therefore become

$$\frac{C}{m} = \left(S_1 + S_2\right) = -2P_1 \frac{k}{m} = S_1 S_2 = P^2 + q^2 \tag{6}$$

From equation (6), it is shown that for negative P_1, c/m must be positive and for positive $P^2 + q^2$, $\frac{k}{m}$, must be positive. Thus the system will be dynamically stable if C and k are positive (assuming that M is positive).

2.3.1. Balancing operation and result

The necessary mass was added at the chosen shaft end shown in figure 3 in order to determine the desired dynamic behaviour. Due to the relatively small rotor radius, it was necessary to use a significant mass; otherwise the obtained influence would have been too low.

Figure 3. Picture of the used balancing plane; *Source:ShiyuandJianjun* (2001)

2.4. Rotor dynamic model of the shaft line

The complete shaft line was modeled (figure 4) by using the MADYN 2000 software. The model was based on scaled drawings. The four fluid film bearings were calculated with the ALP3T program. The static load of the different bearings was determined by aligning the shaft only, taking into account the flexibility of the different rotors, in a way that the couplings are free of bending moments. The present oil film thickness at nominal speed was not considered in this static calculation.

All bearing pedestals were modeled as pure stiffness and mass. This assumption was tested by performing impact tests on the bearing structure in both vertical and horizontal direction. No resonance frequencies were detected below 50Hz or at multiples of this frequency. Therefore it was decided to determine the static stiffness obtained at 50Hz and use this value for the complete frequency range of the different calculations.

There was only poor rotor dynamic information given by the manufacturer, so it was not possible to completely verify the model. However, the calculated results fitted both the basic available rotor dynamic info arid the measured vibration data quite well. From the calculated eigen values at 50Hz two modes seemed to be present near the operating speed of the shaft line (figure 4).

http://dx.doi.org/10.5772/58829

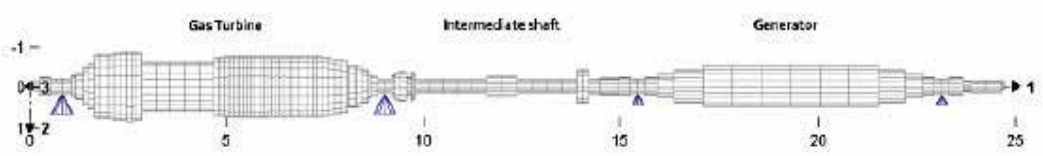

Figure 4. Rotor dynamic shaft line model; *Source: Kris, et. al* (2010)

The closest modes influencing the dynamic behaviour are at respectively 51.9Hz and 53.3Hz. The first eigen mode is the second vertical bending mode of the gas turbine and is unlikely to be causing high vibrations near the generator shaft end. The second eigen mode is a horizontal bending mode of the shaft end. From the eigenvalue analysis it is clear that the damping factor is poor and the mode deformation is almost completely planar (whirling factor of 0). This mode shape is shown in figure 5 and shows clearly the planar deformation near the shaft end. As shown in figure 6, shaft lines can also be represented in 3-D mode shape.

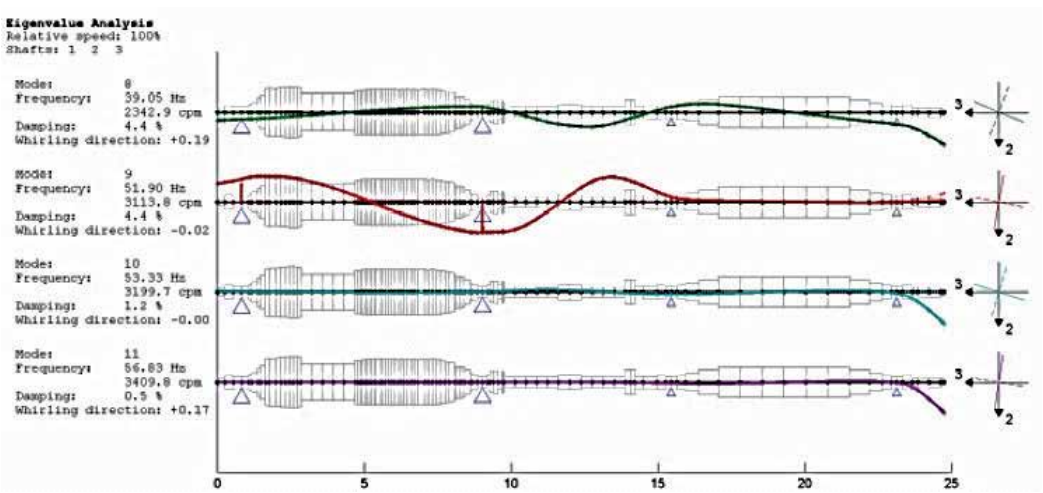

Figure 5. Eigenvalue analysis of the shaft line; *Source: Kris, et. al* (2010)

Based on the measured direct orbit shapes, it was possible to conclude that it was this shaft end mode that was responsible for the high shaft vibrations causing the automatic shutdown of the unit during startup (figure 7). One can clearly see that there is a local horizontal deformation at the generator nondestructive examination measuring plane near nominal speed; but for all the other measuring planes, the relative shaft vibration amplitudes remain rather low.

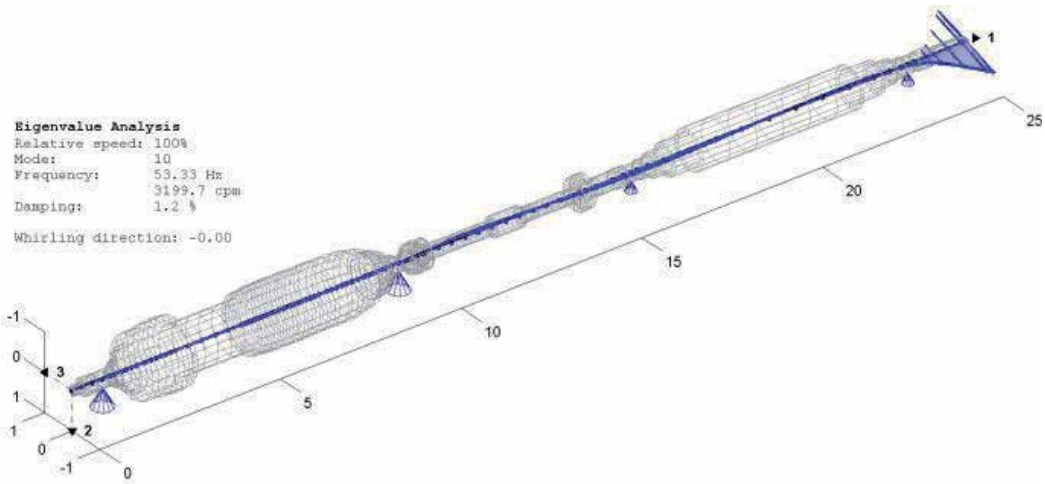

Figure 6. 3D mode shape of the bending critical of the shaft end; *Source: Kris, et. al* (2010)

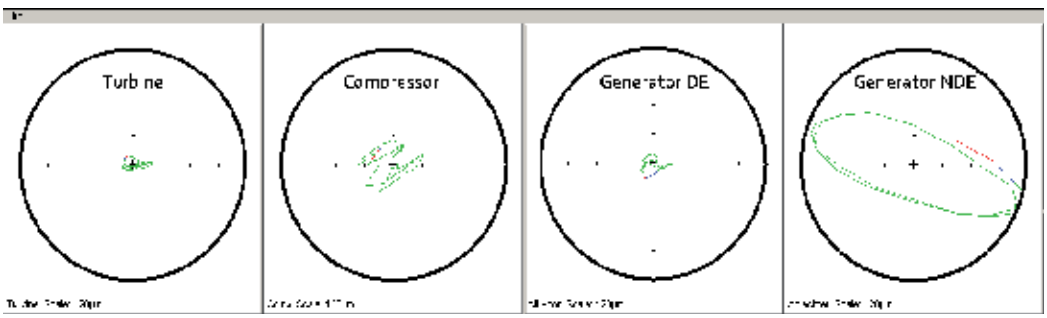

Figure 7. Direct orbit plots at 2980rpm; *Source:Gupta,etal* (2003)

From these results, it was also clear that the "usual" balancing planes at both ends of the generator rotor were not recommended to balance this present unbalance. However, from local inspections of the shaft end, it became clear that it would be possible to do a balancing test run with a mass connected at the end of the shaft line on a rather non-conformistic plane (figure 8). This plane would be the best location because the mode deformation is the highest at the shaft end. This location would also make the balancing plane easily accessible for further adjustment of the mass.

An unbalance calculation was done in order to have an idea of the expected response of the generator. The used weight for this calculation was determined by applying a GT unbalance; based on the weight of this free shaft end (figure 9).

http://dx.doi.org/10.5772/58829

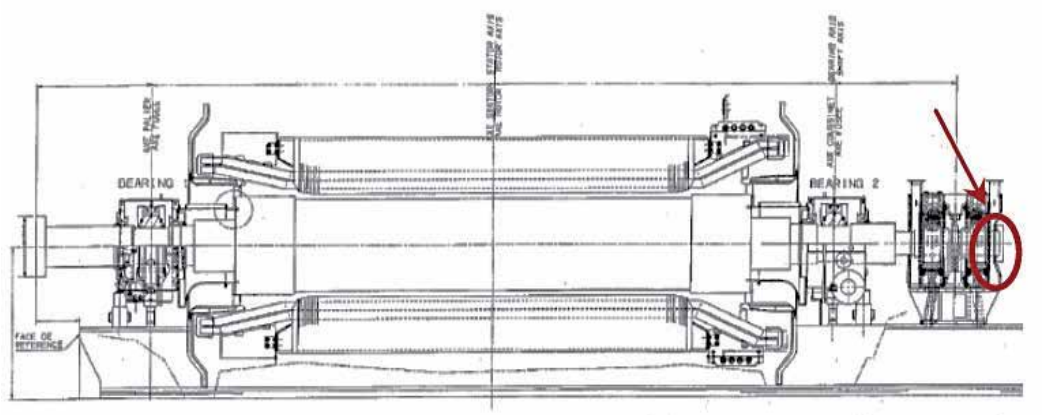

Figure 8. Chosen balancing plane of the generator shaft end; *Source:Gupta,etal* (2003)

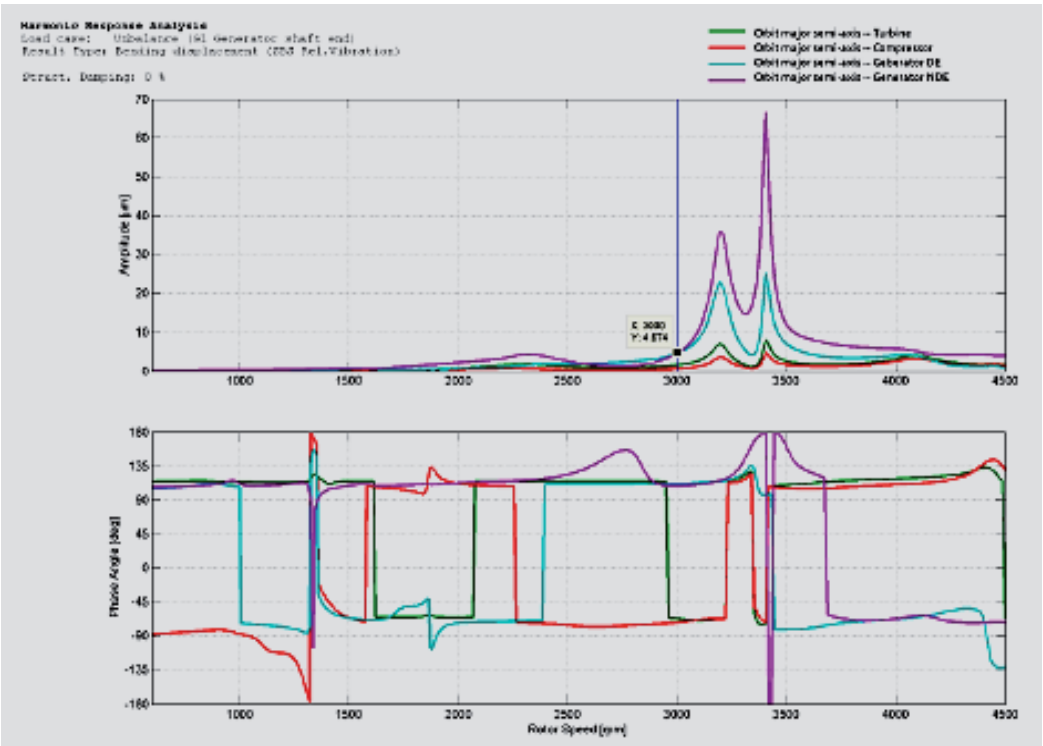

Figure 9. G1 unbalance of the shaft end; *Source:Gupta,etal.* (2003)

This unbalance response shows that there is a certain influence at 50Hz due to this added unbalance, however to balance the shaft end, a correction mass of about 15 times higher would be needed to bring down the actual shaft vibration amplitudes to acceptable levels. The resulting dynamic behaviour of the shaft line is shown in figure 10 and shows that there is an important reduction of the relative shaft vibrations around 3000rpm. This confirms of course that this shaft end mode was the main reason for the increased shaft vibrations.

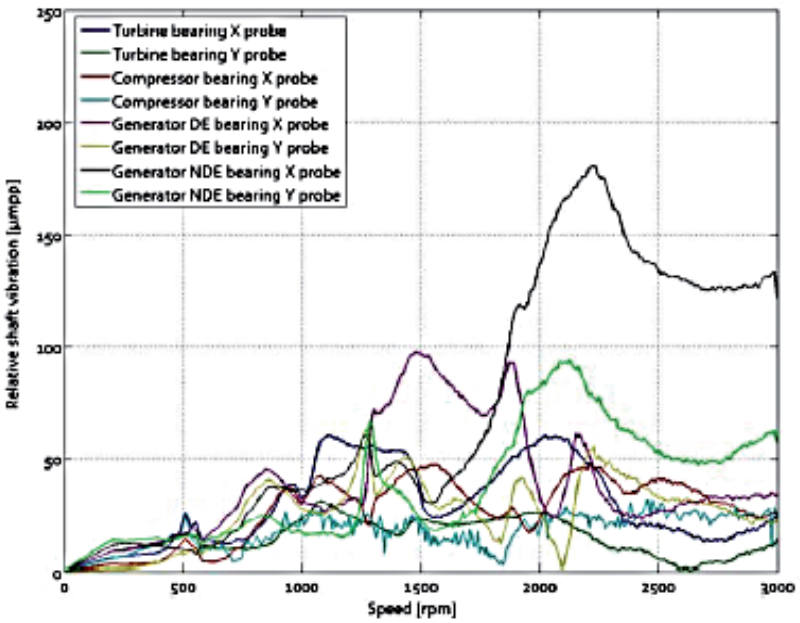

Figure 10. Relative shaft vibration amplitudes after balancing; *Source:Gupta,etal.* (2003)

This balancing correction was done completely remotely. Only a local maintenance responsible went on-site to attach the balancing weight. This made it possible to react quickly on this vibration issue and reduced the unforeseen downtime of the unit to a minimum. The unit could be restarted the same day without any vibrations alarms and a more extensive balancing of the present residual unbalance of the rotor could be scheduled at a more appropriate moment in the maintenance planning.

3. Methodology for blade vibration analysis

Rotor shafts are amongst rotor dynamic components subjected to perhaps the most arduous working condition in high performance rotating equipment used in process and utility plants such as high-speed compressor, steam and gas turbines generators, pumps, etc. Although usually quite robust and well designed, shafts in operation are sometimes susceptible to serious defects that develop without much warning.

http://dx.doi.org/10.5772/58829

In exploitation of rotating machines, some of the observed phenomena are considered to be particularly undesired from the view point of effectiveness and safety. Excessive stress concentrations and rubbing effects occurring between stator and rotors attached to flexible shafts subjected to lateral vibrations can be given as examples of such a detrimental behavior. The modern responsible and heavily affected rotating machines must assure possibly high level of reliability, durability and safety in operation. For these reasons, their design process should be performed very thoroughly in order to obtain relatively small magnitude of unavoidable dynamic excitation, e.g. due to residual unbalance, gas pressure force or electromagnetic force. While aiming at realistic modeling of rotor shaft systems, the actual stochastic nature of important model parameters should be taken into account. In the previous section, different references have been made to the problems of rotor shaft dynamic modeling. A lot of reasons were given as regards to the need to the modeling approach; however, all-inclusive approach must be employed to tame the problems. This involves the understanding of the theoretical model of a rotor shaft, assessment of rotor-shaft vibration due to uncertain residual unbalances and as well as the modeling dynamic response analysis. Therefore, all the modification discussed in this chapter only affects the GT rotor shaft system.

3.1. Theoretical model of a bowed rotor shaft

A typical rotor with a bowed unbalanced shaft is presented in Ogbonnaya (2004). All phase angles are measured with respect to a reference timing mark on the shaft. Suppose the shaft has a residual bow of ∂_r and a phase of ϕ_r, then the mass centre of the disk would be displaced by a distance, e_u from the shaft centre line. This results in a dynamic unbalance response as the shaft rotates.

Suppose the magnitude and phase angle of the combined electrical and mechanical run-out respectively, then the total observed response is:

$$\partial = \partial_r + \partial_s + \partial_o \tag{7}$$

Where:

∂r=bow vector

∂s=response to the mass unbalance vector and the bow vector

∂o=run-out vector

Assumptions:

a. No gyroscopic pull occur (since the disc always rotates in its own plane)

b. Shaft mass is considered negligible (compared to the rigid disc mass)

c. Both shaft and disc rotate with uniform angular velocity, ω

d. The supports are taken as rigid

The equation of motion for a simple rotor with imbalance and shaft bow has been used to obtain the steady state non-dimensionalised rotor response as a function of rotor speed as follows:

$$\bar{z} = \frac{\bar{\delta}_r e^{-i\varnothing r} + f^2 e^{-i\varnothing m}}{1 - f^2 + 2i\xi f} \tag{8}$$

Where:

ϕ_o=angle between the rotor run-out vector and the timing mark (equation 9)

ϕ_r=angle between the bow vector and the timing mark

ϕ_m=angle between the mass unbalance vector and the timing mark

ϕ= phase angle between the shaft centerline response vector and the timing mark (equation 9)

f= frequency ratio, ω / ω_{cr} = $\frac{\text{rotational speed}}{\text{rotor critical speed}}$

ξ =damping ratio, c / c_{cr}

∂_r =residual bow

C=shaft damping, Nm/rad

C_{cr} =critical speed (with low compensation C)

Consider a shaft with electrical and/or mechanical run-out. The run-out vector is also non-dimensionalized by an unbalance eccentricity given by:

$$\bar{\delta}_o = \frac{\delta_o}{e_u}$$

Where e_u=unbalance eccentricity vector (this run-out vector is constant and independent of the shaft rotational speed).

Using the principles of superposition, the constant response due to run-out may be added to equation 3 for steady state response to yield:

$$\bar{z} = \frac{\bar{\delta}_r e^{-i\varnothing r} + f^2 e^{-i\varnothing m}}{1 - f^2 + 2i\xi f} + \bar{\delta}_o e^{-i\varnothing o} \tag{9}$$

If $\gamma=\phi_r-\phi_m$, then equation 9 becomes:

$$\bar{z} = \alpha_r \bar{\delta}_r e^{-i\varnothing r} + \alpha_r e^{-i\varnothing m} + \alpha_r \delta_o e^{-i\varnothing o} \tag{10}$$

http://dx.doi.org/10.5772/58829

Where:

α_r= influence coefficient due to bow=$\frac{1}{(1-f^2 2i\xi f)}$

α_m=influence coefficient due to mass unbalance=$\frac{f^2}{(1-f^2 2i\xi f)}$

α_0=influence coefficient due to run-out=1

Separating $\bar{z}$ in equation 10 into real and imaginary components $(\bar{z} = {}_r + i_i)$, yields

$$\bar{z}_r = \frac{\left(\bar{\delta}_r, \cos\varphi, + f^2 \cos\varphi_m\right)\left(1-f^2\right) - 2\varsigma f\left(\bar{\delta}_r, \sin\varphi_r + f^2 \sin\varphi_m\right)}{\left(1-f^2\right)^2 + \left(2\varsigma f\right)^2} + \bar{\delta}_0 \cos\varphi_0 \tag{11}$$

$$\bar{z}_i = \frac{\left(\bar{\delta}_r, \sin\varphi, + f^2 \sin\varphi_m\right)\left(1-f^2\right) + 2\varsigma f\left(\bar{\delta}_r, \cos\varphi_r + f^2 \cos\varphi_m\right)}{\left(1-f^2\right)^2 + \left(2\varsigma f\right)^2} + \bar{\delta}_0 \sin\varphi_0 \tag{12}$$

Therefore, the shaft amplification factor and phase angle are respectively:

$$A = \sqrt{\bar{z}_r} + \bar{z}_i^2 \tag{13}$$

and

$$\theta = \tan^{-1}\left[\bar{z}_i \Big/ \bar{z}_r \right] \tag{14}$$

respectively

For the response of the bowed rotor at slow roll, substitute f=0 into equation 15 to get:

$$\bar{Z}_o = \bar{\delta}_r e^{-i\varnothing r} + \bar{\delta}_o e^{-i\varnothing m} \tag{15}$$

$$\therefore \quad \bar{z}_r\big|_o = \bar{\delta}\cos\phi_r + \bar{\delta}\cos\phi_o \tag{16}$$

$$\text{and} \qquad \bar{z}_i\big|_{\text{o}} = \bar{\delta}\cos\phi_{\text{r}} + \bar{\delta}\cos\phi_{\text{o}} \tag{17}$$

Note: for the case of bowed shaft, the run-out compensator and subtractor compensate for shaft run-out, thereby presenting the response for the rotor as if it had only unbalance with no run-out. Therefore, equations 9 and 10 are the quantities the compensator subtracts from the total response of a bowed rotor at all other speeds. Let this quantity be designated by $\bar{z}_c$ for a bowed rotor compensated for electrical/mechanical run-out.

$$\therefore \qquad \bar{z}_c = \bar{z} - \bar{z}_0 = \frac{\delta_r e^{-i\varphi_r} + f^2 e^{-i\varphi_m}}{1 - f^2 + 2i\xi f} - \delta_r e^{-i\varphi_r} \tag{18}$$

Rearranging equation (18) and combing like terms yields:

$$\bar{Z}_c = \frac{(f^2 - 2i\xi f)\bar{\delta}_r e^{-i\varnothing m}}{1 - f^2 + 2i\xi f} \tag{19}$$

which can also be put as:

$$\bar{Z}_c = \alpha_{rc}\bar{\delta}_r e^{-i\varnothing r} + \alpha_m e^{-i\varnothing m} \tag{20}$$

Where α_{rc}=influence coefficient for compensated bow and given by:

$\alpha_{rc} = \dfrac{(f^2 - 2i\xi f)}{1 - f^2 + 2i\xi f}$ as $\alpha_{rc} \to \alpha_m$ for *large* f.

The response due to compensated bow and an equal unbalance eccentricity are equal.

3.2. Mathematical modeling of dynamic response of GT rotor shaft

When a system is subjected to force harmonic excitation, its vibration response takes place at the same frequency as that of the excitation. Common sources of harmonic excitation are: unbalance of the rotating shaft, forces produced by reciprocating machines, or the motion of the machine itself. These vibrations are undesirable to equipment whose operation may be distributed. Resonance is to be avoided in general, and to prevent large amplitudes, vibration isolators are often used.

http://dx.doi.org/10.5772/58829

3.2.1. Response of single degree of freedom system

According to Ogbonnaya (2004), a rotor shaft can be modeled using the single degree of freedom system shown in figure 11(a) and the free body diagram as presented in figure 11(b).

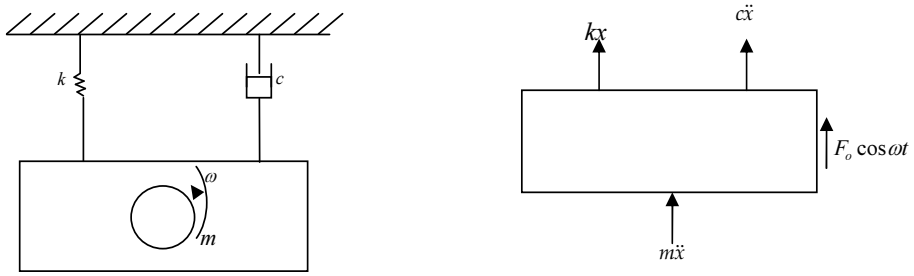

(a) Model of rotor shaft (b) Free body diagram

Figure 11. Model of a rotor shaft system

From the figures above, the equation of motion can be stated as shown in equation 21.

$$m\ddot{x} + c\dot{x} + kx = 0 \tag{21}$$

3.2.2. Impulse response approach

Figures 12 (a) and (b) show the forcing function in the form of a series of impulses and unit impulse excitation at t=ζ, while figure 12 (c) represents the impulse response function.

Here, consideration was given to the forcing function x(t) to be made up of a series of impulse of varying magnitude as shown in figure 12a. Let the impulse applied at time τ be denoted as $x(\tau)\, d\tau$. If $y(t)=H(t-\tau)$ denotes the response of the unit impulse excitation, δ (t-τ), it is called the impulse response function. The response to the total excitation is:

$$y(t)=\int_{-\infty}^{t} x(\tau)h(t-\tau)d\tau \tag{22}$$

Since h (t-τ)=0 when t < τ or τ > t, the upper limit of integration can be replaced by ∞ so that:

$$y(t)=\int_{-\infty}^{\infty} x(\tau)h(t-\tau)d\tau \tag{23}$$

By changing the variables from τ to θ=t – τ, equation 23 can be written as:

$$y(t)=\int_{-\infty}^{\infty} x(t-o)h(o)d\theta \tag{24}$$

The response of the system y(*t*) can be known if the impulse response function h (t) is known.

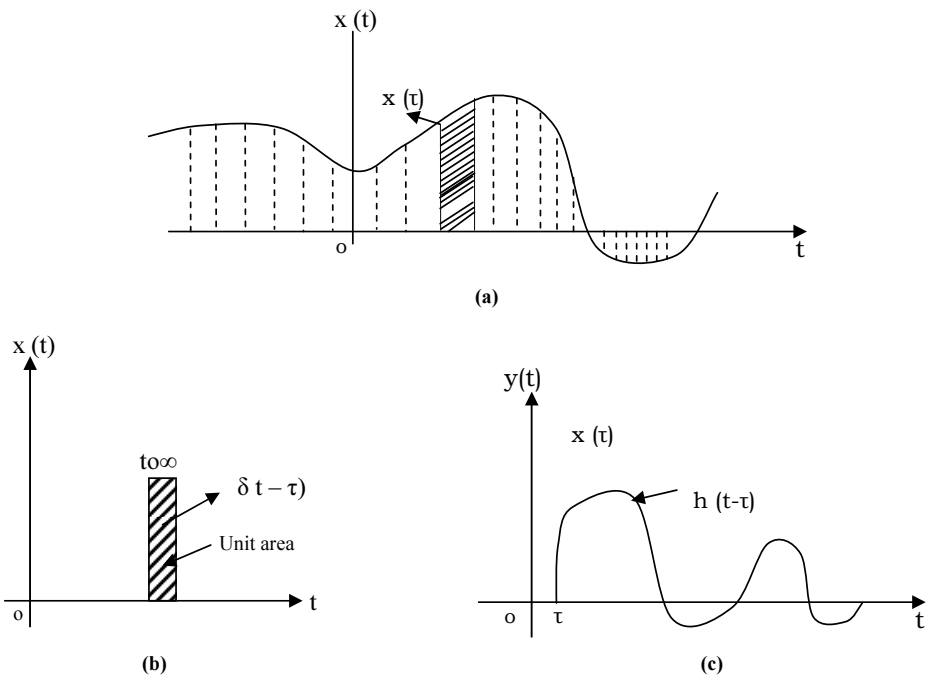

Figure 12. (a) forcing function in the form of series of impulses; (b) Unit impulse excitation at t=τ; (c) Impulse response function; *Source: Sadhu, (2006)*

3.2.3. Frequency response approach

In this case, the transient function x(*t*) can be expressed in terms of its Fourier transform x(*ω*) as:

$$x(t)=\frac{1}{2\pi}\int_{\omega=-\infty}^{\infty}x(\omega)e \tag{25}$$

Consider the forcing function of unit modulus as:

$$\bar{x}(t)=e^{i\omega t} \tag{26}$$

Its response can be denoted as;

$$\bar{y}(t)=H\left(\omega\right)e^{i\omega t} \tag{27}$$

Where: H (ω) is called the complex frequency response function. Thus, the total response is:

$$y(t)=H(\omega)x^{t}=\int_{-\infty}^{\infty}H(\omega)\frac{1}{2\pi}x(\omega)e^{i\omega t}d\omega \tag{28}$$

If y (ω) denotes the Fourier transform of the response function y (t), then:

$$y(t)=\frac{1}{2\pi}\int_{-\infty}^{\infty}x(\omega)e^{i\omega t}d\omega \tag{29}$$

Comparing equations 27 and 28 we get:

$$x(\omega)=H(\omega)x(\omega) \tag{30}$$

Equation (30) can be used to find the response of the system once H (ω) is known.

3.2.4. Computation of dynamic response of GT rotor shaft system

From the model of the rotor shaft system shown in figures 11(a) and (b), the equation of the motion for equilibrium can be written as:

$$\sum F=ma=m\ddot{x} \tag{31}$$

$F_o\cos\omega t+\omega-k(d_{st}+x)=m\ddot{x}$

Where d_{st} = elongation of the spring (meter)

$F_o\cos\omega t+\omega-kd_{st}-kx=m\ddot{x}$

But $\omega=kd_{st}$

$F_o\cos\omega t+kd_{st}-kd_{st}-kx=m\ddot{x}$

$F_o\cos\omega t-kx=m\ddot{x}$

$$m\ddot{x}+kx=F_o\cos\omega t \tag{32}$$

By considering damping force, equation (32) can be further expressed as:

$$m\ddot{x}+c\dot{x}+kx=F_o\cos\omega t \tag{33}$$

$$\ddot{x}+\frac{c}{m}\dot{x}+\frac{k}{m}x=\frac{\ddot{F}_o\cos\omega t}{m} \tag{34}$$

but $\frac{c}{m}=2\mu$ and $\frac{k}{m}=\omega_n{}^2$ (Ogbonnaya, et al; 2013); where μ is the slip factor which is the parameter describing how much the rotor exit flow angle deviate from the actual blade angle; i.e. fouling/corrosion factor. Hence, equation (34) is modified as:

$$\ddot{x}+2\mu\dot{x}+\omega_n{}^2x=0 \tag{35}$$

Equating the complementary function to zero, gives:

$$x_1=C_1e^{\left[-\mu+\sqrt{\mu^2-\omega^2}\right]t}+C_2e^{\left[-\mu+\sqrt{\mu^2-\omega^2}\right]t} \tag{36}$$

$x_1=C_1e^{\left[-\mu+\sqrt{\mu^2-\omega^2}\right]t}+C_2e^{\left[-\mu+\sqrt{\mu^2-\omega^2}\right]t}$

$x_2=[C_1+C_2t]e^{-\mu t}$

$x_3=e^{-\mu t}[A\cos\sqrt{(\omega^2-\mu^2)}t+B\sin\sqrt{(\omega^2-\mu^2)}t$

The general solution of equation (34) thus, is given by:

$$X=\frac{F_o}{m}\left[\frac{\sqrt{4\mu^2\omega^2+(\omega_n{}^2-\omega^2)^2}}{4\mu^2\omega^2+(\omega_n{}^2-\omega^2)^2}\cos(\omega t-\alpha)\right] \tag{37}$$

The overall solution is a combination of the complementary function and the general solution given as follows:

$$X=\frac{F_o}{m\sqrt{4\mu^2\omega^2+(\omega_n{}^2-\omega^2)^2}} \tag{38}$$

The vibration displacement amplitude is observed as:

$$F_o=XM\sqrt{4\mu^2\omega^2+(\omega_n{}^2-\omega^2)^2} \tag{39}$$

where:

$$F_o=XM\sqrt{4\mu^2\omega^2+(\omega_n{}^2-\omega^2)^2} \tag{40}$$

http://dx.doi.org/10.5772/58829

Figure 13 shows the flow chart for obtaining the dynamic response of a rotor shaft. This is actualized by evaluation of the program code written in C++programming language from figure 12a. The program helped in the calculation of dynamic response by inputting the values obtained from GT 17 of Afam Power Station into the equation 40. The result shows that the rotor vibration response takes place at the same frequency as that of the excitation.

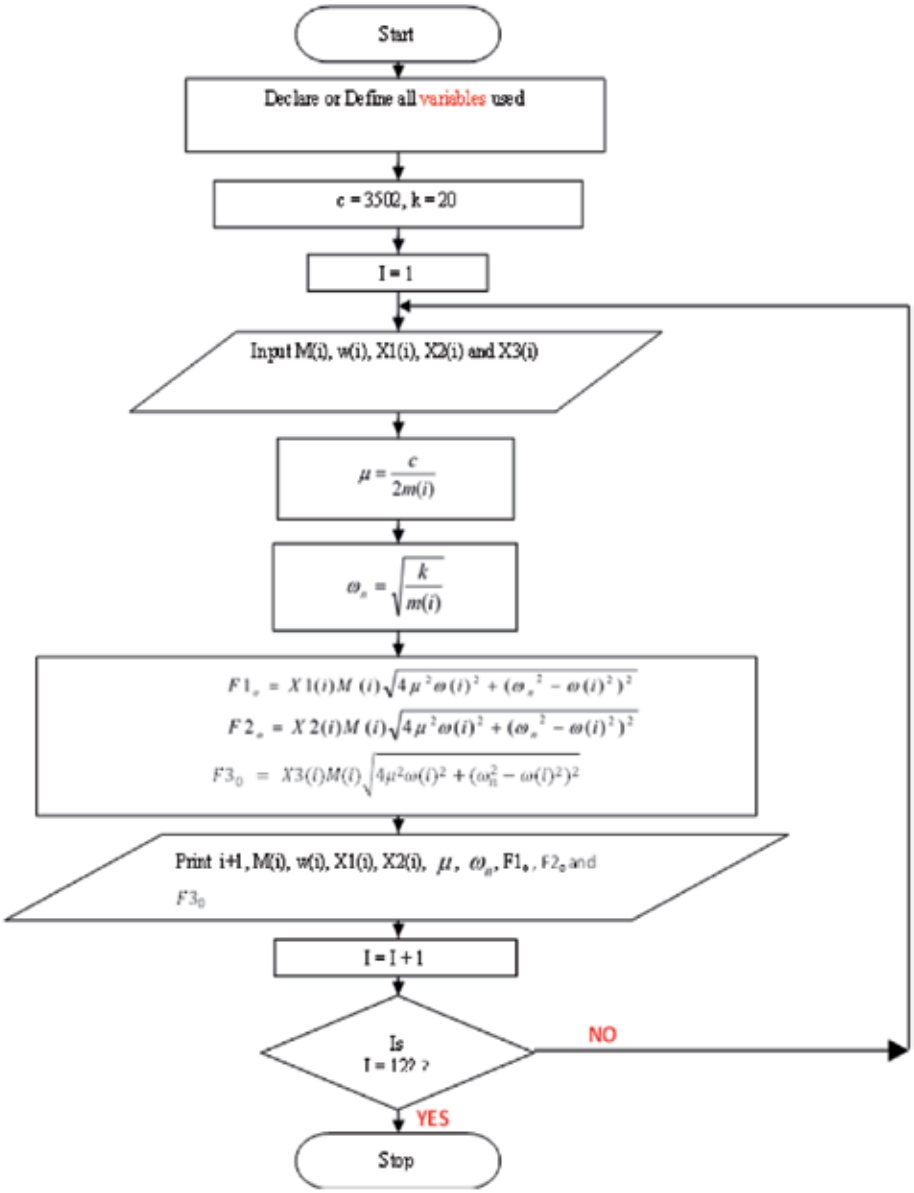

Figure 13. Program Flow Chart of the rotor Shaft Dynamic Response

4. Analysis

Gas Turbine, GT unit 17 is a healthy engine. The horizontal readings of natural frequency (ω_n) taken from healthy GT 17 and engine data are presented in Table 1, while the other parametric characteristics of the Afam GT 17 system used are shown in Appendix A. However, these readings were taken alongside the corresponding speed at different times for active and reactive loads.

Time (hr)	Speed (RPM)	Active load (KW)	Natural frequency, (ω_n)	Vibration amplitude (Br1) (mm)	Vibration amplitude (Br2) (mm)	Vibration amplitude (Br3) (mm)
01.00	3063	50	321.7	4.8	6.2	0.9
02.00	3076	50	322.3	4.8	6.2	0.8
03.00	3074	50	321.7	4.6	6.2	0.9
04.00	3077	50	322.3	4.9	6.2	0.8
05.00	356	50	320.4	4.9	6.2	0.9
06.00	3001	50	316.7	5.1	6.3	1.0
07.00	3063	45	321.0	5.1	6.5	1.0
08.00	3076	40	322.3	5.3	6.5	0.9
09.00	3028	40	318.6	5.0	6.7	1.2
10.00	3081	36	323.6	5.1	6.4	0.9
11.00	3053	35	319.8	5.2	6.5	1.0
12.00	3.53	45	316.0	5.2	6.4	1.2
13.00	3005	37	314.2	5.2	6.6	1.7
14.00	3060	42	319.8	5.0	6.7	0.9
15.00	3056	41	319.2	5.3	6.5	0.9
16.00	3021	41	319.2	5.1	6.6	0.9
17.00	3077	40	322.9	51.2	6.6	0.9
18.00	3070	42	318.6	5.0	6.5	0.9
19.00	3074	42	321.0	5.0	6.5	0.9
20.00	3074	47	322.9	5.0	6.4	1.0
21.00	3065	40	321.0	5.0	6.6	1.2
22.00	3072	42	421.7	5.0	6.5	1.4
23.00	3077	50	322.3	5.0	6.4	1.3
24.00	3086	30	321.7	5.0	6.3	1.2

Table 1. Operational Data from Healthy GT 17 of Afam Power Station

http://dx.doi.org/10.5772/58829

4.1. Discussion

Table 1 shows the result of vibration displacement amplitude of bearings 1, 2 and 3 as a function of time. From the graph presented in figure 14, it was observed that bearing 1 and 2 started vibrating as soon as the engine was powered, while bearings 3 delayed for some operational interval before vibrating. The graph shown in figure 14 also shows that the machine tends to vibrate in higher displacement amplitude and sometimes slows down as the engine continues in operation (i.e. in fluctuating manner).

Depicted in figure 15 is the graph of the response of the system against time. Here, it is shown clearly that the forcing function x (t) is made up of series of impulses of varying magnitude. The impulse response was found to correspond with the sinusoidal shape as expected.

Figure 16 conversely shows the graph of natural frequency against time. From the graph, the result shows that the natural frequency tends to vary with time. It is observed also that the vibration of the engine occurs as a function of natural frequency at a given time.

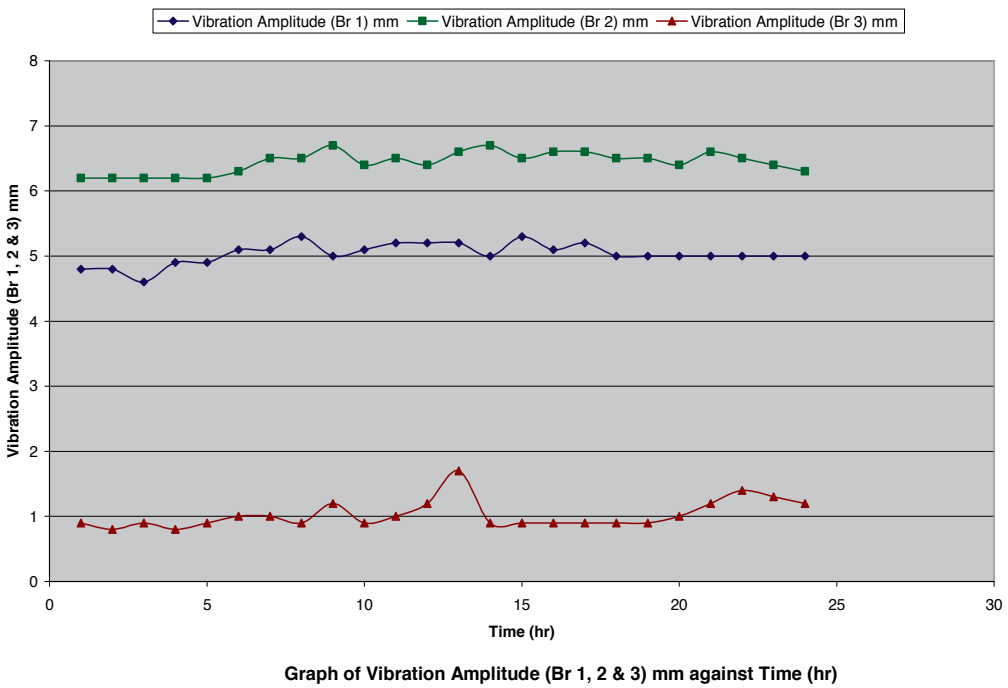

Figure 14. Vibration amplitude (Br 1, 2 & 3) mm against time (hr)

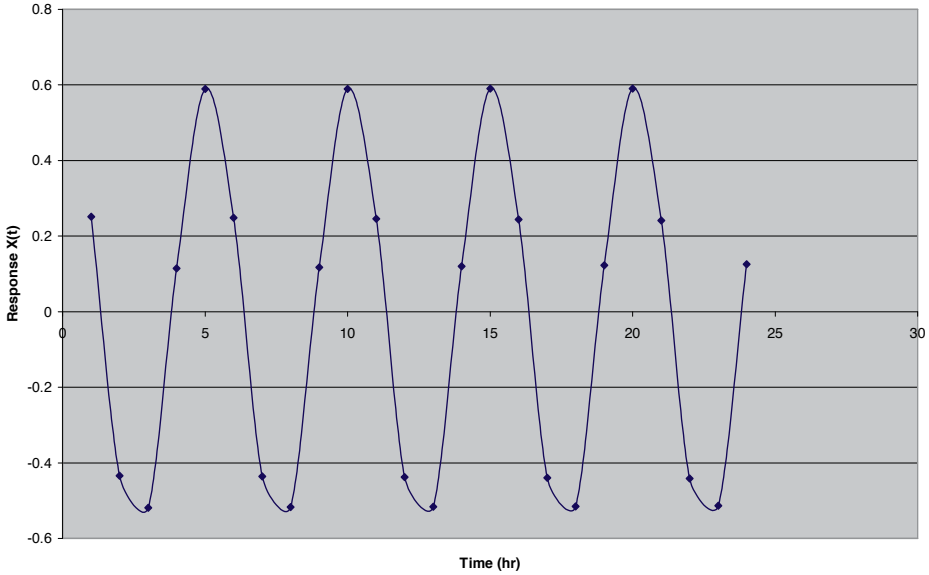

Figure 15. Response, X (t) against time (hr)

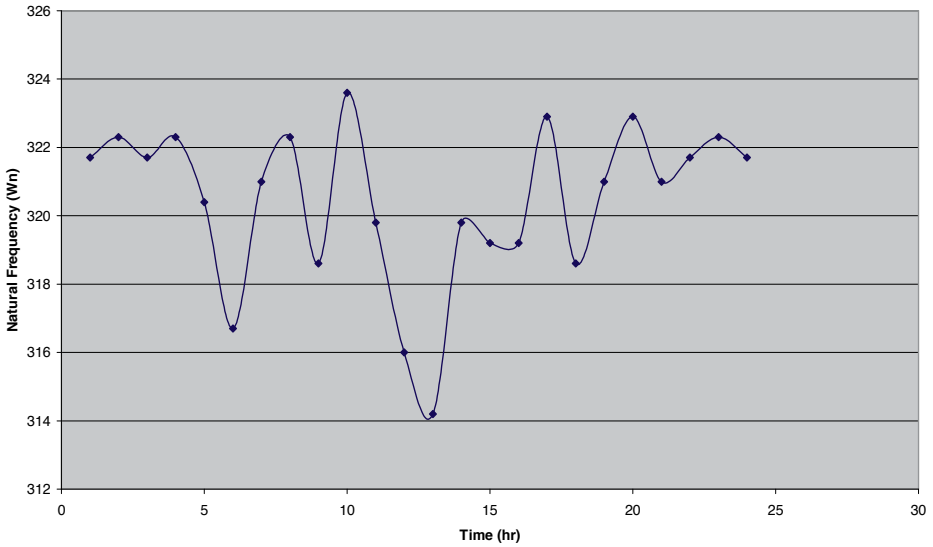

Figure 16. Natural frequency (ω_n) against time (hr)

Figure 17 further shows the graph of speed (rpm) with time. Hence, the sudden increase in speed as presented in the figure is capable of resulting to an increase in vibration at the given interval.

http://dx.doi.org/10.5772/58829

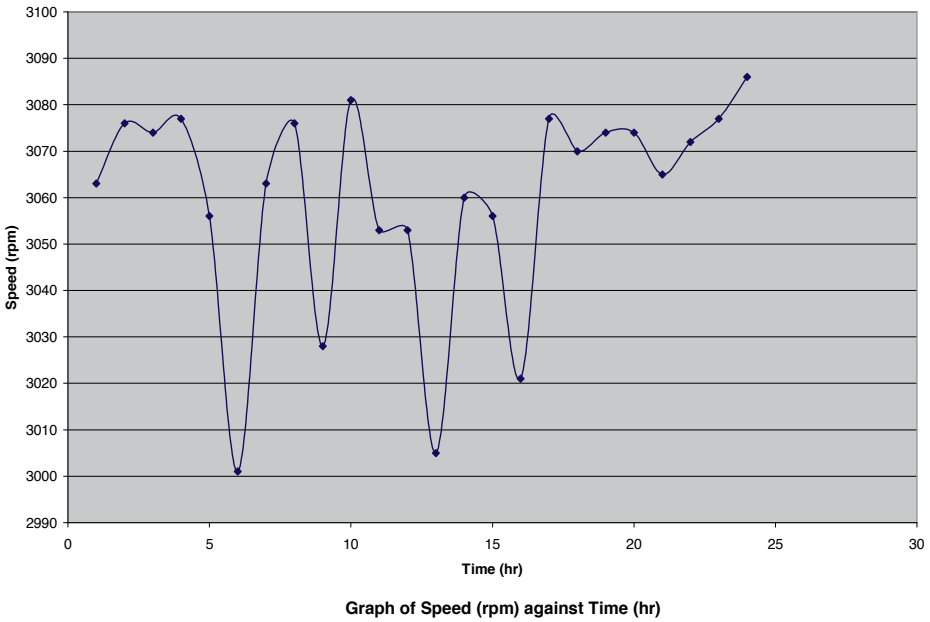

Figure 17. Speed (rpm) against time (hrs)

5. Conclusion

A work has been carried out on the modeling of dynamic response of marine GT rotor shaft systems. It is shown that when a system is subjected to force harmonic excitation, its vibration response takes place at the same frequency as that of the excitation.

To determine the response of the shaft under vibration, readings were collected from bearings 1, 2, and 3 of GT 17 in Afam thermal Station as shown in table 1, while the engine characteristics are shown in Appendix A. Equation 40 was developed to determine the response of the system under vibration. This mathematical equation is used to run a computer programme with a code in C++programming language.

6. Recommendations

The recommendations are as follows:

1. More attention should be paid to shaft vibrations as is the case with vibration on bearing.
2. Some factors which affect the performance of gas turbines on industrial duty should be considered while carrying out vibration based simulation of GT rotor shafts.

3. Errors and extraneous environmental factors should be put into consideration when modeling the response of rotor shaft under vibration.

4. GT rotor shaft systems should be provided with more supports to prevent adverse effects of eccentricity which leads to bow and whirl.

7. Appendix A

7.1. Characteristics of AFAM GT 17 system relevant to this work

Name of Equipment: Brown Boveri	Sulzer Turbo Maschinen
Manufacturer:	Asea Brown Boveri
Capacity:	75 MW
Year of Manufacture:	1981
Year of installation	1982
Year of commissioning	Nov 1982
Type:	13D
No of Turbine Rows:	5
No. of Compressor Rows:	17

Particulars of Rotor

Length of Rotor shaft:	8000mm
Moment of Inertia, I:	$586.2m^4$
Modulus of Elasticity, E:	$207GN/m^2$
Mean Diameter, :	1400mm
Density, ρ:	$7850kg/m^3$
Modulus of Rigidity, G:	$80GN/m^2$
Mass of Turbine shaft:	23500kg
Mass of Compressor shaft:	24000kg
Natural frequency, ω_n:	350rad/s
Damping Ratio, ζ:	0.9
Spring stiffness, K:	$1.5x10^6N/mm$
Maximum vibration limit:	7.0mm/s

Author details

E.A. Ogbonnaya[1], R. Poku[1], H.U. Ugwu[2], K.T. Johnson[3], J.C. Orji[3] and N. Samson[3]

1 Department of Marine/Mechanical Engineering, Niger Delta University, Wilberforce Island, Bayelsa State, Nigeria

2 Department of Mechanical Engineering, Michael Okpara University of Agriculture, Umudike, Abia State, Nigeria

3 Department of Marine Engineering, Rivers State University of Science and Technology, Port Harcourt, Rivers State, Nigeria

References

[1] Api 617 (2002) Axial and centrifugal compressor and expander-compressor for petroleum, chemical and gas industry services, 7th edition, Washington D.C, API publishing.

[2] Bader K.A (2010) Rotor dynamic analysis requirements in API Standards with case studies.Proceedings of *ASME Turbo Expo*. 2010. Power for land and sea and air, June 14-181010 Glasgow Paper No. GT 2010-23127.

[3] Choi, S.Y. and Mau (2009) Dynamitic analysis of geared rotor-bearing systems by the transfer matrix method.*ASME Design Engineering Technical Conferences*.(Part B), 84: 2967-2976.

[4] Eshleman, R. and Eubanks, A (2007) On the critical speeds of a continuous rotor, *Journal of Engineering for Industry*, 91: 1180-1188.

[5] Gupta, K. D.,Gupta K.and Athre, K (2003) Unbalance response of a dual rotor system: (theory and experiment) *Trans. Journal of Vibration and Acoustics*, 115: 427-435.

[6] Harilirua and Srinivasan P.S. (2010). Vibration analysis of flexible coupling by considering unbalance, *Middle East Journal of Scientific Research* 5 (5): pp 336-345, 2010.

[7] Hibner (2007) Dynamic response of viscous-damped multi-shaft jet engines. *Journal of Aircraft*, 12(4): 305-312.

[8] Iwatsubo, S.Arii, and Kawai, R, 2009. Coupled lateral-torsional vibration of rotor system trained by gears, *Bulletin of ASME*, 27(224): 271-277.

[9] Kahraman, A., Ozguven, H. N.,Houser D. R.and Zakrajsek, J. J, 2009.Dynamic analysis of geared rotors by finite elements, Transactions.*Journal of Mechanical Design*, 114: 507-514.

[10] Kris, M., Marco, P and Koenraad De B, (2010) Rotor dynamic modeling as a powerful support tool for vibration analysi on large turbomachinery.*The 8thIFFoMM International Conference on rotor dynamics,* September 12-15, 2010/kist, seoulkora, pp 700-706.

[11] Lee, W. and Ha, D.H. (2003) Coupled lateral and torsional vibration characteristics of a speed increasing geared rotor-bearing system, *Journal of Sound and Vibration*, 263(4): 725-742.

[12] Lida., Tamura K and Kikuch, H (2009) Coupled torsional-flexural vibration of a shaft in a geared system of rotors (1st report), *Bulletin of the ASME*, 23(186): 2111-2117.

[13] Mitchell, L.D. and Melleu, D.M. (2005) Torsional- lateral coupling in a geared high-speed rotor system, *ASME Design Engineering Technical Conferences*. 3 (Part B), 84(2): 977-989.

[14] R. B., Bhat,T. S and Sankar (2009) Coupled torsional flexural vibration of a geared shaft system using finite element method, *Shock and Vibration Bulletin* (Part 3), 55: 13-25.

[15] Ogbonnaya, E.A. (2004) *Modeling vibration base faults in Rotor Shaft of Gas Turbine*. Ph.D work Department of Marine Engineering, Rivers State University of Science and Technology, Port Harcourt, Rivers State, Nigeria, pp 64- 79.

[16] Ogbonnaya, E.A., Johnson, K.T, Ugwu, H.U and Orji, C.U (2010) Component model-based condition monitoring of a Gas Turbine, *ARPN Journal of Engineering and Applied Sciences*, ISSN 1819-6680, Vol., No. 3, p 40

[17] Ogbonnaya, E.A., Ugwu, H. U. and Diema, E.J (2013) A model-based mixed data approach for optimizing the performance of an offshore gas turbine compressor, Journal of Vibration Analysis, Measurement and Control, *Columbia International Publishing*, doi:10.7726/jvwp.2013.1001, pp30-43

[18] Rao, J.S., Chang, J. R and Shiau, T. N2007. Coupled bending-torsion vibration of geared rotors, *ASME* Design Engineering Technical Conferences. 3 (Part B), 84-2: 977-989.

[19] Rao, J.S, (2006) *Rotor Dynamics*, 3rd edition, New Age International Publishers, India.

[20] Shiyu, Z. and Jianjun S. (2001) Active balancing and vibration control of rotating machine: *A survey journal of shock and vibration digest*. vol. 33, No. 4 July, 2001. Pp 361-371 (C) September, 2001 Saye Publication.

[21] Surial, A and Kaushal A. (2008) Dynamic analysis of flexible turbo-rotor system using super elements.Rolls Roycc, Materials Polytechnics University Toronto Canada, pp 1-8.

[22] Zhu, X, and Andres, S.L., (2007).Rotor dynamic performance of flexure pivot hydrostatic Gas bearing for oil free turbo machinery *ASME . Eng. Gas Turbines Power*, 129 pp 1020-1027.

Chapter 2

The Influence of Inlet Air Cooling and Afterburning on Gas Turbine Cogeneration Groups Performance

Ene Barbu, Valeriu Vilag, Jeni Popescu,
Bogdan Gherman, Andreea Petcu, Romulus Petcu,
Valentin Silivestru, Tudor Prisecaru,
Mihaiella Cretu and Daniel Olaru

Additional information is available at the end of the chapter

http://dx.doi.org/10.5772/59002

1. Introduction

Usually, cogeneration is defined as combined production of power and thermal energy from the same fuel source, represented by natural gas, liquid fuel, refinery gas, etc. In conventional energy production the efficiency is approximately 40 %, but through cogeneration it can reach even 90 %. Fuel supply and increased performance requirements, environment concerns, continuously variable market conditions have contributed to the development of the gas turbines. The performances, exploitation costs, safety in operating conditions have made these installations to be selected for cogeneration processes.

2. State of art

Gas turbine systems operate on the ideal thermodynamic cycle (consisting in two isentropic and two isobars) represented by Brayton cycle. The real Brayton cycle consists in quasiadiabatic expansion and compression processes, but unisentropic, and the heat transfer processes are not isobar processes, due to flow pressure losses. In addition, the air and hot gases are not perfect gases and not have the same flow rates. Brayton cycle thermal efficiency depends on: compression ratio; ambient temperature; air temperature at turbine inlet; compressor efficiency and turbine components efficiency; blade cooling requirements; increased performance systems (exhaust gases heat recovery, intercooling, intake air cooling, afterburning imple-

mentation, fluids injection – water/steam, etc.). The main parameters that define the operating thermodynamic cycle of gas turbine installations (usually disclosed by the suppliers in catalogues) are the temperature at the gas turbine inlet (T_3) and the compression ratio. Generally, gas turbine manufacturers declare performances without taking into consideration the inlet and outlet pressure losses. Gas turbine installations performances are affected by the variation of these parameters as follows [2]: temperature increase at the gas turbine inlet leads to an increase in power and efficiency; the efficiency becomes maximum at a given value of the compression ratio (in T_3=const. hypothesis); there is a value of the compression ratio for which the power is maximum (T_3 and compressor intake air flow rate remains constant). The productivity of a gas turbine cogeneration group depends on the quantity of heat recovered from the turbine exhaust gases (approximately 60-70 % from the fuel energy). This is achieved by adding a heat recovery steam generator in order to supply hot water or steam. Determining factors in total efficiency of the cogeneration group are the gas turbine outlet temperature and the temperature at the stack of the heat recovery steam generator. The combination temperature at the gas turbine inlet – compression ratio determins the outlet temperature. The gas turbine, being located at the upstream of the heat recovery steam generator, significantly influences the cogeneration group performances. The air is induced by the gas turbine compressor in ambient conditions imposed by the location of the cogeneration plant. Compressor inlet temperature and intake air density dictates mechanical work required by the compression process, the fuel and quantity of fuel to be used in order to obtain the necessary temperature at the gas turbine inlet (T_3). Consequently, output power, efficiency, exhaust gases mass flow and outlet temperature (respectively the quantity of heat recovered) are influenced by ambient conditions [3]. The location of the gas turbine cogeneration plant imposes climatic conditions and requires adequate technical solutions in order to ensure performances. Generally, for cogenerative applications, the gas turbine is designed to operate in standard conditions, established by the International Standards Organization and defined as ISO conditions: 15 ^{0}C, 1.013 bar and 60 % humidity. During summer season air temperature rises and its density decreases, leading to a decrease in the intake air mass flow; consequently decreases and power output because it is proportional to the intake air mass flow rate. Without taking supplementary measures, both gas turbine output power and efficiency drop. In the scientific literature there are various papers that deal with the gas turbine's performance dependence of the intake air temperature variation [3-10]. In [4] it is shown that: an increase of 10 ^{0}C at the compressor inlet reduces the gas turbine outlet power with 18%; in comparison with the operation during winter season, the increase of ambient temperature leads to a decrease in gas turbine plants power output with 25-35%, also leading to an average increase of the consumption of 6%. The effect of intake air temperature over the performances differs from one gas turbine to another, but, generally, aeroderivative gas turbines are more sensitive to this phenomenon than the industrial gas turbines [5]. During summer season, when the days are long and hot, the power requirements increase for the residential spaces ventilation, offices, store rooms, etc. Additional energy consumption can be ensured by starting other backup groups, or compensating the loss of power through various other methods. The usual compensation methods of power loss are [6, 7]: compressor inlet air cooling (pre-cooling), intermediate cooling (intercooling), using recovery cycle. Mainly there are two basic com-

http://dx.doi.org/10.5772/59002

pressor inlet air cooling methods: evaporative cooling (with evaporative media cooling or water injection in the inlet air-fogging); refrigeration system cooling [8]. For a 79 MW gas turbine, equipped with a fogging cooling system, the researches conducted at Mashhad (in Iran) showed that during a day, the maximum increase in power is achieved in the afternoon, when the temperature is higher and relative humidity is lower [9]. Inlet air cooling systems analysis in order to be applied to a gas turbine V94.2, in terms of efficiency increase, led to the conclusion that the fogging cooling system meets the design requirements and leads to an increase in power output of approximately 6 MW [10]. With the help of GT PRO software the performances of a 100 MW gas turbine model were analyzed, for a various types of inlet air cooling systems, and it had been reached that a decrease of air temperature of 1 ^{0}C (in the 25-35 ^{0}C interval) leads to an increase in power output of approximately 0.7 MW [11]. For a gas turbine cycle, with intermediate cooling (intercooler), the decrease of inlet air temperature causes the output power to rise and the intercooling leads to a 5-9% gain of power and a 8% reduction in fuel consumption [12]. Reduction of fuel consumption represents a priority both for industrial gas turbine manufacturers and also for the civil aviation. The search is on for new materials that meet the requirements imposed by the higher strains of the gas turbines [13] and also the development of new technologies, including technological transfer from aviation domain to power generation domain. Thus, in aviation, afterburning is used in order to increase traction of supersonic engines. The introduction of afterburning into cogenerative applications leads to an increase in flexibility and global efficiency of the cogeneration group. Afterburning application is possible due to the fact that exhaust gases at turbine outlet have a 11-16% (volumes) content of oxygen [14]. The afterburning installation, located between the gas turbine and the heat recovery steam generator, interacts with the gas turbine but influences the heat recovery steam generator operation especially [14, 15]. To increase the performance of gas turbine cogeneration groups research focused specifically on [16]: increase in burning temperature; increase in compression ratio; improving the methods of design, cooling and burning technologies, and also advanced materials; technological transfer from the aviation domain in the industrial gas turbine domain and conversion of aviation gas turbine (with outdated lifetime) to energy conversion; integrated systems (combined cycles, compressor inlet air cooling, intercooling, turbine exhaust gases heat recovery, afterburning implementation, chemical recovery, etc.). Following the direction displayed in the field, the chapter integrates data from scientific literature with research developed at INCDT COMOTI Bucharest, regarding gas turbine inlet air cooling and afterburning application, as base methods for increasing performances and flexibility of cogenerative group.

3. Influence factors and methods of increasing performances in gas turbine cogenerative groups

For a combined cycle (considering as variables ambient temperature, gas turbine outlet temperature and stack temperature) it is shown that the dominant factor in global efficiency rise is stack temperature [17]. Obtaining a high efficiency involves the optimization of the entire cogenerative plant (gas turbine, afterburning installation, heat recovery steam generator, etc.).

The efficiency must be maintained even at partial loads (even under 50%) in variable conditions modification. In general, although the target is obtaining a maximum efficiency, nevertheless an adequate flexibility to process requirements is desired, the afterburning installation contributing to this.

3.1. Influence factors

Ambient parameters (humidity, pressure, temperature) can vary significantly depending on geographic location and season, affecting air density and implicitly the gas turbine cogenerative group performances. In the past, the effect of air humidity was neglected but the increase in gas turbine cogenerative groups power and the introduction of water/steam in the combustion chamber made this effect to be reconsidered. Thus, some authors [18] consider that air relative humidity (even at temperatures higher than 10 ^{0}C) has a neglectable influence over the gas turbine output power (as the other performance parameters). This leads to the fact that in some calculus (especially when the results are presented in correlation to ISO conditions) the variations in atmospheric humidity and pressure to be neglected. Others consider that due to the fact that water content modifies thermodynamic properties of inlet air (density, specific heat), at certain gas turbines (depending on specific processes) the performances may increase when humidity rises and in the case of some gas turbines the performances may decrease in the same conditions [19]. However, the increase in relative humidity leads to a significant reduction of NO_x emissions [20].

Ambient pressure is defined by the conditions from plant location, altitude modification leading to air density modification and implicitly to power output variation. Thus, 3-4% losses occur for each 304.8 m (1000 ft) rise in altitude [21].

Power and efficiency of the gas turbine group decrease along with ambient temperature, in figure 1 linear approximate variations being presented. Specific fuel consumption increases with the ambient temperature rise [22].

Gas turbines operate on a wide variety of gaseous fuels (natural gas, liquefied natural gas-LNG, liquid petroleum gas-LPG, refinery gas, etc.) and liquid fuels (kerosene. no. 2 diesel, jet A, etc.). Using a certain type of fuel for the gas turbine has a profound impact both on the design and also on material selection. Usage of liquid fuels imposes: ensuring burning without incandescent particles and residues on the combustor and turbine; reducing hot gas corrosive effect due to aggressive compounds (sulphur, led, sodium, vanadium, etc.); resolving pumping and pulverization (filtering, heating, etc.) issues. In case of using gaseous fuels, a simpler solution is presented due to their higher thermal stability, higher heating power, lack of ash and smut. However, in order to ensure pressure level (required by the gas turbine, afterburning installation, etc.), water and various impurities elimination implies a control-measuring station for the gaseous fuels used (natural gas in the case of cogenerative plant 2xST18 – Figure 2). Although the main fuel for the operation of gas turbine cogenerative groups is natural gas, the economic rise and environmental requirements issued an alternative. The gas turbine can be designed to operate on a variety of fuels, but the rapid transition to other fuel operation, without machine damage or exceeding the level of emissions, still remains an issue subjected to study.

http://dx.doi.org/10.5772/59002

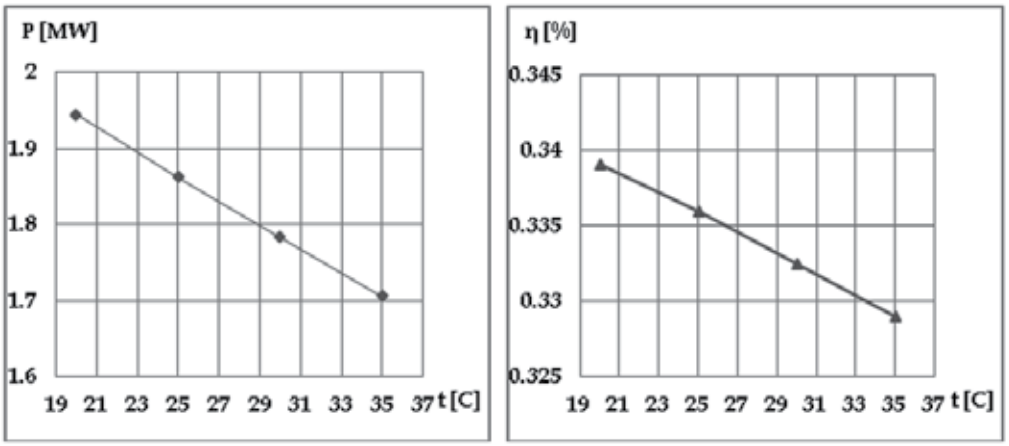

Figure 1. Power output (left) and efficiency (right) variations versus ambient temperature, at a simple gas turbine cycle

Interchangeability at gaseous fuel gas turbine cogenerative groups, represents the ability to change a fuel with another one, without affecting the application or the equipment in which the gaseous fuel is burned [15]. At a constant fuel composition (in the case that the holes through which the fuel passes to the burner have fix dimensions), the quantity of heat delivered by the burner is proportional with the mass flow and heating power. When the composition varies and it is the problem of replacing a fuel with another equivalent, Wobbe index (after John Wobbe-engineer and mathematician) is used as comparison criteria. It is defined as ratio of the lower heating value (LHV) and the square root of relative fuel density respectively, in relation to air (d_{rel}):

$$Wo = LHV / (d_{rel})^{0.5} \tag{1}$$

$$d_{rel} = \rho_{comb} / \rho_{air} \tag{2}$$

Thus, two gaseous fuels (with different chemical compositions), with the same Wobbe index, are interchangeable and the quantity of heat delivered to the equipment is equivalent at the same fuel supply pressure. In order to take into account the fuel temperature, a Wobbe temperature corrected index can be used. According to [23], two gaseous fuels are interchageable if the following relation is satisfied:

$$\frac{\Delta p_2}{\Delta p_1} = \left(\frac{Wo_2}{Wo_1}\right)^2 \left(\frac{A_1}{A_2}\right)^2 \tag{3}$$

where Δp_1 and Δp_2 represent the overpressures of gas 1 and gas 2 respectively, Wo_1 and Wo_2 – Wobbe indices of fuels 1 and 2, A_1 and A_2 – gaseous fuel injection nozzle surface areas.

Figure 2. Cogenerative plant 2xST 18 – Suplacu de Barcau (left) and afterburning installation (right) [14, 15]

Thus, the validation criteria of adequate replacement of one fuel with another equivalent fuel are given by: self-ignition, flame temperature (with a high influence on NO_x emissions forming), flame speed, flashback, efficiency, NO_x and CO emissions, flue gas dew point, etc. Resolving gas turbine cogenerative group fuels interchangeability, by developing high performance alternative fuel burning technologies, especially hydrogen, will have a major impact over system and environment efficiency. Thus, the studies conducted on more fuels (H_2, CH_4, C_3H_6, C_6H_6, CH_3OH) revealed that [24]: hydrogen and methyl alcohol have the same higher maximum efficiency than other fuels in the same operating conditions; hydrogen fuel has the lowest specific fuel consumption in comparison with other fuels, followed by methane, propen, benzene, and finally methyl alcohol; in the reheating cycle the increase in thermal efficiency is lower than the increased in the intercooling cycle; hydrogen fuel is ideal promising fuel in the gaseous plant which has greater thermal efficiency and greater improvement in the performance of modified gas turbine power plant occurred with intercooling and heat exchanger rather than simple and reheat cycle.

From the point of view of reusing aviation gas turbines for industrial purposes, the possibilities of using liquid fuels are limited, leading to the development of new technologies on gaseous fuels. Thus, the transition of a TV2-117A gas turbine engine from liquid to a gaseous fuel, in order to benefit from landfill gas energy value, has been conducted in many stages: transition from liquid fuel (kerosene) operation to gaseous fuel (natural gas) operation, thus obtaining TA2 gas turbine engine; the transition of TA2 gas turbine engine from natural gas operation to landfill gas operation, thus obtaining TA2 bio gas turbine engine. In order to obtain the two gas turbine engines (TA2 and TA2 bio), numerical simulations were conducted in CFD environment, constructive modifications and gas turbine test bench experiments in order to

http://dx.doi.org/10.5772/59002

validate adopted solutions [15]. In this way, TA2 gas turbine engine was integrated in the structure of afterburning installation test bench facilities, from INCDT COMOTI Bucharest (figure 3).

Figure 3. TA2 gas turbine engine mounted on the stand (left) and afterburning installation (right)

Efficiency and reliability are two major parameters that are taken into account since the beginning of a new gas turbine cogenerative group design. In order to obtain a higher efficiency (in balance with cost and reliability), the design team must reach a balance between burning temperature rise and compression ratio, special material selection and complicated cooling systems, customer's specification, etc. Based on a continuum dialogue with Siemens customers, as far back as the predesigned stage, a 36 MWe SGT-750 gas turbine was elaborated [25]. It can be used both in cogenerative applications as well as driving different equipment, stable operation at partial load but also allows the transition to another fuel (operates on dual fuel). Since 2002, Siemens began focusing attention to reliability, so that they give up the high pressure tambour from the recovery boiler (usually used in order to prevent high thermal tensions, a long period of time is imposed in order to reach a certain temperature). Regarding efficiency, flexibility and emission reduction at gas turbine cogenerative groups, important steps were achieved towards: integrating low NO_x burners, lifecycle was analyzed in order to increase efficiency, maintenance interval was enlarged and the transition from one fuel to another was improved at polifuel groups.

3.2. Methods of increasing performances

The development of gas turbine application in various regions of the globe, encouraged researchers to find new methods of increasing performances and to apply new cooling technologies to compressor inlet air, specific to the location. Actually the advantages of inlet air technology application are represented by power losses prevention, losses that occur when ambient temperature exceeds 15 ^{0}C (ISO design temperature), and fuel usage efficiency. In general, the studies of selecting a new method of cooling air take into account each method (see chapter 1) and compare them with a reference case [8]. Evaporative cooling systems imply lower investments, operating and maintenance costs than refrigeration systems but the

increase in gas turbine performances is lower. Evaporative cooling system is based on the transition of an air flow through a water soaked environment, system efficiency depending on the surface area of the water soaked environment exposed to air and exposure time. The system is efficient in low humidity regions. In the case of fogging system, the demineralized water is sprayed in the gas turbine inlet air flow, through high pressure nozzles (70 – 200 bar). Figure 4 shows a fogging system, located downstream of the filtering system, in a gas turbine. The air induced through the filtering system reaches the suction chamber, where the water, sprayed in fine droplets (<30 microns), is evaporated in the air flow and produces a cooling effect. In general, the water injected mass flow required represents 2 % from the inlet air, depending on the ambient parameters (temperature and humidity).

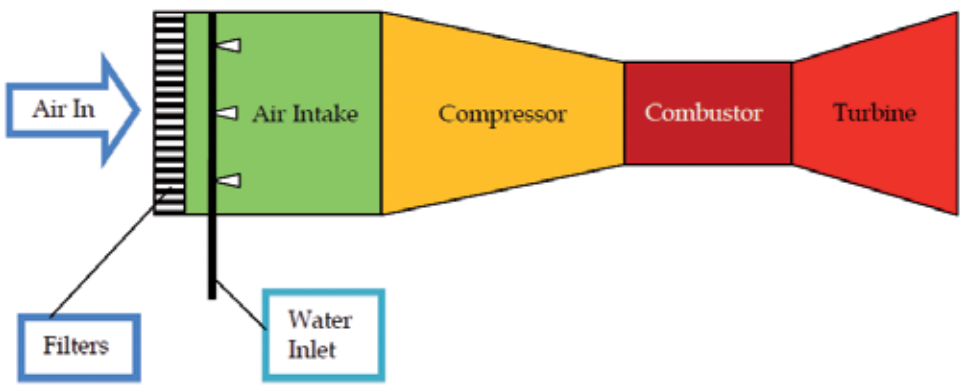

Figure 4. Fogging system scheme, located downstream of the filtering system

Water injection system (with fog) has the advantage of lower pressure drops, higher efficiency, lower refurbishment costs but requires demineralized water, parasite loads occur due to water injection pumps and the control system is complex. Fogging systems, increasingly popular in time, are capable of cooling gas turbine intake air to the temperature of the wet-bulb thermometer, being more efficient than the ones with evaporative media. Although significant investments are required, refrigeration cooling systems (mechanical, absorption, storage) can practically maintain any temperature of gas turbine intake air, recommended in variable humidity regions. In general, fogging system are designed to operate in such a way that the formed droplets should evaporate until entering the compressor, in order to avoid blade damage. In some cases overspray phenomenon can occur (a certain amount of water would not evaporate until entering the gas turbine). In this way overspray phenomenon is similar with water injection between compressor stages (intercooling phenomenon occurring). In certain operating regimes it is possible that evaporative cooling (upstream of the compressor) combined with overspray phenomenon (intercooling) lead to compressor aerodynamic instability (although intercooling effect is added to evaporative cooling) [26]. Combining overspray phenomenon with the usage of a low power heating fuel, steam injection in the combustion chamber or a high level of blade wear can lead to catastrophic results for the gas turbine. Some authors [27] consider that at gas turbine cogenerative cycles, intercooling is

http://dx.doi.org/10.5772/59002

recommended, in order to reduce high pressure compressor stage power consumption. Thus, the factors that need to be taken into account when adopting a new technology of cooling the inlet air are [28]: plant configuration (gas turbine engine can be used within an open cycle, a cogenerative cycle, a combined cycle with high operation – intermittent or basic); the amount of compressed air per kW (requiring a small amount of compressed air the cooled air required decreases and, implicitly, exploitation costs decrease), the ambient air enthalpy at given conditions by the design (selecting a high enthalpy of air per kg of dry air leads to a large cooling system, with high exploitation costs); air cooling temperature (for each gas turbine engine model exists an optimum cooling temperatures at given environment conditions).

Although the integration of an afterburning installation (figure 2 and 3) can lead to an increase in cost (with approximately 10-15 % from the cost of the heat recovery steam generator) certain advantages are highlighted: an increase in steam amount at the heat recovery steam generator; thermal energy can be managed more easily; steam amount efficiency, depending on technological process requirements; the heat recovery steam generator can operate even at gas turbine shutdown; it can compensate ambient parameter variations; in some cases can contribute to NO_x emissions reduction by interacting with gas turbine emissions; can burn other fuels usually inadequate to gas turbines (biogas, furnace gas, flammable gases resulted from gasification, etc.).

4. Theoretical research developed at INCDT COMOTI Bucharest

At INCDT COMOTI Bucharest, theoretical research approached issues concerning: processes regarding water spray in gas turbine intake; intercooling; influence of air cooling over gas turbine performances; thermogasodynamic processes from the afterburning installation's burner.

Thus, in order to understand the phenomenon of cooling air at water spraying through an impact body nozzle [29], numerical simulations in CFD environment were conducted, with the working domain consisting in air (gas) and water (liquid). In the first version the impact body (a cone with 1.2 mm base and generator lines) was not taken into account. In the second version the cone was positioned, firstly, at 0.4 mm towards the pipe's end, then moved at 0.8 mm, and 1 mm respectively. Sprayed water reaches in the calculus domain (a cylinder of 1m in diameter and 2.5 m in length) through a 1.2 mm diameter and 12 mm length pipe positioned along the cylinder's symmetry axis. In order to capture as accurately as possible the turbulence phenomenon that occurs in the cone and pipe area, at the same time with water flow sprayed around the cone, the mesh was refined (figure 5).

Also, along the pipe and cone walls boundary layers were created, in order for an accurate capturing of the flow near the walls. Water is sprayed into the atmosphere with an axial speed of 15 m/s, as droplets of 100 μm diameter, having a temperature of 288 K. Boundary conditions for the cone and pipe are of smooth adiabatic wall type. The turbulence model used was k-ε. Work methodology was based on the model described in [30]. Numerical simulation results

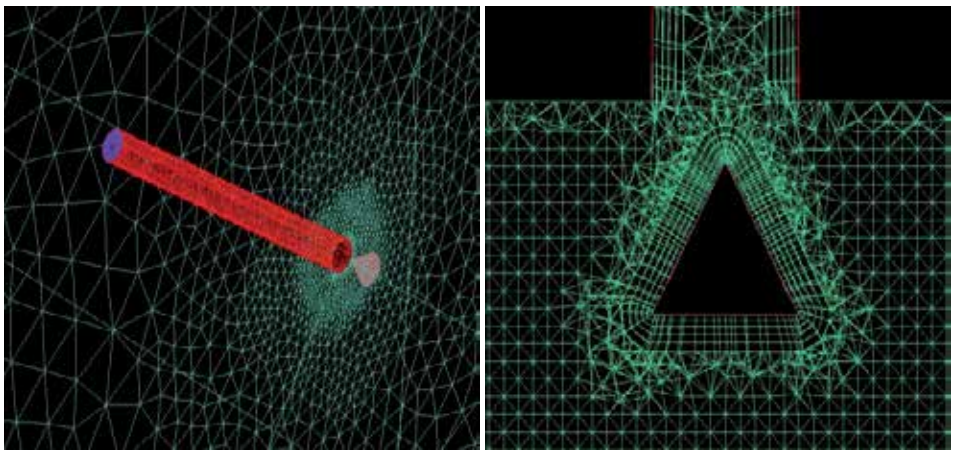

Figure 5. Calculus mesh at the inlet zone of sprayed water in the domain (left) and around the cone (right)

are presented in figures 6 and 7, highlighting the spray without impact body and with impact body positioned at 1 mm distance from the pipe outlet.

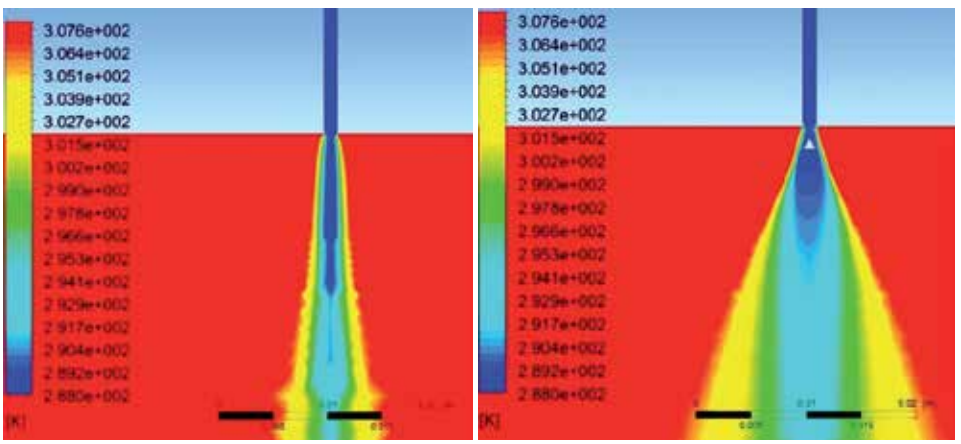

Figure 6. Detail regarding temperature field at water output: without cone (left) and with the cone positioned at 1 mm distance (right)

Figure 6 reveals that cone insertion leads to pronounced water jet flaring. Cone position modification has a minimum effect over the water spray flare angle. For a better observation of sprayed water jet along the calculus domain, 300 mm in diameter planes were created (comparable with TA2 gas turbine engine intake-figure 3) along the symmetry axis corresponding to z axis coordinate of 0.5 m, 1 m, 1.5 m, 2 m, and 2.5 m respectively.

Figure 7 shows that in case of numerical simulations without the cone, the water jet is directioned along the symmetry axis, while in case of impact body numerical simulations the water

http://dx.doi.org/10.5772/59002

jet is more dispersed, as expected. In the case of numerical simulations without the cone, the average temperatures decrease more rapidly.

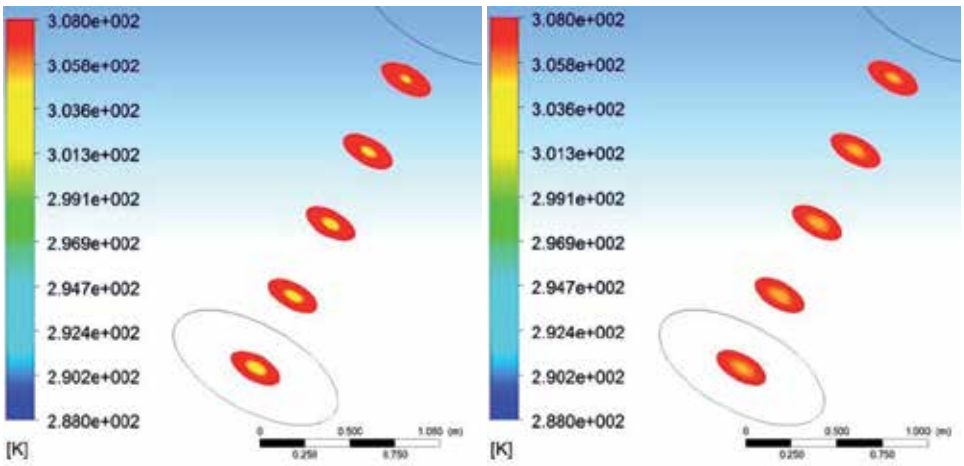

Figure 7. Temperature field in different cross planes: without cone (left) and with the cone positioned at 1 mm distance (right)

Compressor performances are influenced by flow steadiness at the rotor outlet, more specifically if the flow angle varies from hub to shroud than the flow within the diffuser will be unsteady and will lead to separations on the blade vane. Also, the flow at the tip of the blade and at the centrifugal rotor outlet is intensily distorted and unsteady. In order to quantify the impact of intercooling on a two stage compressor, a CFD study was conducted in which the second stage inlet temperature was reduced. Performance impact was monitored, in comparison with the case in which between the two compression stages no cooling was applied. Thus, two CFD analyses were conducted, in which the total inlet second rotor temperature was considered 460 K, for the case without cooling between the compression stages and 313 K, for the case with cooling.. The calculus mesh for this case is a structured mesh and has approximately 1 million elements. The walls are considered to be adiabatic, waterproof and velocity at wall is considered to be zero. In order to improve calculus time, a single channel has been considered (rotor consisting in 15 blades and 15 splitters), using the periodicity function. For spatial discretization was used a second order scheme. A compressible flow was considered in calculus, the governing equations being written as Reynolds Averaged, time and mass averaged. Shear Stress Transport k-ω was considered as turbulence model. SST k-ω model is based on tangential tensions transport. With the help of this turbulence model, accurate results and separation zone dimension (that forms under the influence of high pressure gradients) can be obtained. The results are presented in figures 8-10.

Analyzing the CFD simulations results, it can be observed that along with temperature reduction at rotor inlet, streamlines in the rotor indicate that a recirculation zone is forming on the splitter. This shows that flow angles in the rotor have changed, fact that led to boundary

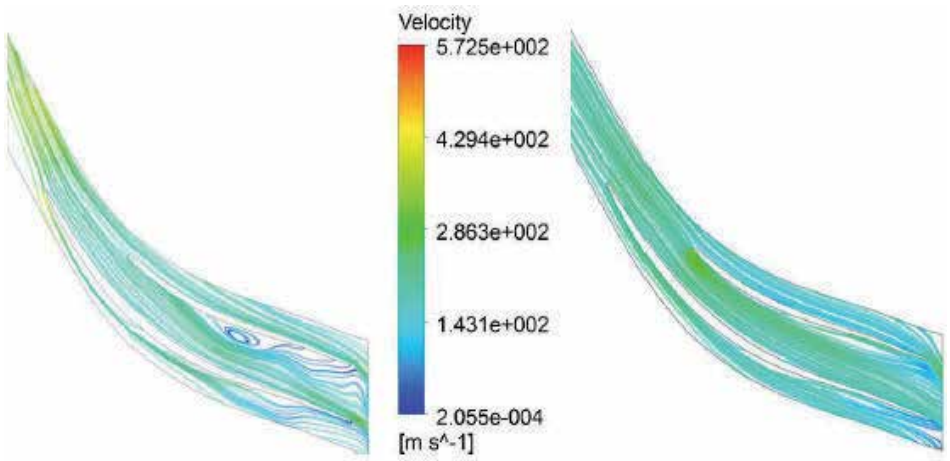

Figure 8. Streamlines, at 50 % of blade height, measured from the hub, in the case of cooling (left) and in the case without cooling (right)

layer separation in the case of intercooling (figure 8). Also, it can be observed (in meridional plane) the fact that Mach number rises at the rotor outlet, from 0.88 in the case without intercooling to 1.055 in the case with intercooling (figure 9).

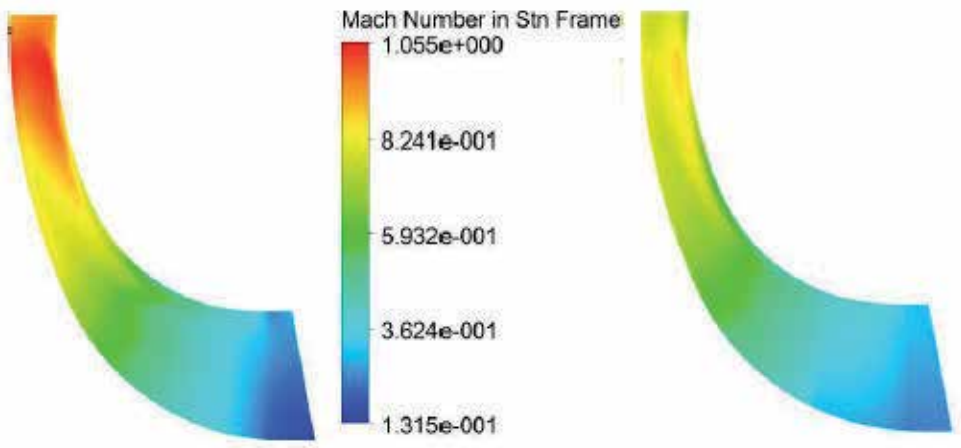

Figure 9. Mach number in meridional plane, in the cooling case (left) and in the case without cooling (right)

Another difference can be observed also in outlet rotor total pressure, the pressure increases in the case of intercooling (figure 10). Thus, at centrifugal rotor outlet, in the case of intercooling, an increase of 0.2 in Mach number can be observed, reaching 0.938. This indicates a transonic regime at rotor outlet. Corroborated with the fact that the flow angle at rotor outlet reached 12.72^0 from 17.713^0, it means that the existing stator must be redesign.

http://dx.doi.org/10.5772/59002

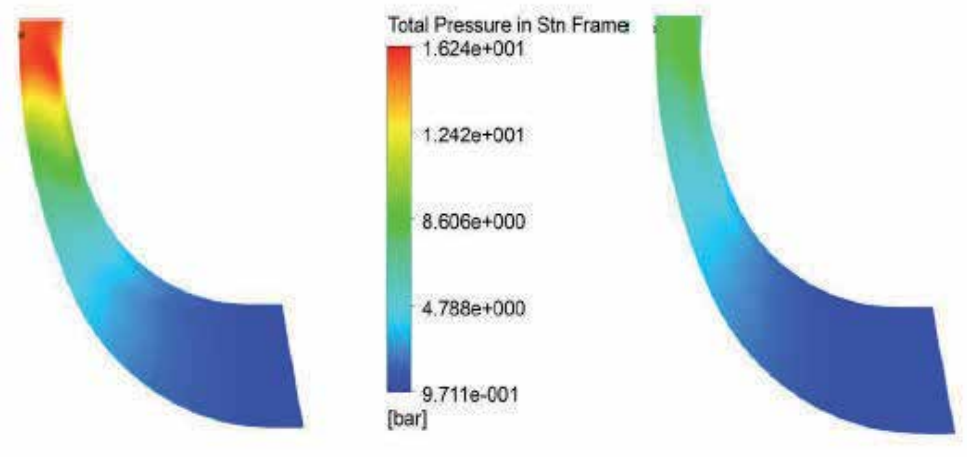

Figure 10. Total pressure in meridional plane, in the cooling case (left) and in the case without cooling (right)

In general, the performances of a turboshaft engine is compared with the ones given by ideal cycle calculus, thermodynamic analysis including thus, the ideal gas turbine work range. Gas temperature at turbine inlet, as gas turbine outlet section and outlet pressure, are equal in the case of ideal and real gas turbine [31].

Thus, the main configuration to be taken into account for thermodynamic analysis is the one for a monorotor turboshaft engine, with two high and low pressure compressor stages, coupled with a turbine that includes both gas generator stages, as well as power shaft supply stages. For performance calculus, the above configuration is considered (figure 11-left) and intercooling configuration (between compressor low and high pressure stages – figure 11 right). The heat exchanger, that provides intercooling, decreases air temperature in the high pressure compressor inlet section at 40 °C (313 K). Intercooling application decreases the mechanical work consumed by the compressor, without affecting the mechanical work produced by the turbine, leading to an increase in the mechanical load available at the output shaft [32]. In thermodynamic analysis, for the two gas turbine engine configurations presented above, a series of parameters were imposed for operational purposes. The calculus method used is in accordance with [33]. Common conditions to both configurations refer to: ambient temperature, whose variation influences gas turbine performances (shaft power, thermal efficiency, specific fuel consumption); gas temperature in the turbine inlet section, having the same value in all the cases presented, does not vary with ambient temperature, parameter imposed by turbine alloy properties; turbine outlet pressure, in order to ensure exhaust, in the context of pressure losses on the exhaust; burned gases pressure at the exhaust outlet so that the gases can pass through the heat recovery steam generator; coefficients of pressure, speed, energy losses with compressor and turbine efficiencies, and compression ratio (in initial configuration), low pressure compressor (in intercooling configuration) respectively are considered constant. In addition, for the configration that includes intercooling, the following parameters are imposed: temperature at high compressor inlet, the same for all calculus cases, that allows

the use of a low temperature resistant material and allows to obtain a high compression ratio at the same mechanical work consumed on the second compressor; the pressure loss coefficient in the heat exchanger; air pressure at combustion chamber inlet, that derives from total compression ratio imposition. In these conditions, the gas turbine output power variation depending on the inlet air temperature (for the various compression ratio), for simple configuration and intercooling and for different compression ratios, is presented in figure 12.

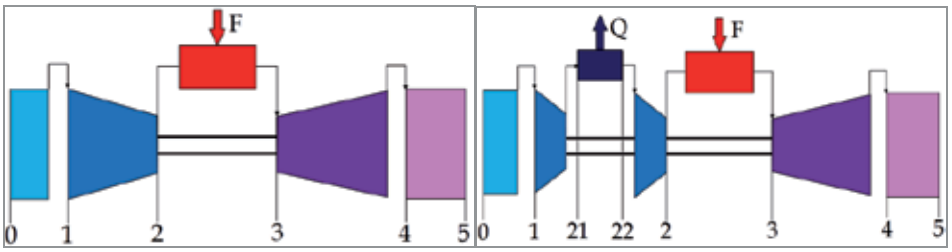

(0 – intake inlet; 1 – compressor inlet (low pressure compressor); 21 – heat exchanger inlet; 22 – high pressure compressor inlet; 2 – combustion chamber inlet; 3 – turbine inlet; 4 – exhaust inlet; 5 – exhaust outlet)

Figure 11. Gas turbine engine configurations – general schemes

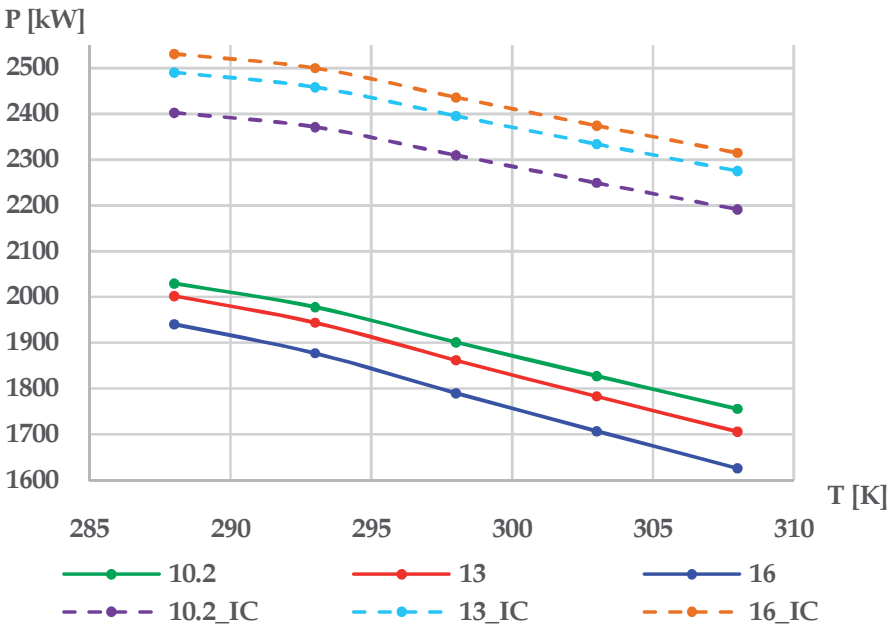

Figure 12. Gas turbine output power variation versus inlet air temperature (at the various compression ratio), for simple configuration and intercooling-IC

http://dx.doi.org/10.5772/59002

It is noticed a decrease of shaft power and thermal efficiency, simultaneous with an increase in specific fuel consumption, at an ambient temperature increase, phenomenon that occurs for all cases in which thermodynamic analysis was conducted, both in the initial gas turbine configuration, as well as in intercooling. For the initial configuration, a pronounced variation occurs with ambient temperature increase, easily noticeable in the case of high compression ratios. In the case of intercooling gas turbine, performance variation is approximately linear for all the three compression ratios, with a decrease in power of 2.5 % for each 5 degrees of the environment.

In the field of afterburning, the theoretical research has soughed: to obtain a reduced pollutants afterburning installation, in comparison with the existing cogeneration power plant 2xST 18 (figure 3); afterburning installation flexibility when supplied with gaseous fuels; to study the influence of water spraying into the gas turbine's combustion chamber upon the afterburning [14, 15]. Thus, the numerical simulations performed in CFD environment have showed that (at nominal conditions), by modifying the afterburning module of the cogenerative plant 2xST 18, the NO_x concentration in the exhaust gases is lowered three times [14, 15]. The base module of the cogenerative plant has been mainly modifying by flaring at 15° and by introducing a concentrator.

5. Inlet air cooling installation and afterburning integration within gas turbine cogenerative group — Future research

Gas turbines usually function with high air excess, between 3 and 6 at nominal regime, and even higher at partial-load regimes [34]. This enables the use of an afterburning module, but the control of the air/fuel mixing requires the minimization of the air excess. Thus, reducing the exhaust emissions must be balanced against providing the cogenerative group's performances in a flexible manner.

5.1. Efficiency-emissions binom

The main pollutant emissions produced by gas turbines consist of: nitrogen oxides (NO_x), carbon monoxide (CO), volatile organic compounds (VOCs). Gas turbines typically operate at high loads which make their design for optimum combustion and maximum efficiency to be made at nominal load. Controlling the concentration of all pollutants is difficult in the conditions of variable loads operating. In high loads operating regimes the concentration of NO_x is higher, while in lower loads operating regimes (under 50 %) the thermic efficiency decreases and the concentrations of CO and volatile organic compounds increase. Thus the factors which determine the formation of pollutants in the exhaust gases are [14, 15]: the temperature and the excess of air in the primary zone; the process homogenization degree in the primary zone; the combustion process products residence time; the "freezing" characteristic of the reaction near the fire tube; etc. To decrease the emissions of NO_x is necessary to reduce the temperature in the area in which the combustion reaction takes place and in the high temperature zones, respectively to rethink the distribution of the air flows (combustion

in stages). The final version of the gas turbine's combustion chamber will be a compromise between the level of the pollutant emissions, performance and flexibility. Depending on the combustion temperature, in figures 13 and 14 are represented the NO_x and CO emissions levels typical for a class of industrial gas turbines, using different fuels and at various operating regimes [35]. The high CO emissions level indicates an incomplete combustion and a decrease in efficiency. From figures 13 and 14 it can be observed that for temperatures up to 760 ^{0}C, the levels of NO_x and CO are comparable (especially for natural gases), while in the case of higher temperatures the NO_x emissions increases rapidly, while the CO emissions level remains practicly constant. By comparison, in the case of micro gas turbines, operating at 70-100 % loads, the CO emissions are low (figure 15) but they increase fast when operating at under 70 % load [36]. In the case of micro gas turbines the NO_x emissions level are low over a wide range of operating regimes (30-100 % load). Adding a heat recovery steam generator and a cooling system for the intake air (with fog) could be a solution for increasing the performance and decreasing the influence of high temperature in the summer. The high content of vapours in the combustion gases (by injection of water/steam) leads to: acid corrosion (when using fuels which contain sulfur); increase thermal solicitations of the combustion chamber, reduce the heat recovery level, etc. The exhaust gases flow at the gas turbine exit is turbulent and uneven in the transversal section. Thus there might appear reverse flows in some areas of the heat recovery steam generator transveral section. The unevenness of the flow at the combustion chamber exit and the variation of the exhaust gases compozition influence the functioning of the afterburning module. Thus the afterburning is influenced in terms of efficiency, pollutants, flame stability but also in terms of corossion of the elements subject to the action of the exhaust gases. Generally, for a good design of the exhaust gases flow into the heat recovery steam generator, the following factors must be taken into acount [15]: the geometry of the gas turbine exhaust and its direction; the size of the heat exchange surfaces; the position of the afterburning; masic flow and mean speed at the gas turbine exit; local speeds near the walls and at the entrance of the first heat exchange surface. In general the gas turbine's evacuation is not directly coupled with the heat recovery steam generator; after leaving the evacuation of the gas turbine (in the case of the cogenerative power plant 2xST 18 – Suplacu de Barcau, figure 2), the exhaust gases pass through a silencer, a by-pass assembly, an adaption section to the afterburning and then they reach the afterburning chamber. An uniform distribution of the flow in the transversal section insures a proper functioning of the heat recovery steam generator, especcially of its overheater. This creates the necessary premises to ensure low emissions for the cogenerative group. If the exhaust gases coming from the turbine or the air flow are not evenly distributed, in the same way as the fuel, serious variations of the temperature can appear downstream of the burner.

In general, the variation of the speed (upstream of the burner), on 90 % of the burner section, mustn't exceed ± 15 % of the mean speed on the whole transversal section. In reality the exhaust gases temperature, downstream of the burner, will never be perfectly uniform. Even with a perfect distribution of the gas flow in the turbine, upstream of the burner, the temperature of the gases in the zone of each afterburning module will be higher than the temperature in the areas between the modules. These requirements must fall in the market trends, where (in terms of fluctuation of the electricity and fuel prices) the flexibility in functioning has become a major

http://dx.doi.org/10.5772/59002

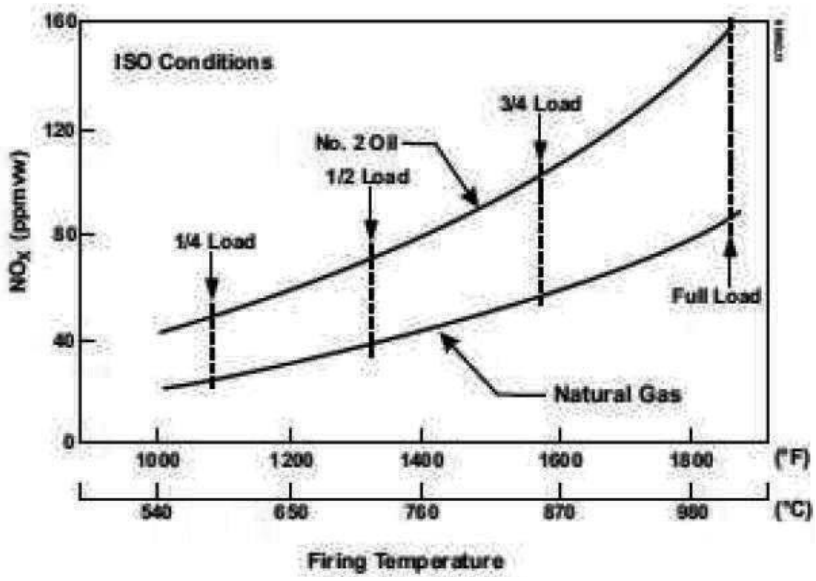

Figure 13. NO_x emissions variation for a class of industrial gas turbines - © 2010 Richard 'Layi Fagbenle. Originally published in [35] under CC BY-NC-SA 3.0 license. Available from: http://dx.doi.org/10.5772/10206

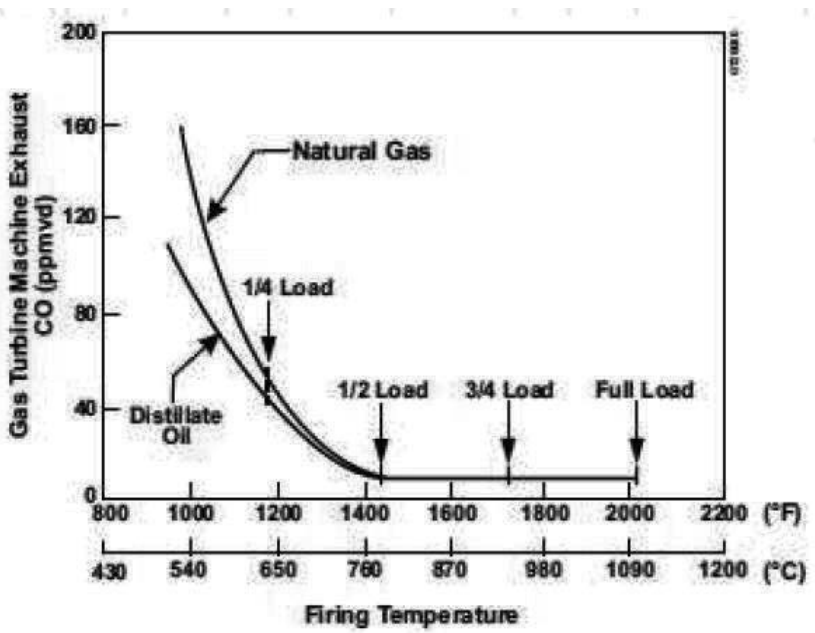

Figure 14. CO emissions variation for a class of industrial gas turbines - © 2010 Richard 'Layi Fagbenle. Originally published in [35] under CC BY-NC-SA 3.0 license. Available from: http://dx.doi.org/10.5772/10206

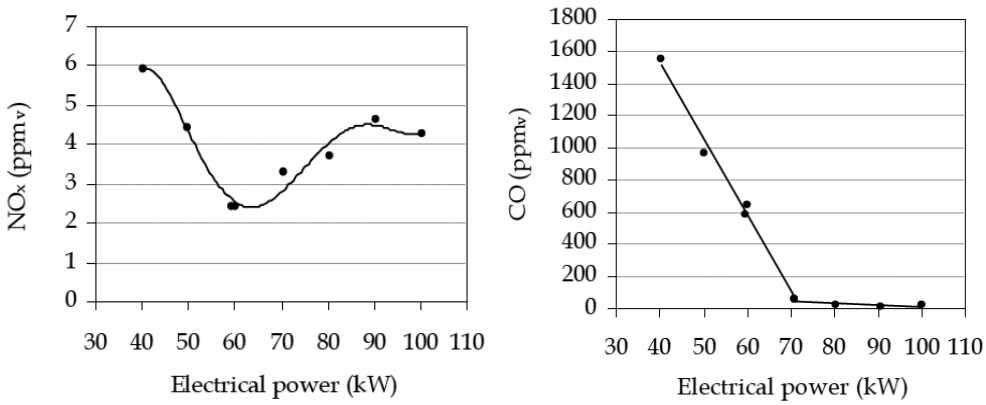

Figure 15. NO_x (left) and CO (right) emissions variation for a class of micro turbines - © 2010 Flavio Caresana, Gabriele Comodi, Leonardo Pelagalli, Sandro Vagni. Originally published in [36] under CC BY-NC-SA 3.0 license. Available from: http://dx.doi.org/10.5772/10211

subject, new concepts being imposed. Increased flexibility aims [37]: rapid start and stop; rapid change of the load; increase reliability in the case of quick start and load predictability; frequency control and of auxiliary services.

5.2. Experimental research conducted at INCDT COMOTI Bucharest

The experimental research carried out at INCDT COMOTI Bucharest, in close relation with the theoretical research (see chapter 4), have concentrated on: obtaining an afterburning installation on gaseous fuel, with low emissions; the realization of water spraying systems and their testing; experimenting water injection in the intake device of the gas turbine, at nominal functioning regime.

The numerical simulations carried out in CFD environment show that, by modifying the afterburning module of the cogenerative power plant 2xST 18, three times lower NO_x emissions can be obtained at nominal functioning regime [14, 15]. Up until now there have been carried out comparative experiments (figure 16) using gaseous fuel, at partial load (3 % of the nominal load). Thus the experiments at partial load show a reduction of the NO_x emissions with 30 %. From figure 16, right, it can be observed that the flame better fills the fire tube of the new afterburning module, and the temperature field is more uniform, being in good correlation with the results.

Before beginning the experiments regarding the effects of water injection in the intake device of the TA2 gas turbine, there has been studied the form of the water spray jet using a liquid fuel atomizer from TV2-117A gas turbine (figure 17). In these tests there has been chosen the atomizer circuit which ensures a droplet diameter (figure 17 left) comparable with the dimension of the gas turbine's intake device (figure 18 left). During the tests the water (untreated) has been sprayed at a pressure of 30±0.5 bar, the atomizer being position on the TA2 gas turbine axis. The distance between the atomizer and the gas turbine intake has been varied between 1500 mm and 2000 mm. The testing rig is composed by: TA2 gas turbine,

http://dx.doi.org/10.5772/59002

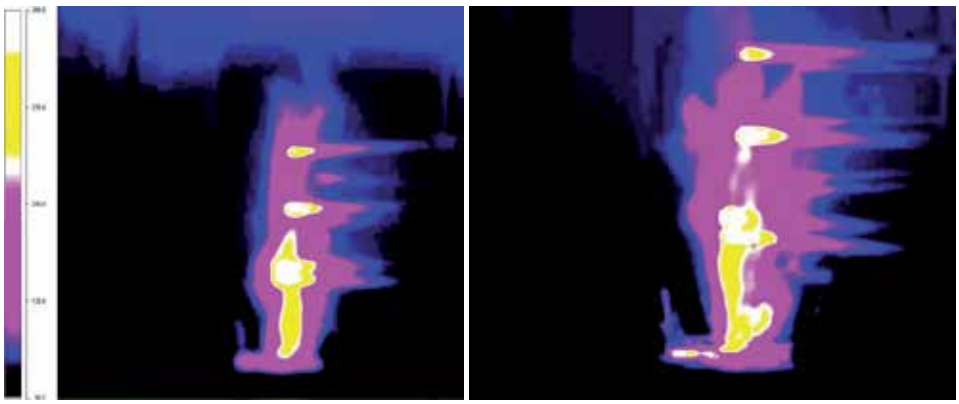

Figure 16. Comparative analysis, in infrared, of the afterburning modules (the existing module on the 2xST power plant – left; numerical simulation result – right) [15, 38]

natural gas afterburning installation – positioned on the vertical, water spraying instalation, command and data acquisition chamber. The emissions measurement has been realized using the Horiba PG 250 gas analyzer, positioned on the stack (the exit of the afterburning chamber – figure 18 right). The experiments conducted on the TA2 gas turbine, using gaseous fuel, have been carried out at starting regime (10500±6 rpm; 75±5 Nm^3/h natural gas flow).

Figure 17. Water spraying tests, using a liquid fuel atomizer from TV2-117A gas turbine

The mean temperature T_{3M} (the gases mean temperature before the gas turbine) has been determined using 17 thermocouples (figure 19 left), using the methodology presented in [15]. The free turbine speed has rezulted from the vibration analysis, data acquisition being realized unsing module IEPE BNC Ni9233 (National Instruments). The exhaust gases temperature (T_5 – figure 19 right) has been measured using a thermocouple.

The experiments included several series of 20 minutes in which the gas turbine functioned at starting regime (without the afterburning module), using natural gases as fuel (for 10 minutes

Figure 18. Experiments regarding the injection of water in TA2 gas turbine (left) and gas analyser PG 250 (right)

the gas turbine functioned without water injection, followed by 10 minutes of functioning with water injection). The results regarding NO_x emissions during the experiments conducted on the TA2 gas turbine using natural gases as fuel, with/without water injection (the atomizer is positioned on the gas turbine's axis, at 1500 mm from the gas turbine's intake device) are presented in figure 20. The results obtained so far regarding water injection in the intake device of TA2 gas turbine (for power increase) are more qualitative, although by introducing water the speed of the free turbine is increased with about 20 rpm. Simultaneously with the introduction of water, temperatures T_{3M} and T_5 decrease with about 5 °C, and the NO_x emissions decrease with about 4 ppm. It is expected that the influences will be more conclusive when the load of the gas turbine and the water quantity are increased.

Figure 19. The thermocouples position for determining T_{3M} (left) and T_5 (exhaust device exit - right)

http://dx.doi.org/10.5772/59002

After about 10 series of experiments, of 20 minutes each, the boroscopic examination of the gas turbine didn't revile any significant deposits. Possibly in the future it will be necessary to appropriately treat the water injected in the intake device.

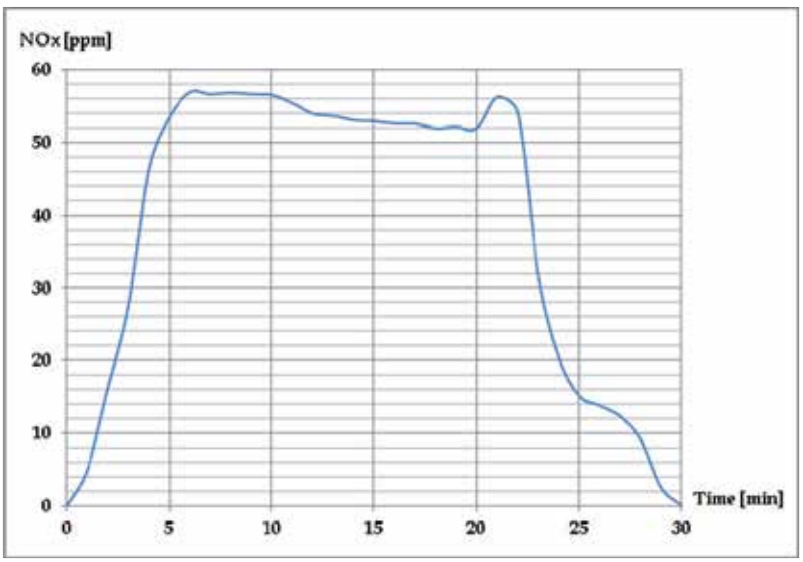

Figure 20. NO_x emissions variation during the experiments carried out on TA2 gas turbine, with water injection in the intake device

5.3. Future research

Future research to be conducted at INCDT COMOTI Bucharest will follow the general context given by the efficiency-emissions reduction-flexibility triad, by numerical simulations and experiments concerning: processes that take place during the cooling of the intake air; combustion in the gas turbine and afterburning installation; increase of the efficiency and pollutants reduction; flexibility regarding the used fuels.

6. Conclusions

1. The selection of a location for a gas turbine cogenerative plant imposes climatic conditions and demands adequate technical solutions to meet performance requirements, especially during summer season when inlet air temperature rises, leading to a decrease in power output and efficiency.

2. Water content modifies thermodynamic properties of intake air (density, specific heat) affecting power output and heat mass flow resulted from the gas turbine. If in the past air humidity was neglected, in present day cogenerative gas turbine power increase, but also water/steam injection impose the need for it to be taken into account.

3. The main research directions in the area of cogenerative groups with gas turbines efficiency increase are: combustion temperature increase; compression ratio increase; improvement of design methods, combustion technology and advanced materials; technological transfer for aviation domain to industrial turbines domain; integrated systems (combined cycles, intake air cooling, exhaust turbine gases heat recovery, afterburning, etc.).

4. Determinant factors concerning the overall efficiency of the cogenerative group are: gas turbine exit temperature, temperature at the heat recovery steam generator stack; ambient environment temperature. For these the most influential factor upon the increase of the overall efficiency is the temperature at the heat recovery steam generator stack.

5. Operating flexibility of equipment has become a major subject. Gas turbines are designed to function generally at nominal regime, in maximum efficiency conditions and minimum pollutants. At cogenerative groups with heat recovery steam generator, for producing technological steam, is preferable that the flexibility to the process demands to be achieved using afterburning installation.

6. Theoretical and experimental research conducted at INCDT COMOTI Bucharest, allowed: to be showed that, in the case of a gas turbine with intercooling, the performances variation is approximately linear for a compression ratio between 10.2-16, with a power decrease of 2.5 % for each 5 degrees increase of the environment temperature; to be obtained a afterburning module with a 30 % reduction of the NO_x reduction (at partial load) in comparison with the existing cogenerative power plant 2xST 18 – Suplacu de Barcau; to demonstrate the power increase and NO_x emissions reduction when injecting water in the intake device of TA2 gas turbine.

Acknowledgements

The research have been made based on contracts 22-097/2008, 22-108/2008 (Programme "Partnerships in priority fields") and 7N/2009, financed by Romanian Ministry of Education, Research, Youth and Sports. The consortium involved in contracts 22-097/2008, 22-108/2008 includes several companies in Romania: INCDT COMOTI Bucharest, SC OMV PETROM SA, UPB-CCT Bucharest, SC OVM-ICCPET SA Bucharest, SC ICEMENERG SA Bucharest, SC ERG SRL Cluj, SC TERMOCAD SRL Cluj.

Author details

Ene Barbu[1*], Valeriu Vilag[1], Jeni Popescu[1], Bogdan Gherman[1], Andreea Petcu[1], Romulus Petcu[1], Valentin Silivestru[2], Tudor Prisecaru[1], Mihaiella Cretu[1] and Daniel Olaru[1]

*Address all correspondence to: barbu.ene@comoti.ro

1 INCDT COMOTI, Bucharest, Romania

2 Politehnica University, Bucharest, Romania

References

[1] Technology characterization: Gas turbines, 2008, http://www.epa.gov/chp/documents/catalog_chptech_gas_turbines.pdf (accessed 17 July 2014).

[2] Notiuni introductive privind ciclurile termodinamice ale motoarelor termice si turbinelor cu gaze. Diagrame entropice de stare, determinarea randamentelor termodinamice, http://www.rasfoiesc.com/inginerie/tehnica-mecanica/Notiuni-introductive-privind-c67.php (accessed 17 July 2014).

[3] Contemporary Cogeneration Technologies, http://www.energymanagertraining.com/Journal/02112007/ContemporaryCogenerationTechnologies.pdf (accessed 25 June 2014).

[4] Abam F., Ugot I., Igbong D., Performance analysis and components irreversibilities of a (25 MW) gas turbine power plant modeled with a spray cooler, American J. of Engineering and Applied Sciences 2012; 5 (1): 35-41, http://thescipub.com/html/10.3844/ajeassp.2012.35.41 (accessed 17 June 2014).

[5] Pankaj P., Better power generation from gas turbine along with improved heat rate, International Conference–PowergenIntl 2000-Florida, Bangkok, ASME 2003-Atlanta, http://www.energymanagertraining.com/announcements/issue25/winners_papers_Issue25/05_PankajKPatel.pdf (accessed 17 June 2014).

[6] Hosseini R, Beshkani A., Soltani M., Performance improvement of gas turbines of Fars (Iran) combined cycle power plant by intake air cooling using a media evaporative cooler, Energy Conversion and Management 2007; 48: 1055–1064,

[7] Bagabir A., Khamaj J., Hassan A., Experimental and theoretical study of micro gas turbine performance augmentation, Emirates Journal for Engineering Research 2011; 16 (2): 79-88, http://www.engg.uaeu.ac.ae/ejer/issues/V16/pdf_iss2_16/7%20Ahmed%20Bagabir-22-22-F11_EXPERIMENTAL_Formatted%20_2__authors.pdf (accessed 22 June 2014).

[8] P. dos Santos, Andrade Cl., Zaparoli E., Comparison of different gas turbine inlet air cooling methods, World Academy of Science, Engineering and Technology 2012; 6, http://www.waset.org/publications/2686/comparison-of-different-gas-turbine-inlet-air-cooling-methods.pdf (accessed 17 June 2014).

[9] Etminan V., Moghiman M., Bajestan E., Boghrati M., Performance improvement of simple cycle gas turbine by using fogging system as intake air cooling system, http://www.google.ro/url?sa=t&rct=j&q=&esrc=s&source=web&cd=95&ved=0CGMQFjAEOFo&url=http%3A%2F%2Fprofdoc.um.ac.ir%2Farticles%2Fa%2F102366.doc&ei=lTpaU7KUFeOI7Abs-jYHQDQ&usg=AFQjCNHCYaE5k7lhoIXTYF2D03ETtWw-ww (accessed 17 June 2014).

[10] Espanani1 R., Ebrahimi S., Ziaeimoghadam H., Efficiency Improvement Methods of Gas Turbine, Energy and Environmental Engineering 2013; 1(2): 36-54, 2013 DOI: 10.13189/eee.2013.010202, http://www.hrpub.org/download/201309/eee.2013.010202.pdf (accessed 17 June 2014).

[11] Gopinath V., Navaneethakrishnan G., Performance Evaluation of Gas Turbine by Reducing the Inlet Air Temperature, International Journal of Technology Enhancements and Emerging Engineering Research 2013; 1 (1): 20-24, http://www.ijteee.org/final-print/aug2013/Performance-Evaluation-Of-Gas-Turbine-By-Reducing-The-Inlet-Air-Temperature.pdf (accessed 20 June 2014).

[12] Al-Doori W., Parametric Performance of Gas Turbine Power Plant with Effect Intercooler, Modern Applied Science 2011, 5 (3): 173-184

[13] Kyprianidis K., Future Aero Engine Design: An Evolving Vision, Advances in Gas Turbine Technology, Dr. Ernesto Benini (Ed.), InTech, 2011, ISBN: 978-953-307-611-9, DOI: 10.5772/19994. Available from: http://cdn.intechopen.com/pdfs-wm/22893.pdf (accessed 27 June 2014).

[14] Barbu E., Vilag V., Popescu J., Ionescu S., Ionescu A., Petcu R., Cuciumita C., Cretu M., Vilcu C., Prisecaru T, Afterburning Installation Integration into a Cogeneration Power Plant with Gas Turbine by Numerical and Experimental Analysis, Advances in Gas Turbine Technology, Dr. Ernesto Benini (Ed.), InTech, 2011, ISBN: 978-953-307-611-9, DOI: 10.5772/19994. Available from: http://www.intechopen.com/books/advances-in-gas-turbine-technology/afterburning-installation-integration-into-a-cogeneration-power-plant-with-gas-turbine-by-numerical-(accessed 17 June 2014).

[15] Barbu E., Petcu R., Vilag V., Silivestru V., Prisecaru T., Popescu J., Cuciumita C., Tomescu S., Gas Turbine Cogeneration Groups Flexibility to Classical and Alternative Gaseous Fuels Combustion, Progress in Gas Turbine Performance, Dr. Ernesto Benini (Ed.), InTech, 2013, ISBN: 978-953-51-1166-5, Available from: http://www.intechopen.com/books/progress-in-gas-turbine-performance/gas-turbine-cogeneration-groups-flexibility-to-classical-and-alternative-gaseous-fuels-combustion (accessed 17 June 2014).

[16] Motahar S., Alemrajabi A., Performance augmentation of an aero-engine gas turbine using steam injection, International Conference on Energy and Environment 2006 (ICEE 2006), http://www.iasj.net/iasj?func=fulltext&aId=57646 (accessed 27 June 2014).

[17] Tyagi K., Khan M., Effect of gas turbine exhaust temperature, stack temperature and ambient temperature on overall efficiency of combine cycle power plant, International Journal of Engineering and Technology 2010; 2 (6): 427-429, http://www.enggjournals.com/ijet/docs/IJET10-02-06-18.pdf (accessed 17 June 2014).

[18] Begovic M., Maintaining declared performance in gas turbines during increased ambient temperatures, Energija 2009; 58 (2): 192-207.

[19] Kurz R., Gas turbine performance, Procedings of the thirthy-fourth turbomachinery Symposium, 2005, 131-146, http://turbolab.tamu.edu/proc/turboproc/T34/t34-14.pdf (accessed 17 June 2014).

[20] Pavri R., Moore G., Gas turbine emissions and control, http://site.ge-energy.com/prod_serv/products/tech_docs/en/downloads/ger4211.pdf (accessed 27 June 2014).

[21] Homji C., Mee Th., Gas turbine power augmentation by fogging of inlet air, http://turbolab.tamu.edu/proc/turboproc/T28/Vol28010.pdf (accessed 27 June 2014).

[22] Kumar P., Krishna A., Raju G., Comparative Analysis on Performance of a Gas Turbine Power Plant with a Spray Cooler, International Journal of scientific research and management (IJSRM) 2013; 1 (7): 354-358.

[23] Ionel I., Ungureanu C., Popescu F. Analiza nivelului de emisii poluante prin schimbarea combustibilui la cuptoarele de tratament termic. http://www.tehnicainstalatiilor.ro/articole/images/nr12_76-82.pdf (accessed June 14, 2014).

[24] 24. Al-dawoodi M., Theoretical study for the effect of different fuels on the perfomance of open gas turbine power plant, http://www.google.ro/url?sa=t&rct=j&q=&esrc=s&source=web&cd=119&ved=0ciybebywcdhu&url=http%3a%2f%2fwww.uobabylon.edu.iq%2fpublications%2fapplied_edition4%2fpaper_ed4_32.doc&ei=3unau5halir07abm_yh4aq&usg=afqjcnho5qxani118jnp9p733fwu7ki5uq (accessed 17 June 2014).

[25] Anderson L., Gas turbine design for cogeneration balancing efficiency and reliability for maximum economy, http://www.gasnet.com.br/conteudo/11938/Gas-turbine-design-for-cogeneration-balancing-efficiency-and-reliability-for-maximum-economy (accessed 27 June 2014).

[26] Brun K., Kurz R., Gas turbine life limiting rffects on inlet and interstage water injection, Procedings of the thirthy-fourth turbomachinery Symposium 2005, 45-52, http://turbolab.tamu.edu/proc/turboproc/T34/t34-06.pdf (accessed 27 June 2014).

[27] Ibrahim Th., Rahman M., Alla A., Study on the effective parameter of gas turbine model with intercooled compression process, Scientific Research and Essays 2010;

5(23): 3760-3770, http://www.academicjournals.org/article/article1380620575_Ibrahim%20et%20al.pdf (accessed 27 June 2014).

[28] Dharap A., Ghanwat A., Inlet Air cooling for Gas turbines, Air Conditioning and Refrigeration Journal, October-December 1999, http://www.ishrae.in/journals/1999oct/article01.html (accessed 27 June 2014).

[29] Suryan1 A. et all., Experimental investigations on impaction pin nozzles for inlet fogging system, Journal of Mechanical Science and Technology 2011; 25 (4): 839-845.

[30] Makky A., Spray modeling tutorial using ANSYS-CFX, 2012, http://www2.warwick.ac.uk/fac/sci/eng/study/pg/students/esrhaw/spray_modelling_using_ansys.pdf (accessed 27 June 2014).

[31] Wilson C.D., Riggins D.W. Performance characterization of turboshaft engines: work potential and second-law analysis. American Helicopter Society 58th Annual Forum. Montreal, Canada, June 11-13. 2002.

[32] Boyce M. P., Gas Turbine Engineering Handbook, Fourth Ed., Butterworth-Heinemann, 2012, ISBN 978-0-12-383842-1.

[33] Pimsner V., Maşini cu palete (Bladed machines). Ed. Tehnică, Bucharest, 1988.

[34] Carlanescu C., Manea I., Ion C., Sterie St. (1998). Turbomotoare – Fenomenologia producerii si controlul noxelor, Editura Academiei Tehnice Militare, Bucuresti

[35] Fagbenle R., (2010). Exergy and Environmental Considerations in Gas Turbine Technology and Applications, Gas Turbines, Gurrappa Injeti (Ed.), ISBN: 978-953-307-146-6, InTech, DOI: 10.5772/10206. Available from: http://www.intechopen.com/books/gas-turbines/exergy-and-environmental-considerations-in-gas-turbine-technology-and-applications (accessed 27 June 2014).

[36] Caresana F, et all, (2010). Micro Gas Turbines, Gas Turbines, Gurrappa Injeti (Ed.), ISBN: 978-953-307-146-6, InTech, DOI: 10.5772/10211. Available from: http://www.intechopen.com/books/gas-turbines/micro-gas-turbines-mgts-(accessed 27 June 2014).

[37] Henkel N, Schmid E., Gobrecht E., Operational flexibility enhancements of combined cycle power plants, 2007, https://www.cee.siemens.com/web/ua/ru/production_energy/Documents/Service_Operational%20Flexibility%20Enhancements%20of%20Combined%20Cycle%20Power%20Plants.pdf (accessed 27 June 2014).

[38] Barbu E., Fetea G., Petcu R., Vilag V., Dragasanu L., Afterburning installation of 2xST 18 cogeneration power plant – investigations on combustion and NO_x emissions, Chemical Engineering Transactions 2013; 34: 37-42, DOI:10.3303/CET1334007, 2013.

Chapter 3

The Importance of Hot Corrosion and Its Effective Prevention for Enhanced Efficiency of Gas Turbines

I. Gurrappa, I.V.S. Yashwanth, I. Mounika,
H. Murakami and S. Kuroda

Additional information is available at the end of the chapter

http://dx.doi.org/10.5772/59124

1. Introduction

Advanced gas turbine engines essentially need novel materials to exhibit forever-greater efficiency by increasing their operating temperatures. Higher operating temperatures lead to high temperature corrosion of the components and thereby reduce their life significantly. The blades in modern aero, marine and industrial gas turbines are manufactured primarily from Ni - based superalloys. Oxidation and hot corrosion are the two important factors (under high temperature corrosion), which determine the life of gas turbine engine components. The rate of degradation is slow under oxidation conditions, while it is significantly fast under hot corrosion conditions and catastrophic failures are imminent if proper materials in association with appropriate coatings are not used. Hot corrosion is major problem for marine and industrial gas turbines while aero gas turbines experience it while they move across the sea. Assessment of current status on hot corrosion problems in different gas turbine engines is imperative in order to improve their life by selecting advanced hot corrosion resistant materials and coatings. This process helps in highlighting the issues that need to be addressed not only for enhancing the efficiency of gas turbine engines but also to avoid failures during service.

A section of a typical gas turbine engine is shown in Fig.1 [1]. It is important to note that hot section components of the engine are manufactured from Ni-based superalloys. Advances in processing of Ni-based superalloys have allowed evolution of microstructures from equiaxed structures about three decades ago to directionally solidified (DS) multi-grain and single crystal (SC) components today. With added capability from compositional flexibility coupled with advances in processing over that time period, high-pressure turbine blade temperatures have increased marginally and metal surface temperature at the hottest locations approach 1150^0 C in state-of-the–art gas turbine engines. The most severe combinations of stress and

temperature in the present engine designs correspond to bulk average metal temperatures approaching 1000^0 C using the first generation single crystal alloys.

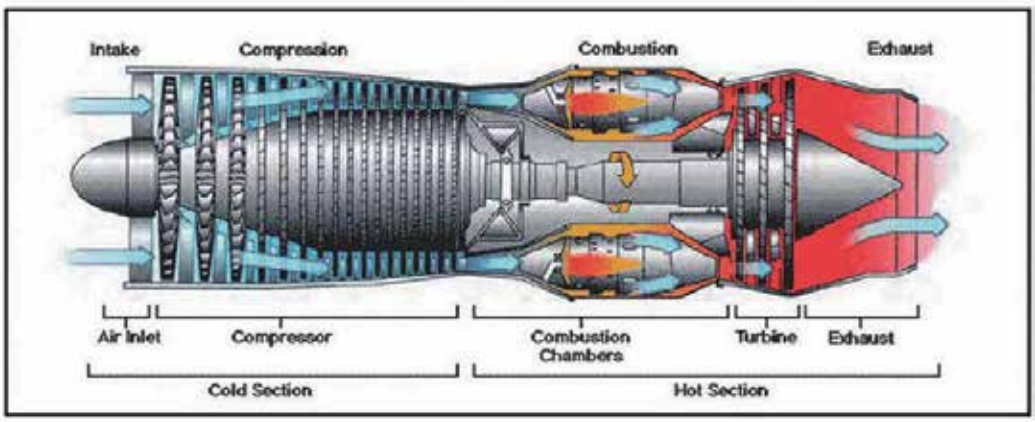

Figure 1. Gas turbine engine showing the usage of superalloys and titanium based materials [1]

One of the most critical components in the engine is the gas turbine blade. The high-pressure turbine blade operates under the most arduous conditions of temperature and stress than any component in the engine. Not only does the blade experience high temperature and direct stress, it also experiences rapid temperature transients at various points during the engine cycle. The hot gases surrounding the blade are highly oxidizing and contain high levels of contaminants like sulphur and chlorine if low-grade fuels are used. An ideal superalloy / coating should be able to survive this harsh corrosive environment.

The efficiency of a gas turbine is proportional to firing or turbine inlet temperature. Increase in engine operating temperature has meant that the traditional corrosion resistant turbine blade alloys such as IN 738 and IN 939 are no longer strong enough to last the expected 25,000 hours minimum life [2]. It implies that higher strength alloys like Mar M247, CM247 LC, single crystal alloys, CMSX-4, CMSX-10 etc. are required for creep strength. Progress in aero and industrial gas turbine blade materials is illustrated in Fig.2 [2]. During the last one decade, dramatic competition in the power equipment industry has boosted technology to the levels achieved in the aviation turbines just years before. Latest industrial gas turbines use single crystal, rhenium containing Ni-based superalloys and directionally solidified blades and vanes. These alloys have relatively poor hot corrosion resistance and hence have to rely on advanced protective coatings to prevent severe and potentially life limiting damage.

The majority of Ni - based superalloy development efforts has been directed towards improving the alloy high temperature strength with relatively minor concern being shown to its hot corrosion resistance. Further, it is not always possible to achieve both high temperature strength and hot corrosion resistance simultaneously because some alloying elements help to improve hot corrosion resistance while some may help to improve high temperature strength. It is rare that an alloying element leads to enhancement both in high temperature strength and

http://dx.doi.org/10.5772/59124

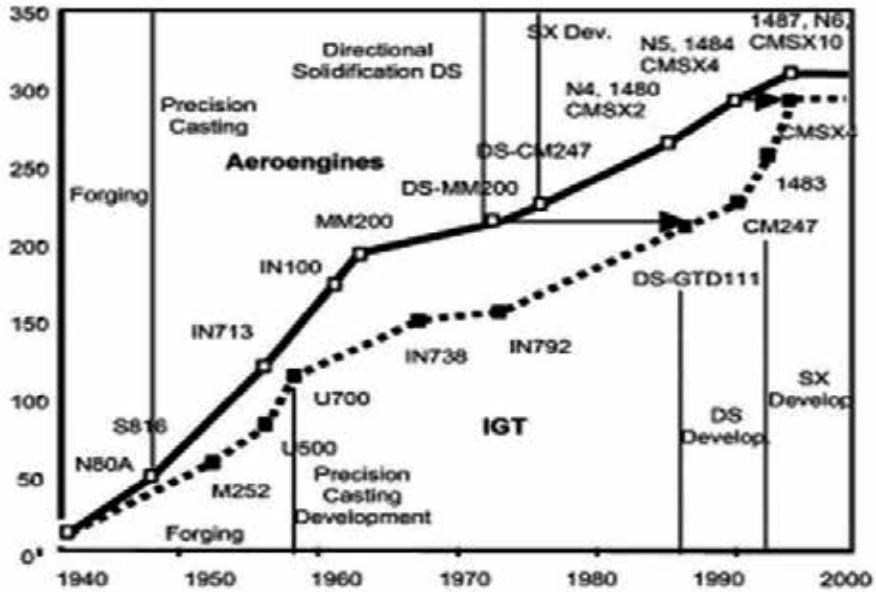

Figure 2. Progress in aero and industrial gas turbine blade superalloys [2]

the hot corrosion resistance. This is further complicated for marine applications by the aggressivity of the environment, which includes sulphur and sodium from the fuel and various halides contained in seawater. These features are known to drastically reduce the superalloy component life and reliability by consuming the material at an unpredictably rapid rate, thereby reducing the load-carrying capacity and potentially leading to catastrophic failure of components [3-5]. Thus, the hot corrosion resistance of superalloys is as important as its high temperature strength in gas turbine engine applications. Recent studies have shown that the high temperature strength materials are most susceptible to hot corrosion and the surface engineering plays a key role in effectively combating the hot corrosion problem [6-7]. Therefore, the two materials (base and coating) must be considered as an integral system and the interface between them is also equally important as it can often be the limiting factor.

This chapter explains the critical issue of hot corrosion of superalloy components in gas turbine engines and methodologies to select appropriate materials and coatings for its prevention. It is followed by an assessment of current status of coatings, coating techniques and finally, some of the critical areas that need to be addressed for development of more efficient and smart coatings.

2. Hot corrosion

Hot corrosion became a topic of important and popular interest in the late 60s as gas turbine engines of military aircraft suffered severe corrosion during the Vietnam conflict during

operation over seawater. Metallographic inspection of failed components showed sulphides of nickel and chromium and hence the process was named 'sulphidation'. However, the process has subsequently been renamed "hot corrosion" because corrosion by a thin electrolyte film bears some common features with 'atmospheric corrosion' by an aqueous film at room temperature.

Break down of protective oxide layers by chemical interaction with certain aggressive species contained in the combustion environment can produce accelerated attack on the underlying metal. This process is known as hot corrosion. Hot corrosion takes place mainly because of high concentrations of sulphur, vanadium and sodium in the fuels, which may be as high as 4, 0.05 and 0.01% (all are in wt%) respectively. Chlorides and sulphates enter the engine with the air; sulphur, vanadium and sodium oxidize during combustion and mostly volatile compounds such as SO_2, SO_3, NaOH, NaO, Na_2O, VO $(OH)_3$, V_2O_5, and V_2O_4 are formed. These compounds condense at 500 to 900^0 C and build up deposits depending on the fuel. Na_2SO_4 is the main component of deposits in engines running on high sulphur and low vanadium fuel. Table I summarizes the main contaminants likely to be formed in working environment for three types of gas turbine engines i.e. aero, marine and industrial gas turbines [8]. Table II provides the composition of slag actually formed on first stage vanes in gas fired stationary gas turbine during operation [9]. Table III provides the relevance and importance of hot corrosion in various energy fields and the associated contaminants, which are responsible for degradation of components during the service [10].

Engine application	**Contaminants**
Aero	Na, Cl, S, Ca (All low)
Marine	Na, Cl, S, Mg (All high)
Industrial	Na, V, S, Pb, Cl

Table 1. Contaminants in gas turbine fuel and air [8]

Na_2SO_4	4.3
$CaSO_4\ 2H_2O$	22.7
Fe_2O_3	22.3
$ZnSO_4\ H_2O$	20.6
K_2SO_4	10.4
MgO	2.8
Al_2O_3	6.5
SiO_2	10.4
Temperature : 850^0 C	
Atmosphere : Air containing 0.015 vol-%SO_2 -0.015 vol-%SO_3	
Flow rate: 60 l h^{-1}	

Table 2. Composition of slag (all are in wt%) [9]

http://dx.doi.org/10.5772/59124

Energy systems	Mixed oxidant reactions	Hot corrosion
Batteries and Fuel cells	SO_2 ,SO_3 ,O_2, H_2, H_2S and H_2O attack of alloys	Fused halides and carbonate cells
Coal conversion and combustion systems	CO,CO_2 , H_2 , H_2S and H_2O attack of alloys	Slag films, residue films, fly ash films, salt films in MHD*, salt film assisted coal combustion
Solar energy and energy storage	-	Salt spillage or leakage from thermal storage tanks
Nuclear Energy	H-O-C in HTGR Steam reactions with Zircaloy	Fission product, salt condensation on cladding
Gas Turbines	SO_2, SO_3 and O_2 attack of alloys	Na_2SO_4 , NaV_xO_y , NaCl attack of alloys
Gas and Oil recovery and Magma Energy	H_2, H_2S and H_2O attack of alloys	-

* Magneto Hydrodynamic

Table 3. Relevance and importance of hot corrosion in energy systems [10]

2.1. Types

Two different forms of attack have been identified, types II hot corrosion, and I, which occur over different temperature ranges; 600-750^0 C and 800-950^0 C respectively. Type I results from a fluxing process where modification of the sodium sulphate deposit chemistry permits ingress of sulphur into the underlying metal; this produces localized depletion of protective elements and progressive internal attack occurs. The net process of type I hot corrosion produces a characteristic of attack which includes a porous oxide scale, an irregular metal / scale interface and internal attack with preceding metal sulphides.

On the other hand, type II hot corrosion requires sodium sulphate and sufficient sulphur trioxide to maintain low melting deposit, which readily fluxes the surface oxide. Thermodynamics favour sulphur trioxide formation in the lower temperature range. The associated attack is normally localized, producing pits with a lamellar scale rich in sulphur through progressive fluxing action of the deposits; sulphur generally does not enter the alloy to form internal sulphide with this type of attack [6, 11].

2.2. Mechanism

Many mechanisms have been proposed for hot corrosion. All the mechanisms involve deterioration of the reaction product barrier that forms on the alloys when the deposits are not present. Basically, the hot corrosion process proceeds in three stages (Fig.3);

a. An incubation stage during which the reaction proceeds at a rate essentially similar to that of normal oxidation

b. An initiation step during which the corrosion is accelerated

c. A propagation stage during which rapid corrosion takes place and

d. Ultimate failure of a component

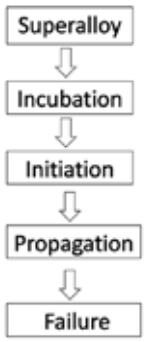

Figure 3. Various stages of hot corrosion processes, which lead to catastrophic failures of superalloy components

2.2.1. Incubation Period

During this period, the alloy undergoes normal oxidation similar to that observed in the absence of salt deposit. Initially, the oxides of most of the alloying elements are formed as given below:

$$Ni + 1/2\ O_2 = NiO$$
$$2\ Cr + 3/2\ O_2 = Cr_2O_3$$
$$2\ Al + 3/2\ O_2 = Al_2O_3$$

Due to the reaction with oxygen in the initial stages, rapid weight gain of the alloy takes place. At the end of incubation stage, thermodynamically stable oxides such as Cr_2O_3, Al_2O_3 (depending on the composition) are formed as a dense oxide scale on the surface of alloys. This oxide scale acts as a diffusion barrier for the ingress of deleterious species such as oxygen and sulphur.

2.2.2. Initiation stage

Cracking or spalling of oxide scale occurs in this stage due to the stresses developed during oxide growth. Thus, fresh alloy surface, which is depleted of scale forming alloying elements, is exposed to the action of deposit as shown below:

$$Ni + SO_4^{2-} = NiO + SO_2 + O^{2-}$$

SO_2 will be in the form of dissolved gas.

http://dx.doi.org/10.5772/59124

2.2.3. Propagation stage

The propagation stage during hot corrosion is substantially different from the behaviour of the alloy in the absence of a deposit. It is accompanied by a very severe attack of the alloy as a result of fluxing of oxides as shown below:

$$2\ NiO + 2\ O^{2-} = 2\ NiO_2^{2-}\ (\text{nickelate})$$
$$Al_2O_3 + O^{2-} = 2\ AlO_2^{-}\ (\text{aluminate})$$
$$Cr_2O_3 + 2\ O^{2-} + 3/2\ O_2 = 2\ CrO_4^{2-}\ (\text{chromate})$$

The dissolved sulphur dioxide formed during initiation period can react with the alloying elements to produce oxides, sulphides and sulphur.

$$2\ Ni + SO_2 = 2\ NiO + 1/2\ S_2$$
$$4/3\ Cr + 3/2\ Ni + SO_2 = 2/3\ Cr_2O_3 + 1/2\ Ni_3S_2$$

The relationship between the initiation and propagation stages and the factors that are important in preconditioning the alloy during the initiation stage are explained by Pettit and Meurer [12].

If the deposits contain chloride ions, it can selectively remove certain elements such as chromium or aluminium from the alloy. This process involves the formation of highly volatile gaseous chlorides inside the pores of the alloy and thereby metal chlorides diffuse out from the alloy. As a result, mechanical properties of the alloy reduce significantly as the cracks are formed on the alloy surface. The metallic components of these chlorides convert to oxides eventually but these oxides form as particles and not as continuous layers. Hence, severe attack of the alloy can take place.

The mechanisms have been explained based on acidic and basic fluxing of protective oxide scales depending upon the conditions. The protective oxide scale, for example Cr_2O_3 is fluxed either as acidic solutes such as $Cr_2(SO_4)_3$ or CrS or as basic solutes such as Na_2CrO_4 and $NaCrO_2$. As a result, the oxide scale can become non-protective. Such non-protective scales can be formed by dissolution of the oxide near the alloy surface and re-precipitation as discontinuous particles from the molten deposit. It is important to emphasise that there are other means by which an oxide scale can become non-protective via a fluxing process. For example, the fluxing reaction may cause a certain element to be removed from the alloy, which in turn gives rise to a non-protective scale on the surface of the alloy. Rapp and his group [13-14] carried out extensive studies pertaining to hot corrosion fluxing mechanisms, different oxide solubilities and electrochemical evaluation methods for hot corrosion resistance. Kinetic studies of various materials at high temperatures under hot corrosion conditions were reported by the earlier workers [15-16]. Natesan et al [17-18] have studied the high temperature corrosion of Ni- based superalloys in coal conversion environments.

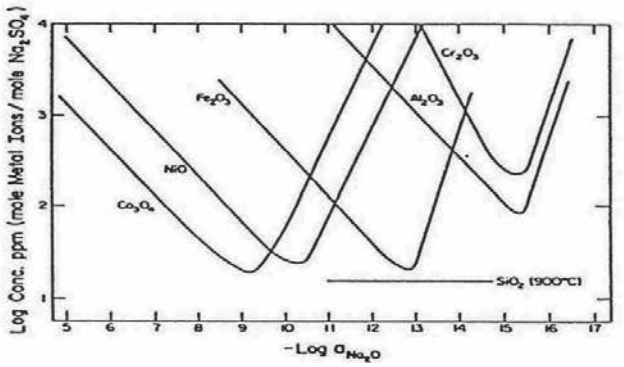

Figure 4. Measured solubilities for different oxides in fused pure sodium sulphate at 1200 K [13]

As fluxing of the protective scale is important in hot corrosion attack, the selection of alloys or coatings for hot corrosion resistance should be based on the solubility of protective oxides. For a given deposit and environmental conditions, the most favoured oxide is the one that has the least solubility and can form a protective scale in the presence of salt film. Fig.4 presents the measured solubilities of various oxides in fused Na_2SO_4 at 1200 K [13]. The difference of six orders of magnitude in basicity between minima for the most basic Co_3O_4 to the acidic SiO_2, Cr_2O_3 and Al_2O_3 is striking and is consistent with important known alloy systems and coatings under hot corrosion conditions. Cobalt based alloys and coatings are more vulnerable to acidic fluxing than Ni-based alloys and coatings. Cr_2O_3 is resistant to acidic fluxing because the minimum in its solubility curve corresponds approximately to the acidity of gas turbine environments.

It is very essential to assess the materials / coatings in the laboratory under simulated engine conditions for testing their performance, since it is not feasible to test each material directly in the engine. A satisfactory test should yield a prediction of service performance, with an estimation of component life as a desirable objective. The next section covers different techniques, which are used for evaluation of various materials / coatings for hot corrosion resistance.

2.3. Assessment techniques

The following laboratory hot corrosion techniques are in use for assessing a variety of materials /coatings for gas turbine engine applications:

i. Burner rig test

ii. Furnace test

iii. Crucible test

iv. Thermo gravimetric test

v. Electrochemical methods

http://dx.doi.org/10.5772/59124

2.3.1. Burner Rig test

This test simulates the operating conditions in gas turbine engines, the gas composition, pressure, velocity and temperature. In this test, rigs are composed of a combustion chamber from a small turbine, supplying air from compressors and burning fuel in the usual way. Salt can be sprayed into the combustion chamber. The hot exhaust gases are brought into the sample chamber, where several specimen coupons are placed and rotated in the gas stream. Here, the test variables (such as gas pressure, velocity, sample temperature, salt concentration and fuel-to-air ratio) can be selected to simulate aero, marine and land based gas turbine engine's operation. This test was used extensively for evaluation of coated and uncoated materials for hot corrosion resistance [19-22]. It was also established that the materials tested showed generally similar behaviour during service. Therefore, this test is more appropriate for testing the materials as well as coatings to get comparable results with the service conditions of gas turbine engines.

2.3.2. Furnace test

In this test, a furnace having two zones, whose temperature can be controlled independently is employed. The specimen is placed in one zone and a crucible containing the test salt is placed in the other. Using a carrier gas, the vaporized salt is carried from one zone into the other where it deposits on the specimen. In this manner, the deposition of salt per unit time can be strictly controlled. In modified method known as 'Dean Test', the corrosion conditions can be controlled from very mild to very severe, by simply altering the temperature differential within the two zones. This test was used mainly to study kinetics of various materials in different environments.

2.3.3. Crucible test

This method involves direct immersion of the sample to half its length in molten salt in air atmosphere and measurement of weight change to monitor the reaction rate. Gas may be bubbled through the melt or passed over it to provide oxidizing or reducing environments. This test was used by Simons et al [23] for the first time followed by other researchers for evaluation of a number of bare and coated materials for hot corrosion resistance. The corrosion test conditions are severer than that in normal operating condition of the engines, but it is a simple and helpful test for screening of different materials and coatings [24-34].

2.3.4. Thermo gravimetric test

It is also called "Salt coated test". In this test, a coupon of the material is coated with saturated salt solution, then dried, weighed and placed in a heated furnace. The coupon weight is continuously recorded. In most cases, the weight increases as oxidation proceeds, as the vaporization rate is small compared with the oxidation rate. This method was adopted by many researchers for determining the hot corrosion kinetics because the experimental parameters such as gas composition, temperature and salt loading can be controlled very easily and precisely.

2.3.5. Electrochemical methods

This method involves measurement of corrosion current as a result of oxidation-reduction reaction continuously and provides instantaneous corrosion rates. The net reaction is the oxidation of metal to form oxide scales and the reduction of SO_4^{2-} to a lower oxidation state. Generally, corrosion is accelerated only when the salt film is molten such that the material and the gas are physically separated by the ionically conducting fused salt. Fused sodium sulphate is a dominant ionic (Na^+) conductor like in normal solutions. Thus, the reaction must involve electrochemical steps and hence this method is most ideal for assessing materials / coatings for hot corrosion resistance.

The electrochemical polarization of alloys in molten salts can cause corrosion attack which is qualitatively similar to that found for a thin salt film in a combustion- product environment. In addition, the 600 hours burner rig test results are well comparable with 4 hour electrochemical test method. It proves that electrochemical techniques are extremely helpful in evaluating the materials / coatings at a faster rate compared to other tests developed so far and hence this method was used extensively by the researchers for the above purpose as well as to study reaction mechanisms and on line monitoring of corrosion rates in the actual plants [35-37]. The advantages and disadvantages of each technique are presented in Table IV. It is important to mention here that no established ISO standard testing procedure is available till now for evaluation of materials and coatings for their hot corrosion resistance and hence the need to establish such standards in near future. In fact, it is an important issue that needs special attention by all researchers in the field.

Technique	Advantages	Disadvanges / limitations
Burner Rig Test	Simulates gas composition, pressure, velocity and temperature of gas turbine engines	Complex process and requires long running time. Difficult to control all the parameters accurately
Furnace Test	Corrosion conditions can be controlled depending upon the requirements i.e. severe or mild corrosion	Difficult to maintain salt deposition rate for longer times
Crucible Test	Most simple and highly useful for preliminary screening of the materials and coatings	Corrosion is severe for alloys or coatings having low or intermediate resistance to hot corrosion
Thermo-gravimetric Test	Precise weight gain measurement possible under different test conditions i.e. gas composition, temperature, salt composition etc.	Not useful for predicting the life of materials and coatings
Electrochemical Test	Fast and useful for ranking the materials and coatings based on oxidation-reduction Phenomenon	Yet to be established fully

Table 4. Comparison of hot corrosion evaluation techniques

http://dx.doi.org/10.5772/59124

2.4. Influence of superalloy composition

Different superalloys of varied categories namely forged alloys such as Nimonic 75, Nimonic 105, Inconel 718 etc., conventional casting (CC) alloys like Inconel 713, Inconel 100 etc., and directionally solidified alloys such as CM 247 LC, MAR-M200, MAR-M247 etc. were reported for their hot corrosion resistance in different environments. Single crystal superalloys of different generations such as first generation namely CMSX-2, TMS-12, TMS-26, PWA1480, Rene N4 etc., second generation with up to 3 mass % rhenium (CMSX-4, Rene N5, TMS 82+ etc.), third generation with up to 6 mass % rhenium (CMSX-10, TMS-75, TMS 80+ etc., and fourth generation with rhenium and ruthenium (TMS-138 etc.) have been developed recently. The 3rd and 4th generation superalloys contain large amount of rhenium (Re) as mentioned above and less amount of chromium, exhibits good hot corrosion resistance but susceptible to oxidation. As one of the directionally solidified (DS) superalloys, CM 247 LC alloy exhibits comparable properties as the single crystal alloys. Table V presents different superalloys for which hot corrosion characteristics have been reported in the literature [6, 32, 38-44]. Advancements in superalloys as well as processing techniques have permitted the hot gas path components now to operate in modern gas turbine firing at increased temperatures for significantly increased duration (many thousands of hours) under severe conditions of centrifugal, thermal and vibratory stresses.

Few superalloys have been designed and developed based on phase stability and utilizing predictive techniques by balancing the levels of critical elements (Cr, Mo, Co, Al, W and Ta) in order to maintain good hot corrosion resistance at higher strength levels. One among them is IN 738 superalloy. Therefore, IN 738 is notable as being one of a very small class of modern superalloys that has an outstanding combination of elevated temperature strength and hot corrosion resistance. The balance of these two properties was optimal for heavy-duty gas turbine applications. It was significantly designed for application in land-based gas turbine, as opposed to aircraft use. This alloy was first developed by the international nickel company and subsequently modified its chemistry to improve its castability. This work enabled the successful application of IN 738 over the past 20 years in General Electric gas turbines. Indeed this alloy is now used throughout the entire heavy-duty gas turbine industry with platinum aluminide coatings. Developmental efforts were focused on single processing and advanced DS alloy development. Single crystal airfoils offer the potential to further improve component high temperature materials strength and by control crystal orientation, can provide an optimum balance of properties. In single crystal material, all grain boundaries are eliminated from the material structure and a single crystal with controlled orientation is produced in an airfoil shape. By eliminating all grain boundaries and the associated grain boundary strengthening additives, a substantial increase in the melting point of the alloy can be achieved, thus providing a corresponding increase in high temperature strength. The transverse creep and fatigue strength is increased compared to equiaxed or DS structures. The advantages of single crystal alloys compared to equiaxed and DS alloys in low cycle fatigue (LCF) are shown in Fig. 5. The single crystal alloys (2nd generation) have been in use in gas turbine engines since 1995. Together with improved protective coatings, the new materials like third and fourth generation alloys will provide enhanced growth capability for gas turbine engines in the years to come.

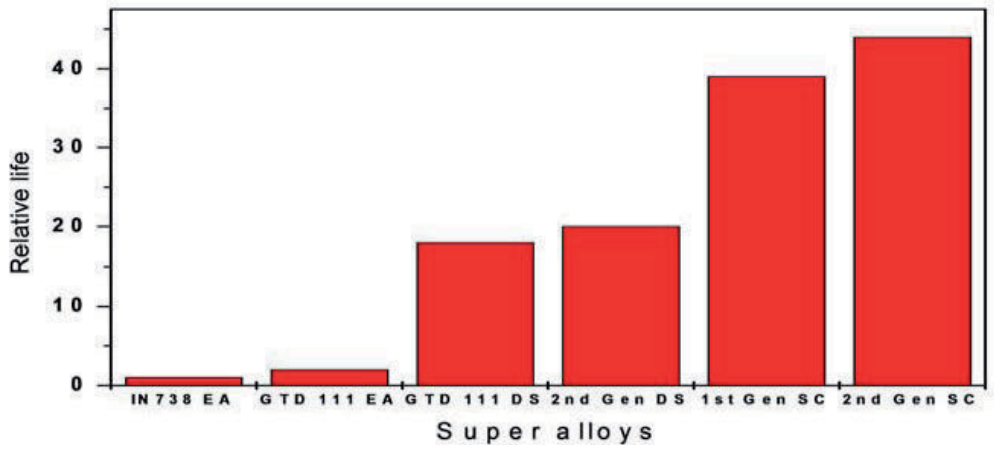

Figure 5. Low cycle fatigue (LCF) of various superalloys

Single crystal superalloys containing rhenium and iridium with low chromium, TMS-75 and TMS-75 + Ir respectively, was observed to exhibit balanced intermediate and high temperature creep, strengths with good hot corrosion resistance based on short term laboratory studies (20 hours only) in 75% Na_2SO_4 + 25% NaCl (Fig.6) [38]. However, further research is needed on these materials on long term basis with aggressive species like NaCl and V_2O_5 in order to establish their characteristics.

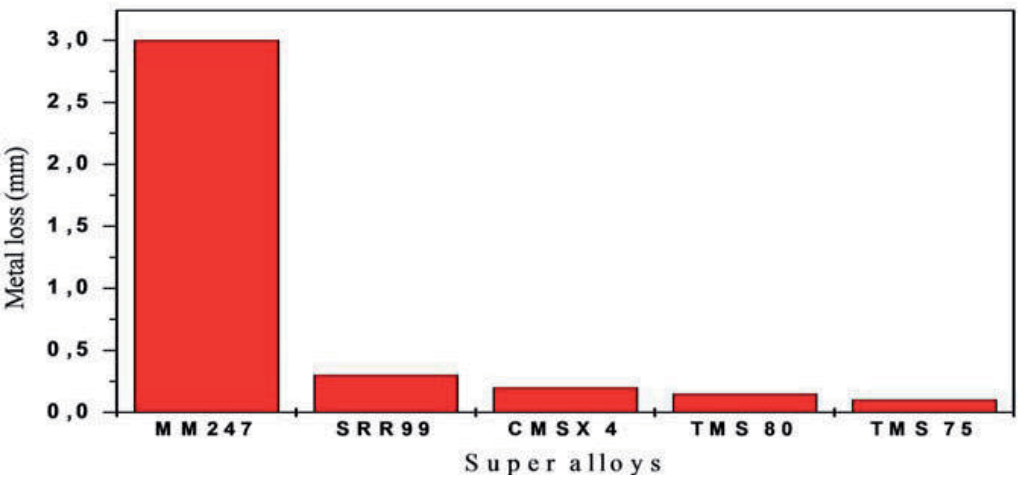

Figure 6. Hot corrosion resistance of different superalloys in 75% Na_2SO_4 + 25% NaCl at 900^0 C for 20 hours [38]

Fig.7 shows the hot corrosion behavior of few superalloys like IN 792, CMSX-4 and DMS-4 under type I conditions. The hot corrosion resistance of CM 247 LC and Rene 80 Superalloys

http://dx.doi.org/10.5772/59124

under type II and type I conditions in chloride and vanadium environments are also presented in Fig.7. Appreciable corrosion was observed for all the superalloys. It indicates that hot corrosion plays a significant role in causing faster degradation, thereby reducing the superalloy life considerably. Among the superalloys, CM 247 LC was corroded severely indicating that the superalloy is highly susceptible to hot corrosion. The appreciable corrosion attack of CM 247LC superalloy was clearly evidenced by observing big cracks, broken samples (Fig.7) and large corrosion affected zone (due to appreciable diffusion of corrosive elements present in the environment). Sulphur diffusion and formation of metal sulphides preferentially chromium and nickel sulphides was reported to be the influential factor [6]. When sulphide phases are formed in superalloys, Ni- based alloys are inferior to cobalt and iron based alloys, which are especially effective in destroying the corrosion resistance of alloys [26, 36-42]. In fact, the alloying elements play a significant role and decide the life of superalloys under hot corrosion conditions.

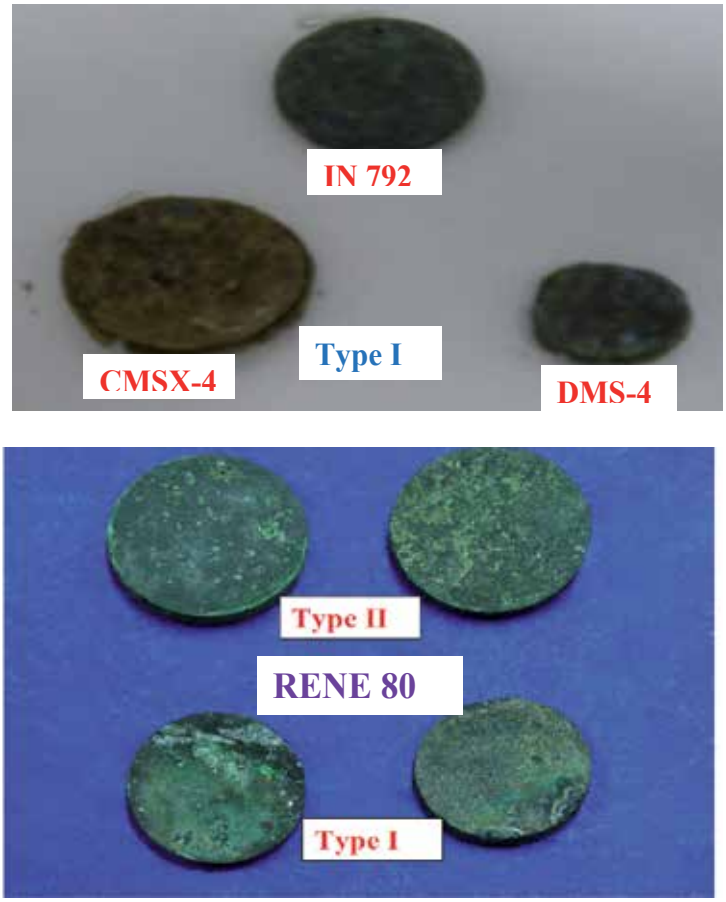

Figure 7. As hot corroded superalloys in various environmental conditions

Alloy	Al	Ti	Cr	Co	Ni	W	Ta	Re	Mo	Hf	Ir	Others
NIMONIC 75	-	0.4	20	-	Bal	-	-	-	-	-	-	Fe, C
NIMONIC-105	4.7	1.3	15	20	Bal	-	-	-	5.0	-	-	C
INCONEL 100	5.5	5.0	10	15	Bal	-		-	3.0	-	-	Zr,C,B,V
INCONEL 713	6.0	0.8	12.5	-	Bal	-	1.75	-	4.2	-	-	Zr,C,B,Nb
MAR M200	5.0	2.0	9.0	10	Bal	12.5	-	-	-	-	-	Zr,B,C,Nb,Fe
IN 738	3.4	3.4	16	8.3	Bal	2.6	1.75	-	1.75	-	-	Cb,Fe,C
CMSX-4	5.3	1.0	6.5	10.4	Bal	6.1	4.9	0.8	-	-	-	-
MAR M-247	5.5	1.0	8.0	10.0	Bal	10.0	3.0	-	0.6	1.5	-	B,Zr,C
MAR M-509	-	0.2	23.5	55	10	7	3.5	-	-	-	-	Zr,C
CM 247LC	5.6	0.7	8.1	9.2	Bal	8.5	3.2	-	0.5	1.4	-	B,Zr.C
INCONEL 718	-	-	18	-	Bal	-	-	-	3.0	-	-	Fe,Cb-
CMSX-10	5.7	0.2	2.0	3.0	Bal	5.0	8.0	6.0	0.4	0.03	-	-
TMS-75	6.0	-	3.0	12.0	Bal	6.0	6.0	5.0	2.0	0.1	-	-
TMS-80	5.8	-	2.9	11.6	Bal	5.8	5.8	4.9	1.9	0.1	3.0	-

Table 5. Typical superalloys characterised for their hot corrosion resistance [6, 32, 38-44]

Some Ni-based superalloys were designed with the aid of d-electrons concept for industrial turbines. They developed based on the molecular orbital calculations of the electronic struc-

http://dx.doi.org/10.5772/59124

tures of Ni-alloys i.e. based on two electronic parameters such as bond order between an alloying element and nickel atoms Bo, and d-orbital energy level of alloying element Md. Some single crystal superalloys were designed based on this concept. The experimental data on the designed single crystal superalloys was reported to be satisfactory [38-39]. However, the need is essential in order to establish the concept for development of hot corrosion resistant Ni-based superalloys as the superalloys should satisfy both high temperature strength and high temperature corrosion resistance, which is a highly difficult task. It is due to fact that same alloying elements never help to improve both high temperature strength and corrosion resistance simultaneously as mentioned earlier.

From the metallurgical point of view, it is known that high temperature strength can be obtained by maintaining certain phases that are responsible for high temperature strength. Since the main motive for metallurgists is to improve the mechanical strength of an alloy at elevated temperatures, the addition of certain alloying elements is essential in order to form γ' and solid solution strengtheners. Among the alloying elements, the significant reduction of chromium content and addition of certain elements like tungsten, molybdenum, vanadium etc. makes the superalloys highly susceptible to hot corrosion [6, 26, 41]. Tungsten (W) and Mo dissolve in γ-phase of the matrix and strengthen the alloy. These elements are particularly effective for improving long-term strength of the alloy. However, excessive addition causes the formation of harmful sigma phase and affects the strength of the alloy. Suitable contents for obtaining good strength are 2 to 15% of W and 6% or less of Mo. The addition of titanium and tantalum produces beneficial effects while small additions of manganese, silicon, boron and zirconium do not significantly influence the hot corrosion resistance of superalloys. Carbon addition is detrimental as the carbide phases provide sites for initiation of hot corrosion [26]. With a large content of chromium and small amount of titanium, hot corrosion resistance of Nimonic-75 is very good [32]. The addition of molybdenum and iron made the Inconel 718 less corrosion resistant [6]. The addition of 9.5% tungsten and minor additions of other elements rendered CM 247LC highly susceptible to hot corrosion [6]. The tungsten present in the alloy forms acidic tungsten oxide (WO_3), due to which fluxing of protective oxide scale takes place easily. It is important to mention that this type of acidic fluxing is self-sustaining since WO_3 forms continuously that leads to severe degradation of superalloys. The degradation mechanism comprises two steps as follows:

a. The tungsten present in the superalloys reacts with the oxide ions present in the environment and forms tungsten ion

$$WO_3 + O^{2-} = WO_4^{2-}$$

b. As a result, the oxide ion activity of the environment decreases to a level where acidic fluxing reaction with the protective alumina can occur

$$Al_2O_3 = Al^{3+} + O^{2-}$$

A similar reaction mechanism occurs if the superalloys contain other refractory elements like vanadium and molybdenum [26, 40].

Cobalt (Co) and chromium (Cr) contents affect the hot corrosion resistance of superalloys. If Co is added excessively, it promotes precipitation of harmful inter-metallic compounds that deteriorates high temperature strength. An appropriate content of Co is 10.5% or less. Cr improves hot corrosion resistance. However, if it is added excessively, it causes precipitation of harmful sigma-phase and coarsening of carbides, thereby deteriorating high temperature strength. An appropriate additive amount of Cr is in a range of 5 to 14%. Aluminium and titanium contribute to improvement of high temperature strength by forming γ'-phase i.e. $Ni_3(Al,Ti)$, which is a strengthening factor of the Ni-based alloys. They improve hot corrosion resistance. Appropriate amounts of Al and Ti are in ranges of 4 to 7% and 0.5 to 5% respectively.

Nb, Ta and Hf dissolve in γ'-phase, which is a strengthening factor and improve high temperature strength of the superalloy. However, if they are added excessively, they segregate at grain boundaries and reduce the strength of the alloy. Appropriate additive contents of Nb, Ta and Hf are, respectively, 3 % or less, 12% or less and 2% or less and preferably 0.2 to 3% of Nb, 3 to 4% of Ta and 0.5 to 1.o% of Hf. Zr and B strengthen grain boundaries and improve high temperature strength of the alloy. Since the addition of these elements are in the low range and there is no much effect on hot corrosion resistance of the superalloys.

The common alloying element for the new generation superalloys is rhenium [41-44]. In rhenium containing superalloys, the Re atoms dissolve preferentially in γ matrix, retards the over-ageing of γ' dispersed phase thereby increase γ-γ' misfit. In addition, Re atoms form small domains (clusters) of approximately 1nm diameter, act as barriers to the dislocation movements. The formed clusters improve the creep resistance of the superalloys. Kobayashi et al have reported that Re also helps in improving the hot corrosion resistance though significantly low chromium is present in superalloys [38]. However, the exact mechanism based on which the hot corrosion resistance improved was not reported. It was also reported that rhenium containing superalloys are susceptible to oxidation. It indicates that the oxide scale that forms upon exposure is not protective. It should not form either alumina or chromia scale due to significantly low contents of aluminium and chromium. Extensive studies have been carried out recently with and without Re containing superalloys in order to understand the role of rhenium and confirmed that Re containing superalloys are highly susceptible to high temperature oxidation as well as both types of hot corrosion [41, 45-47].

2.4.1. Degradation mechanisms

The mechanisms proposed earlier are sulphides formation and subsequent transformation to corresponding alloy element oxides. Later, it was reported that degradation of superalloy take place due to fluxing processes. Fluxing processes are divided into two types such as acidic and basic fluxing process. The nature of fluxing process depends on the alloying elements and their concentration in the superalloys. It also depends on the environment to which the superalloys are exposed. In the fluxing process, the corresponding oxides dissolve in the components of environment and cause to degrade the superalloys at a much faster rate.

http://dx.doi.org/10.5772/59124

Recently, an electrochemical mechanism was proposed and experimentally proved that all the superalloys, irrespective of their alloying elements and concentration and any type of environments to which they are exposed, degrade due to electrochemical reactions that take place during hot corrosion process. Hence, the electrochemical techniques are more suitable for assessing newly developed superalloys and their ranking [6].

3. Coatings

There are a number of cases reported in the literature where the gas turbine blades suffered severe corrosion due to which failures took place [2-5]. Failure investigations confirmed that it was due to hot corrosion, in which extensive penetration of sulphur took place into the material leading to the formation of metal sulphides that in turn led to reduction in mechanical properties of the materials resulting in catastrophic failures (Figs. 8, 9, 10). From literature it is also understood that it is not possible to develop an alloy having both high temperature strength and hot corrosion resistance simultaneously since alloying elements often have opposing effects on the two properties. Particularly, tungsten, molybdenum and vanadium additions to superalloys are helpful in improving the high temperature strength, but their presence make the superalloys highly susceptible to hot corrosion as mentioned above. High performance coatings that can withstand environmental degradation problems such as oxidation and hot corrosion become important. Therefore, it is mandatory to prevent hot corrosion by using appropriate coating technology [41, 46] so as to increase the life of gas turbine components to the designed service life (Fig.11).

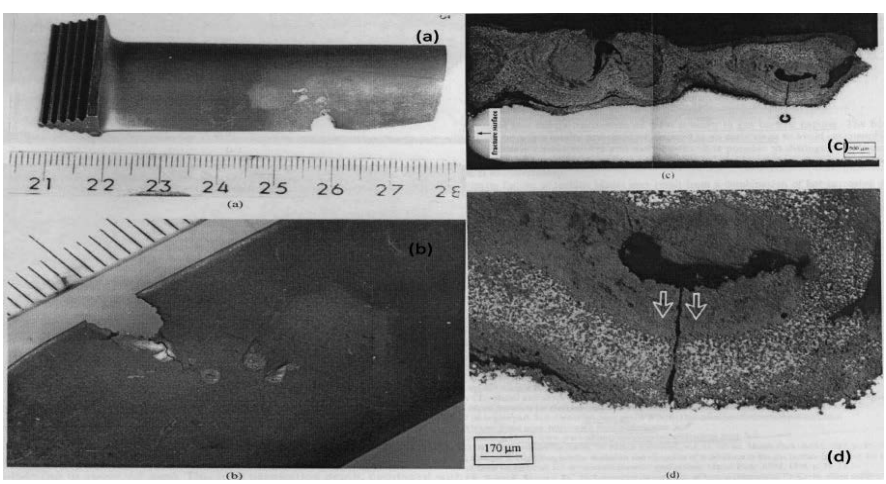

Figure 8. a) Macroscopic view of damaged blade b) a crack propagating into remainder material c) micrograph showing advanced hot corrosion attack d) secondary crack propagation [3]

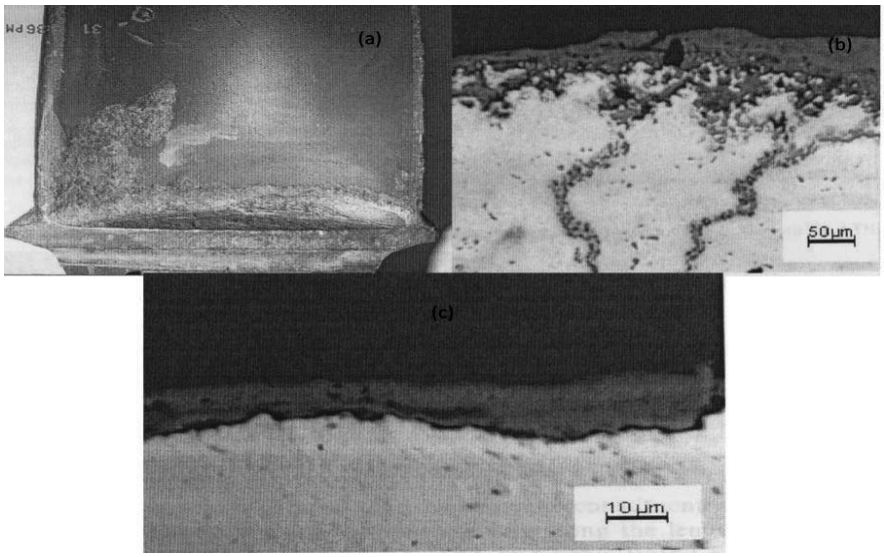

Figure 9. a) Macroscopic view of hot corrosion affected blade b) grain boundary diffusion and subscale sulphide particles indicating type I hot corrosion c) no grain boundary diffusion and subscale sulphide particles indicating type II hot corrosion [4]

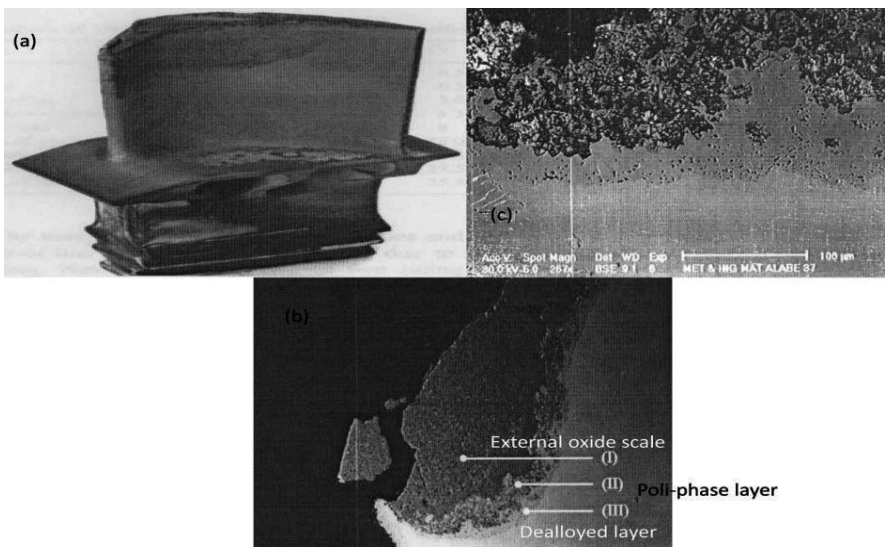

Figure 10. a) Macroscopic view of failed blade b) corroded region consisting of three layers c) internal layer of corrosion products [5]

http://dx.doi.org/10.5772/59124

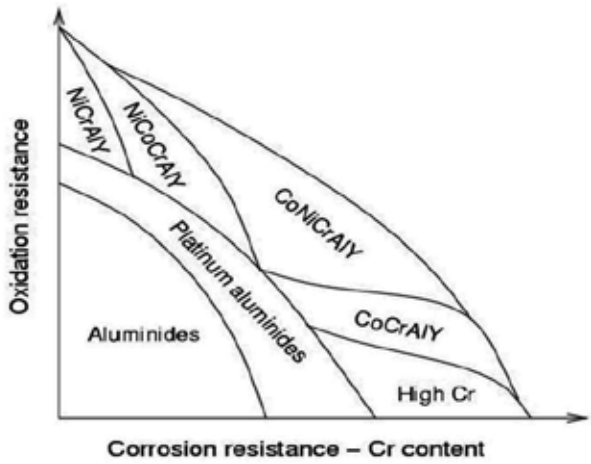

Figure 11. Oxidation and hot corrosion resistance of various coating systems [46]

The blade coatings are usually of either MCrAlY type (where M is Ni or NiCo) or aluminides. These coatings can provide protection against oxidation and hot corrosion and act as bond coatings for zirconia based thermal barrier coating (TBC) systems. In both the cases, slow growth rates and optimum adherence of the alumina scales formed on the coatings during high temperature exposure are of significant for component life. These requirements can be fulfilled only by using coatings with sufficiently high aluminium contents to ensure protective alumina scale formation and re-healing after oxide spallation / reaction with the environment. The life of a coating is mainly limited by aluminium depletion occurring upon aluminium consumption as a result of alumina scale growth and repeated spallation and re-healing of the alumina scale during oxidation process. If a point is reached where the aluminium level in a bond coating falls below the level at which protective alumina scale can not be formed preferentially, faster interaction between the corrosive species present in the environment and the non-protective oxides of other constituents of the bond coating occurs and thereby affects the coating life considerably under hot corrosion conditions. Further, the constituents of ceramic thermal barrier coatings react easily with the corrosive species and shorten the coating life significantly. These aspects are covered in detail in subsequent sections.

Another important aspect is the selection of suitable surface engineering technique by which the coatings are applied since the life of a coating depends not only on coating composition but also on the surface engineering technique employed for coating. Therefore, selection of appropriate surface engineering technique as well as suitable coating composition becomes a challenging task.

3.1. Technologies

Surface engineering technique, which modifies properties of the component's surface to enhance their performance should not only be effective but also economical. The following are the most common surface engineering techniques available at present:

a. Electro-deposition

b. Diffusion coating processes

c. Thermal spray techniques

d. Ion implantation

e. Hardening & cladding

f. Selective surface hardening by transformation of phase and

g. vapour deposition.

Electro-deposition, diffusion and thermal spraying techniques are widely in use to improve the surface of components for hot corrosion resistance. Particularly, thermal spray and vapour deposition techniques are the most efficient techniques for prolonging the life of components significantly.

3.2. Thermal spraying processes:

The coatings applied by these processes have the advantage over other techniques i.e. the coating composition can be tailored to suit the specific requirements. Thermal spraying processes can broadly be divided into following techniques:

i. Flame Spraying

ii. Arc Spraying

iii. High Velocity Oxyfuel Spraying

iv. Detonation Gun

v. Air Plasma Spraying

vi. Vacuum Plasma Spraying

3.2.1.1. Flame Spraying

In this process, an oxygen-acetylene mixture is passed through a nozzle and ignited to form a combustion flame. Coating powder or wire is fed into the flame, accelerated and projected onto the substrate to form deposit. The combustion flame temperature is limited to 3000^0 C and gas particle velocities are relatively low.

3.2.1.2. Arc spraying

This process involves the production of molten particles at the tips of two consumable wires via resistance heating. The material is subsequently atomized and projected onto the substrate by a compressed air jet. The process is limited to the spraying of conductive wires, relatively cheap and can achieve high deposition rates.

http://dx.doi.org/10.5772/59124

3.2.1.3. High Velocity Oxy-fuel Spraying (HVOF)

This process involves combustion of a fuel gas with oxygen at high pressure. This creates high velocity flame propelling powdered coating materials onto a substrate. This technique can produce high quality coatings for gas turbine applications.

3.2.1.4. Detonation gun spraying

D-Gun and Super D-Gun are developed by Union Carbide, use the energy released by a controlled series of oxygen-acetylene to heat and accelerate the coating powder to high velocities and to propel the powder onto the substrate. The resulting coatings are highly dense and of high quality with a low content of oxide and unprocessed particles.

3.2.1.5. Air Plasma Spraying (APS)

In air plasma spraying, a DC arc struck between a central inert cathode and an annular copper anode is used. An inert gas is fed into the arc to form high temperature plasma. Powder is fed into the plasma and is ejected at a high velocity towards the substrate.

3.2.1.6. Vacuum Plasma Spraying (VPS)

This process has several advantages over APS. The problems associated with air contamination of the plasma jet gets eliminated, the plasma jet is longer than in air and can achieve 400-600 ms^{-1} particle velocities due to which high purity and dense deposits are obtained. A further advantage is coating adhesion. Table VI illustrate the characteristics of various thermal spraying processes [47].

Kuroda et al were developed a novel coating technique namely "warm spray" process recently which incorporates the advantages of both HVOF and cold spray [48]. Further developments may enable them to develop coatings with enhanced hot corrosion resistance.

Process	Gas temperature^0	Particle Velocity m/s	Adhesion Mpa	Oxide content %	Porosity %	Deposition Rate Kg/Hour	Typical Deposit thickness mm
Flame	3000	40	8	10-15	10-15	2-6	0.1-15
Arc wire	N/A	100	12	10-20	10	12	0.1-50
HVOF	3000	800	>70	1-5	1-2	2-4	0.1-2
Detonati-on gun	4000	800	>70	1-5	1-2	0.5	0.05-0.3
APS	12000	200-400	4 to >70	1-3	1-8	4-9	0.1-1
VPS	12000	400-600	>70	ppm	<0.5	4-9	0.1-1

Table 6. A comparison of thermal spraying processes [47]

3.3. Electron Beam Physical Vapour Deposition (EB-PVD) processes

The electron beam-PVD process has made the most significant impact over the PVD processes in respect of coating rotating blades. The microstructure of the coating is controlled very closely in this process and coating process is slow compared to conventional PVDs. Thermal barrier oxide coatings obtained with this process has a unique columnar structure with high in-plane compliance, which tends to have higher thermal conductivity and has shown to survive longer thermal cycle life as compared to plasma sprayed TBC. Table VII provides the comparison of different processes and their limitations [47].

Coating type	Advantages	Disadvantages /limitations
Diffusion (e.g. Aluminides)	Simple to produce, proven ability <900^0 C, inexpensive	Thickness limited to 50 μm. Brittle at <750^0 C and degrade by inter-diffusion. Available compositions are limited.
Plasma overlays	High rates of coating and wide range of compositions are available. Thickness not process limited (100 μm)	Rough surface and single line of sight coating than EB coatings. Thin multi-layers more difficult than EB. About 15% porosity and degrade by inter-diffusion.
EB-PVD overlays	Good control of microstructure, low contaminant level and control the composition within limits. Layered and graded coatings easily achieved and multi component processing is possible.	Low rates of deposition and expensive process. Degrade by inter-diffusion.
Plasma Spray Thermal Barrier	High rate of coating and wide range of compositions are available. Layered and graded coatings are possible. Porosity is an advantage and not limited by inter-diffusion.	Single line of sight coating and difficult to modify microstructure. High stresses generated in coatings.
EB-PVD Thermal Barrier	Good control of microstructure and low contamination level. Layered and graded coatings are possible and not limited by inter-diffusion.	Low rate of deposition and multiple component processing is possible. Expensive process and generates high stresses but relieved by structure control.

Table 7. Comparison of thermal spray and EB-PVD processes [47]

3.4. Metallic coatings

The present coatings are broadly divided into two types, diffusion and overlay.

3.4.1. Diffusion coatings

In diffusion coating application process, aluminium is made to react at the surface of substrate, forming a layer of mono-aluminide. For coatings applied over Ni-based superalloys, nickel

http://dx.doi.org/10.5772/59124

aluminide is the resulting species. This type of coatings and surface modification is one of the most widely used for tailoring the surface properties of components. Pack cementation is well-established chemical vapour deposition technique, which has been in use for nearly three decades. It is relatively a simple technique, which consists of immersing the components to be coated in a powder mixture placed in a sealed or semi-sealed retort. The entire apparatus is placed inside a furnace and heated in a protective atmosphere to a high temperature for a sufficient period to form a coating. Most blade and vane coatings were applied by pack cementation since 1970 and subsequently chemical vapour deposition (CVD) process. The surfaces of internal cooling passages are coated more effectively by forced flow gas phase aluminizing and by vacuum pulse aluminizing. From 1970's onwards, developments in the area of diffusion coatings include modification of aluminide coatings with chromium, silicon and platinum. In 1990's aluminide coatings were recognised as useful bond coatings for thermal barrier coatings (TBCs). Advanced systems started using platinum aluminides and MCrAlY coatings [24, 28, 49-50]. The most developed pack cementation processes include aluminizing, chromizing and siliconising. Under this category, two types of processes can be applied; low activity, where the aluminide coating is formed by outward diffusion of nickel from the base metal, or high activity, where the aluminide coating is formed by inward diffusion of aluminium and subsequent heat treatment. High activity process is most suitable for gas turbine applications to combat oxidation but it is susceptible to hot corrosion.

The most important improvement in the diffusion coatings has been the incorporation of platinum in aluminide coatings. This process involves the deposition of platinum by electro-chemical method followed by aluminizing at the suitable temperature for the required period. These coatings became the accepted standard for turbine hot components to combat oxidation as well as hot corrosion. The principal reason for superior performance of these coatings is that the coefficient of thermal expansion of the coating is lower compared to that of underlying superalloy. In addition, platinum enhances the activity of aluminium and allows the formation of continuous alumina scale during high temperature exposure coupled with good adherence, thereby prolonging the life of turbine blades considerably. Failure of coatings under turbine service conditions takes place due to inter-diffusion between the coating and the substrate, with the loss of protective capability. Though diffusion coatings are well bonded to the substrate they have limited compositional flexibility and their usefulness is strongly dependent on substrate chemistry.

3.4.2. Overlay coatings

To develop coatings with compositions nominally independent of substrates and with capabilities for tailoring to a wide range of requirements for gas turbine applications, overlay coatings were emerged. Coatings of this type are generally called MCrAlY coatings and essentially comprise a mono-aluminide component contained in a more ductile matrix of a solid solution. The supply of aluminium for formation of protective alumina scale comes largely from the dispersed mono-aluminide phase during the useful life of such coatings. Overlay coatings are typically well bonded and have a wide compositional flexibility. Research and development on this type of coatings has led to a variety of compositions with improved

scale adherence. The function of all coatings is to provide a surface reservoir of critical elements that will form very protective and adherent oxide layers, thus protecting the underlying base materials from oxidation as well as hot corrosion.

Low pressure plasma spraying has been mostly used to apply MCrAlY coatings to critical components such as the high pressure rotor blades because it can produce dense coatings with little oxidation and good adhesion. It has been shown that MCrAlY coatings prepared with air plasma spraying has much inferior oxidation resistance due to severe oxidation during spraying and resultant loss of aluminium during spraying. HVOF sprayed MCrAlY has been increasingly adopted due to its dense and well-controlled oxidation.

3.4.3. Advances in metallic coatings

The efficiency of a gas turbine engine (aircraft, industrial, marine) is directly proportional to firing or turbine inlet temperature. Increase in temperature is facilitated by improved structural design and airfoil-cooling technology applied to higher strength-at-temperature alloys cast by increasingly complex processes and coated with steadily improved protection systems. First stage turbine blades, the most critical components of gas turbines, made from Ni-based superalloys and augmented by coatings, have been singularly successful materials for the past several years. The turbine airfoils coatings are simple and modified diffusion aluminides, MCrAlY overlay systems and overlay thermal barrier coatings.

The oxidation resistance of alloys and coatings depends upon selective oxidation of elements such as aluminium, chromium or silicon present in the alloy / coating. Oxide scales of Al_2O_3 are more effective means for developing oxidation resistance at higher temperatures and Cr_2O_3 or SiO_2 at lower temperatures. However, under hot corrosion conditions, the properties of oxide scales are different. The protective oxide scale should not react with the corrosive environment and at the same time, it should not allow the corrosive species to diffuse into the coating. Therefore, development of a suitable coating is of great interest for such applications. Recent results have demonstrated the necessity of protective coatings with a higher degree of high temperature capability than the existing coating systems in order to prolong the life of superalloy components under hot corrosion conditions [26-30]. Coatings with sufficiently high aluminium contents to ensure protective and chemically inert alumina formation and re-healing after reaction with the corrosive environment can only satisfy these requirements. Literature review reveals that the platinum aluminide coatings perform well under high temperature oxidation and type I hot corrosion conditions, but the performance is poor under type II hot corrosion conditions, although the performance is superior to conventional aluminides. The choice therefore, appears to be MCrAlY based overlay coatings. The chromium rich and /or silicon containing MCrAlY coatings offer improved corrosion resistance at lower temperatures that are encountered in gas turbine engines. However, recent results have shown that Si containing MCrAlY coatings are detrimental to hot corrosion and life reduces significantly at higher temperatures. However, the MCrAlY coatings without Si offer good oxidation and hot corrosion resistance at higher temperatures. As mentioned earlier, the lives of the coatings are mainly limited by aluminium depletion occurring upon aluminium consumption as a result of alumina scale growth and repeated spallation / reaction and re-

http://dx.doi.org/10.5772/59124

healing of the alumina scale during oxidation and type I hot corrosion conditions. Similar is the case with chromia scales under type II hot corrosion conditions.

Stringer has outlined the basic rules for proper selection of a coating for the given application [51]. The hot corrosion resistance of the aluminide coating has improved by the addition of yttrium. Swadzaba et al [52] have shown that regeneration of aluminide coatings on turbine blades, which have worked in highly corrosive environments, is possible to regain their initial properties. The recommended regeneration techniques are pack cementation for vanes and the slurry technique for rotating blades. The degradation of aluminide-coated first-stage blades in the engines of a light military helicopter operated by the Royal Australian Navy (RAN) was reported [53]. The different modes of degradation are foreign object damage, erosion, hot corrosion, coating cracking and coating alloy inter-diffusion. Small concentrations of NaCl, as low as 10 ppm in the gas stream with Na_2SO_4 cause hot corrosion more severe and attack is greater if NaCl is in solid state.

An overview on protective coatings for gas turbine applications, their role and design was given by Goward [54]. The performance of various pack, gas phase, and noble metal aluminide and overlay coatings applied on F100 first stage turbine blades under simulated service conditions were studied and estimated their relative lives [55]. Ni-Co-Cr-Al-Y overlay coating showed superior performance compared to other coatings in 300 hrs tests. The novel technique namely "Law of mixtures" for evaluation of mechanical properties of aluminide coatings over the temperature range 20-1000^0 C and the ability of the technique to predict the mechanical behaviour was reported [56]. The high temperature corrosion of a commercial aluminide coating on IN-738LC and MAR-M002 at 700 and 830^0 C was found to degrade with different mechanisms at two temperatures. Meethan reviewed various types of protective coatings used in the turbine and combustor sections of gas turbine engines operating in aero environments [57]. He described the factors affecting the coating selection for turbine rotor blade applications and the aluminide coatings continue to provide good and cost effective protection on many turbine blades. The several environmental effects on the mechanical properties of coated superalloys and comparative performance of various coatings are provided [58].

It is widely accepted that multi-layered and graded compositions can offer significant advantages over single layered coatings. A composite coating of aluminide-yttrium exhibits good stability and excellent corrosion resistance in a cyclic high temperature hot corrosion environment [59]. Yttrium addition helps in forming Y_2O_3 and (Y, Al) O-type compounds in grain boundaries of Al_2O_3 and NiAl effectively prohibits the fast diffusion of oxidants, thus helps to improve the hot corrosion resistance significantly. Improvement of hot corrosion resistance of the aluminide coating by the addition of yttrium has also been reported in another study. There is a work by a Japanese group showing that elimination of yttrium from MCrAlY has a positive effect on slowing down the TGO growth rate [60].

Platinum aluminide coatings are more resistant to hot corrosion than simple aluminides on land based gas turbines. The role of platinum in improving the hot corrosion resistance of pt-modified aluminide coating through electrochemical method revealed that platinum significantly improves the resistance to basic fluxing by increasing $Al_2 O_3$ content in the platinum rich surface. Due to this, the difference in breakthrough potential between the two coatings

was found to be 400 mV. The platinum free coating was found to corrode severely while coating with platinum showed slight corrosion after 310 hrs in free corrosion test. However, platinum modified aluminide coatings and simple aluminide coatings are having the same resistance to acidic fluxing.

Significant amount of work was carried out in developing the hot corrosion resistant MCrAlY bond coatings [8, 28, 61-62] and the lifetimes of various coatings including platinum aluminide, tested in number of engines is presented in Table VIII. The lifetime of MCrAlY system has been found to be improved considerably by aluminizing or incorporating platinum into the system. MCrAlY based bond coatings play a significant role in providing rough surface for the application of thermal barrier coatings and to provide protection for the alloy from oxidation and / or hot corrosion. Due to proven performance of these coatings for a variety of superalloys for over two decades in different applications, MCrAlY coatings have been studied extensively [28, 63-65]. It is important to mention that the durability of the MCrAlY coating also depends on the coating technique employed. The life of coating applied by arc ion plating is significantly lower as the attack occurs at the edges due to large variation in thickness i.e. about 6 times less than the coating thickness at the middle. Different degradation mechanisms proposed are oxidation followed by scale cracking and spallation, mixed oxidant attack, erosion and molten salt induced attack.

System	Coating	Relative lifetime
Land based aircraft DS MAR-M200+Hf	Uncoated	<<0.5
	Standard aluminide (PWA 73)	1.0
	Rh-Al (BB)	<1.5
	Gas phase aluminide (PWA 275)	<1.5
	Modified aluminide (PWA 263)	1.5
	Pt-Al (RT 22)	1.5
	NiCoCrAlY overlay (PWA271)	2.75
Marine aircraft MAR-M002	Standard aluminide	1
	Pt-Al	2.5-3
	CoCrAlY	2
Industrial IN 738	Uncoated	1
	PtCrAl	>3
	CoCrAlY (plasma sprayed)	>2
	CoCrAlY (clad) plus Al diffusion coating	>6
	FeCrAlY	2
Marine Rene 80	Standard aluminide	1
	Rh-Al	1-2
	CoCrAlHf	2
	CoCrAlY	1
	CoCrAlY+Pt/Hf	2
	CoCrAlHfPt	2.3

Table 8. Lifetimes of coatings for aero, industrial and marine gas turbines [8]

http://dx.doi.org/10.5772/59124

The effect of aluminium in forming a thermodynamically and chemically hot corrosion resistant layer and thereby improving the life of the components by reducing mass gain in MCrAlY coatings is very essential. Further, optimum content of aluminium in the coatings is extremely necessary to enhance their lifetime. In fact, it only decides the lifetime of coatings and hence the essentiality of aluminium reservoir in the coatings.

3.5. Optimization of aluminium content

Fig.12 illustrates the influence of aluminium on weight loss in the MCrAlY based coating model alloys [30]. It is very clear that aluminium plays a major role in affecting the hot corrosion resistance of MCrAlY alloys though the concentration of other alloying elements remains constant. The weight loss is maximum for the model alloy containing 6% aluminium, decreases with increase in aluminium content to 9% and minimum weight loss is observed for the alloy containing 12% aluminium. The behaviour is same for all the model alloys irrespective of cobalt content i.e. whether the cobalt is 10 % or 20% (Fig.12). Therefore, the minimum amount of aluminium required to be present in the MCrAlY based bond coatings is 9%. It is very important to mention that the optimum content of aluminium required for providing good hot corrosion resistance is 12%, though its effect is marginal when compared with 9% aluminium containing alloys [26-28].

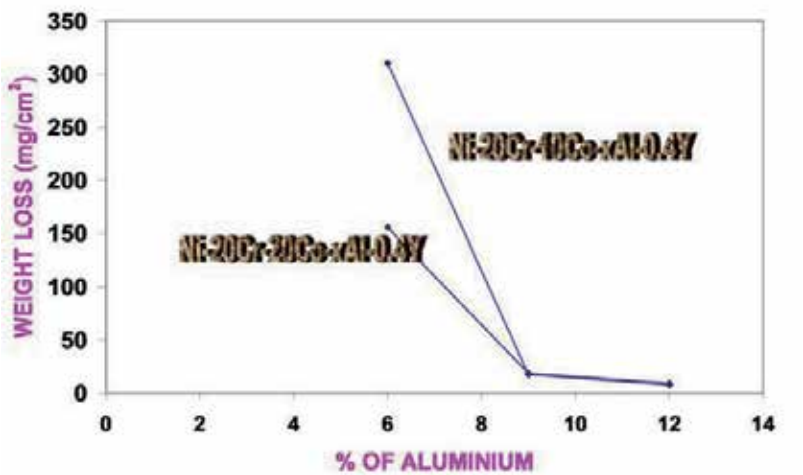

Figure 12. Effect of aluminium on hot corrosion of MCrAlY based coating model alloys [30]

It is also important to mention that the combination of cobalt and aluminium contents is a must to exhibit good hot corrosion resistance. The recent results clearly showed that cobalt plays a significant role in supporting aluminium to form a chemically and thermodynamically stable oxide scale. The optimum amounts of aluminium and cobalt are to be present in the MCrAlY bond coatings. Hence, the combination of cobalt and aluminium in association with chromium, yttrium and nickel provides good hot corrosion resistance [26-29].

3.6. Identification of new coating composition

The lives of different typical coatings applied on CM 247 LC alloy exposed at 900^0 C in NaCl and vanadium containing environments showed that the life of coatings varies with the composition and the environment (Table IX) [28]. The NiCoCrAlY coating exhibits maximum life both in sodium chloride as well as in vanadium containing environments. It is interesting to note the effect of absence of cobalt in NiCrAlY and nickel in CoCrAlY coating in reducing the lifetime as maximum lifetime is observed for the NiCoCrAlY coating in both the environments. It is clear that NiCrAlY and CoCrAlY coatings do not improve the lifetime, but the lifetime will be enhanced only if the coating contains Co in NiCrAlY and Ni in CoCrAlY coating. It is also observed that traces of silicon as well as hafnium reduce the coating life drastically (Table IX). It means that hafnium or silicon-containing compounds readily react with the corrosive salts at elevated temperatures and thereby reduce the coating life considerably [26-29]. Therefore, the ideal combination is 22% cobalt and 12% aluminium along with 18% chromium and 0.5% yttrium.

MCrAlY coating	Chloride environment (hrs)	Vanadium environment (hrs)
CM 247 LC alloy	<4	<2
Ni-16Cr-5Al-0.5Y	38	140
Co-30Cr-18Al-0.5Y	152	155
Ni-18Cr-22Co-12Al-0.5Y	>480	>300
Ni-18Cr-22Co-12Al-0.5Y + traces Hf	285	140
Ni-18Cr-22Co-12Al-0.5Y+ traces Si	35	158

Table 9. Lifetimes of different MCrAlY type coatings in various evironments [28]

To obtain maximum durability of a coating even with low-grade fuels with high pollutant content levels, an innovative coating should contain maximum aluminium reservoir together with high chromium content. Such coatings are usually MCrAlY type. A new MCrAlY coating was innovated by using electro-less technique [66-67]. The aluminium concentration was modified with the use of a modified aluminization and / or by introducing a diffusion barrier and the aluminium was changed by use of platinum aluminide coating. Using platinum aluminide altered chromium solubility [67].

In the new coating, a Ni-W diffusion barrier (5 μm thick), which is rich in W up to 50% mass, was introduced to prevent aluminium to diffuse from coating to the substrate. Over this layer 75 μm thick MCrAlY coating (NiCrAlYTa) was deposited by electro-less route. Subsequently 7 μm thick platinum and inward pack aluminizing was done (Fig.13). The hot corrosion tests with sodium sulphate showed improved performance over typical (SC/LPPS) MCrAlY / platinum aluminides and the innovative coating (SC / NiW + NiCrAlYTa + Pt + HA) maintained its integrity even after exposure for 1000 hours in pure sodium sulphate environment [67]. In order to prove the performance of a new coating, further experimentation with aggressive species like NaCl and V_2O_5 is extremely necessary.

http://dx.doi.org/10.5772/59124

Another new coating namely Ir-Ta applied by EB-PVD followed by pack aluminizing was developed for Ni-based superalloys. This coating exhibited good high temperature oxidation and hot corrosion resistance [68-69]. Ir has a high melting temperature (2716K), excellent chemical stability and low oxygen permeability, while Ta also has high melting temperature (3269K), chemical resistance to aggressive propellant gases and low diffusion rates in Ni-based superalloys. During the hot corrosion process, a high melting point compound $NaTaO_3$ (2083K) forms ($Ta_2O_5 + Na_2O = 2\ NaTaO_3$), which is stable. Further, both α– Al_2O_3 and Ta_2O_5 (2163 K) form on the surface of coating and prevents inward diffusion of sulphur and oxygen and outward diffusion of chromium and nickel from the substrate, thereby eliminating the formation of sulphides which in turn enhances the hot corrosion resistance. The addition of Ir in platinum aluminide is also promising. Deposition of Pt-30at% and Pt-50at% Ir alloys followed by conventional aluminizing demonstrated enhanced oxidation and type I hot corrosion resistance [70-71]. Ir-Ta-Al coating appears to be another effective novel metallic bond coating materials for Ni-based single crystal superalloys. However, the conclusions are based on short-term tests in the presence of pure sodium sulphate. Hence, detailed research is needed in the presence of aggressive species like sodium chloride and vanadium pent oxide to prove its performance.

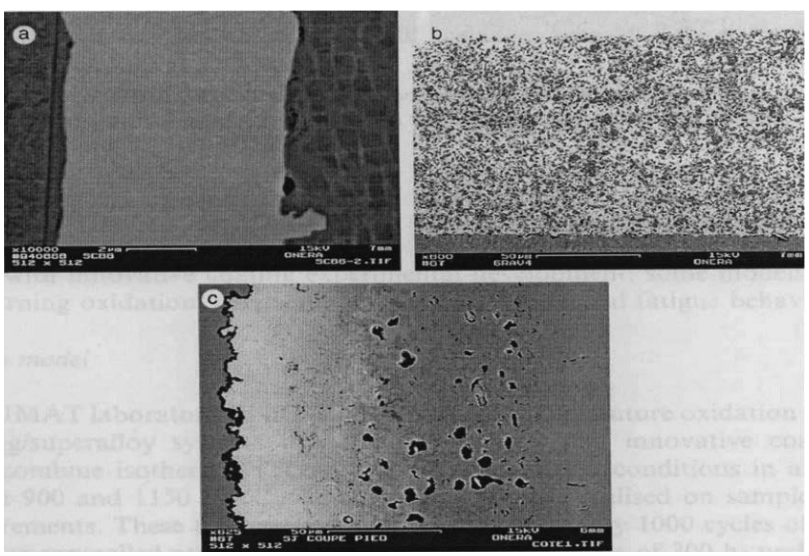

Figure 13. New coating deposit details a) 5 μm thick NiW layer b) 75 μm thick composite Ni-CrAlYTa c) 75 μm thick composite Ni-CrAlYTa + 7 μm thick platinum + inward pack aluminization [67]

Kawagishi et al have proposed an equivalent coating system for high temperature corrosion resistance of Ni- based superalloys [72]. This coating composition is designed to be thermodynamically in equilibrium with the substrate so that no inter-diffusion should occur between them. It is also reported that this coating technique helps in repair of turbine blades. Seraffon

et al have attempeted to use combination of physical vapour deposition and magnetron sputtering technique to deposite Ni-Co-Sr-Al coatings of varied compositions and tested for their high temperature oxidation resistance [73]. However, hot corrosion tests have not been studied.

3.7. Influence of major and trace elements

As mentioned earlier, the NiCoCrAlY coating exhibits maximum lifetime among the coatings (Table IX) under type I hot corrosion conditions [28]. Neither NiCrAlY nor CoCrAlY coatings prolong the superalloy's life. In fact, CoCrAlY coating contains maximum amounts of chromium (30%) and aluminium (18%), but their positive effect is not observed. Similar is the case with NiCrAlY coating. It is also mentioned that traces of silicon and hafnium make the NiCoCrAlY coating highly susceptible to hot corrosion. Traces of silicon or hafnium modify oxide growth rate, the composition of oxide scale and consequently reduce the coating life significantly. The fluxing of oxide scale also becomes easy when traces of silicon or hafnium are present in the scale. The underlying mechanism is that hafnium and silicon are present in the grain boundaries of alumina scale leach out selectively by readily reacting with chlorine, vanadium, sodium and sulphur present in the environment to form corresponding compounds [28]. This results in dislodging the grains of alumina scale and creates instability of the oxide scale and thereby reducing the life of coatings significantly [28]. Further, the oxides of silicon and hafnium are soluble in molten basic sulphate and the basic fluxing dominates in the high temperature hot corrosion region (850-950^0 C). By observing the maximum life for the NiCoCrAlY coating which does not contain either silicon or hafnium at 900^0 C evidences it. The reaction mechanisms leading to reducing the life of coatings containing silicon or hafnium are given below:

$$HfAl_2O_3 + Na_2SO_4 + NaCl = NaAlO_2 + HfCl_4 + SO_3$$
$$HfAl_2O_3 + Na_2SO_4 + NaCl + V_2O_5 = NaAlVO_2 + HfCl_4 + SO_3$$
$$SiAl_2O_3 + Na_2SO_4 + NaCl = NaAlO_2 + Na_2SiO_3 + SO_3$$
$$SiAl_2O_3 + Na_2SO_4 + NaCl + V_2O_5 = NaAlVO_2 + Na_2SiO_3 + SO_3$$

The superior performance was confirmed by observing minimum corrosion affected zone for NiCoCrAlY coatings and more for other coatings [26]. It was further evidenced by observing a uniform, protective and adherent alumina scale on the surface of NiCoCrAlY coating (Fig. 14). The above results clearly confirm that silicon addition is not beneficial for type I hot corrosion resistance rather it helps to combat type II hot corrosion [26]. Luthra et al and Bauer et al were reported that chromium [74] and silicon [75] respectively are particularly beneficial in coatings for protection against type II hot corrosion [76]. Reactive active element research related to oxidation characteristics and relevant mechanisms were the major works in overlay type coatings for the last one-decade [77]. However, the effect of reactive elements on hot corrosion resistance is still not well understood. Therefore, it may not be advisable to use silicon for protection of superalloys against both types of hot corrosion. Rather chromium addition is more appropriate to develop coatings for protection of components against hot corrosion (type I and II) as its presence does not have detrimental effect on type I hot corrosion.

http://dx.doi.org/10.5772/59124

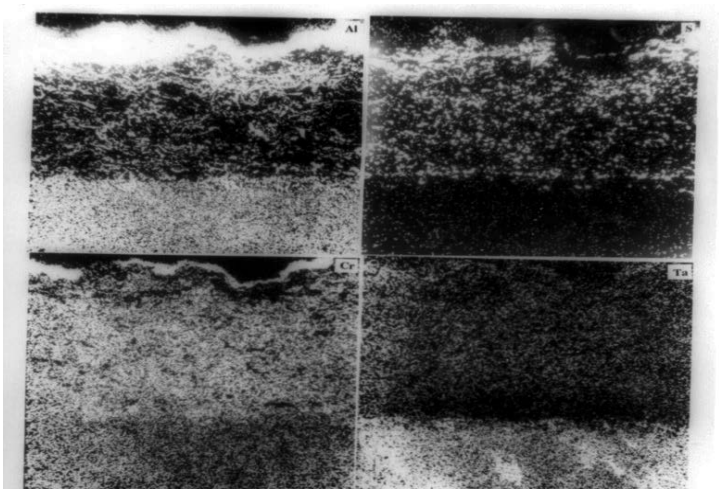

Figure 14. EPMA data showing the formation of continuous and protective alumina scale on coating surface [28]

3.8. Degradation mechanisms

Inter-diffusion of aluminides with the base alloys resulting decrease in life is the dominating degradation mechanism in diffusion aluminide coatings. Lower sulphur contents of diffusion coatings improves alumina scale adherence and the adherence of alumina scale is very good with platinum aluminide coatings. Though platinum improves the adherence and improves the life of coating, the degradation is same at the end. Clear understanding on the effects of platinum and various forms of active metals and their oxides will help to improve the use of aluminide coatings as well as bond coatings for thermal barrier coatings.

During service, coatings degrade at two fronts: the coating / gas path interface and the coating / substrate interface. Deterioration of the coating surface at the coating / gas path interface is a consequence of environmental degradation mechanisms. Solid-state diffusion at the coating / substrate interface occurs at high temperatures, causing compositional changes at this internal interface that can compromise substrate properties and deplete the coating of critical species. In the worst case, inter-diffusion leading to the precipitation of brittle phases can cause severe loss of fatigue resistance. The following section describes a novel mechanism namely an electrochemical phenomenon that explains MCrAlY based bond coating degradation process in detail.

If NiCoCrAlY coating is considered, hot corrosion takes place by oxidation of nickel, cobalt, chromium and aluminium at the anodic site (forms Ni^{2+}, Co^{3+}, Cr^{3+} and Al^{3+} ions) while at the cathodic site, SO_4^{2-} is reduced to SO_3^{2-} or S or S^{2-}. Since the metal ions i.e. Ni^{2+}, Co^{3+}, Cr^{3+} and Al^{3+} are unstable at the elevated temperature and therefore reacts with the sulphur ions to form metal sulphides. The metal sulphides can easily undergo oxidation at high temperatures and form metal oxides by releasing free sulphur ($MS + 1/2\ O_2 = MO + S$). As a result, sulphur concentration increases at the surface of the coating and enhances sulphur diffusion into the

coating and forms sulphides inside the coating. The practical observation of sulphides in hot corroded components clearly indicates that electrochemical reactions take place during the hot corrosion process [26, 28]. Similar reactions take place in vanadium environments except the formation of oxides at cathodic sites. Fig.15 illustrates an electrochemical model showing the NiCoCrAlY degradation is electrochemical in nature.

Therefore, the hot corrosion of NiCoCrAlY coating can be considered electrochemical in nature and the relevant electrochemical reactions are shown below:

At the anode	At the cathode
$Ni = Ni^{2+} + 2e^-$	$1/2\ O_2 + 2e\_ = O^{2-}$
$Cr = Cr^{3+} + 3\ e^-$	$SO_4^{2-} + 2e^- = SO_3^{2-} + O^{2-}$
$Co = Co^{3+} + 3e^-$	$SO_4^{2-} + 6e^- = S + 4O^{2-}$
$Al = Al^{3+} + 3e^-$	$SO_4^{2-} + 8e^- = S^{2-} + 4O^{2-}$

Similar mechanism is applicable to MCrAlY coatings family.

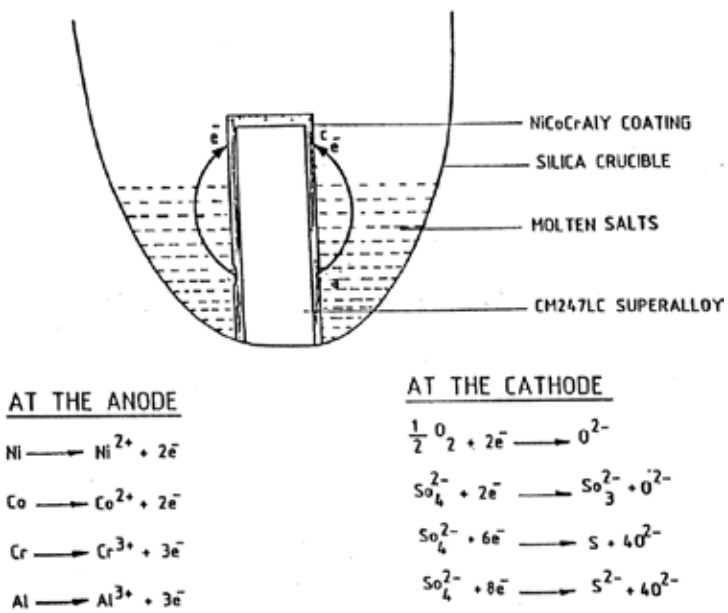

Figure 15. An electrochemical model showing degradation of MCrAlY type coatings is an electrochemical phenomenon [26]

The motivation behind suggesting an electrochemical model is to show that degradation of materials (alloys or coatings) in molten salts is electrochemical in nature and thereby to develop a rapid hot corrosion test, which will be extremely useful to select the most potential candidate materials. The normal weight gain method requires hundreds of hours to test one material

http://dx.doi.org/10.5772/59124

whereas the electrochemical method needs hardly 4 to 5 hours. It is a major advantage of electrochemical techniques over conventional weight change methods. Electrochemical monitoring of corrosion by linear polarization, coulostatic and A.C. impedance techniques have been established and widely used in aqueous solutions. On the contrary, the evaluation of corrosion resistances of various metals and alloys in molten salts are usually conducted by weight loss methods. Since the degradation of superalloys [6] and MCrAlY coatings [26,28] is shown as an electrochemical process, same as in aqueous solution, the electrochemical techniques should be quite helpful not only in evaluating coatings for hot corrosion resistance, understanding their hot corrosion mechanisms but also for developing hot corrosion resistant coatings for the superalloys [6,28].

3.9. Ceramic coatings

Thermal barrier coatings (TBCs) are finding increased application on overall component design. Over the past 25 years, cooling technology has contributed roughly 370^0 C (700 F) (from solid blades to advanced film cooling) in turbine temperature capability; further advances may be achieved with even more sophisticated cooling schemes. Superalloy material and processing advances (from equiaxed crystalline structure to third generation single crystal) have added approximately 120^0 C (250 F). However, superalloys now operate in some applications at 90% of their melting point. TBCs have the potential to reduce the substrate temperatures further with improved current production methods.

Application of zirconia thermal barrier coatings over diffusion aluminide and / or MCrAlY bond coatings is known to increase the life of components further. The function of the ceramic topcoat is to insulate the metallic substrate from high surface temperature, thereby lower the components temperature and reduce the oxidation and hot corrosion of bond coatings. The ceramic coating can lower the temperature of a cooled blade by up to 170^0 C (306^0 F), while simultaneously reducing cyclic thermal strains and has gained prominence in coating technology. ZrO_2 stabilized or partially stabilized by the addition of MgO, CaO, Y_2O_3 is found to exhibit good performance because of its high coefficient of thermal expansion and very low thermal conductivity. It has been demonstrated that columnar structures applied by EB-PVD (Fig.16) has a significant improvement in life over plasma sprayed coatings [46]. The early work used EB-PVD ceramic coatings on NiCoCrAlY bond coating applied by low-pressure plasma. The latest trend is to use platinum aluminide as bond coatings. EB-PVD is often favoured over plasma deposition for TBCs on turbine airfoils since it provides a smooth surface of better aerodynamic quality with less interference to cooling holes [47]. However, the widely used plasma spray process has benefits, including a lower application cost, an ability to coat a greater diversity of components with a wider composition range and a large installed equipment base. The established ceramic topcoat for effective prevention of high temperature corrosion is the use of ZrO_2 partially stabilized with 8 wt% Y_2 O_3. This coating exhibits satisfactory performance for aero gas turbines and primary degradation mechanism is due to bond coating oxidation. An encouraging trend was observed by chemical vapour deposition of Al_2O_3 over NiCoCrAlY bond coating surface prior to overlaying a ZrO_2-$8Y_2O_3$ topcoat to the cyclic life of partially stabilized zirconia by suppressing the bond coating oxidation effectively.

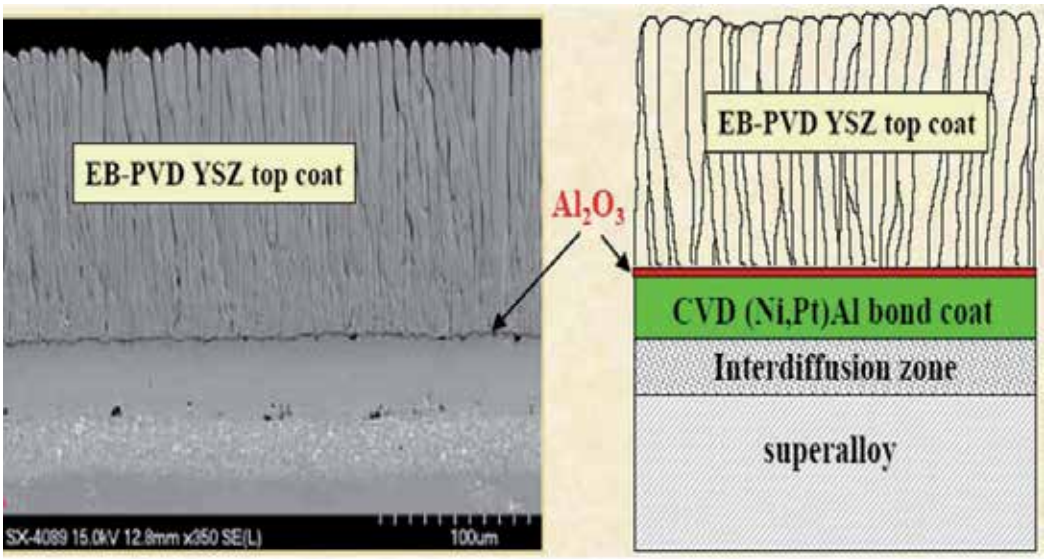

Figure 16. TBC structure deposited by EB-PVD over (Ni/Pt) Al bond coating [47]

However, it is not useful to marine gas turbines or industrial gas turbines because yttria (Y_2O_3), which is the stabilizer for zirconia reacts with vanadium present in many industrial quality fuels or $NaVO_3$ and forms YVO_4 [31]. Vanadium depletes the Y_2O_3 stabilizer from ZrO_2 matrix and thus destabilization of zirconia (i.e. transformation of zirconia from tetragonal and/or cubic to monoclinic phase upon cooling, which is accompanied by a large volume change) takes place. Destabilization of zirconia eventually causes delamination and spalling of the ceramic coating. In addition, molten salt can penetrate into the YSZ through pores and cracks (present in YSZ) and react with the metallic bond coatings. As a result, various corrosion products are generated, leading to crack formation and propagation within the oxide scale. In order to combat this problem, the pores and cracks should be sealed either by using lasers or application of an additional protective layer. Silicates like mullite ($3Al_2O_3.2SiO_2$) or cordienite ($2MgO.2Al_2O_3.5SiO_2$), CAS ($CaO.Al_2O_3.5SiO_2$), BAS ($BaO.Al_2O_3.2SiO_2$) and calcium silicate (1.8 $CaO.SiO_2$) applied over ceramic TBC helps in improving the hot corrosion resistance due to formation of high melting point sodium-alumino-silicates (>1573K) [78-85]. The rate of destabilisation of zirconia was restrained by the presence of additional over layers. However, as the pores can be present in over layered coatings, the molten salt can easily penetrate and interact with zirconia to form YVO_4 but the time required to reach the ceramic layer is higher. This aspect led to identifying CeO_2, an effective alternative to Y_2O_3 for marine and industrial gas turbine applications. Alternative stabilizers to ziconia are needed to further prolong the life of TBC coatings.

Knowledge that active elements in Ni-based superalloys and / or platinum modifications caused improved scale adherence in diffusion aluminide coatings might have led to the use of these coatings as bond coatings. The large beneficial effects possible in gas turbine efficiency by the use TBCs have sparked a resurgence in research on all aspects of scale adherence and

http://dx.doi.org/10.5772/59124

failure mechanisms involved in loss of ceramic layers or reactions with hot corrosive salts. It was expected that future research will yield incremental improvements in scale adherence towards the goal of perfection required to attain prime reliant status necessary to take full advantage of saved cooling air. Research in this direction led to the application of TBCs directly on an advanced yttrium containing superalloy without the need for a bond coating [86-87].

In practice, the inlet gas temperature in the state-of-the-art gas turbines has already reached 1773 K, which exceeds the melting points of Ni-based superalloys used for gas turbine blades and vanes. Therefore, the necessity of improving the performance of TBC is highly essential. In addition, the coating degradation takes places due to erosion as well. Therefore, it is essential to apply multilayered coatings in a perfectly ordered manner to protect the components from all attacks / damages. It is worthwhile to concentrate on the development of appropriate coating system (multilayered) including thickness for different types of gas turbine engines. Optimization of coating process taking all the experimental parameters into account is another area of critical importance.

3.10. Life prediction modelling

Because of the dependence of blade integrity on TBCs, considerable efforts are necessary to develop life prediction models to aid the gas turbine design. It is important to validate the developed model with experimental data obtained both in the laboratory as well as in the field. Development of a suitable laboratory test for predicting the life of developed materials / coatings accurately in service is an important task for the Corrosion Engineers. Recently, Renusch and Schutze [88-89] have developed a prototype software to predict the lifetimes of yttria stabilized zirconia (YSZ) top coating as a function of a bond coating temperature for a given input of hot dwell time and temperature gradient and the results have been validated with laboratory data. Attempts were made to find a solution for the transient temperature transfer problem in bare and thermal barrier coated alloys with the computational fluid dynamics (CFD) part of analysis by application of ANSYS Fluent code receiving the temperature field of combustion gas, whereas computational structural mechanics (CMS) part concerning the temperature distribution inside the turbine blade was done by ABAQUS [90-94]. Degradation modelling is most important to coating design and development. Process modelling is most important to coating manufacture. Coating life and inherent substrate environmental resistance are key determinants in setting the intervals for engine inspection and overhaul. Only few models exist in the public domain that addresses any of these needs.

It is pertinent to note that predicting the lifetimes of same YSZ top coating under hot corrosion conditions has not been attempted yet. In fact, it is a complex and challenging aspect as software development involves taking into account various reaction mechanisms that takes place under a variety of service conditions [95]. Serious attempts are needed to develop such software, which will have tremendous improvement in enhancing the efficiency of various advanced gas turbine engines. As mentioned above, the results have to be validated with both laboratory and field data and achieve an excellent agreement.

3.11. Reliability

Reliability is a critical design factor that is needed for further development if TBCs are to be fully exploited to increase turbine efficiency [96-97]. TBCs fail as a result of erosion, impact damage, and interfacial oxidation of the bond coating or thermo-mechanical strain at the ceramic / metal interface. These factors and process variability, more than any other design factor, has slowed the introduction of these coatings for turbines. Improved understanding of interfacial behaviour is required to control coating properties and to predict performance. A more compatible and high temperature corrosion resistant bond between the TBC and either the metallic substrate or the bond coating requires continued long-term emphasis [98]. The processes by which TBCs are currently applied, namely air plasma spray and EB-PVD will likely continue to be the major manufacturing methods.

Engineers currently rely heavily on visual inspection to assess the condition of coated structures [97]. As a result, in-service condition monitoring and repair decisions focus on deterioration at the coating / gas path interface. Improved non-destructive evaluation methods would provide information on when the coating has to be removed and on the extent of base metal attack. An important need for repair of industrial gas turbine components is industry wide repair specifications and regulations of the quality of repairs. The most effective method to achieve a consensus of all interested parties remains unclear. Methods to make local repairs of coatings are needed both during manufacture and operation. Also required are standard, industry-accepted methods to determine the durability and properties of refurbished coatings.

Aircraft engine repair needs are parallel to those for the industrial turbines, with the further complexity that these coating structure systems include more advanced designs and materials that tend to limit repair options. Incorporation of better models and data from condition-monitoring sensors will improve repair / replacement decisions. Still unclear is the extent to which many of the advanced coatings, such as TBCs, lend themselves to repair. Although some TBC overhaul is currently done, the extent to which TBC coated components can be repaired and re-used has never been fully determined.

Exploiting existing and advanced non-destructive evaluation (NDE) methods can aid significantly in developing and qualifying coating systems, improving process control during coating operations and characterising the integrity of coated structure during turbine engine manufacture, in-service condition monitoring and repair and overhaul operations [98-101]. Since each of these applications has specialised requirements, no single NDE technique will likely to serve all purposes. Development of programs for advanced NDE methods should focus on supporting these key areas with the goal of bringing the new methods into practice. The highest priority for further NDE development should be for those non-contacting methods that can examine the interior structure of the coating system, such as the coating / substrate interface and base metal. For aircraft engines in particular, the development of advanced NDE techniques and cost effective models will be essential for the assessment of components that are expected to be multi-wall or thin-wall structures with multilayered coatings used as an integral part of the component design and manufacture.

http://dx.doi.org/10.5772/59124

Future generations of higher-performance aerospace turbine structures will require newer materials, because in service superalloys are approaching the upper limit of their inherent temperature capability as mentioned earlier. Potential candidate materials to replace superalloys are inter-metallic compounds, monolithic and composite ceramics and refractory alloys. In addition, advanced cooling concepts will result in processing modifications and more complex cooling paths to meet the demands of advanced component designs. Most advanced materials and design modifications may result in component structures with inherently less resistance to aggressive environmental attack than current superalloys.

An important element that must be considered in innovative coating systems is the stability of structural components in the high temperature environment of an operating engine. The stability includes the long-term ability of the material to maintain its initial mechanical properties, chemical and micro-structural morphology. Research is needed on continuously graded coatings. Graded coatings like functionally graded materials (FGM) and nanostructures, offer potential advances in coating performance. The need also exists for ceramic coatings that can withstand higher temperatures. Graded coatings may demand alternative materials as well as alternative applications processes. Most significant in this area would be critical assessment of the use of FGMs as coatings and definition of the influence of multilayer and nanostructure morphology on resulting properties. However, the inherent in-homogeneity in the microscopic scale of these materials raises questions of high temperature stability that must be answered to establish the viability of these approaches. Advanced substrates like composites, ceramics and inter-metallic compounds will possess coating ability characteristics (e.g., diffusion rates and surface chemistry) very different from current superalloys. Novel concepts may be needed for coatings and surface treatments to protect these substrates. In essence, advanced processes and intelligent coatings are needed to manufacture future gas turbine engines for exhibiting ever greater efficiency.

4. Correlation between laboratory and service experience

Performance evaluation of materials / coatings in actual gas turbine engines is hardly practicable. Therefore, several simple methods were developed to asses the hot corrosion resistance of possible materials for blades and vanes. A satisfactory test should yield a prediction of service performance, with an estimation of component lifetime as a desirable objective. Attempts were made earlier to compare the results of laboratory corrosion tests with service experience. It is important to note that the corrosion of gas turbine components is greatly influenced by fuel and air quality. Generally, highly rated engines use relatively pure fuels and the air purity is also good unless move in marine environments.

In general, a more complete gas turbine engine environment can be simulated in burner rigs and the ranking of materials / coatings are in good agreement with the engine experience. The crucible test results are in agreement with burner rig test results in ranking the alloys. On the basis of corrosion products identification, it is concluded that burner rig test give the most realistic reproduction of corrosion mechanisms found in service, although furnace test as well

as crucible tests could give satisfactory results. The burner rig and electrochemical tests produce similar corrosion morphology and corrosion rates are in good agreement with each other [22]. The performance of materials tested in electrochemical tests behaved in a similar manner in actual engines.

General Electric developed an advanced burner rig test cycle for studying the combined effects of oxidation and hot corrosion on gas turbine materials [22]. This test combines the cyclic elements of an aircraft engine operation cycle with the fundamental elements of the standard oxidation and hot corrosion tests. A dilute sea salt solution is atomized inducted into one atmosphere burner rig to simulate hot corrosion conditions present at coastal airports. Specimens are romped to oxidizing conditions similar to those present during take off and climb. The thermal gradients present along the length of the test specimens simulate those present on actual aircraft engine hardware and produce areas of oxidation, hot corrosion and combined hot corrosion / oxidation attack. This burner rig test was reported to be successful in reproducing the accelerated combined hot corrosion / oxidation attack observed in factory engine testing. The ranking of substrate / coating obtained with this method vary greatly from those obtained with conventional test methods. This is due to the fact that the ranking recorded in advanced burner rig test is a function of location on the pin and distinctly different rankings can occur in each attacked region.

The advanced burner rig test was used to test tube specimens that can be internally cooled during exposure to the combustion system. Several thermal gradients can be established across specimen walls like actual turbine hard ware by using this method. With the advanced burner rig test, it is possible to compare life times of TBC coatings with the function of thickness [22]. Nevertheless, significant surprises in terms of actual versus predicted coating performance continue to occur in the field. As a result, new laboratory tests or improved existing procedures are needed in real world applications.

5. Smart coatings

5.1. Concepts

A primary requirement for a coating to use in high temperature applications is slow growth rates and optimum adherence of the protective scales that forming on the metallic coatings during high temperature exposure. As the gas turbine engines experience both types of hot corrosion as well as oxidation and hence the need to develop smart coatings to effectively combat high temperature corrosion problems for obtaining maximum efficiency.

If a single coating can operate successfully over a range of temperatures with different forms of corrosion attack like type I and II hot corrosion and high temperature oxidation, the coating essentially respond to local temperature in such a way that it will form either alumina or chromia protective scale as appropriate. High purity alumina scales offer best protection against high temperature oxidation and type I hot corrosion and chromia scales against type II hot corrosion. Ideally a single coating should satisfy both the requirements. It is possible for

http://dx.doi.org/10.5772/59124

a coating only if it contains chromium and aluminium rich graded coatings (Fig.17). The base coating should be a standard MCrAlY coating enriched with aluminum at its outer surface and a chromium rich layer at its inner surface. Under high temperature oxidation and type I hot corrosion conditions, the outer layer of the coating forms alumina scale, which provides protection and it, offers less protection under low temperature conditions. Under type II hot corrosion conditions, chromium rich layer forms chromia scale at a faster rate and provides protection. Thus, the smart coating can provide optimum protection by responding suitably to the temperatures that are encountered under actual service conditions of gas turbine engines. This optimum protection is possible because of the formation of the most suitable protective oxide scale in each temperature range of operation envisaged. In this sense, the coating responds to its environment in a pseudo-intelligent manner and hence the name **SMART COATING** [102-103]. The smart coating permits operation of gas turbine engines over a wide range of temperatures successfully for more than the designed life and helps in enhancing the efficiency significantly by effectively preventing oxidation, type I and type II hot corrosion. Such coatings were developed by the principle author and recommended to use for marine, industrial and aero gas turbines (Fig.18) [102, 104-105].

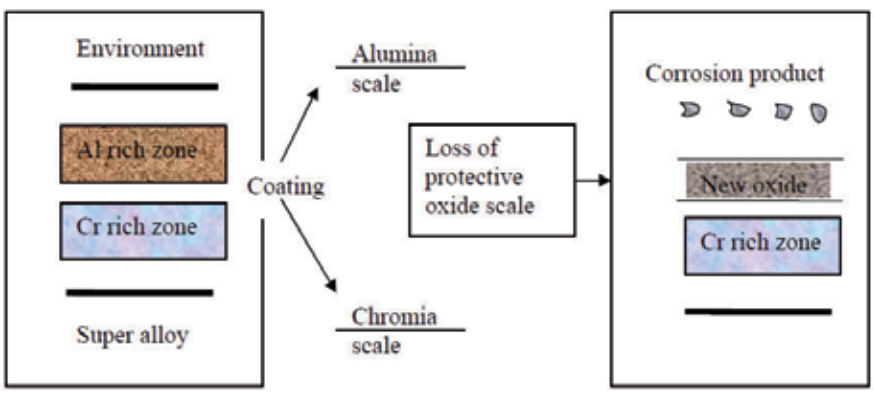

Figure 17. Schematic representation of response of a smart coating [102, 103]

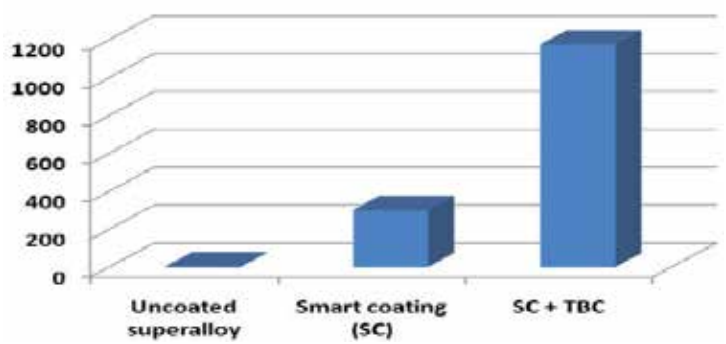

Figure 18. The performance of a Smart Coating (SC) [102]

5.2. Preparation

Preparation of smart coatings is really a challenging task. Therefore, selection of suitable surface engineering techniques to produce a quality coating is extremely essential. Here, selection of a single technique may not be of any help, but a combination of techniques is quite useful [102]. Further, the order of usage of selected techniques is also important as the microstructures of coatings vary and play a significant role in enhancing the life of components. The selection of technique for coating preparation should be based on the parameters that are controllable to get required microstructure. As mentioned earlier, the smart coating is a graded coating consisting of different zones (Fig.19) [102]. Each zone has its specific microstructure with definite composition and extends the life of gas turbine engine components significantly. Extensive research is needed both at the laboratory and field in order to establish the appropriate coating compositions, thickness, microstructures, coating techniques and superior performance of new smart coatings over conventional coatings.

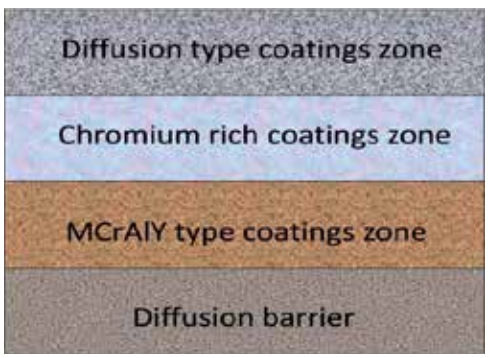

Figure 19. A schematic representation of microstructure of a smart coating [102]

6. Mechanical properties of coated superalloys

The mechanical properties of superalloys (especially cast alloys, which have their optimum mechanical properties in the as-cast condition) may deteriorate during the coating process (e.g. on thermal cycling during coating, during post-coating heat treatment, or by coating surface effects). The degradation of mechanical properties of the base material may lead to an increase in creep rate, thereby the elongation that can be tolerated before the coating starts to crack will be reached in a shorter time. In a corrosive environment, stresses are enhanced due to corrosion of coating and result in a measurable reduction of the cross section or by selective corrosion attack after a crack is initiated in the coating and propagates rapidly along grain boundaries or by both general and selective attack.

With the solid blades that used to be installed in turbines, the interaction between coating and base material was not significant because the potential influence on the load-bearing cross-

http://dx.doi.org/10.5772/59124

section was very less. However, today's channelled, cooled blades have thin walls and a substrate-coating interaction over a depth of only few tenths of a millimetre can have a significant effect. Such interactions have been investigated in detail and reported [106]. It is important to mention that the coating-substrate interaction complicates the task of determining the various factors that are involved. The effectiveness of a protective coating for a particular material under service conditions can therefore be assessed only by techniques in which all the parameters like substrate, coating and environment as shown in Fig.20 are taken into account [40].

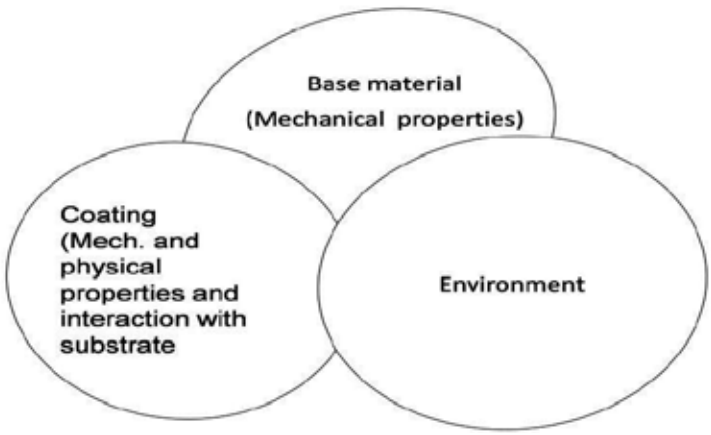

Figure 20. Factors affecting the coated superalloy components [108]

Swindells [107] and Cooper and Strang [108] have shown that one of the major problems faced by all coating systems is their mechanical properties. To achieve a good coating without discontinuity at the interface some inter-diffusion is required, but, if this diffusion occurs to any significant level during operation, the coating will slowly be degraded. The work on diffusion mechanisms is important in determining the long-term stability of the coatings. However, it has particular significance when discussing the mechanical properties of coated components, reviewed by Strang [109] and Czech et al [110].

The major problem is how to compare the properties of a coated component with an uncoated component. When such comparisons are made, it is of great importance how the cross section is measured, whether comparisons are made on the dimensions of the section before coating or whether the total thickness of base metal and coating are compared with a similar thickness of uncoated metal. This choice dominates the results in thin-section components, particularly when the coating has very different mechanical properties from the underlying metal. It effects the results obtained in creep, fatigue and thermal fatigue tests. However, the problem of the effect of coating properties on the mechanical integrity of the component is only of interest in some cases. For instance, as pointed by Goward [111] if failure is by thermal fatigue as in aircraft turbines, then the surface coating effects on mechanical stability are important; if failure is by hot corrosion, as in industrial and marine turbines, then the effect on mechanical properties is generally of a second order compared to the protection afforded by the coating.

7. Summary and future research trends

7.1. Summary

High temperature corrosion i.e. oxidation, type I and II hot corrosion are the degradation modes for the gas turbines. Hot corrosion is a major problem for the gas turbines engines due to which failures take place during service. Though advanced superalloys comprising new alloying elements such as rhenium, ruthenium and iridium (4^{th} and 5^{th} generation) that have been developed recently, exhibit considerably improved high temperature strength properties, their hot corrosion resistance is found be very poor. Therefore, there is a need to apply appropriate hot corrosion resistant coatings on the superalloys as the gas turbine engine components should exhibit both high temperature strength as well as hot corrosion resistance. Considerable amount of research has been carried out in the coatings area. As a result, new compositions, graded coatings have been emerged and efforts have also been made to predict their lives. However, no work was reported to predict the lives of coatings under hot corrosion conditions. Recently, smart coatings with varied techniques and compositions have been reported, which provides total protection to the superalloy components against high temperature oxidation, type I and II hot corrosion with their intelligent behaviour which in turn enhances the efficiency of gas turbines by eliminating failures during service. Therefore, it is recommended to apply smart coatings for the advanced superalloys as bond coatings used in all types of modern gas turbines i.e. aero, industrial, marine in order to obtain ever greater efficiency, which is essential in the present world.

7.2. Future research trends

No established ISO standard procedure is available till now for evaluation of materials and coatings for their hot corrosion resistance and hence the need to establish such standards in near future. In fact, the immediate concentration should be focused on this issue. Development of new alloys with a combination of experimentation, modelling and black art is necessary as further improvements in Ni-based superalloys are less possibility because the superalloys now operate at about 90% of their melting temperature. The future generation of high performance aerospace structures or potential candidate materials to replace superalloys are inter-metallic compounds, monolithic and composite ceramics, refractory alloys and research is needed in this direction. The developmental work should take place concurrently with coating system. Improved understanding of interfacial behaviour of TBCs and a more compatible hot corrosion / oxidation resistant bond coatings either by modification of chemistry or more stringent control of undesirable elements to control coating properties and to predict their performance is highly essential. Hence, the development of constructive life prediction modelling under simulated gas turbine engine conditions is necessary. Improved on-line control to ensure reproducible coated structures and within the service limits is also needed as increased improvements to current coating technologies are unlikely to meet the goals of future generation high performance turbine engines. Then, development of Smart Coatings to combat type I & type II hot corrosion and high temperature oxidation for gas turbines is a challenging task to the Corrosion Engineer and developmental work in this area has lead to some smart

http://dx.doi.org/10.5772/59124

coatings. Further research is highly essential for their understanding and to develop alternative smart coatings. Extensive research is needed both at the laboratory level and field to optimize coating composition, thickness, microstructure, identification of appropriate surface engineering techniques, and their priority of use and to prove their performance for manufacture of advanced gas turbine engines for exhibiting ever-greater efficiency.

Acknowledgements

The principle author (IG) is grateful to Japan Society for Promotion of Science (JSPS) for providing financial assistance for his stay at National Institute for Materials Science, Tokyo, Japan.

Author details

I. Gurrappa[1*], I.V.S. Yashwanth[2], I. Mounika[1], H. Murakami[3] and S. Kuroda[3]

*Address all correspondence to: igp1@rediffmail.com

1 Defence Metallurgical Research Laboratory, Kanchanbagh PO, Hyderabad, India

2 University of Louisiana, Lafayette, LA, USA

3 National Institute for Materials Science, Sengen, Tsukuba City, Ibaraki, Japan

References

[1] www.salvatoreaiello.com/main.shtml

[2] M. Konter and M. Thumann, J. Mater. Process Technol., 2001, 117, 386-390

[3] M.R. Khajavi and M.H. Shariat, Engineering Failure Analysis, 2004, 11, 589-597

[4] J.M. Gallardo, J.A.Rodriguez and E.J. Herrera, Wear, 2002, 252, 264-268

[5] N. Eliaz, G. Shemesh and R.M. Latanision, Engineering Failure Analysis, 2002, 9, 31-43M.

[6] I.Gurrappa, Oxid. Met., 1999, 50, 353-382

[7] C.J. Wang and J.H. Lin, Mater. Chem. Phys., 2002, 76, 123-129

[8] S.R.J.Sandrs, Mat.Sci.Tech, 1986, 2, 282-285.

[9] P.Sterimtz,C. Duret and R.Morbioli, Mate.Sci.Tech, 1986, 2, 262-271.

[10] R.A.Papp, J.H. Devan,D.L. Druglass,p.C. Nordine, F.P. Pettit and D.P. Whiltler, Matr.Sci.Engg, 1981, 50, 1-17

[11] J.F.G.Conde, E.Erdos and P.Huber, High temperature Alloys for Gas Turbines (eds.) R.Brunetaud et al., D.Reidel publishing Co., The Netherlands (1982) p 99

[12] F.S. Pettit and G.H.Meurer, Super alloys 1984, 651-687

[13] R.A.Rapp, Pure & Appl.Chem., 1990, 62, 113-122

[14] N.Otsuka and R.A.Rapp, J.Electrochem. Soc., 1990, 137, 46-52

[15] V.S.Bhide and W.W. Smeltzer, J.Electrochem. Soc., 1981, 128, 902-908

[16] F.C.Yang and D.P. Whittle, Corr. Sci., 1983, 23, 285-290

[17] K.Natesan, Corrosion, 1985, 41, 646-655

[18] K.Natesan, Materials for Coal Gasification (ed.,) W.T. Bakker, S. Dapkunas and V.Hill, American Soc. for Metals, Metals Park, Ohio, (1988) 137-146

[19] M.P.Srivastava, T.H.Rao and R. Sivakumar, Trans.IIM., 1985, 38, 357-361

[20] P.Hancock, Corr. Sci., 1982, 22, 51-65

[21] A.Anderson,B.Haflan, P. Kofstad and P.K.Lillerud, Mater. Sci. & Tech., 1987, 87, 45-50

[22] J.A. Cinner and W.B. Connor, J. Met., 1994, 21, 35-41

[23] E.L.Simons, G.V.Browing and H.A.Liebhafskers, Corrosion, 1955, 11, 505-511t

[24] I.Gurrappa, J.Mater.Sci.Eng., A 2003, 356, 372-380

[25] I.Gurrappa, Oxid. Met., 2003, 59, 321-340

[26] I.Gurrappa, Mater.Sci.Technol., 2003, 19, 178-185

[27] I.Gurrappa, J.Mater.Sci.Lett., 2001, 20, 2225-2229

[28] I.Gurrappa, Surf.Coat.Technol., 2001, 139, 272-280

[29] I.Gurrappa, Mater. Manuf.Process, 2000, 15, 761-769

[30] I.Gurrappa, J.Mater.Sci.Lett., 1999, 18, 1713-1721

[31] I.Gurrappa, J.Mater. Sci.Lett., 1998, 17, 1267-1272

[32] I.Gurrappa, J.High Temp.Mater.Sci., 1997, 38, 137-144

[33] I.Gurrappa, Corr.Prev.Control., 1997, 44, 151-178

[34] I.Gurrappa, J.Electrochem.Soc., 1999, 48, 187-195

[35] I.Milosev and B. Navinsek, Surf. Coating & Tech., 1994, 63, 173-180

[36] X.Zhang and R.A.Rapp, J.Electrochem.Soc., 1993, 140, 2857-2863

[37] Y.S.Hwang and R.A. Rapp, J. Electrochem. Soc., 1990, 137, 1276-1281

[38] T.Kobayashi, Y.Koizumi, S. Nakazawa, T. Yamogata and H. Harada, Proceedings of Fourth International Charles Parsons Turbine Conference on "Advances in Turbine Materials, Design and Manufacturing", November 1997, New Castle, UK pp 766-773

[39] P.Canon and T. Khan, Aerospace Sci. Technol., 1999, 3, 513-521

[40] I.Gurrappa, I.V.S. Yashwanth and A.K.Gogia, The selection of materials for marine gas turbines, Gas Rurbines ISBN:979-953-307-816-7, Volkov Konstarton (Editor), 2012, INTECH Publishers, USA, p 51-70

[41] I.V.S. Yashwanth, I.Gurrappa and H.Murakami, J. Surf. Engg. Mater. Adv. Technol., 2011, 1, 130-135

[42] K. Matsugi, Y.Murata, M.Morinaga and N. Yukawa, Proceedings of 7th International Symposium on Superalloys ed. By S.D.Antolovich et al. TMS, Warrendale, PA, (1992) p 307

[43] Md.Moniruzzaman, Y. Murata, M.Morinaga, N.Aoki and T. Hayashida, ISIJ International, 2002, 42, 1018-1125

[44] Y.Murata, S.Miyazaki, M.Morinaga and R.Hashizume, "Hot corrosion resistant and high strength Ni-based single and directionally solidified super alloys developed by the d-electrons concept", Super alloys 1996 ed. by R.D.Kissinger, D.J.Deye, D.L.Anton, A.D.Cetel, M.V.Nathal, T.M.Pollock and D.A.Wood ford, The Minerals Metals & Materials Society 1996

[45] I. Gurrappa, A. Wilson, H.L.Du, J.S. Burnell-Gray and P.K. Datta, ECS Trans., 2008, 6, 67-75

[46] H.W. Grunling, H. Rechtanbacher and L. Singheiser, Mater. Sci. Forum, 1997, 251-254, 483-502

[47] Hancock, P., Malik, M., "Coating Systems and Technologies for Gas Turbine Applications", Materials for Advance Power Engineering, Part 1, 1994, pp. 685-704

[48] S.Kuroda, J.Kawakita, M. Watanabe and H. Katamoda, Sci. Tech. Adv. Mater., 2008, 9, 33002

[49] G.W.Goward and L.Cannon, J,Eng.Gas Turbines Power, 1998, 110, 150-154

[50] G.W.Goward and L.L.Seigle, ASM Handbook, Surface Engineering, 1994, 5, 611-620

[51] J.Stringer, Mater.Sci.Eng., 1987, 87, 1-10

[52] L.Swadzaba, B.Formanek and A.Maciejny, Meter.Sci.Eng.,A 1989, 121, 407-412

[53] J.A.Cocking, N.A.Burley and G.R.Johnston, High Temp.Tech., 1986, 4, 175-180

[54] G.W.Goward, Surf.Coat.Technol., 1998, 108-109, 73-79

[55] A.J.A.Mom and H.J.C.Hersbach, Mater.Sci.Eng., 1987, 87, 361-367

[56] P.Hancock, H.H.Chien, J.R.Nicholls and D.J.Stephenson, Surf.Coat.Tech., 1990, 43/44, 359-370

[57] G.W.Meethan, Mater.Sci.Tech., 1986, 2, 290-294

[58] N.Czech, W.Eber and F.Schmitz, Mater.Sci.Tech., 1986, 2, 244-249

[59] K.Y.Kim, S.H.Kim, K.W.Kwan and L.H.Kim, Oxid.Met., 1994, 41, 179-188

[60] http://sciencelinks.jp/j-east/article/200604/000020060406A0061342.php

[61] J.H.Sun, E.Chang, B.C.Wu and C.H.Tsai, Surf.Coat.Tech., 1993, 58, 93-99

[62] R.Knight, D.Zhagxiong, E.H.Kim, R.W. Smith, P.Sahoo and B.Bucci, proceedings of 15th International Thermal Spray Conference, May 1998, NIC, France, vol.II p 1549

[63] C.Leyens,K.Fritcher, M.Peters and W.A.Kayser, Surf.Coat.Technol., 1997, 94-95, 155-161

[64] W.Beele, N.Czech,W.J.Quadakkers and W.Stamn, 1997, 94-95, 41-48

[65] Q.M.Wang, Y.N.Wu, P.L.Ke, H.T.Cao, J.Gang, C.Sun and L.S.Wen, Surf.Coat.Techonol., 2004, 186, 389-397

[66] M.P.Bacos, B. Girare, P.Josso and C.Rio, Surf.Coat.Technol., 2003, 162, 248-260

[67] M.P.Bacos, P. Josso, N.Vialas, D. Poquillon, B.Pieraggi, D.Monceau, J.R.Nicholls, N. Simms, A.Encinas-Oropesa, T.Ericsson and S.Stekovic, Appl.Thermal.Eng., 2004, 24, 1745-1753

[68] F.Wu, H. Murakami, A. Suzuki and H. Harada, Surf. Coat. Tech., 2003, 168, 62-69

[69] P. Kuppusami, H. Murakami and T. Ohnuma, J. Vac. Sci. Tech., A 2004, 22, 1208-1217

[70] Y.N. Wu, A. Yamaguchi, H.Murakami and S. Kuroda, J. Mater. Res., 2007, 22, 206-216

[71] A. Suzuki, Y.Wu, A. Yamaguchi, H. Murakami and C.M.F. Rae, Oxid. Met., 2007, 68, 53-64

[72] K. Kawagishi, A. Sato and H. Harada, JOM (2008) 31-35 (www.tms.org/jom.html)

[73] M. Seraffon, N.J. Simms, J. Sumner, J.R. Nicholls, Surf. Coat Technolo. 2011, 206, 1529-1537

[74] K.L.Luthra and J.H.Wood, Thin Solid Films, 1984, 119, 271-280

[75] R.Bauer and H. Gunling, Thin Solid Films, 1982, 1, 3-20

[76] G.W.Goward, J.Eng.Gas Turbines Power, 1986, 108, 421-425

[77] B.A.Pint, Oxid.Met., 1996, 45, 1-37

[78] A. Aygun, A.L. Vasiliev, N.P. Padture, Xinqing Ma, Acta. Mat, 2007, 55, 6734-6745

[79] M.H. Vidal-Setif, N. Chellah, C. Rio, C. Sanchez, O. Lavigne, Surf. Coat. Tech, 2012, 208, 39-45

[80] Y. Wang and G. Sayre, Surf.Coat. Technol, 2009, 203, 2186-2192

[81] M. Abbas, L. Guo and H. Guo, Ceram. Intl, 2013, 39, 5103-5111

[82] C.V. Cojocaru, D. Lévesque, C. Moreau, R.S. Lima, Surf. Coat. Tech., 2013, 216, 215-223

[83] X. Xie, H.Guo, S. Gong, H. Xu, J. Europ.Ceram. Soc, *2011*, 31,*1677-1683*

[84] J. M. Drexler, A. Aygun, D. Li, R.Vaßen, T.Steinke and N.P. Padture, Surf. Coat.Technol, 2010, 204, 2683-2688

[85] M. S. Majewski, C. Kelley, W. Hassan, W.Brindley, E.H. Jordan, M.W. Renfro, Surf. Coat.Tech, 2011, 205, 4614-4619

[86] S.W. Kandebo, Aviation week, 1998, 148, 34-35

[87] J.C.Schaffer, W.H.Murphy, W.B.O'Connor, B.J.Nagaraj and H.V.Vakil, US patent 5,538,796 (1996)

[88] D. Renusch and M. Schutze, Mater. Sci. Firum, 2008, 595-598, 151-158

[89] D. Renusch and M. Schutze, Mater. Corr., 2008, 59, 547-555

[90] T. Sadowski, P. Golewski, Comput. Mat.Sci, 2011, 50,1326-1335

[91] A.H. Rossette, C.Z.Mazur, A. Demeulenaere, J.A. R.L. Hernández, App.Ther. Eng, 2009, 29, 3056-3065

[92] T. Beck, M. Schweda and L. Singheiser, Proc. Eng, 2013, 55,191-198

[93] T. Beck, R.Herzog, O.Trunova, M. Offermann, R.W. Steinbrech, L. Singheiser, Surf. Coat.Technol, 2008, 202, 5901-5908

[94] M.S. Majewski, C.Kelley, J.Lake, M.W. Renfro, W. Hassan, W. Brindley, E. H. Jordan, Surf.Coat.Technol, 2012, 206, 2751-2758

[95] I. Gurrappa and A. Sambasiva Rao, Surf. Coat. Technol., 2006, 201, 3016- 3029

[96] Y. Ito, Handbook of Advanced Ceramics (Second Edition*), 2013*, *789-806*

[97] M.T. Kim and S.W. Lee, *Appl. Thermal Eng., 2012*, 40, *304-310*

[98] H. Aleksanoglu, A. Scholz, M. Oechsner, C. Berger, M. Rudolphi, M. Schütze and W. Stamm, *Intl. J. Fatigue*, *2013*, 53, *40-48*

[99] A.Kulkarni, A. Goland, H. Herman, A. J. Allen, T. Dobbins, F. DeCarlo, J. Ilavsky, G.G. Long, S. Fang and P. Lawton, *Mater. Sci. Eng., A 2006*, 426, *43-52*

[100] M.Okazaki, S.Yamagishi, Y. Yamazaki, K. Ogawa, H.Waki and M. Arai, Intl. J.Fatigue, *2013*, 53, *33-39*

[101] R.Ghasemi, R. Shoja-Razavi, R. Mozafarinia and H. Jamali, *Ceram. Intl*, *2013*, 39, *8805-8813*

[102] I. Gurrappa and I.V.S.Yashwanth, Design and Development of Smart Coatings for Gas Turbines, "Gas Turbines" ISBN: 978-953-307-146-6, Injeti Gurrappa (Editor), 2010 SCIYO Publishers, USA, pp 65-78

[103] J.R.Nicholls, N.J.Simms, W.Y.Chan and H.E.Evans, Surf.Coat.Technol., 2001, 149, 236-244

[104] I.Gurrappa, J. Coat.Tech.Res., 2008, 5, 385-391

[105] I.Gurrappa, European Commission Marie Curie Final Report, July 2008

[106] K. Schneider, H.G. Von Arnim and H.W. Grunling, Thin Solid Films, 84 (1981) 29-36

[107] N. Swindells, Mater. Sci.Tech., 1986, 2, 250-255

[108] S.P.Cooper and A. Strang, Mater. Sci.Tech., 1986, 2, 256-261

[109] A.Strang, Mater. Sci. Tech., 1986, 2, 243-249

[110] N. Czech, W. Esser and F. Schmitz, Mater. Sci. Tech., 1986, 2, 244-249

[111] G.W. Goward, Mater. Sci. Tech., 1986, 2, 194-200

Chapter 4

High Temperature Oxidation Behavior of Thermal Barrier Coatings

Kazuhiro Ogawa

Additional information is available at the end of the chapter

http://dx.doi.org/10.5772/59794

1. Introduction

In power generating gas turbine plants, increasing turbine inlet gas temperature (TIT) results in enhancement of turbine efficiency and energy saving. State-of-the-art gas turbine plants aiming at more than 60% turbine efficiency, have to operate at temperature above 1700°C [1, 2]. Therefore, thermal barrier coatings (TBC) have been used in the gas turbine plants for improved durability and performance [3-5]. Typically, the TBC consists of an inner layer of metallic bond coating (MCrAlY, where M indicates Ni, Co, Fe or their combinations) and an outer layer of ceramic top coating (8wt% yttria stabilized zirconia (YSZ)). In the plant, the surface of 1st rotating blades of the gas turbines is exposed to temperature over 900°C. Accordingly, these harsh operational environments may result in degradation such as cracking, delamination, or spalling of the TBC [6]. If the delamination and the spallation occur due to high temperature and long-term operation, serious accidents might break out. Thus, an analysis of the degradation mechanisms of the TBC is important and indispensable in order to prolong service life time. As a result of the delamination or the spallation, Wu et al. [7] suggested that the degradation mechanism is oxidation of the bond coating, coupled with unrelieved coefficient of thermal expansion mismatch stress caused by the pegging effect of protruded bond coating out-grown oxides growing into radial cracks of the top coating. Moreover, Wu et al. [8] described that NiO and $Ni(Cr,Al)_2O_4$ were observed on both the bottom of the spalled TBC top coating and the outer surface of the MCrAlY bond coating oxide scale after the TBC top coating had spalled on all the test specimens used in their study. This indicates that NiO or $Ni(Cr,Al)_2O_4$ is the weakest link of the bond coating oxide scale, which might accelerate TBC failure. Bartlett and Maschio [9] expressed that failure of TBC initiated in the thermally grown oxide (TGO) layer is caused by thermal expansion mismatch stresses associated with a nonplanar interface. Furthermore, they reported that crack propagation

occurred in the YSZ top coating in all cases, due to the high fracture energy of the interface. Maier et al. [10] proved that oxidation of the elements of YSZ and MCrAlY reduces the protective capacity of the bond coat during thermal aging. Moreover, both severe degradation of the bond coating and large amounts of nickel oxide have been observed. This nickel oxide was shown to grow outward into the thermal barrier, which appears to result in increase of the stresses in the thermal barrier and contributed to its failure near the interface between YSZ top coat and MCrAlY bond coat. As indicated above, a significant amount of work has been done on the analysis of TBC degradation mechanisms. However, only few attempts have so far been made to investigate TBC degradation associated with TGO growth behavior.

In this chapter, it is described that formation and growth behaviour of the TGO, influence of top coats for formation and growth of the TGO, and improvement of interface strength by controlling TGO morphology.

2. Growth behavior of Thermally Grown Oxide (TGO)

The emphasis has been on failure modes governed by the thermally grown oxide (TGO) [6, 11, 12], predominantly α-Al_2O_3, that forms between the thermal barrier coating (TBC) and the bond coat (see Fig. 1). This thin layer develops large residual compressive stress because of growth and thermal expansion misfit, causing the layer to be unstable against out-of-plane displacements.

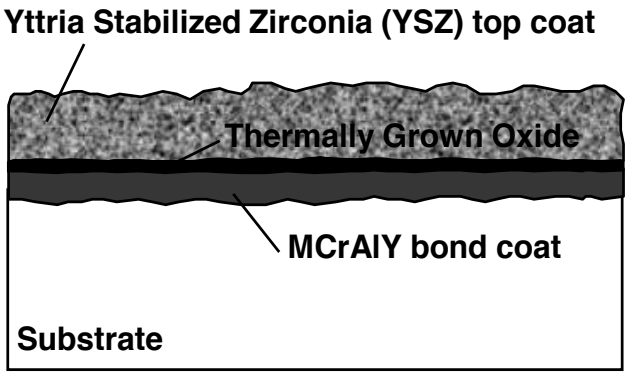

Figure 1. TGO at the interface between top coat and bond coat.

2.1. Experimental procedure

Ni base superalloy was used as a substrate material in this study. The substrate was initially grit blasted, and then positioned into a low-pressure plasma spray (LPPS) coating system for

http://dx.doi.org/10.5772/59794

overlaying of MCrAlY bond coating (approximately 100μm thickness). Furthermore, the substrate with MCrAlY bond coating was coated by 8wt% Y_2O_3-ZrO_2 (Yttria Stabilized Zirconia: YSZ) TBC top coating (approximately 300μm thickness) by an air plasma spraying (APS) coating system.

The specimens were uniformly aged at 1000°C by using high temperature furnace in the ambient air. The reason for the choice of 1000°C was to simulate the surface temperature of the first rotating blades of 1500°C class gas turbine plants. The coated specimens were aged at 1000°C for various lengths of time viz, 10, 50, 100, 500, 1000 and 3000 hours. The aged specimens were compared with as-received specimen due to investigation of an extent of degradation. Before aging, the TGO was identified at the TBC/MCrAlY interface. On the other hand, in the case of the aged specimens, TGO formation was confirmed.

In order to understand the relationship between the aging time and the growth of TGO layer, cross-section of thermally aged specimens was characterized with use of scanning electron microscope (SEM). The thickness, porosity, and microcracks of TGO layer for the specimens were measured at over 50 points by using SEM. Furthermore, due to identification of chemical composition of the TGO, analyses were using energy dispersive X-ray spectroscopy (EDX) and electron probe micro analyzer (EPMA) performed.

2.2. Results and discussion

2.2.1. Observations and identifications of thermally grown oxide

SEM observation gave information on the initial degradation such as microcracks, pores, and TGO as well as microstructure. Typical SEM images of TBC of as-received and 3000hours thermally aged specimen are shown in Fig.2. Moreover, typical SEM images of the cross-section in the vicinity of the TBC/MCrAlY interface are displayed in Fig.3. It is confirm that the TGO is formed at TBC/MCrAlY interface. Furthermore, the TGO layer has irregular shape and its thickness varies at the TBC/MCrAlY interface. This TGO layer contains at least two layers with different color contrasts on SEM images. There is black layer closer to the bond coating, and gray layer near the YSZ. Observation of the TGO layer at higher magnification, Fig.3, reveals that there are many pores, especially in the gray layer.

Energy dispersive X-ray spectroscopy (EDX) analysis was performed in order to investigate the chemical composition of the black and the gray layers. The results of the EDX analysis are presented in Fig. 4. It turns out that the black layer in Fig.4 contains only Al and O.

Consequently, the black layer is identified as Al_2O_3 (Alumina). The EDX spectrum of the gray layer contains various peaks of Al, O, Co, Cr and Ni, suggesting that the layer can be a mixed oxide consisting of a combination of NiO, CoO, Cr_2O_3, $Ni(Cr, Al)_2O_4$ spinels. Since the composition of the gray layer is not well defined, it will be referred to as mixed oxide layer in this work.

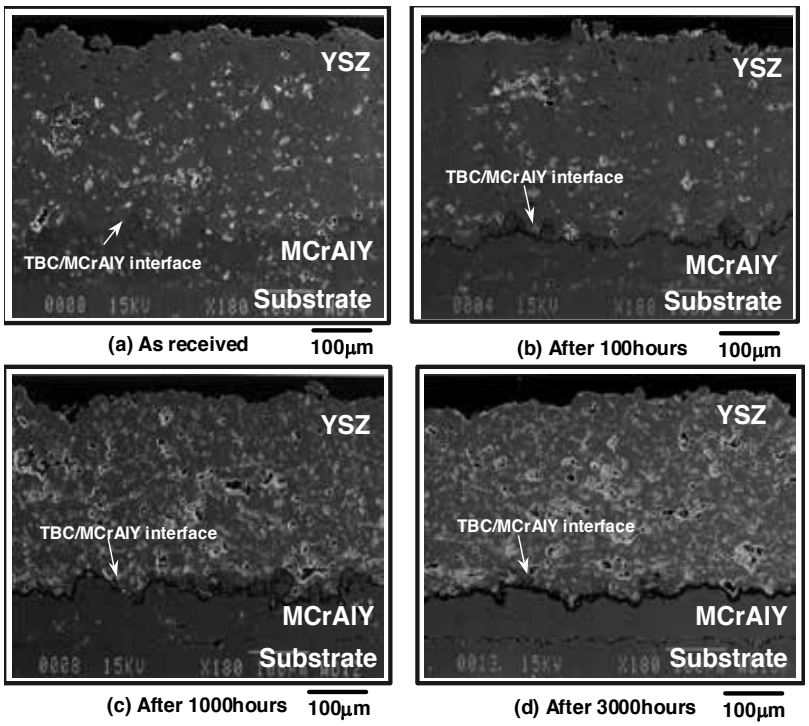

Figure 2. Typical SEM images of the cross-sections of TBC.

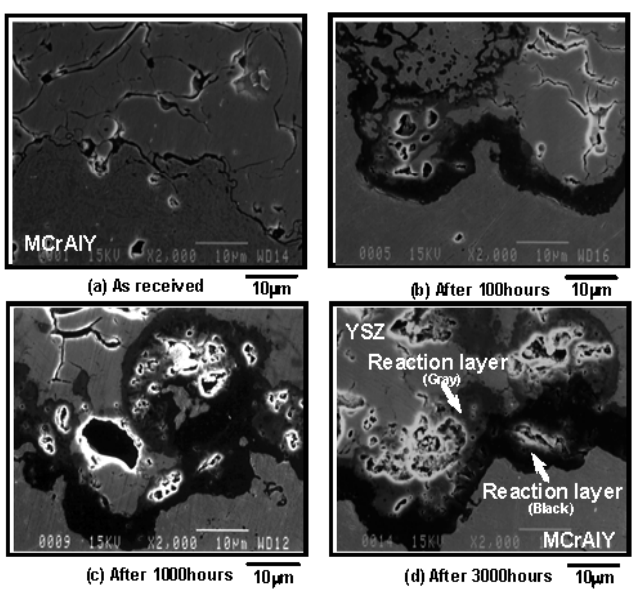

Figure 3. Typical SEM images of the cross-sections in the vicinity of the TBC/MCrAlY interface.

http://dx.doi.org/10.5772/59794

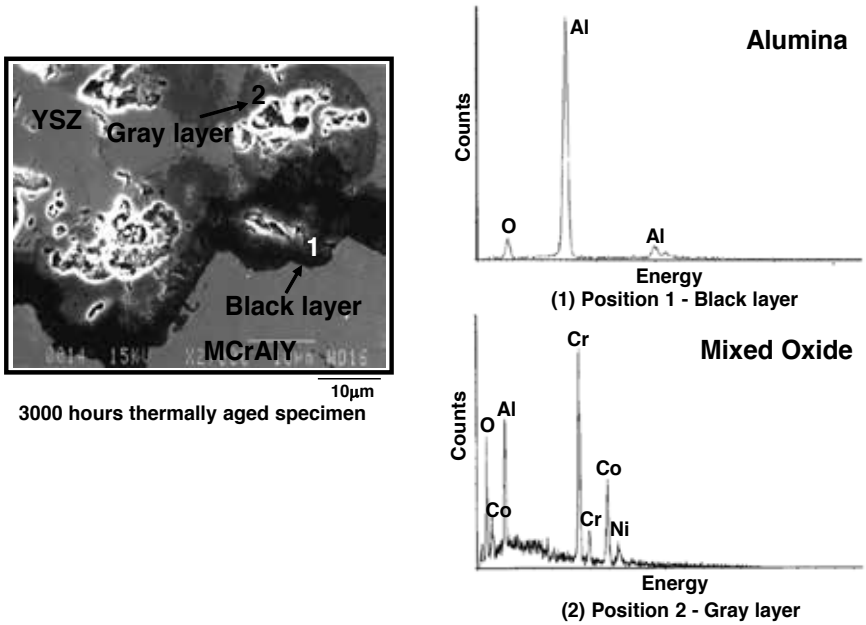

Figure 4. Results of EDX analysis.

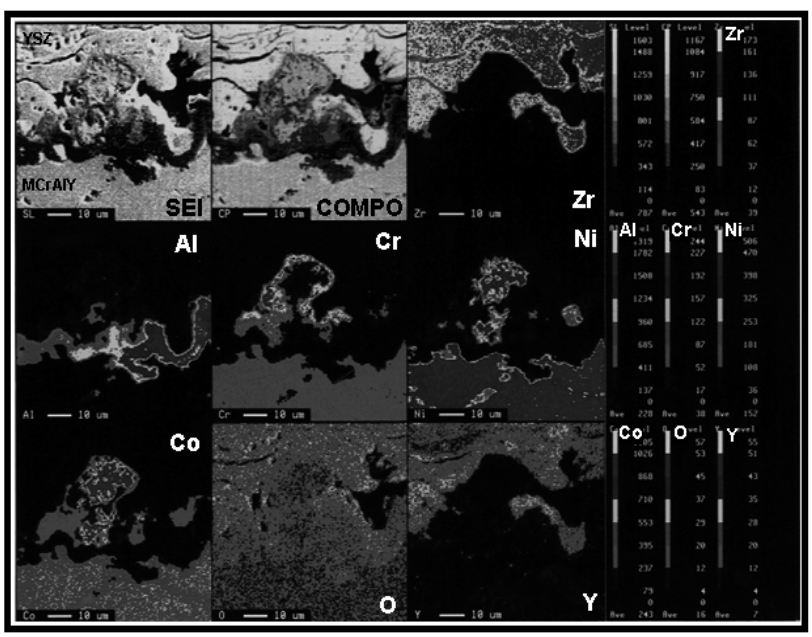

Figure 5. EPMA analysis of the cross-section of TBC/MCrAlY interface.

In addition, EPMA elemental mapping was carried out due to identify the alumina and mixed oxide in detail. The result of EPMA analysis is shown in Fig.5. In black layer, only O and Al are present as it was displayed in Figs.2 and 3. Namely, the black layer was identified as Alumina. However, there is hardly any Al in MCrAlY bond coating. It is supposed that almost all Al in the MCrAlY is combined with oxygen forming alumina at the interface. In case of mixed oxide, Cr-rich layer was identified at outer of the oxide. On the other hand, Co and Ni-rich phase were found in inside of mixed oxide. As a result, it is thought that the outer of the mixed oxide is chromium oxide (Cr_2O_3), and the inner of the mixed oxide is CoO, NiO, or spinels.

2.2.2. Oxidation process of TGO

It is important to evaluate the oxidation behavior of TGO (alumina layer and mixed oxide layer) for prediction of remaining life time of TBC. Accordingly, we investigated thickness growth of alumina and mixed oxide layer in dependence on aging time. The relationship between average thickness of each layer and aging time is shown in Fig.6.

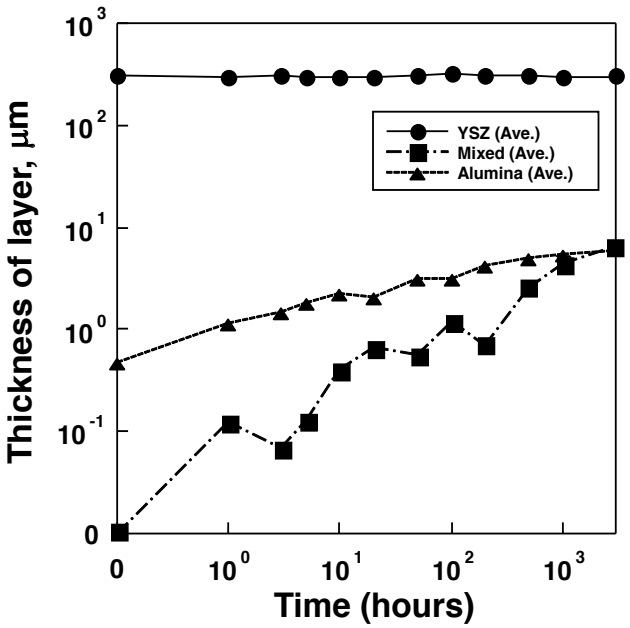

Figure 6. Variation of thickness of each layer with aging time.

The YSZ layer as top coating has scarcely thickness variation in spite of increasing aging time. On the other hand, it is clearly visible that longer aged specimens contain thicker TGO layer, and the TGO layer gradually increases with aging time. For short aging time, the TGO is predominantly alumina rather than mixed oxide. However, when the thermal aging exceeds 1000 hours, the thickness of the mixed oxide layer becomes similar to that of the alumina layer due to significant increase of the thickness of the mixed oxide layer.

http://dx.doi.org/10.5772/59794

Relationship between TGO thickness and square root of time is depicted in Fig.7. From this figure, it is determined that the growth of mixed oxide obeys parabolic law. Therefore, the mixed oxide is protective film in spite of having many pores. On the other hand, the alumina thickness cannot be expressed in terms of a parabolic law in this study. Generally, it is known that alumina monolayer obeys parabolic law [13], however, the oxidation rate of alumina decreases as the thickness of mixed oxide increases due to the formation of protective mixed oxide over the alumina layer. It is thought that protective mixed oxide has an effect on penetration of oxygen or on reduction of oxygen potential. The oxidation rate constant k_A of alumina can be expressed as a function of the thickness of mixed oxide.

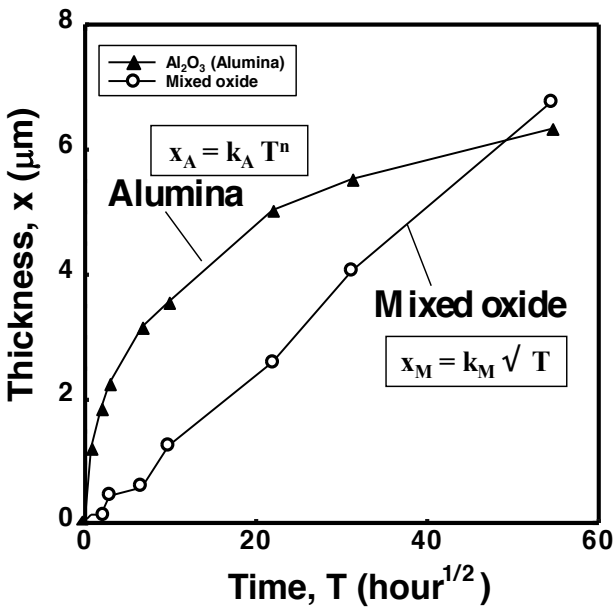

Figure 7. Relationship between TGO thickness and square root of time.

The thickness of the mixed oxide, x_M, and the alumina, x_A, can be expressed as follows:

Mixed oxide layer:

$$x_M = k_M\sqrt{T} = 0.125\sqrt{T} \quad (1)$$

Alumina layer:

$$x_A = 1.29T^{0.21} = k_A\left(x_M\right)\sqrt{T} = 0.388\, x_M^{-0.580} \times \sqrt{T} \quad (2)$$

where T is aging time, k_M and k_A are oxidation rate constant of mixed oxide and alumina, respectively.

It is assumed in Eq. (2) that the alumina thickness obeys anomalous parabolic law. As a result, the calculated value corresponded to the experimental value very well. Furthermore, it has been made clear that oxidation behavior of the mixed oxide layer obeys parabolic law. On the other hand, it is thought that the oxidation rate constant of the alumina is a function of thickness of mixed oxide.

2.2.3. Variation of microcracks and porosities for each layer

In case of formation of defects such as microcrack or porosity in the aged TBC specimen, these defects increase with stress in the vicinity of the tip. Accordingly, it is thought that macrocrack or delamination initiate from tip of these defects. There are some microcracks and porosities in the YSZ and TGO layer of aged specimens in this study. Consequently, the influence of increase in porosity and microcrack was investigated. The relationship between ratio of porosity and microcrack is displayed in Fig.8. The porosities and the microcracks ratio are drastically increasing after more than 500 hours aging. The amount of the porosities and the microcracks in the each layer increased with aging time. Especially, the microcrack in the YSZ top layer is notably increased. Moreover, the porosities in the mixed oxide are remarkably formed. On the other hand, there is no remarkable increase in the porosities and the microcracks of the alumina layer. Normally, it is thought that YSZ layer decreases the porosity and the microcrack in inner of this layer due to sintering. However, countless porosity and microcrack in the YSZ layer are formed due to thermal expansion mismatch accompanied with formation and growth of TGO. Moreover, it is thought that formation of numerous porosities in the mixed oxide is caused by Kirkendall porosity [14] due to difference in diffusion rates. The increasing porosities ratio is result of condensation of the porosities during thermal exposition.

2.2.4. Formation of the macrocracks

It is thought that the macrocracks and delamination in the YSZ were caused by the increasing amount of the porosity and microcrack. Correspondingly, the interface between TBC and MCrAlY was observed for the long-term aged specimen. The example of observation in the vicinity of the interface is shown in Fig.9. In case of 500 and 1000 hours aged specimens, there is almost no macrocrack in the vicinity of the interface. However, in case of 3000 hours aged specimen, the macrocrack was detected at everywhere in the TGO. The macrocrack passed though the porosity of the mixed oxide or the microcrack of the YSZ. Furthermore, the macrocrack grew to vertical direction of the thickness. It is supposed that a reason for the formation of the macrocrack only in case of the log-term aged specimen is increase in thermal stress accompanied by thermal expansion mismatch due to increasing thickness of the alumina. This effect can be one of driving forces of delamination and macrocrack formations. However, the driving force is not only thermal stress but also decreasing bonding force or formation of stress concentration site caused by formation of porosity or microcrack. Almost all macrocracks passed through the porosity in mixed oxide or microcrack in YSZ layer.

http://dx.doi.org/10.5772/59794

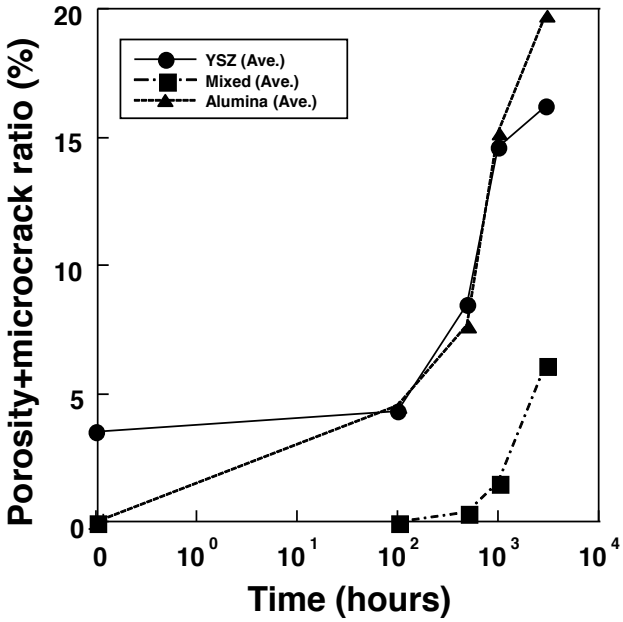

Figure 8. Time dependence of porosity and microcrack ratio.

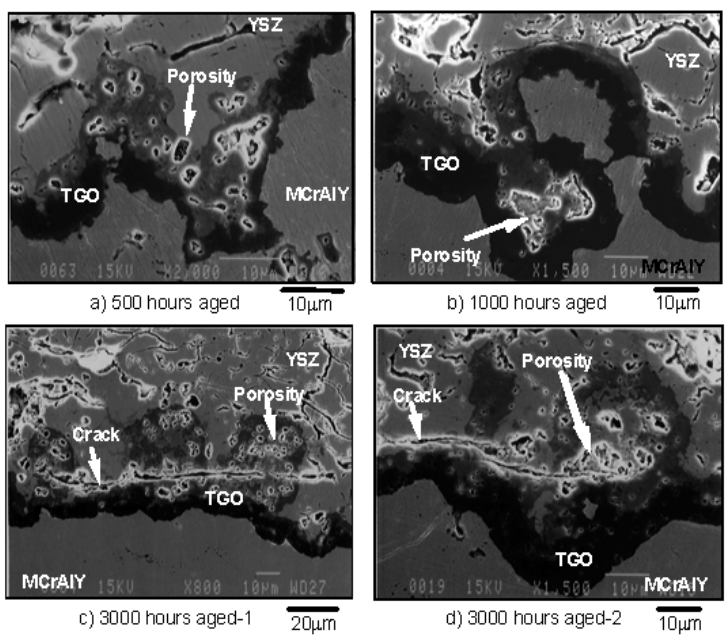

Figure 9. Macrocracks in the vicinity of TBC/MCrAlY interface.

The microcracks were formed everywhere inside of YSZ. This means that there is some possibility of initiating macrocrack from the all of microcracks. However, almost all macrocracks were formed in the vicinity of the YSZ/MCrAlY interface, which is supposed to be caused by thermal expansion mismatch in the part close to interface.

2.3. Summary

The kinetics of thermally grown oxide at interface between TBC and MCrAlY was investigated. Moreover, the driving force of macrocracks formation was suggested. The following conclusions are drawn:

During thermal aging, a TGO is formed at the TBC/MCrAlY interface. SEM and EDX analysis show that the TGO contains two different oxide films. One is alumina closer to the MCrAlY, and the other one is mixed oxide closer to the TBC.

Thickness of both alumina and mixed oxide increased with aging time. On the other hand, the YSZ layer as top coating has scarcely thickness variation in spite of increasing aging time.

The thickness of mixed oxide film obeys parabolic law, and the mixed oxide is protective film in spite of having many porosities. On the other hand, the alumina thickness cannot be expressed by parabolic law. The oxidation rate of alumina decreases, which is accompanied by increasing thickness of mixed oxide increases, due to the formation of protective mixed oxide over the alumina layer. Correspondingly, it is assumed that the alumina thickness obeys anomalous parabolic law.

In the case of 500 and 1000 hours aged specimens, there is no macrocrack in the vicinity of the interface. However, in case of 3000 hours aged specimen, the macrocrack was identified everywhere in the TGO. This reason indicates that thermal expansion mismatch accompanied by formation and growth of alumina is one of the driving forces of macrocracks formation. However, the driving force is not only thermal stress but also decrease in adhesive force or formation of stress concentration site caused by formation of porosity or microcrack. Almost all macrocracks passed through the porosity in mixed oxide or microcrack in YSZ layer.

It is thought that the delamination or the spalling is initiated and propagated due to an interaction of these degradation factors such as thermal stress, initiation of stress concentration sites, and decreasing adhesive force due to formation and growth of alumina, porosities and microcracks.

3. Influence of top coats for formation and growth of the TGO

During exposure to high temperatures, thermally grown oxide (TGO) forms at the interface between the top-coat and bond-coat as has mentioned in previous section. However, there is almost no investigation on the influence of YSZ top coat for formation and growth of the TGO. Therefore, in order to understanding existence of the YSZ top coat on TGO growth, specimens with and without YSZ top coat are compared.

http://dx.doi.org/10.5772/59794

3.1. Experimental

3.1.1. Specimens

Two kinds of specimens are prepared. One is a specimen with TBC; the other is a specimen without TBC. Regarding other factor such as thermal spraying condition, used powders for spraying, used material, environment, both specimens are indiscernible. In both specimens, Tomilloy, Ni base superalloy, is used as a substrate material. These two kinds of specimens are used for examining the microstructural and compositional changes and microcracks formation in the oxides at TBC/MCrAlY interface region for the specimen with TBC, and MCrAlY surface for the specimen without TBC. Analysis was performed using scanning electron microscope (SEM), energy dispersive X-ray spectroscopy (EDX), and electron probe micro analyzer (EPMA).

The substrate is grit blasted initially, and then positioned into a LPPS system for overlaying of CoNiCrAlY bond coating (approximately 100μm thickness). In case of the specimen with TBC, the YSZ-TBC top coating (approximately 300μm thickness) is further coated using an APS system. The geometry of the tested specimen is shown in Fig.10. The surface size of the specimens is 10mm times 10mm.

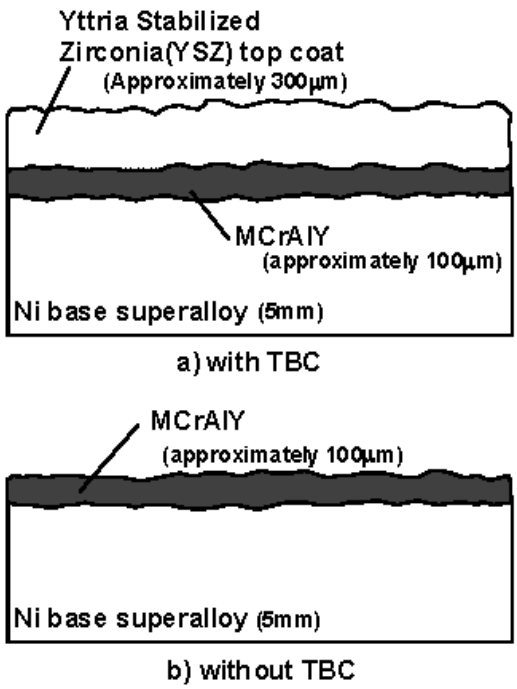

Figure 10. Geometry of cross-section of the tested specimens.

3.1.2. Thermal aging treatments

The two kinds of specimens are aged at 1000°C by using high temperature furnace. The reason for that temperature choice of 1000°C is to simulate the surface temperature of the first rotating blades of state-of-the-art gas turbine plants. The coated specimens (with and without TBC) are aged at 1000°C for various length of times viz, 10, 50, 100, 500, and 1000 hours. Only the specimen with TBC is aged for 3000 hours at 1000°C. The environment is ambient condition. In order to understand the relationship between the aging time and the growth of TGO layer, cross-section of thermally aged specimens is observed by SEM. The thickness of TGO layer for both specimens is measured at 100 points by SEM observations.

3.2. Results and discussion

3.2.1. Characterization for the specimen withTBC

SEM obserbation gives not only microstractural information but also information of initial degradation such as microcracks, porosities, and TGO. Therefore, cross-sections of TBC and MCrAlY interface for with-TBC specimen are observed by SEM. Typical SEM images of the cross-section of as-received and 3000 hours thermal aged specimen were shown in Fig.2 of the previous section. It is seen that TGO is formed at the TBC/MCrAlY interface. Furthermore, it is concluded, from this figure, that thickness of YSZ layer is almost constant in spite of the prolonged aging time up to 3000 hours. Moreover, TGO layer has irregular shape and variable thickness at the TBC/MCrAlY interface. Typical SEM images of the cross-section around TBC/MCrAlY interface of the specimen aged for 500, 1000, and 3000 hours were shown in Fig.3 of the previous section. It is proven that the TGO layer forms at TBC/MCrAlY interface. This TGO layer contains at least two layers with different color contrast, namely Al_2O_3, a black layer in this image closer to the bond coating, and mixed oxide, a gray layer in this image closer to YSZ. Furthermore, it is seen from the SEM images that the thickness of the TGO layer increases with the thermal aging time. A close look at the TGO layer reveals that there are many porosities, especially in the mixed oxide. These porosities can be referred to as Kirkendall porosity[14, 15], and they can reduce the adhesive strength of the TBC/MCrAlY interface.[16]

3.2.2. Comparison between the oxide thickness of the specimen with and without TBC

The oxide film thickness variation with aging time is understood from the results of section 2.2.2. However, the effect of TBC on TGO oxidation is not clarified. In order to investigate whether the growth of TGO is accelarated or reduced by TBC, detailed SEM study has been carried out for both specimens. Furthermore, the chemical composition of the TGO layer is determined by a comparison between secondary electron images and backscattered electron images. The results are presented in Fig.11.

For the specimen with TBC, mixed oxide is observed on the entire interface of TBC/MCrAlY. On the other hand, the specimen without TBC contains only island of thin mixed oxide on the surface.

http://dx.doi.org/10.5772/59794

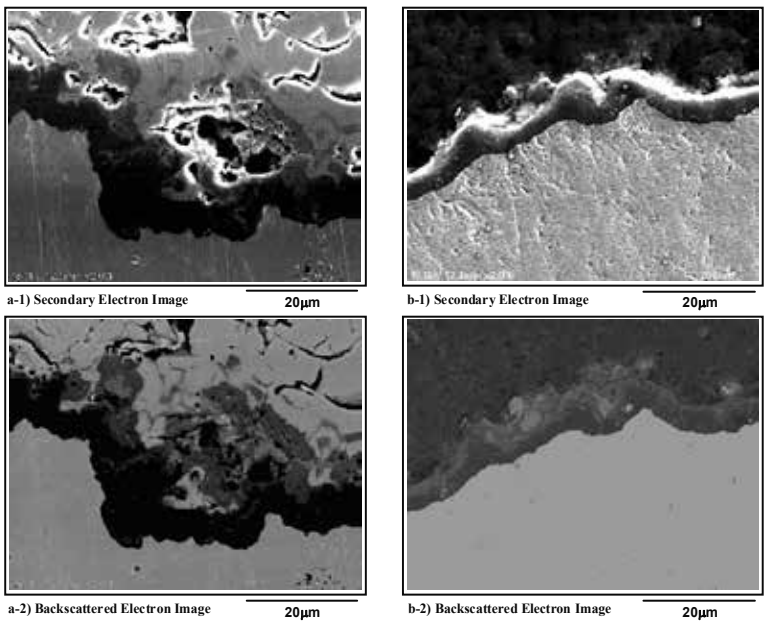

Figure 11. Typical SEM images of the cross sections for the specimens.

The dependence of average thickness of the TGO as a function of aging time for the both specimens is shown in Fig.12. Surprisingly, the TGO thickness of the specimen with TBC is larger than without TBC. It is expected that the average TGO thickness should be smaller for the specimen with TBC with respect to the specimen without TBC. However, the result is quite different. Therefore, SEM analysis to distinguish between the alumina and the mixed oxide layer was carried out.

Comparison between the thickness of each layer of the specimens with and without TBC is performed in Fig.13. It is seen that the alumina thickness is almost same for both specimens. On the other hand, thickness of mixed oxide is quite different in these two cases. Correspondingly, the difference in TGO thickness between the specimens with and without TBC is a result of difference between the mixed oxide thicknesses. The reason why the specimen without TBC has thinner mixed oxide can be that this specimen forms dense TGO due to smaller thermal expansion mismatch stress than the specimen with TBC.

For the specimen without TBC, the thickness of the mixed oxide, x_{mn}, and the alumina, x_{an}, for the specimen without TBC are expressed as follows:

Mixed oxide layer:

$$x_{mn} = k_{mn}\sqrt{T} = 0.052\sqrt{T} \tag{3}$$

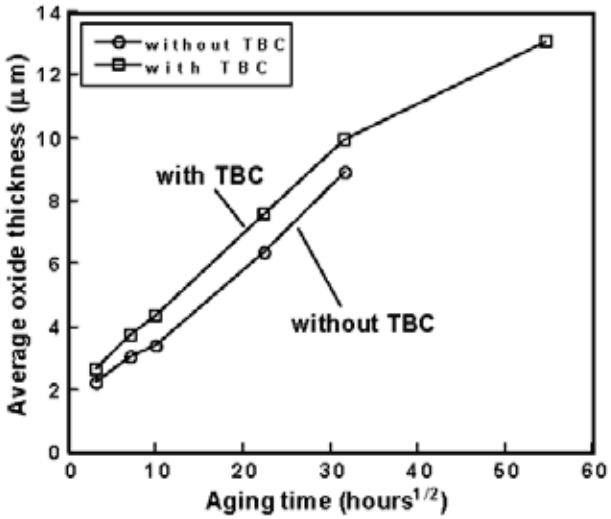

Figure 12. Dependence of the TGO thickness with the aging time for both specimens.

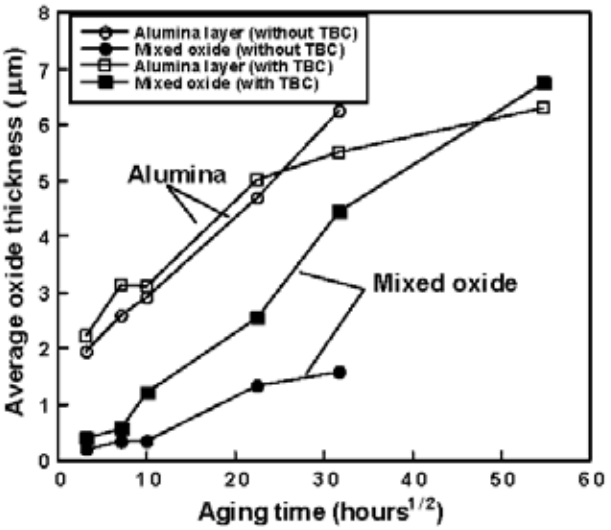

Figure 13. Comparison between the specimen with and without TBC concerning each layer thickness with aging time.

Alumina layer:

$$x_{an} = k_{an}\left(x_{mn}\right)\sqrt{T} = 0.232\, x_{mn} - 0.497 \times \sqrt{T} \tag{4}$$

where k_{mn} and k_{an} are respectively oxidation rate constant of mixed oxide and alumina for the specimen without TBC.

It is noted the constants in the corresponding oxide film equations with and without TBC are different, as well as that the mixed oxide and the alumina obeyed parabolic law and anomalous parabolic law, respectively for the specimen with TBC. The mixed oxide can enhance on degradation, which indicates that it is beneficial to decrease the thickness of mixed oxide.

3.3. Summary

Owing to understanding the oxidation behavior, a comparison is made between a specimen with TBC and without TBC. A comparison between the specimen with and without TBC shows that TGO is thicker for the specimen with respect to the specimen without TBC. These specimens had different oxidation behavior, which is due to specimen notable growth of mixed oxide for the specimen with TBC. The existence of the TBC has an influence of acceleration on TGO growth. The mixed oxide can enhance on degradation, which indicates that it is beneficial to decrease the thickness of mixed oxide. To do that, we must know the mechanism of TGO growth. Correspondingly, this work is helpful in analyzing mechanisms of TGO growth behavior, and in prolonging TBC life.

4. Effects of Ce and Si additions to CoNiCrAlY bond-coat material on oxidation behavior and bonding strength of thermal barrier coatings

It is generally accepted that the formation of the TGO accelerates TBC failures, and the bonding strength of the TBCs is reduced by the growth of TGO [6]. In section 2, it was indicated that the formation of porosity in a mixed oxide caused stress concentration sites and a decrease in bonding strength. Therefore, inhibition of the TGO formation would be an effective means for improving bonding strength. It is reported that the TGO growth rate depends on chemical composition, existence of atomic-order defects in the bond-coat, top-coat materials etc. [12, 17, 18]. Some approaches, such as modification of the bond-coat or of the coating processes, along with optimization of coating conditions to control the formation of TGO have been considered. In this section, a modified bond-coat material is described, namely adding Ce and Si to a conventional CoNiCrAlY [19].

4.1. Experimental procedure

4.1.1. Used materials

Ni base superalloy, Inconel 601, was used as a substrate material. The substrate was initially grit blasted, and then positioned into a low-pressure plasma spray (LPPS) coating system for several overlaying bond-coats approximately 100μm thick. Six different Ce and/or Si added bond-coat materials were developed. The chemical compositions of bond-coat materials were shown in Table 1. In developed powders, Ce contents were in between 0 to 1.5 wt% and Si

conatents were in between 0 to 2 wt%. These Ce and/or Si added bond-coat materials were compared with conventional CoNiCrAlY. A yttria (8 wt%-Y_2O_3) stabilized zirconia (YSZ) TBC top coating approximately 300 μm thick was then applied using an air plasma spraying (APS) coating system.

Bond-coat materials	Chemical compositions (wt%)						
	Co	Ni	Cr	Al	Y	Ce	Si
CoNiCrAlY	Bal.	32	21	8	0.5	-	-
0.5Ce1Si	Bal.	32	21	8	0.5	0.5	1
0.5Ce	Bal.	32	21	8	0.5	0.5	-
0.5Ce2Si	Bal.	32	21	8	0.5	0.5	2
1Si	Bal.	32	21	8	0.5	-	1
1Ce1Si	Bal.	32	21	8	0.5	1	1
1.5Ce1Si	Bal.	32	21	8	0.5	1.5	1

Table 1. Nominal chemical composition and particle size range of spraying powders.

4.1.2. High temperature exposure tests

High temperature exposure tests were performed in 1100°C atmospheric environment inside a muffled furnace. TGO formation was investigated by scanning electron microscopy (SEM) and energy dispersive X-ray spectrometry (EDX) for TBCs with seven different bond-coat materials.

4.1.3. Four-point bending tests

Fig.14 showed a schematic of the four-point bending tests. Specimens, which has dimensions of 40 mm × 5 mm × 4 mm, were aged for 100 and 1000 hours at 1100°C. During the test, an acoustic emission (AE) sensor and a strain gauge measured AE energy and the compressive strain on the specimens' backside, respectively. Assuming that the starting point of a rapid increase in cumulative AE energy corresponds to the occurrence of delamination, bonding strength was evaluated quantitatively by the amount of backside strain at the rapid increase point in cumulative AE energy.

4.2. Results and discussion

4.2.1. High temperature exposure tests

Cross-sectional SEM observation was performed for the TBC coated with several bond-coats aged at 1100°C for 100 hours. Firstly, in order to investigate the influence of Ce and Si additions, TGO morphologies, where located at the top-coat / bond-coat interface, were compared for

http://dx.doi.org/10.5772/59794

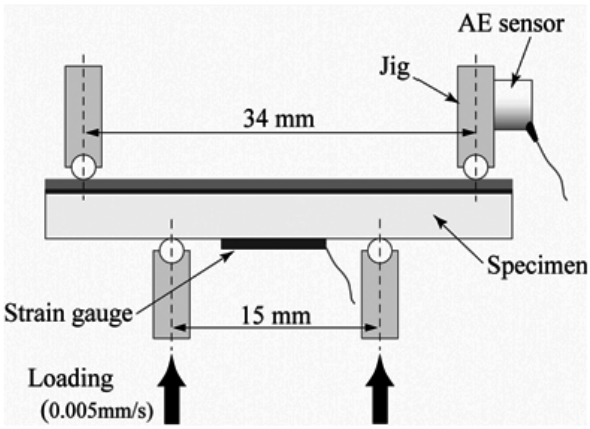

Figure 14. Schematic diagram of four point bending test

TBC coated with CoNiCrAlY, with 1Si, and with 0.5Ce bond-coat materials, and were shown in Fig.15. From these images, mainly a continuous Al_2O_3 film was formed at the interface between YSZ top-coat and bond-coat for all specimens.

In the case of Si addition, the TGO morphology was not changed compared to TBC coated with conventional CoNiCrAlY. In the case of Ce addition, TGO morphology between TBC coated with 0.5Ce bond-coat and the others were completely different. In particular, the formation and the growth of the mixed oxide (gray oxide in SEM images) were different. In the case of a TBC coated with CoNiCrAlY, the mixed oxides formed on the Al_2O_3. On the other hand, in TBC coated with 1.5Ce1Si bond-coat material, it seems that the mixed oxides grow into the bond-coat. That means that the oxide was interwoven with bond-coat.

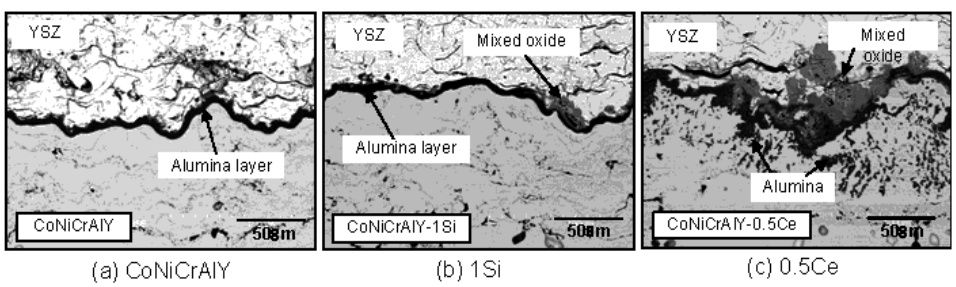

Figure 15. Cross-sectional SEM images of TBCs aged for 100 h at 1100°C. (Effects of separate addition of Si and Ce); (a) CoNiCrAlY, (b) 1Si and (c) 0.5Ce

Secondly, in order to evaluate the amount of Si content, TBCs coated with different Si added bond-coats were compared. Typical SEM images are shown in Fig.16. A significant difference was not shown among the three kinds of TBCs with Si added bond-coats. Accordingly, it is thought that there is almost no effect of Si addition on oxidation behavior.

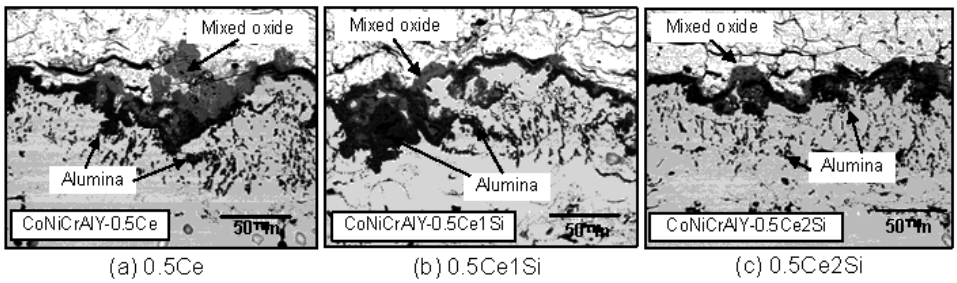

Figure 16. Cross-sectional SEM images of TBCs aged for 100 h at 1100°C. (Effects of variation of Si contents); (a) 0.5Ce, (b) 0.5Ce1Si and (c) 0.5Ce2Si

Furthermore, in order to evaluate the amount of Ce content, TBC coated with several Ce added bond-coat were compared. Typical SEM images are shown in Fig.17. From this figure, internal oxide, hereafter call wedge-like oxide, was observed under the interface. The wedge-like oxide was accelerated by over 1 wt% Ce addition. However, there were not much difference between TBCs coated with 1Ce1Si and 1.5Ce1Si. From these results, growth of the wedge-like oxide was enhanced by Ce addition to the conventional CoNiCrAlY. However, it can be thought that the effect may be saturated with over 1wt% Ce addition.

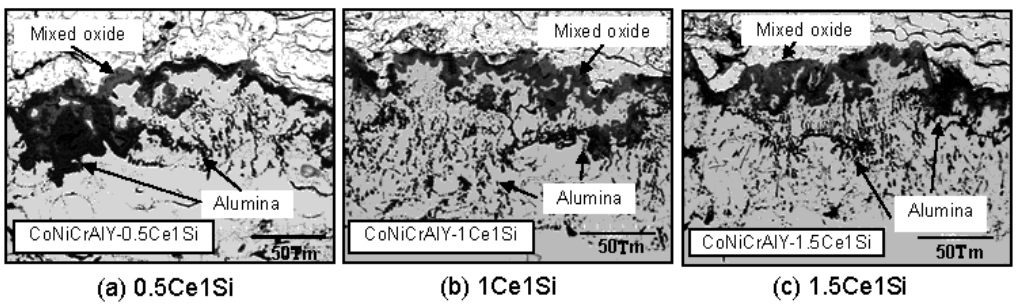

Figure 17. Cross-sectional SEM images of TBCs aged for 100 hours at 1100°C. (Effects of variation of Ce contents)

4.2.2. Mechanisms of formation of wedge-like oxide

From SEM observation, the addition of Ce led to the generation of wedge-like oxide inside the bond-coat. However, the mechanism of wedge-like oxide has not been made clear. Growth process of wedge-like oxide was observed regarding TBC coated with 1.5Ce1Si which showed most remarkable oxide formation. Results of SEM observation results are shown in Fig.18.

As a result, 1 hour aged samples did not observe formation of the wedge-like oxide inside the bond coat. However, the wedge-like oxide started to form after 5 hours aging, and then the thickness of the oxide gradually increased. After 10 hours aging, the wedge-like oxide completely formed inside the bond coat. Due to making clear the mechanism of formation of wedge-like oxide, 1 hour aged sample was observed by energy dispersive X-ray spectroscopy

http://dx.doi.org/10.5772/59794

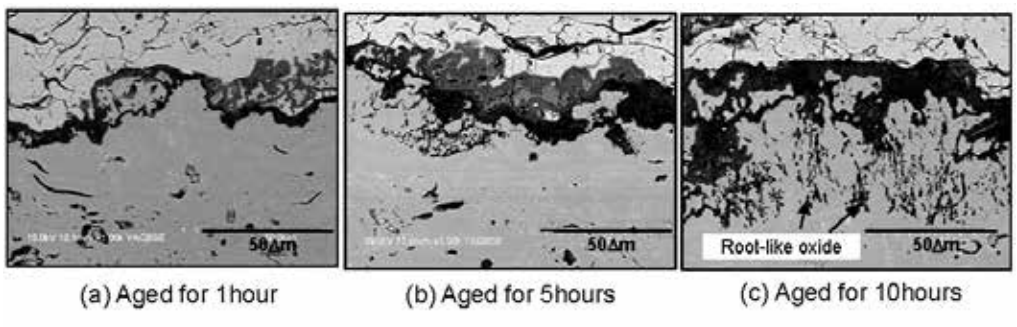

Figure 18. The growth process of wedge-like oxide of TBC coated with 1.5Ce1Si aged at 1100°C.

(EDX). The result of the SEM and the EDX analysis are shown in Fig.19. From SEM image of the figure, there were gray and white regions. In the gray regions, mainly Al and Ni were identified. Therefore, the gray regions can be NiAl intermetallic, namely β-phase. On the other hand, in the white regions, Ce and O were identified by EDX analysis. From this result, Ce-oxide (CeO_2) already existed inside the bond coat at this point. The result indicates that Ce oxidized preferentially rather than Al. From Ellingham diagram, Al oxidized preferentially rather than Ce under 1100°C. However, in this case, opposite result was obtained. The reason can be considered as follows:

Al makes the intermetallic with Ni. The intermetallic is relatively stable. Therefore, Al cannot be easy to oxidize. The solid solubility limit of Ce in CoNiCrAlY is very low. There is a possibility that Ce, which exceeded the solid solubility limit, independently segregated.

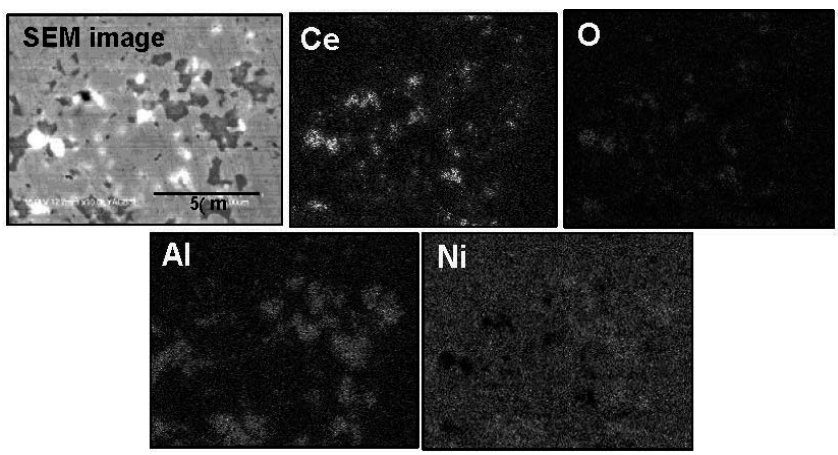

Figure 19. EDX analysis of TBC coated with 1.5Ce1Si aged for 1 hour at 1100°C

And the Ce-oxide, which observed inside bond coat in 1 hour aged sample, can affected oxidation behavior of bond coat. It is known about characteristics of Ce-oxide as follows:

1. Ce-oxide is higher diffusion rate than Al_2O_3.
   - Diffusion rate of O into Al_2O3: $D_{Al_2O_3} \sim 10^{-15} \sim 10^{-27} m^2/s$ (1000°C) [20]
   - Diffusion rate of O into CeO_2: $D_{CeO_2} \sim 10\text{-}8 \sim 10^{-12} m^2/s$ (1100°C) [21]
   - Diffusion rate of Al into MCrAlY (12 wt%Al): $D_{Al} \sim 10^{-14}$ m²/s (1100°C) [22]
2. Ce has non-stoichiometric property, and has oxygen storage function.

From these characteristics, it is suggested that Ce-oxide can be an oxygen path in bond-coat.

In the case of 5 hours aged sample, the Ni_3Al intermetallic (β-phase) did not recognize inside the bond coat. This means that Al in Ni_3Al oxidized and formed Al_2O_3. As a result, it can be decreased that Al concentration gradient between the interface and inside of bond-coat, due to decreasing Al concentration in bond-coat. Furthermore, focused on the Al_2O_3 at the interface, the Al_2O_3 was a porous film. Generally, Al_2O_3 was formed densely, and should play a role of oxygen barrier. However, in this case, it can be easy to penetrate oxygen via such porous Al_2O_3. From the result of observation of 1 hour aged specimen, Ce-oxide was formed diffusion path for oxygen in the bond-coat. Therefore, the Al, which remained in the bond coat, was oxidized at the inside of bond coat. From the results, it is suggested that the oxidation mechanism of the bond coat in case of TBC coated with Ce added bond-coat. The schematic illustration of the TGO formation mechanism is shown in Fig.20.

Due to high temperature exposure, firstly, Ce in the bond-coat was oxidized. And then, Al_2O_3 was formed at the interface between the TBC and the bond-coat. If there is Ni3Al intermetallic (β-phase) in the bond-coat, diffusion of Al to the interface and growth of Al_2O_3 proceed due to existence of Al concentration gradient. When the β-phase depleted, the diffusion rate of Al to the interface can be decrease. And then, due to formation of porous Al_2O_3 layer at the interface, it is easy to penetrate oxygen to the inside of the bond coat. Moreover, oxygen penetrates deeper through the Ce-oxide. As a result, wedge-like oxide can be formed.

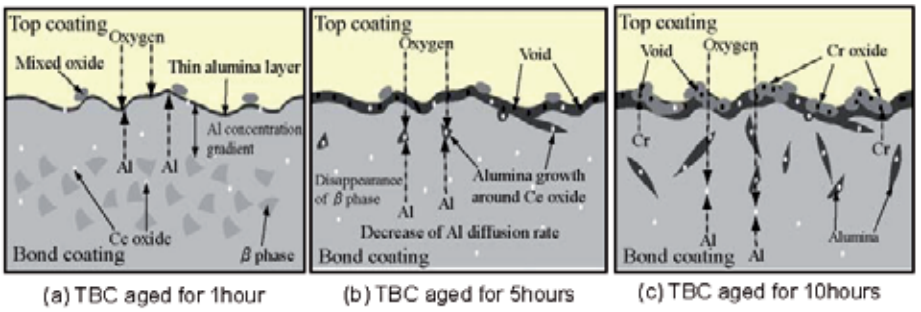

Figure 20. Schematic illustration of the TGO formation mechanism. (In case of TBC with Ce content bond coat aged at 1373 K).

http://dx.doi.org/10.5772/59794

4.2.3. Four-point bending tests

Results of the specimens aged for 100 hours and 1000 hours at 1100°C are shown in Fig.21 (a), (b), respectively.

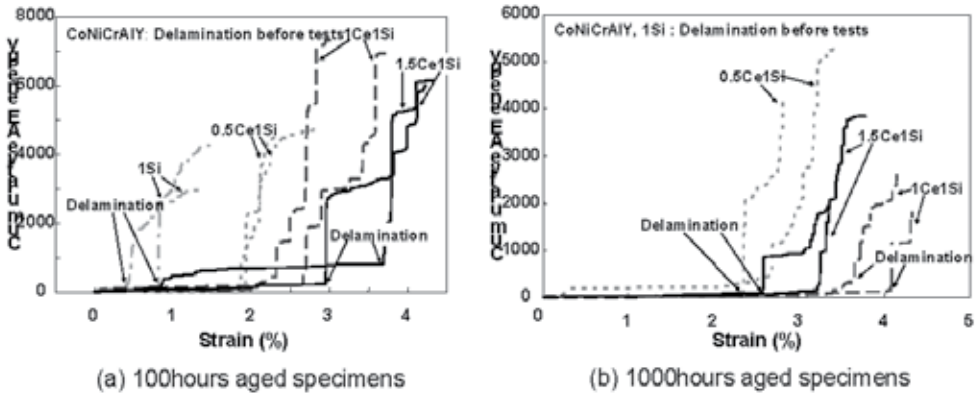

Figure 21. Results of four-point bending tests for the TBCs aged at 1100°C.

In the case of TBC coated with the conventional CoNiCrAlY, delamination occurred during heat treatment. Accordingly, this specimen could not be tested. This result shows that the TBC coated with the conventional CoNiCrAlY has low bonding strength. In case of 100 hours aged specimens, bonding strength increased with increasing Ce addition to the bond-coat. In samples aged for 1000 hours, TBC coated with 1Si delaminated only high temperature exposure. As a result, Si addition cannot be effective for the improvement of the bonding strength. And the TBC coated with 1Ce1Si was the highest bonding strength. In this specimen, the strain value of starting point of delamination was approximately 4%. Normally, due to degradation, the bonding strength gradually decreases. Therefore, it was supposed that the 1000 hours aged TBCs were lower bonding strength than the 100 hours aged TBCs. However, due to addition of Ce, the bonding strength did not drop down. That means effect of Ce addition. When Ce includes over 1wt%, the effect of Ce addition can be saturated. The wedge-like oxide can improve the bonding strength. And in case of the TBCs coated with low Ce added bond-coat, a delamination was mainly observed in the vicinity of the interface. On the other hand, in TBCs with relatively high Ce added bond-coat, a delamination was formed in YSZ top-coat. From the Figs.15-17, Ce addition to the bond-coat drastically changed thermally grown oxide morphologies, namely formation of wedge-like oxide. The wedge-like oxide can improve the bonding strength. It is supposed that the reason of the improvement is an anchor effect.

4.3. Summary

In this section, in order to promote the improvement of bonding strength of the interface between the thermal barrier coating and the bond coating, chemical composition of Ce and Si

added to the conventional CoNiCrAlY powders was investigated. The following conclusions are drawn:

1. By adding Ce and Si to convetional CoNiCrAlY, morphologies of the thermally grown oxide changed drastically. Furthermore, the influence became more pronounced when the amount of Ce increased.
2. Si addition to the conventional CoNiCrAlY cannot be effective for the improvement of the thermally grown oxide morphology and the bonding strength.
3. The bonding strength increased with increasing Ce addition to the bond-coat. Therefore, Ce addition can be effective for the improvement of bonding strength at the interface.
4. In case of TBCs coated with Ce added bond-coat, although high temperature exposure test was performed for a long period of time, the bonding strength did not drop down.
5. Ce addition to the bond-coat made the wedge-like oxide. The wedge-like oxide can improve the bonding strength. It is supposed that the reason of the improvement is an anchor effect.

5. Conclusions

Formation and growth behavior of thermally grown oxide (TGO) at the interface between ceramic thermal barrier coating and metallic bond coating was described.

During thermal aging, a TGO is formed at the TBC/MCrAlY interface. SEM and EDX analysis show that the TGO contains two different oxides. One is alumina closer to the MCrAlY, and the other is mixed oxide closer to the TBC. Thickness of both alumina and mixed oxide increased with aging time. In the case of aged specimen for a long time, the macrocrack was identified everywhere in the TGO. This reason indicates that thermal expansion mismatch accompanied by formation and growth of alumina is one of the driving forces of macrocracks formation. However, the driving force is not only thermal stress but also decrease in adhesive force or formation of stress concentration site caused by formation of porosity or microcrack. Almost all macrocracks passed through the porosity in mixed oxide or microcrack in YSZ layer. It is thought that the delamination or the spalling is initiated and propagated due to an interaction of these degradation factors such as thermal stress, initiation of stress concentration sites, and decreasing adhesive force due to formation and growth of alumina, porosities and microcracks.

And kinetics of TGO growth were obtained. It has been made clear that oxidation behavior of the mixed oxide layer obeys parabolic law. On the other hand, it is thought that the oxidation rate constant of the alumina is a function of thickness of mixed oxide. Consequently, the alumina thickness obeys anomalous parabolic law.

Furthermore, improvement technique for bonding strength between TBC and bond coat was suggested. By adding Ce and Si to conventional CoNiCrAlY, morphologies of the thermally

grown oxide changed drastically. Furthermore, the influence became more pronounced when the amount of Ce increased. Ce addition to the bond-coat made the wedge-like oxide. The wedge-like oxide can improve the bonding strength. From these results, if we can control the morphology of the TGO, we can control the bonding strength between TBC and bond coat.

Acknowledgements

This study was supported in part by the collaboration with Tohoku Electric & Power Co., Ltd. And the author would like to express thanks to Prof. T. Shoji, all of students and staffs in our laboratory, and collaborators involved in this study.

Author details

Kazuhiro Ogawa*

Address all correspondence to: kogawa@rift.mech.tohoku.ac.jp

Fracture and Reliability Research Institute, Tohoku University, Sendai, Japan

References

[1] Ito S, Saeki H, Inomata A, Ootomo F, Yamashita K, Fukuyama Y, Koda E, Takahashi T, Sato M, Koyama M, Ninomiya T, Conceptual Design and Cooling Blade Development of 1700°C Class High-Temperature Gas Turbine, Transaction of ASME 2005; 127 358-368.

[2] Hirano K, Application of eutectic composites to gas turbine system and fundamental fracture properties up to 1700°C, Journal of the European Ceramc Society 2005; 25 1191-1199.

[3] Meier S.M, Gupta D.K, The Evolution of the Thermal Barrier Coatings in Gas Turbine Engine Application, Journal of Engineering for Gas Turbines and Power 1994, 116 250-257.

[4] Gill B.J, Tucker Jr. R.C, Plasma spray coating processes, Materials Science & Technology 1986; 2 207-213.

[5] Goward G.W., Protective coatings - purpose, role, and design, Materials Science and Technology 1986, 2 194-200.

[6] Ogawa K, Shoji T, Aoki H, Fujita N, Torigoe T, Mechanistic Understanding For Degraded Thermal Barrier Coatings, JSME international Journal 2001; 44A(4) 507-513.

[7] Wu B.C, Chang E, Chao C.H, Tsai M.L, The oxide pegging spalling mechanism and spalling modes of ZrO_2-8wt%Y_2O_3/Ni-22Cr-10Al-Y thermal barrier coatings under various operating conditions, Journal of Materials Science 1990, 25 1112-1119.

[8] Wu B.C, Chang E, Chang S.F, Tu D, Degradation Mechanisms of ZrO_2-8wt%Y_2O_3 / Ni-22Cr-10Al-1Y Thermal Barrier Coatings, Journal of the American Ceramic Society 1989, 72 212-218.

[9] Bartlett A, Maschio R, Failure mechanisms of a zirconia-8wt% Yttria thermal barrier coating, Journal of the American Ceramic Society 1995, 78(4) 1018-1024.

[10] Maier R, Scheuermann C.M, Andrews C.W, Degradation of a Two-Layer Thermal Barrier Coating under Thermal Cycling, Ceramic Bulletin 1981, 60(5) 555-560.

[11] Newaz G.M, Nusier S.Q, Chaudhury Z.A, Damage Accumulation Mechanisms in Thermal Barrier Coatings, Journal of Engineering Materials and Technology 1998, 120 149-153.

[12] Ogawa K, Kato T, Shoji T, Improvement of Interface Bonding strength Between Ceramic Thermal Barrier Coatings and Metallic Bond-coats, Proceedings of the International Thermal Spray Conference 2002, 900-904.

[13] Smeltzer W.W, Oxidation of Aluminum in the Temperature Range 400 ^oC -600 ^oC, Journal of the Electrochemical Society 1956; 103(4) 209-214.

[14] Son Y.H, Morrral J.E, The Effect of Composition on Marker Movement and Kirkendall Porosity in Ternary Alloys, Metallurgical and Materials Transactions A 1989; 20(11) 2299-2303.

[15] Nesbitt J.A, Heckel R.W, Interdiffusion in Ni-Rich, Ni-Cr-Al Alloys at 1100 and 1200 deg.C, Metallurgical and Materials Transactions A 1987; 18(12) 2061-2073.

[16] L.Peichl, G.Johner, High-temperature behavior of different coatings in high-performance gas turbines and laboratory tests, Journal of Vacuum Science & Technology A 1986; 4 2583-2593.

[17] Newaz G.M, Nusier S.Q, Chaudhury Z.A, Damage Accumulation Mechanisms in Thermal Barrier Coatings, Journal of Engineering Materials and Technology 1998; 120 149-153.

[18] Choi H, Yoon B, Kim H, Lee C, Isothermal oxidation of air plasma spray NiCrAlY bond-coats, Surface & Coatings Technology 2002; 150 297-308.

[19] Tanno M, Ogawa K, Shoji T, Effect of Cerium and Silicon Additions to MCrAlY on the High-Temperature Oxidation Behavior and Bond Strength of Thermal Barrier Coatings, Key Engineering Materials 2004; 261-263 1062-1066.

[20] Zhu D.M, Miller R.A, Thermal Conductivity and Elastic Modulus Evolution of Thermal Barrier Coatings under High Heat Flux Conditions, Journal of Thermal Spray Technology 2000; 9(2) 175-180.

http://dx.doi.org/10.5772/59794

[21] Eaton H.E, Novak R.C, Sintering Studies of Plasma-Sprayed Zirconia, Surface Coating and Technology 1987; 32(1-4) 227-236.

[22] Chen H.C, Pfender E, Heberlein, Structural Changes in Plasma-Sprayed ZrO_2 Coatings After Hot Isostatic Pressing, Thin Solid Films 1997; 293(1-2) 227-235.

Chapter 5

Combustion Modelling for Training Power Plant Simulators

Edgardo J. Roldán-Villasana and
Yadira Mendoza-Alegría

Additional information is available at the end of the chapter

http://dx.doi.org/10.5772/59003

1. Introduction

In 2013, the Comisión Federal de Electricidad (CFE[1]), the Mexican Utility Company, had a production capacity of about 41.1 GW with a brute generation of 174.4 TW-h and transmits, distributes and commercialises electric energy for about 37 millions of clients that represent almost 105 millions of people [1]. In that same year, external energy producers generated about 32% of total energy consumed in Mexico.

Between others, like modernisation, an important factor of economical and performance results of a power plant, including those based on gas turbines, is the training of their operators. It is not easy to quantify the impact of training but there exists some feedback from plant's directors about improvement in operation skills. A classical study [2] demonstrated the importance of training power plants operators.

The Simulation and Advanced Training Systems Department (GSACS) is part of the Electrical Research Institute (IIE) and it is formed by a specialised group in training simulators that designs and implements tools and methodologies to support the simulators development, exploiting and maintenance.

Modelling the process of power plants for training is not an easy task and involves multidisciplinary work. In this chapter a general review of training simulator modelling is addressed with special emphasis on the combustion process.

1 Some acronyms are written after their name or phrase spelling in Spanish. A full definition of the used acronyms in this chapter is listed in Section 8.

The main attribute of a combustion model for training is to reproduce the behaviour of the phenomenon in order to report the variables in the control station of a power plant operator. The measurement of NO_x present in the exhaust gases is a very important variable. The major part of the sulphur, NO_x, and dust emissions from stationary installations result from fuel combustion to produce heat and power [3]. How to simulate these variables in a real time training simulator in a relatively easy approach is the goal of this chapter.

2. Mathematical modelling previous works

Depending on the application, a phenomenon may be represented by a mathematical model formulated by different techniques. Some examples of models applications are: design, analysis, optimisation, education, training, general tendencies, *etc*. Thus, modelling approach may vary from very detailed physical models (governing principles) like finite differences or finite elements, to empirical models like curves fitting, in the extremes. In fact, there is a vast task trying to classify all possibilities a model may be designed.

Some authors detail the general formulation of the combustion process considering the different conditions where the phenomenon is achieved. The model must be solved together with continuity, momentum and transport equations but any possible numerical method is not mentioned [4].

CFD methods model the phenomenon based on Navier–Stokes equations considering a finite volume partitioned normally into millions of cells considering the detailed geometry of the simulated space. Interaction with the solid boundaries is taken in account. A 3-D visualisation is normally achieved but accuracy depends on the detailed models used and, in the case of combustion, serious errors would arise. In fact, for example, it has been claimed that the design and development of combustors, until recent past, was more an art than science [5]. Although the author applies a CFD by using prePDF combustion model (it took nearly 2000 h of CPU time in a 4 node sun server with main memory of 128 GB) he states that validation must be attempted in future studies.

Studies consider different phenomenology like supersonic combustion [6], chilling of the combustor liner by film cooling [7], micro-turbine engine with annular combustion chamber design [8], comparison of several turbulence models [9], swirling air flow [10,11], and many others. In spite of the promise of having good results, this approach is far enough to be used in real time applications.

Models with less spatial details are intended for design. A "simplified" methodology has been developed where different fuels and inlet conditions were studied for steady state conditions [12]. Direct fuel injection and diffusion flames, together with numerical methods like Newton-Raphson, LU Factorization and Lagrange Polynomials, are used for the calculations. Diesel, ethanol and methanol fuels were chosen for the numerical study. Finally, a computer code sequentially calculates the main geometry of the combustor. Design modes are not suitable for real time simulators.

http://dx.doi.org/10.5772/59003

A model was presented to study the influence of different air cooling systems validated against real plant data [13]. Gas composition was not included and an ideal gas model was considered. The input data were the air cooling system configuration and the ambient conditions. The combustion was simulated just increasing the gas temperature as a function of the mass flowrate and the fuel high heating value.

A model for desktop for excel was elaborated for a standard air Brayton cycle [14]. A total of five components and the combustion reaction stoichiometric with possibilities of excess of oxygen were considered. The output temperatures of the turbine were simulated as a second degree equation in function of the enthalpy instead using well known thermodynamic properties. The inputs variables are efficiencies, some pressure drops, temperatures, *etc*.

In other approach, the ideal gas assumption was adopted even when other aspects were modelled in detail like the flow through the equipment, the heat transfer phenomena and basing the process on a temperature-entropy diagram [15]. In this case the gas composition and the combustion process were ignored (considering only an increase of the temperature of gas) and the model, designed for optimisation, runs around the full load point.

A model based on Simulink was used to analyse the dynamical behaviour of an industrial electrical power system [16]. An ideal gas approach was used. The model was validated against real data but not details of the combustor model are mentioned.

The most important feature of a combustion model for training is the capacity of reproducing the behaviour of, at least, the variables reported in the control station of a power plant operator in such a way he cannot distinguish between the real plant and the simulator. Nowadays, the measurement of NO_x present in the exhaust gases is a very important factor to consider in an operator training program. However, the authors did not find a single paper where this theme is developed for real time training simulation.

Combustion models used specifically for training simulators are those created by companies that develop real time simulators, so the information is proprietary and the formulation is not available [17], in [18] an excellent explanation of the uses of training simulators is explained but presents not a single equation of the process model.

For a real time simulator application, the variables affecting the operation of a plant, including the combustion process, may be taken in account. The model is not developed to design a combustion chamber or burners, but to reproduce the plant operation data with the capacity to predict the plant behaviour during the transients occurred during all the normal and emergency operational scenarios. The real time execution characteristics required by a training simulator is accomplished by the present model.

3. Power plant simulation for training

High-performance computing help engineers and scientists apply modelling and simulation. One of the most useful applications is the use of software to make environments for training

in different technological areas. In a power plant, for example, it is important to train personnel in risk and unusual actions; a tool which has been widely tested is training simulators.

The IIE has developed several power plant simulators for Thermal-Electric Units, Nuclear, Geo-Thermal, Dual (Coal and liquid fuel), Gas Turbine, Combined Cycle, VU-60 Boiler and simulators with new web technologies.

The simulators must accomplish the ANSI norm [19] and are tested in the whole operation range; including malfunctions and transients according the operation procedures designed by the clients who are the final users of the simulator.

A simulator is designed to recreate a particular control room where operators may practise the plant procedures. An instructor coordinates and guides the simulator sessions (practical lessons).

3.1. Typical software configuration

The simulation environment is called MAS a trade mark software of the IIE; designed as a general tool to support simulators. MAS is both: a development tool and a man-machine interface for instructors; basically consists of three independent and coordinated tasks: *The Real Time Executive*, *The Operator Module*, and *The Instructor Module*.

The *Real Time Executive* is a function to manage the execution sequence of each mathematical model with all tasks performed by the simulator. These models may be executed in a parallel scheme, with a distributed architecture of PCs or with multi-core equipment or sequentially.

The Operator Module coordinates the interactive process diagrams (IPD) execution (IPD conforms the operation consoles). This module manages command messages of the operation consoles, controls the alarms system, the historical trends and the control of each IPD component (valve, pump, controllers, *etc*.). It refreshes each IPD periodically, and coordinates the sequence of events in the operation consoles.

The Instructor Module executes the instructor actions in a synchronized way during simulation; receives and responds the commands from-to the instructor console actions as start, stop and freeze a simulation session, actives malfunctions, modifies external conditions, *etc*. Figure 1 represents the standard instructor console.

The instructor console has icons for fast access; also has the possibility to modify the simulation velocity of the simulator to be increased up to ten times or to be decreased up to 10 times respect to real time. Another function is to simulate step by step, it means to run the whole simulation cycle on the minimum unit time in which simulator models are executed; it is equivalent to 0.1 s.

Most of first level instructor console menus are shown in Figure 2.

3.1.1. Control menu

The main functions of this menu are *Run/Freeze Simulation, Backtrack and Automatic function. Run/Freeze Simulation: wi*th this function the instructor may run or stop a simulation session.

http://dx.doi.org/10.5772/59003

This is an alternating button, which means that if simulator is in stop mode, clicking the button, simulation runs, and *vice versa. Backtrack*: allows reproducing automatically all instructor and operator actions that were made in a simulation session. *Automatic function:* allows the instructor to design training sceneries by pre-programming automatic actions during a simulation session as introduce malfunctions or modifying variables as ambient, temperature, humidity, *etc*. in pre-established times.

Figure 1. Instructor console

Figure 2. Menus of the instructor console

3.1.2. Initial conditions menu

An initial condition (IC) contains the necessary information to start-up a simulation session in any predefined plant condition (from cold condition up to nominal operation point). In the simulator are four IC options, namely P*reprogramed, Instructor, Periodic,* and *From Last Stop*. *Preprogramed:* are those IC with the whole information from cold condition up to nominal operation point and all the instructors may establish it. The *Instructor* IC is defined by one particular user and only he may access it. *Periodic* are IC automatically created when the simulator is running; default period is established in 2 minutes; this function is useful if instructor desires to get back to a previous condition within simulation session to explain some effect. *Last Stop* IC is automatically created, when the simulation session is freeze.

3.1.3. Instruction functions menu

There are three set of functions in this menu: *External Parameters*, *Malfunctions* and *Remote Functions*. *External Parameters*: permit simulates changes on external conditions of the plant that operator cannot control like environment pressure or temperature, gas fuel composition, *etc*. *Malfunctions:* modifies the behaviour of the system by simulating an abnormal event as broken pipes, fouling filters, loss of pilots, trip of pumps, *etc*. *Remote Functions:* represents actions that in a plant would be realized by a worker through manual actions because they cannot be made from the control room, for example: opening and closing valves; in the simulator, these actions are achieved by the instructor (requested by the operator). Malfunctions and remote functions are organized in groups related with the plant modelled systems. They may be modified according to some options like delay, evolution time and severity percentage.

3.1.4. Information functions menu

These functions are: *Tabulation, Monitoring*, and *Trending*. *Tabulation*: this function permits to select some variables from a predefined variables group and register them in a file during a simulation period defined by the user. *Monitoring*: this function permits to select a group of variable for its supervision during a simulation session, normally used while a simulator is being developed. *Trending*: this tool permits to create variables groups on line to be displayed graphically during a simulation session. Trending is available for the operators too.

3.1.5. Miscellaneous functions menu

This menu is formed by *Logbook*, *Change of instructor* and *Create a user account*. *Logbook*: is a function than can save and display the operator and/or the instructor actions during a simulation session. *Change of Instructor:* It permits to establish another instructor account to guide a simulation session. *Create a User Account:* permits to create new instructors.

3.2. Hardware configuration

The standard hardware configuration consists in a PC network and several monitors for the Instructor and operation consoles; normally the instructor console is installed in a different room than the operation console separated by a glass wall; in the first area the simulation sessions are initiated and guided by the instruction consoles and in the second area the hardware looks as a replica of the real plant control stations and it is here where the operator is trained. Figure 3 shows a typical hardware configuration of a simulator.

An example of an IPD where the operator may monitor the whole process and act on the plant is presented in Figure 4. In this case is the main screen of a gas turbine power plant with the summary of the plant conditions.

http://dx.doi.org/10.5772/59003

Figure 3. Hardware configuration (instructor and operation consoles)

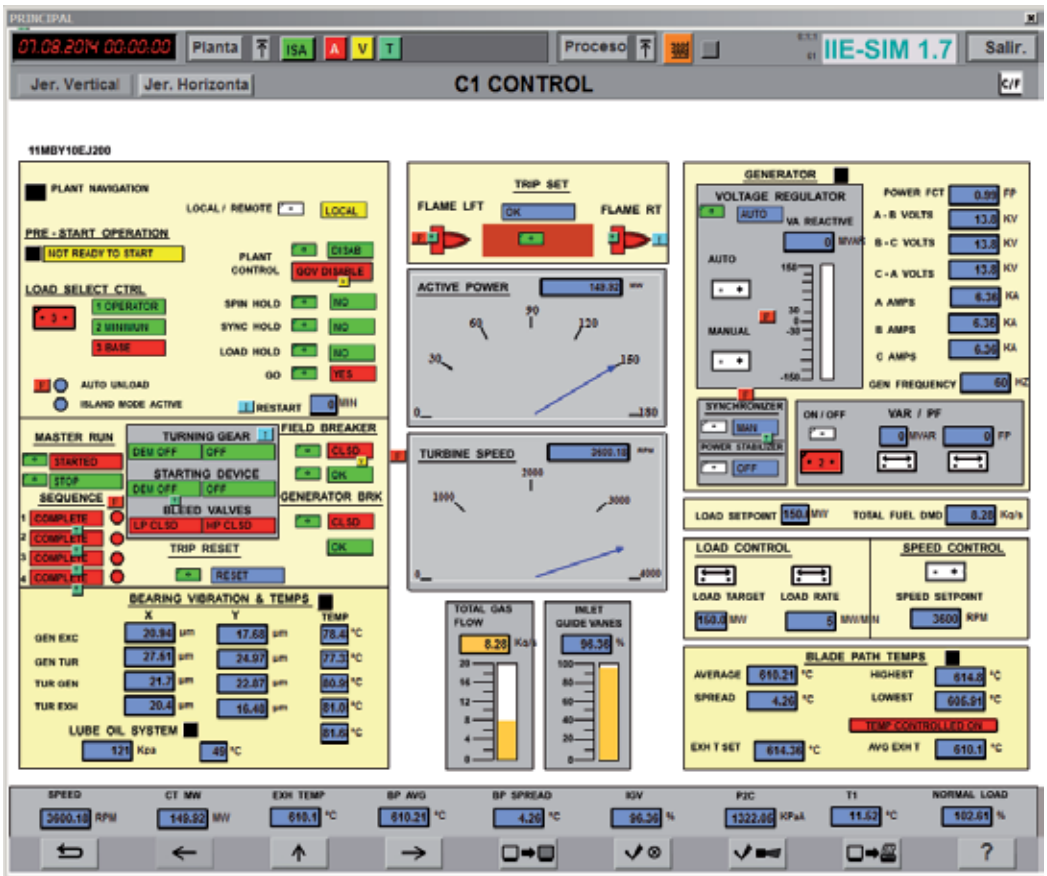

Figure 4. Example of an IPD in the operation consoles

4. Modelling of combustion surrounding systems

The models of any simulated plant were divided in two groups: process and control models.

4.1.1. Process models

Traditional methods of modelling and simulation considered approaches often using empirical relations and approximated procedures in model development. The models of a modern training simulator are a set of algebraic and differential equations obtained from the application of basic principles (energy, momentum, mass balances and constitutive equations). The models are designed to work under a full range of operational conditions, from 0% to 100% of load including all possible transients that may exist during operational manoeuvres, including malfunctions and changes of external parameters, always replicating the real plant comportment. The simulator was developed applying a methodology developed by the IIE [20].

Process models may be divided in electrical, mechanical, and fluid phenomena. All are important but in this chapter only a brief summary on thermal fluid modelling is revised.

Changes in the state of a fluid are not instantaneous. When a system is perturbed to change the steady state conditions of a system (a fluid in this case) takes a minimal time. Time of getting a new steady state is a function of the perturbation magnitude and the inertia of the system (which normally depends on the mass of the system).

In the IIE, the fluid mechanics phenomena are modelled with algebraic equations. A generic model that automatically solves the mass and moment balances and constitutive equations for pressure drops in valves, pipelines and other fittings like elbows, pumps, compressors, fans, turbines, *etc*., has been developed by the GSACS [21]. This program (flupre) is configured with the plant networks of pipelines and fittings and it automatically detects the "active" topology of a network. This is the arrangement of the grid, in a given instant, formed only by the elements allowing flow through them. The active topology may change, for instance, a stream is "eliminated" of the network when a valve is closed or pumps are turned off. The full topology is that theoretically formed if all streams allow flow through them. During a session of dynamic simulation a system may change its active topology depending on the operator's actions. This means that the order of matrix associated to the equations that represent the system changes. Flupre assumes that mass accumulation is not hold in the network.

A flows and pressures network is constituted of nodes and streams. A node is a point where two or more streams converge in or divert from. A stream transports a fluid and has fittings that arise or drop pressure through them. If not mass accumulation is assumed and a simplified expression relating mass flowrate and pressure drop is used, an equation system may be stated with a continuity equation for each node and a flow-pressure drop expression for each stream:

$$\sum w'_{in} - \sum w'_{o} = 0 \tag{1}$$

$$w^2 = k_1 \, \Delta P + \, k_2 \tag{2}$$

http://dx.doi.org/10.5772/59003

The equations are solved simultaneously and the flowrate of each stream and the pressure of each node are then known. Initial values for these variables have to be established as initial value for iterations.

There exist other nodes not being part of the flows and pressures networks. Normally, they are considered to accumulate mass (like a steam header or a pressurised air tank), so, a proper mass balance should be stated, one equation for each stream component *j*:

$$\frac{dm_j}{dt} = \sum w_{in} c_{in,j} - \sum w_o c_j \tag{3}$$

Commonly, elements simulated with differential equations, like Equation (3), are denominated capacitive nodes. The variables associated with derivatives are "state variables" and their values define the condition of a system. These variables have an initial condition to start any simulation session.

For these nodes normally the pressure is also a state variable. The more simple case is when the node is assumed to behave like an ideal gas:

$$\frac{dP}{dt} = \frac{R\,T}{V}\left(\frac{dm}{dt}\right) + \frac{R\,m}{Cp\,V}\left(\frac{dh}{dt}\right) \tag{4}$$

In this case, *m* represents moles.

Also enthalpy is a variable associated with a derivative:

$$\frac{dh}{dt} = \frac{\sum w_{in} h_{in} - w_o\, h - q_o}{m} \tag{5}$$

More complex cases exist by considering other phenomena like phases' equilibrium, separation process, chemical reactions, evaporation and condensation situations, *etc*. However these models are not considered now, except the combustion developed later.

Numerical methods to solve algebraic and differential equations are employed. For algebraic equation the most used method is Newton-Raphson either, with analytical or numerical derivatives calculations. For differential equations, the Euler method is enough for training simulator models. As an example of this method, let's considered the integration of the pressure of any node:

$$P_{t+\Delta t} = P_t + \frac{dP}{dt}\Delta t \tag{6}$$

Normally, the integration step Δt is assigned to a value of 0.1 s.

Capacitive nodes intrinsically have an inertia affecting the derivative calculation.

Algebraic equations, by definition, are assumed to reach instantaneously its final value (an instant, numerically, is a time period with a value of Δt). So, a lag may be defined for these variables. For example, for a calculated flowrate w there exists a flowrate w':

$$w^{'} = w' + (w - w')\,\Delta\, t_{lag} \tag{7}$$

that may be reported in an operation consoles. Note that if Δt_{lag} has a value of 1, no lag exists.

4.1. Control models

The control models acquire and process the actions realised by the operator in the control room by actions on the operation consoles. These models generate, *via* digital and analogic programs, changes on some simulated elements, depending on any particular condition of the simulated plant. For example, the control adjusts demand of valves to regulate some process variables around a set point fixed by the operator (levels of tanks, pressures, temperatures, *etc*.).

For the development of the plant control models, generally two approaches are followed:

a. To develop in a graphic environment a copy of the control diagrams provided by the client or control developer. Once the diagrams have been drawn, this environment is embedding into the simulator to be sequenced and executed in real time. These diagrams are drawn in the format defined by the Scientific Apparatus Makers Association (SAMA).

b. To translate the control algorithms as well as the IPD of the operation consoles, obtained from the control station of the real plant. The control is an exact copy of the functioning control system (both, logical and analogical), including PID constants.

4.2. Combustion chamber surrounding systems

By using the proper equations as that presented in section 4.1, the systems that feed or extract flow or energy from a combustion chamber may be simulated.

A couple of examples of systems around the combustion chamber are shown in Table 1. There are included both, process and control models.

5. Combustion modelling

5.1. General approach

For the so called thermal NO_x, *i.e.* nitrogen oxides, formed from the oxidation of the free nitrogen in the combustion air or fuel, the main factor affecting the formed NO_x in combustion reaction is the stoichiometric adiabatic flame temperature of the fuel, which is the temperature reached by burning a theoretically correct mixture of fuel and air in an insulated vessel. The main factors affecting this flame temperature are [22]:

- NO_x increases strongly with fuel-to-air ratio or with firing temperature.

http://dx.doi.org/10.5772/59003

- NO_x increases exponentially with combustor inlet air temperature.
- NOx increases with the square root of the combustor inlet pressure.
- NO_x increases with increasing residence time in the flame zone.
- NO_x decreases exponentially with increasing water or steam injection or increasing specific humidity.

Gas Turbine Combustor		Boiler Furnace	
Air System:	IGV Control	Air System:	Induced Fan Draft
	Compressor		Forced Fan Draft
	Air Heater		Air/Vapour Pre-Heater
			Ljunström Heater
			BMS Control
Fuel Systems:	Gas	Fuel Systems:	Gas
	Combustion Control		Liquid Fuels
			Atomising Steam
			BMS Control
Water Injection System		Soot Blowers System	
Gas Turbine		Convective Heat Zone	

Table 1. Typical combustion chamber surrounding systems

The formation of NO_x due to oxidation of organically bound nitrogen in the fuel (fuel-bound nitrogen), called "organic NO_x" is important only for crude or residual oils and it is not included in this model.

A generic model for the combustion process was developed by the IIE. The stated objective was to calculate flame temperature and composition of the burned gases including the simulated heat transfer phenomena. It is possible simulate a mixture up to twenty components, all displayed in Table 2.

Thermodynamic properties were calculated using cubic state and corresponding states equations for non-polar substances. The application range is for low pressure up to 80 bars.

Cubic equations properties are in next general form [23]:

$$P = \frac{R\,T}{\hat{v} - b} - \frac{a}{\hat{v}^2 + u\,\hat{v}\,b + w\,b^2} \tag{8}$$

where R is the ideal gas constant, $\hat{v}$ molar volume, and a, b, u and w, are constants that in fact determine the precise cubic equation that may be used: Van der Waals, Redlich-Kwong, Soave, Peng-Robinson, Lee-Kesler, Racket (for saturated liquid only), Hankinson-Brobst-Thompson (for liquid only), and Ideal Gas. Also may be used the corresponding states equation Lee Kesler:

No.		Component	No.		Component
1	N_2	Nitrogen	11	C_6H_{14}	n-Hexane
2	O_2	Oxygen	12	C_7H_{16}	n-Heptane
3	H_2S	Hydrogen Sulphide	13	C_8H_{18}	n-Octane
4	CO_2	Carbon Dioxide	14	C_9H_{20}	n-Nonane
5	CH_4	Methane	15	$C_{10}H_{22}$	n-Decane
6	C_2H_6	Ethane	16	H_2O	Water
7	C_3H_8	Propane	17	CO	Carbon Monoxide
8	C_4H_{10}	n-Butane	18	NO	Nitrogen Monoxide
9	iC_4H_{10}	i-Butane	19	NO_2	Nitrogen Dioxide
10	C_5H_{12}	n-Pentane	20	SO_2	Sulphur Dioxide

Table 2. Possible combustion components

$$Z^{(0)} = 1 + \frac{B}{V_r^{(0)}} + \frac{C}{(V_r^{(0)})^2} + \frac{D}{(V_r^{(0)})^5} + \frac{C_4}{T_r^3 (V_r^{(0)})^2}\left(\beta + \frac{\gamma}{(V_r^{(0)})^2}\right) e^{\frac{-\gamma}{(V_r^{(0)})^2}} \tag{9}$$

$$Z^{(0)} = \frac{P_r V_r^{(0)}}{T_r}\ ;\ Z^{(R)} = \frac{P_r V_r^{(R)}}{T_r}\ ;\ Z = Z^{(0)} + \frac{\Omega}{\Omega_r}\left(Z^{(R)} - Z^{(0)}\right) \tag{10}$$

where B, C, D, C_4, β, and γ are characteristics (constants) Ω is Pitzer's acentric factor.

For the solution of any of the equations for a gas mixture, the Newton-Raphson method is used.

For the water, thermodynamic properties data [24] were adjusted as a function of pressure and enthalpy or temperature. Functions were adjusted by least squares method. The application range is between 0.1 and 4520 *psia* for pressure, and-10 and 720 ^oC (equivalent to 0.18 and 1635 *BTU/lb* of enthalpy).

5.2. Definition of efficiencies

To calculate the products of the reaction as a function of the inlet reactants moles, the stoichiometric coefficients are needed. However, in the approach proposed by the authors, a couple of efficiencies are defined to be used in these calculations.

Total combustion efficiency $\alpha_{j,1}$ for component j is the fraction of the amount of oxygen that is consumed for a total combustion. It is 1 if a complete combustion reaction is hold, for example production of CO_2. It is 0 if the product (for example CO_2) is not at all produced.

Partial combustion efficiency $\alpha_{i,,2}$ for component j is defined as the fraction of the amount of oxygen that is consumed for a partial combustion. It is 1 if partial oxidised products are generated, for example production of CO. It is 0 if the product (for example CO) is not at all produced.

http://dx.doi.org/10.5772/59003

A special case is the production of NO and NO_2. The values of efficiencies are represented on basis of the moles quantity of N_2 instead O_2.

In this approach, by now, the value of efficiencies is proposed by the programmer in order to fit the results of the reference plant.

5.3. Simple example

In order to explain the model used for the combustion in a clear way, a simple reaction will be contemplated.

Let's assume the ideal case where CH_4 is the only fuel component. No inlet water is considered. The possible reactions are presented here (the subscripts nomenclature maintains the numbering of the global equations presented later):

$$\begin{aligned} n_{1,1}N_2 + \quad & n_{1,2}O_2 \quad \rightarrow \quad m_{1,1}N_2 + \quad m_{1,2}O_2 + \quad m_{1,18}NO + \quad m_{1,19}NO_2 \\ & n_{2,2}O_2 \quad \rightarrow \quad m_{2,2}O_2 \\ n_{5,1}CH_4 + \quad & n_{5,2}O_2 \quad \rightarrow \quad m_{5,2}O_2 + \quad m_{5,4}CO_2 + \quad m_{5,16}H_2O + \quad m_{5,5}CH_4 + \quad m_{5,17}CO \end{aligned} \tag{11}$$

Coefficients of Equations (11) represent moles, no mass. Up to now, the stoichiometric is not included.

In general, the O_2/N_2 ratio of atmospheric air is taken as 21/78 whereas 1% other gases as inert [25].

Considering the stoichiometric coefficients and the efficiencies of each reaction, by knowing the reactants feed streams, it is possible to calculate the moles reactions (considering also the possible reactant that appears also as a product, for example the CH_4 that is not consumed).

Let's assume next arbitrary definition of efficiencies just for this example (efficiency values for production of NO, NO_2 and CO are too high compared with actual expected values but works good for this example):

$$\begin{aligned} N_2 \quad & \text{If } O_2 \text{ excess} \geq 200\% \quad \alpha_{1,1} = 0.0046\,; \quad \alpha_{1,2} = 0.0000 \\ & \text{If } O_2 \text{ excess} = 100\% \quad \alpha_{1,1} = 0.0000\,; \quad \alpha_{1,2} = 0.0040 \\ & \text{If } O_2 \text{ excess} \leq 50\% \quad \alpha_{1,1} = 0.0000\,; \quad \alpha_{1,2} = 0.0000 \\ CH_4 \quad & \text{If } O_2 \text{ excess} \geq 200\% \quad \alpha_{5,1} = 1.0000\,; \quad \alpha_{5,2} = 0.0000 \\ & \text{If } O_2 \text{ excess} = 130\% \quad \alpha_{5,2} = 0.4500 \\ & \text{If } O_2 \text{ excess} \geq 100\% \quad \alpha_{5,1} = 0.0000\,; \\ & \text{If } O_2 \text{ excess} \leq 50\% \quad \alpha_{5,1} = 0.0000\,; \quad \alpha_{5,2} = 0.0000 \end{aligned} \tag{12}$$

Considering stoichiometric of reactions:

$$
\begin{array}{lll}
N_2 & n_{1,1} = & input\ data\ 78/21 n_{1,1} \\
 & m_{1,19} = & 2\alpha_{1,1} n_{1,1} \\
 & m_{1,18} = & 2\alpha_{1,2} n_{1,1} \\
 & m_{1,1} = & 0.5\left(2n_{1,1} - m_{1,18} - m_{1,19}\right) \\
 & n_{1,2} = & 0.5 m_{1,18} + 1 m_{1,19} \\
O_2 & n_{2,2} = & input\ data \\
 & m_{2,2} = & n_{2,2} - \Sigma n_{i,2}\ \ for\ i = 1,3,4,\ldots 20 \\
CH_4 & n_{5,1} = & input\ data = 1.0 \\
 & m_{5,4} = & \alpha_{5,1} n_{5,1} \\
 & m_{5,17} = & \alpha_{5,2} n_{5,1} \\
 & m_{5,5} = & n_{5,1} - m_{5,4} - m_{5,17} \\
 & m_{5,16} = & 2n_{5,1} - 2m_{5,5} \\
 & n_{5,2} = & m_{5,4} + 0.5 m_{5,16} + 0.5 m_{5,17}
\end{array}
\tag{13}
$$

Tables 3, 4, and 5 present three different cases for this example. The difference is the inlet moles of air feed to the combustion chamber. The inlet mole flowrates is a function of the oxygen excess (*Oe*), namely: 2.5, 1.5 and 0.45.

In Tables 3, 4, and 5 the way to verify that calculated mole flowrates of products are correct is that sum of moles of elements must be equal in reactants and products.

Inlet mole flowrate of reactants					**Exit mole flowrate of products**				
O_2	$n_{2,2}$	2.5885	**moles of elements**		O_2	$m_{2,2}$	0.5000	**moles of elements**	
N_2	$n_{1,1}$	9.6142	O	5.1769	N_2	$m_{1,1}$	9.5700	O	5.1769
CH_4	$n_{5,1}$	1.0000	N	19.2285	O_2	$m_{1,2}$	0.0000	N	19.2285
O_2	$n_{1,2}$	9.5700	C	1.0000	NO_2	$m_{1,19}$	0.0885	C	1.0000
O_2	$n_{5,2}$	2.0000	H	4.0000	NO	$m_{1,18}$	0.0000	H	4.0000
					CO_2	$m_{5,4}$	1.0000		
					CH_4	$m_{5,5}$	0.0000		
					CO	$m_{5,17}$	0.0000		
					H_2O	$m_{5,16}$	2.0000		
Total		13.2027		29.4054	Total		10.7268		29.4054
$\alpha_{1,1} = 0.0046$; $\alpha_{1,2} = 0.0000$; $\alpha_{5,1} = 1.0000$, $\alpha_{5,2} = 0.0000$									

Table 3. Example of moles balance; oxygen excess=2.5

http://dx.doi.org/10.5772/59003

Inlet mole flowrate of reactants					Exit mole flowrate of products				
O_2	$n_{2,2}$	1.3460	**moles of elements**		O_2	$m_{2,2}$	0.0572	**moles of elements**	
N_2	$n_{1,1}$	4.9994	O	2.6920	N_2	$m_{1,1}$	4.9925	O	2.6920
CH_4	$n_{5,1}$	1.0000	N	9.9988	O_2	$m_{1,2}$	0.0000	N	9.9988
O_2	$n_{1,2}$	0.0138	C	1.0000	NO_2	$m_{1,19}$	0.0138	C	1.0000
O_2	$n_{5,2}$	1.2750	H	4.0000	NO	$m_{1,18}$	0.0000	H	4.0000
					CO_2	$m_{5,4}$	0.3000		
					CH_4	$m_{5,5}$	0.2500		
					CO	$m_{5,17}$	0.4500		
					H_2O	$m_{5,16}$	1.5000		
Total		7.3454		17.6908	Total		7.5635		17.6908
$\alpha_{1,1} = 0.0014$; $\alpha_{1,2} = 0.0000$; $\alpha_{5,1} = 0.3000$, $\alpha_{5,2} = 0.4500$									

Table 4. Example of moles balance; oxygen excess=1.5

Inlet mole flowrate of reactants					Exit mole flowrate of products				
O_2	$n_{2,2}$	0.4659	**moles of elements**		O_2	$m_{2,2}$	0.4659	**moles of elements**	
N_2	$n_{1,1}$	1.7306	O	0.9318	N_2	$m_{1,1}$	1.7306	O	0.9318
CH_4	$n_{5,1}$	1.0000	N	3.4611	O_2	$m_{1,2}$	0.0000	N	3.4611
O_2	$n_{1,2}$	0.0000	C	1.0000	NO_2	$m_{1,19}$	0.0000	C	1.0000
O_2	$n_{5,2}$	0.0000	H	4.0000	NO	$m_{1,18}$	0.0000	H	4.0000
					CO_2	$m_{5,4}$	0.0000		
					CH_4	$m_{5,5}$	1.0000		
					CO	$m_{5,17}$	0.0000		
					H_2O	$m_{5,16}$	0.0000		
Total		3.1965		4.0000	Total		3.1965		4.0000
$\alpha_{1,1} = 0.0000$; $\alpha_{1,2} = 0.0000$; $\alpha_{5,1} = 0.0000$, $\alpha_{5,2} = 0.0000$									

Table 5. Example of moles balance; oxygen excess=0.45

5.4. Full combustion reactions

The whole model considers up to twenty reactants. Full components possible reaction may be stated as:

$$
\begin{array}{llllllll}
n_{1,1}N_2 + & n_{1,2}O_2 & \rightarrow & m_{1,1}N_2 + & m_{1,2}O_2 + & m_{1,18}NO + & m_{1,19}NO_2 & \\
 & n_{2,2}O_2 & \rightarrow & m_{2,2}O_2 & & & & \\
n_{3,1}H_2S + & n_{3,2}O_2 & \rightarrow & m_{3,2}O_2 + & m_{3,3}H_2S + & m_{3,16}H_2O + & m_{3,20}SO_2 & \\
 & n_{4,1}CO_2 & \rightarrow & m_{4,4}CO_2 & & & & \\
n_{5,1}CH_4 + & n_{5,2}O_2 & \rightarrow & m_{5,2}O_2 + & m_{5,4}CO_2 + & m_{5,16}H_2O + & m_{5,5}CH_4 + & m_{5,17}CO \\
n_{6,1}C_2H_6 + & n_{6,2}O_2 & \rightarrow & m_{6,2}O_2 + & m_{6,4}CO_2 + & m_{6,16}H_2O + & m_{6,6}C_2H_6 + & m_{6,17}CO \\
n_{7,1}C_3H_8 + & n_{7,2}O_2 & \rightarrow & m_{7,2}O_2 + & m_{7,4}CO_2 + & m_{7,16}H_2O + & m_{7,7}C_3H_8 + & m_{7,17}CO \\
n_{8,1}C_4H_{10} + & n_{8,2}O_2 & \rightarrow & m_{8,2}O_2 + & m_{8,4}CO_2 + & m_{8,16}H_2O + & m_{8,8}C_4H_{10} + & m_{8,17}CO \\
n_{9,1}iC_4H_{10} + & n_{9,2}O_2 & \rightarrow & m_{9,2}O_2 + & m_{9,4}CO_2 + & m_{9,16}H_2O + & m_{9,9}iC_4H_{10} + & m_{9,17}CO \\
n_{10,1}C_5H_{12} + & n_{10,2}O_2 & \rightarrow & m_{10,2}O_2 + & m_{10,4}CO_2 + & m_{10,16}H_2O + & m_{10,10}C_5H_{12} + & m_{10,17}CO \\
 & n_{11,2}O_2 & \rightarrow & m_{11,2}O_2 + & m_{11,4}CO_2 + & m_{11,16}H_2O + & m_{11,11}C_6H_{14} + & m_{11,17}CO \\
 & n_{12,2}O_2 & \rightarrow & m_{12,2}O_2 + & m_{12,4}CO_2 + & m_{12,16}H_2O + & m_{12,12}C_7H_{16} + & m_{12,17}CO \\
n_{13,1}C_8H_{18} + & n_{13,2}O_2 & \rightarrow & m_{13,2}O_2 + & m_{13,4}CO_2 + & m_{13,16}H_2O + & m_{13,13}C_8H_{18} + & m_{13,17}CO \\
n_{14,1}C_9H_{20} + & n_{14,2}O_2 & \rightarrow & m_{14,2}O_2 + & m_{14,4}CO_2 + & m_{14,16}H_2O + & m_{14,14}C_9H_{20} + & m_{14,17}CO \\
n_{15,1}C_{10}H_{22} + & n_{15,2}O_2 & \rightarrow & m_{15,2}O_2 + & m_{15,4}CO_2 + & m_{15,16}H_2O + & m_{15,15}C_{10}H_{22} + & m_{15,17}CO \\
 & n_{16,1}H_2O & \rightarrow & m_{16,16}H_2O & & & & \\
n_{17,1}CO + & n_{17,2}O_2 & \rightarrow & m_{17,2}O_2 + & m_{17,4}CO_2 + & m_{17,17}CO & & \\
n_{18,1}NO + & n_{18,2}O_2 & \rightarrow & m_{18,2}O_2 + & m_{18,18}NO + & m_{18,19}NO_2 & & \\
 & n_{19,1}NO_2 & \rightarrow & m_{19,19}NO_2 & & & & \\
 & n_{20,1}SO_2 & \rightarrow & m_{20,20}SO_2 & & & &
\end{array}
\tag{14}
$$

The reactions that have an associated efficiency are shown in Table 6:

Component	Partial Combustion		Full Combustion	
	Component	Efficiency	Component	Efficiency
N_2	NO	$\alpha_{1,2}$	NO_2	$\alpha_{1,1}$
H_2S	-	-	SO_2	$\alpha_{3,1}$
CH_4	CO	$\alpha_{5,2}$	CO_2	$\alpha_{5,1}$
C_2H_6	CO	$\alpha_{6,2}$	CO_2	$\alpha_{6,1}$
C_3H_8	CO	$\alpha_{7,2}$	CO_2	$\alpha_{7,1}$
C_4H_{10}	CO	$\alpha_{8,2}$	CO_2	$\alpha_{8,1}$
iC_4H_{10}	CO	$\alpha_{9,2}$	CO_2	$\alpha_{9,1}$
C_5H_{12}	CO	$\alpha_{10,2}$	CO_2	$\alpha_{10,1}$
C_6H_{14}	CO	$\alpha_{11,2}$	CO_2	$\alpha_{11,1}$
C_7H_{16}	CO	$\alpha_{12,2}$	CO_2	$\alpha_{12,1}$
C_8H_{18}	CO	$\alpha_{13,2}$	CO_2	$\alpha_{13,1}$
C_9H_{20}	CO	$\alpha_{14,2}$	CO_2	$\alpha_{14,1}$
$C_{10}H_{22}$	CO	$\alpha_{15,2}$	CO_2	$\alpha_{15,1}$
CO	CO	$\alpha_{17,2}$	CO_2	$\alpha_{17,1}$
NO	NO	$\alpha_{18,2}$	NO_2	$\alpha_{18,1}$

Table 6. Full combustion reactions

http://dx.doi.org/10.5772/59003

Considering basically the same general assumptions that those presented in the simple example explained above, including the linear interpolation between the efficiency definitions as a function of O_2 excess. Efficiencies adjusted for a gas turbine simulator [26] are:

N_2	If O_2 excess $\geq 200\%$	$\alpha_{1,1} = 1.3\text{x}10^{-5}$;	$\alpha_{1,2} = 0.0000$
	If O_2 excess $= 100\%$	$\alpha_{1,1} = 0.0000$;	$\alpha_{1,2} = 1.9\text{x}10^{-5}$
	If O_2 excess $\leq 50\%$	$\alpha_{1,1} = 0.0000$;	$\alpha_{1,2} = 0.0000$
H_2S	If O_2 excess $\geq 200\%$	$\alpha_{3,1} = 7.3\text{x}10^{-5}$	
	If O_2 excess $= 100\%$	$\alpha_{3,1} = 1.1\text{x}10^{-5}$	
	If O_2 excess $\leq 50\%$	$\alpha_{3,1} = 0.0000$	
CH_4	If O_2 excess $\geq 200\%$	$\alpha_{5,1} = 1.0000$;	$\alpha_{5,2} = 0.0000$
	If O_2 excess $= 100\%$	$\alpha_{5,1} = 0.0000$;	$\alpha_{5,2} = 2.3\text{x}10^{-4}$
	If O_2 excess $\leq 50\%$	$\alpha_{5,1} = 0.0000$;	$\alpha_{5,2} = 0.0000$
C_2H_6	If O_2 excess $\geq 200\%$	$\alpha_{6,1} = 1.0000$;	$\alpha_{6,2} = 0.0000$
	If O_2 excess $= 100\%$	$\alpha_{6,1} = 0.0000$;	$\alpha_{6,2} = 2.3\text{x}10^{-4}$
	If O_2 excess $\leq 50\%$	$\alpha_{6,1} = 0.0000$;	$\alpha_{6,2} = 0.0000$
C_3H_8	If O_2 excess $\geq 200\%$	$\alpha_{7,1} = 1.0000$;	$\alpha_{7,2} = 0.0000$
	If O_2 excess $= 100\%$	$\alpha_{7,1} = 0.0000$;	$\alpha_{7,2} = 2.3\text{x}10^{-4}$
	If O_2 excess $\leq 50\%$	$\alpha_{7,1} = 0.0000$;	$\alpha_{7,2} = 0.0000$
C_4H_{10}	If O_2 excess $\geq 200\%$	$\alpha_{8,1} = 1.0000$;	$\alpha_{8,2} = 0.0000$
	If O_2 excess $= 100\%$	$\alpha_{8,1} = 0.0000$;	$\alpha_{8,2} = 2.3\text{x}10^{-4}$
	If O_2 excess $\leq 50\%$	$\alpha_{8,1} = 0.0000$;	$\alpha_{8,2} = 0.0000$
iC_4H_{10}	If O_2 excess $\geq 200\%$	$\alpha_{9,1} = 1.0000$;	$\alpha_{9,2} = 0.0000$
	If O_2 excess $= 100\%$	$\alpha_{9,1} = 0.0000$;	$\alpha_{9,2} = 2.3\text{x}10^{-4}$
	If O_2 excess $\leq 50\%$	$\alpha_{9,1} = 0.0000$;	$\alpha_{9,2} = 0.0000$
C_5H_{12}	If O_2 excess $\geq 200\%$	$\alpha_{10,1} = 1.0000$;	$\alpha_{10,2} = 0.0000$
	If O_2 excess $= 100\%$	$\alpha_{10,1} = 0.0000$;	$\alpha_{10,2} = 2.3\text{x}10^{-4}$
	If O_2 excess $\leq 50\%$	$\alpha_{10,1} = 0.0000$;	$\alpha_{10,2} = 0.0000$
C_6H_{14}	If O_2 excess $\geq 200\%$	$\alpha_{11,1} = 1.0000$;	$\alpha_{11,2} = 0.0000$
	If O_2 excess $= 100\%$	$\alpha_{11,1} = 0.0000$;	$\alpha_{11,2} = 2.3\text{x}10^{-4}$
	If O_2 excess $\leq 50\%$	$\alpha_{11,1} = 0.0000$;	$\alpha_{11,2} = 0.0000$

$$
\begin{array}{lll}
C_7H_{16} & \text{If } O_2 \text{ excess} \geq 200\% & \alpha_{12,1} = 1.0000; \quad \alpha_{12,2} = 0.0000 \\
 & \text{If } O_2 \text{ excess} = 100\% & \alpha_{12,1} = 0.0000; \quad \alpha_{12,2} = 2.3\text{x}10^{-4} \\
 & \text{If } O_2 \text{ excess} \leq 50\% & \alpha_{12,1} = 0.0000; \quad \alpha_{12,2} = 0.0000 \\
C_8H_{18} & \text{If } O_2 \text{ excess} \geq 200\% & \alpha_{13,1} = 1.0000; \quad \alpha_{13,2} = 0.0000 \\
 & \text{If } O_2 \text{ excess} = 100\% & \alpha_{13,1} = 0.0000; \quad \alpha_{13,2} = 2.3\text{x}10^{-4} \\
 & \text{If } O_2 \text{ excess} \leq 50\% & \alpha_{13,1} = 0.0000; \quad \alpha_{13,2} = 0.0000 \\
C_9H_{20} & \text{If } O_2 \text{ excess} \geq 200\% & \alpha_{14,1} = 1.0000; \quad \alpha_{14,2} = 0.0000 \\
 & \text{If } O_2 \text{ excess} = 100\% & \alpha_{14,1} = 0.0000; \quad \alpha_{14,2} = 2.3\text{x}10^{-4} \\
 & \text{If } O_2 \text{ excess} \leq 50\% & \alpha_{14,1} = 0.0000; \quad \alpha_{14,2} = 0.0000 \\
C_{10}H_{22} & \text{If } O_2 \text{ excess} \geq 200\% & \alpha_{15,1} = 1.0000; \quad \alpha_{15,2} = 0.0000 \\
 & \text{If } O_2 \text{ excess} = 100\% & \alpha_{15,1} = 0.0000; \quad \alpha_{15,2} = 2.3\text{x}10^{-4} \\
 & \text{If } O_2 \text{ excess} \leq 50\% & \alpha_{15,1} = 0.0000; \quad \alpha_{15,2} = 0.0000 \\
CO & \text{If } O_2 \text{ excess} \geq 200\% & \alpha_{17,1} = 1.0000; \quad \alpha_{17,2} = 0.0000 \\
 & \text{If } O_2 \text{ excess} \leq 100\% & \alpha_{17,1} = 0.0000; \quad \alpha_{17,2} = 1.0000 \\
NO & \text{If } O_2 \text{ excess} \geq 200\% & \alpha_{18,1} = 1.0000; \quad \alpha_{18,2} = 0.0000 \\
 & \text{If } O_2 \text{ excess} \leq 100\% & \alpha_{18,1} = 0.0000; \quad \alpha_{18,2} = 1.0000
\end{array}
\tag{15}
$$

In order to avoid imbalances in the reactions, next restriction must be addressed at any moment:

$$0 \leq \alpha_{i,1} + \alpha_{i,2} \leq ul \tag{16}$$

Upper limit *ul* usually may have a value of 1, but some off-line tests should be carried on in order to be sure that not negative mole flowrate are calculated as result of Equations (17).

If efficiencies values are known, moles flow of products may be calculated as a function of moles flow of reactants. In next equations, input data ($n_{i,1}$ *for* i=1,20) are known defined by air, injection water and fuel composition. Mole flowrates of oxygen ($n_{i,2}$) are calculated as the required O_2 considering the calculated efficiencies defined by Equations (15):

http://dx.doi.org/10.5772/59003

All reactantes:

	$n_{i,1}$	=	*input data for* $i = 1,20$
N_2	$m_{1,19}$	=	$2\alpha_{1,1}n_{1,1}$
	$m_{1,18}$	=	$2\alpha_{1,2}n_{1,1}$
	$m_{1,1}$	=	$0.5\left(2n_{1,1} - m_{1,18} - m_{1,19}\right)$
	$n_{1,2}$	=	$0.5m_{1,18} + 1m_{1,19}$
O_2	$m_{2,2}$	=	$n_{2,2} - \Sigma n_{i,2}$ *for* $i = 1,3,4,\ldots 20$
H_2S	$m_{3,20}$	=	$\alpha_{3,1}n_{3,1}$
	$m_{3,3}$	=	$n_{3,1} - m_{3,20}$
	$m_{3,16}$	=	$n_{3,1} - m_{3,3}$
	$n_{3,2}$	=	$0.5m_{3,16} + m_{3,20}$
CO_2	$m_{4,4}$	=	$n_{4,1}$
CH_4	$m_{5,4}$	=	$\alpha_{5,1}n_{5,1}$
	$m_{5,17}$	=	$\alpha_{5,2}n_{5,1}$
	$m_{5,5}$	=	$n_{5,1} - m_{5,4} - m_{5,17}$
	$m_{5,16}$	=	$2n_{5,1} - 2m_{5,5}$
	$n_{5,2}$	=	$m_{5,4} + 0.5m_{5,16} + 0.5m_{5,17}$
C_2H_6	$m_{6,4}$	=	$2\alpha_{6,1}n_{6,1}$
	$m_{6,17}$	=	$2\alpha_{6,2}n_{6,1}$
	$m_{6,6}$	=	$n_{6,1} - 0.5m_{6,4} - 0.5m_{6,17}$
	$m_{6,16}$	=	$3n_{6,1} - 3m_{6,6}$
	$n_{6,2}$	=	$m_{6,4} + 0.5m_{6,16} + 0.5m_{6,17}$
C_3H_8	$m_{7,4}$	=	$3\alpha_{7,1}n_{7,1}$
	$m_{7,17}$	=	$3\alpha_{7,2}n_{7,1}$
	$m_{7,7}$	=	$n_{7,1} - 1/3m_{7,4} - 1/3m_{7,17}$
	$m_{7,16}$	=	$4n_{7,1} - 4m_{7,7}$
	$n_{7,2}$	=	$m_{7,4} + 0.5m_{7,16} + 0.5m_{7,17}$
C_4H_{10}	$m_{8,4}$	=	$4\alpha_{8,1}n_{8,1}$
	$m_{8,17}$	=	$4\alpha_{8,2}n_{8,1}$
	$m_{8,8}$	=	$n_{8,1} - 1/4m_{8,4} - 1/4m_{8,17}$
	$m_{8,16}$	=	$5n_{8,1} - 5m_{8,8}$
	$n_{8,2}$	=	$m_{8,4} + 0.5m_{8,16} + 0.5m_{8,17}$

$$
\begin{array}{lll}
iC_4H_{10} & m_{9,4} = 4\alpha_{9,1}n_{9,1} \\
& m_{9,17} = 4\alpha_{9,2}n_{9,1} \\
& m_{9,9} = n_{9,1} - 1/4m_{9,4} - 1/4m_{9,17} \\
& m_{9,16} = 5n_{9,1} - 5m_{9,9} \\
& n_{9,2} = m_{9,4} + 0.5m_{9,16} + 0.5m_{9,17} \\
C_5H_{12} & m_{10,4} = 5\alpha_{10,1}n_{10,1} \\
& m_{10,17} = 5\alpha_{10,2}n_{10,1} \\
& m_{10,10} = n_{10,1} - 1/5m_{10,4} - 1/5m_{10,17} \\
& m_{10,16} = 6n_{10,1} - 6m_{10,10} \\
& n_{10,2} = m_{10,4} + 0.5m_{10,16} + 0.5m_{10,17} \\
C_6H_{14} & m_{11,4} = 6\alpha_{11,1}n_{11,1} \\
& m_{11,17} = 6\alpha_{11,2}n_{11,1} \\
& m_{11,11} = n_{11,1} - 1/6m_{11,4} - 1/6m_{11,17} \\
& m_{11,16} = 7n_{11,1} - 7m_{11,11} \\
& n_{11,2} = m_{11,4} + 0.5m_{11,16} + 0.5m_{11,17} \\
C_7H_{16} & m_{12,4} = 7\alpha_{12,1}n_{12,1} \\
& m_{12,17} = 7\alpha_{12,2}n_{12,1} \\
& m_{12,12} = n_{12,1} - 1/7m_{12,4} - 1/7m_{12,17} \\
& m_{12,16} = 8n_{12,1} - 8m_{12,12} \\
& n_{12,2} = m_{12,4} + 0.5m_{12,16} + 0.5m_{12,17} \\
C_8H_{18} & m_{13,4} = 8\alpha_{13,1}n_{13,1} \\
& m_{13,17} = 8\alpha_{13,2}n_{13,1} \\
& m_{13,13} = n_{13,1} - 1/8m_{13,4} - 1/8m_{13,17} \\
& m_{13,16} = 9n_{13,1} - 9m_{13,13} \\
& n_{13,2} = m_{13,4} + 0.5m_{13,16} + 0.5m_{13,17} \\
C_9H_{20} & m_{14,4} = 9\alpha_{14,1}n_{14,1} \\
& m_{14,17} = 9\alpha_{14,2}n_{14,1} \\
& m_{14,14} = n_{14,1} - 1/9m_{14,4} - 1/9m_{14,17} \\
& m_{14,16} = 10n_{14,1} - 10m_{14,14} \\
& n_{14,2} = m_{14,4} + 0.5m_{14,16} + 0.5m_{14,17}
\end{array}
\qquad (17)
$$

http://dx.doi.org/10.5772/59003

$$
\begin{array}{lll}
C_{10}H_{22} & m_{15,4} = 10\alpha_{15,1}n_{15,1} \\
 & m_{15,17} = 10\alpha_{15,2}n_{15,1} \\
 & m_{15,15} = n_{15,1} - 1/10m_{15,4} - 1/10m_{15,17} \\
 & m_{15,16} = 11n_{15,1} - 11m_{15,15} \\
 & n_{15,2} = m_{15,4} + 0.5m_{15,16} + 0.5m_{15,17} \\
H_2O & m_{16,16} = n_{16,1} \\
CO & m_{17,4} = \alpha_{17,1}n_{17,1} \\
 & m_{17,17} = \alpha_{17,2}n_{17,1} \\
 & n_{17,2} = -0.5n_{17,1} + m_{17,4} + 0.5m_{17,17} \\
NO & m_{18,19} = \alpha_{18,1}n_{18,1} \\
 & m_{18,18} = \alpha_{18,2}n_{18,1} \\
 & n_{18,2} = -0.5n_{18,1} + m_{18,19} + 0.5m_{18,18} \\
NO_2 & m_{19,19} = n_{19,1} \\
SO_2 & m_{20,20} = n_{20,1}
\end{array}
$$

A proper sequence must be addressed in the calculations. Components present in more than one reaction must be calculated at the end of sequence. Total flow of products in more than one reaction is the results of the sum of the products of all reactions.

The efficiencies could be substituted for any function, according the available plant data. A very important factor not used in this work is the actual flame temperature.

Although no kinetics is taken into account, this approach considering these original two efficiencies, allows simulate the behaviour of a combustion chamber for training purposes (whatever, a combustor of a gas turbine or the furnace zone of a boiler).

So, the combustion chamber simulation should be able to predict the amount of heat generated by the reactions, the products temperature leaving and the products flowrates and compositions.

The transferred heat toward the combustion chamber surroundings depends on the desired design. For example, for a combustor, the designer wants the heat not to be transferred in order to have more potential work to be done in the gas turbine (of course a compromise with the NO_x production must be considered). For a furnace, the heat transfer depends on the boiler type (radiant, convective, once-through, *etc.*) and the desired pattern of the heat absorption in all different elements of the boiler (waterwalls, superheaters, economisers, *etc.*).

In any case the heat transference phenomenon it is not treated in detail in this chapter but a couple of general expressions are used. A representative surrounding walls temperature T_{sw} is assumed to be known at any time.

5.5. Calculation sequence

With the mass flowrate of each reactant, their mass composition and the molecular weight of the components, mass flowrates are converted into mole flowrates and mass compositions into mole compositions.

With the inlet temperature of each reactant (water, air and gas fuel), using the thermodynamic properties, the enthalpy of each inlet stream is calculated. And the total reactants enthalpy may be known:

$$h_r = \frac{w_w h_w + w_a h_a + w_{fg} h_{fg}}{w_w + w_a + w_{fg}} \tag{18}$$

According the present reactants they may be predicted the possible combustion products.

Reactants enthalpy (Δh_r^{298}) and formation heat (Δh_r^f) are calculated, both at 298 K.

$$\Delta h_r^f = w_r \Delta h_r^f \; ; \; \Delta h_r^{298} = w_r \Delta h_r^{298} \tag{19}$$

Flame temperature T_f is assumed with an initial value (normally the last instant value). In this point begins an iterative process called Level 1.

Theoretical O_2 flowrate w_{fc} for a complete combustion is calculated applying Equations (17) with efficiencies values calculated considering an *Oe* equal to 9 (to assure a complete combustion).

Oxygen excess *Oe* is assumed with an initial value. In this point begins an iterative process called Level 2.

Efficiencies are calculated with Equations (15) and restrictions shown in Equation (16). These variables are a function of *Oe* and also could be a function of other variables as T_f, burners tilt, *etc*.

O_2 flowrate w_{O2} is calculated with Equations (17) with the estimated efficiencies.

Oxygen excess is calculated as:

$$Oe = \frac{w_{fc}}{w_{O2}} \tag{20}$$

If *Oe* has practically same value than that calculated in the beginning of iterative process Level 2, the calculation process continues, otherwise, a Newton-Raphson with numerical derivatives is used to converge *Oe* from the point where Level 2 initiates.

Actual products flowrates and composition are calculated with Equations (17).

http://dx.doi.org/10.5772/59003

Formation heat and enthalpies at 298 K and T_f are calculated.

$$\Delta h_p^f = w_p \Delta h_p^f ;\ \Delta h_p^{298} = w_p \Delta h_p^{298} ;\ \Delta h_p^{Tf} = w_p \Delta h_p^{Tf} \tag{21}$$

Sensible heat of reactants $q_{s\text{-}r}$ from reactants temperature to 298 K, sensible heat of products $q_{s\text{-}p}$, and combustion heat q_{com} are calculated as (consider that products are the sum of the results of reactions and the reactants going through combustion chamber being not burned):

$$q_{s\text{-}r} = \sum w_r \left(h_r - h_r^{298} \right) \tag{22}$$

$$q_{s\text{-}p} = \sum w_p \left(h_p - h_p^{298} \right) \tag{23}$$

$$q_{com} = \Delta h_p^f - \Delta h_r^f \tag{24}$$

Radiant and convective heat flowing to surrounding metal walls are calculated using known heat transfer coefficients that depends on the geometry and exposed area (these coefficients correlations and calculations are beyond the subject of this chapter):

$$q_{rad} = hA_{rad} \left(T_f^4 - T_{sw}^4 \right) \tag{25}$$

$$q_{con} = hA_{con} \left(T_f - T_{sw} \right) \tag{26}$$

The process is complete if the sum of the heat flowrates is balanced *i.e.* are equal to zero:

$$f = q_{s\text{-}r} - q_{s\text{-}p} + q_{com} - q_{rad} - q_{con} \tag{27}$$

If f is enough near zero, the process is finished; otherwise a numerical Newton-Raphson is used to converge to the proper flame temperature from the point where Level 1 initiates.

The conceptual combustor chamber model is presented in Figure 5. The reaction node represents the reactions procedure explained above to get reaction products and flame temperature. The capacitive node is solved with Equations (4) and (5). Combustion chamber temperature and density are calculated with the proper cubic equations properties.

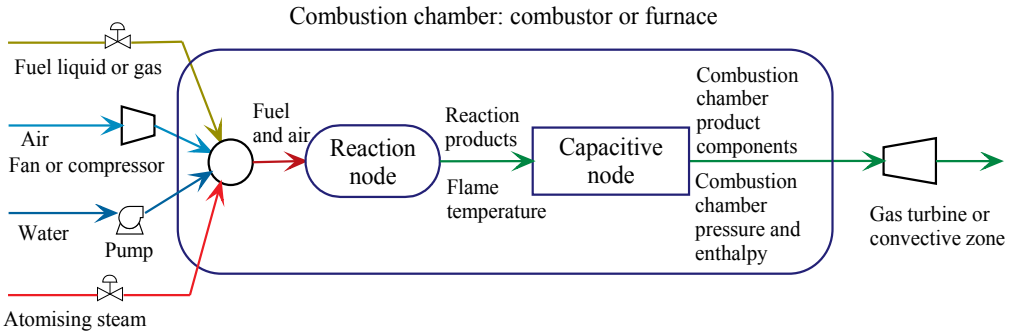

Figure 5. Conceptual model of the combustion chamber.

Although there are not mentioned in the above calculations, there are taken into account possible malfunctions or events as trip of burners, sudden turning off of flame, low efficiency of combustion (simulated as a factor less than one on the combustion heat), change in fuel composition, *etc*.

6. Application examples

More than a validation of the model, in this section one application example is presented. The basis for this example is a model installed in a simulator of a gas turbine power plant developed for CFE by the GSACS [26]. The reference plant produces nominally 150 MW. For this particular application of the combustion model, a linear function was used to represent each efficiency as shown in Equations (15), based only on the oxygen excess. Several real plant data were available and some of them were included in the graphics presented in this section.

The natural gas fuel and air composition of the presented test are shown in Table 7.

Component	N_2	O_2	CO_2	CH_4	C_2H_6	C_3H_8	C_4H_{10}	iC_4H_{10}	C_5H_{12}	C_6H_{14}	H_2O
Air	78.51	20.88	-	-	-	-	-	-	-	-	0.01
Gas Fuel	1.69	-	0.05	88.81	8.89	0.45	0.04	0.02	0.02	0.03	-

Table 7. Mole per cent composition of combustion chamber inlet flowrates

Selected results are presented here simulating an automatic start-up of the gas turbine power plant (Figures 6 to 9).

Figure 6 presents, as a reference, the simulated gas turbine speed and the generated power. Five seconds after the simulation is initiated, the start button is press and the automatic start-up procedure begins.

http://dx.doi.org/10.5772/59003

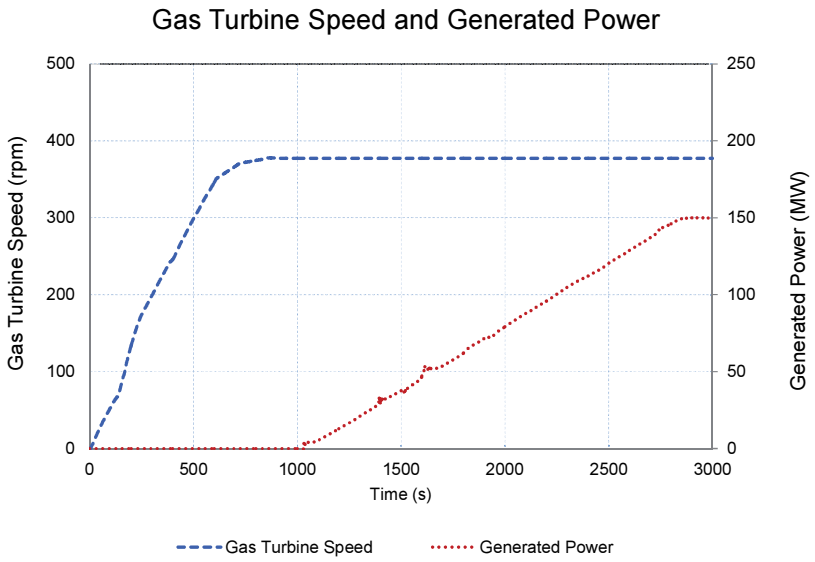

Figure 6. Automatic start-up gas turbine speed and generated power.

Figure 7 has the simulated mole flowrates of gas fuel and air feed to the combustor.

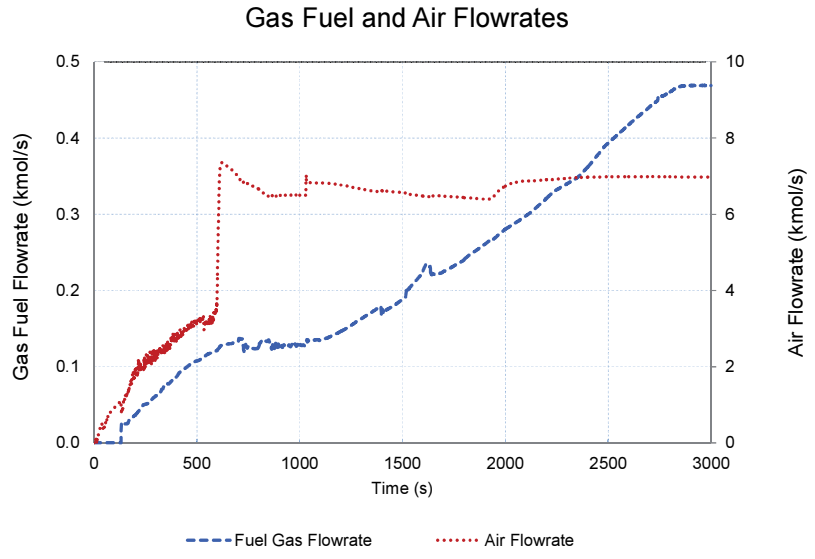

Figure 7. Automatic start-up mole gas fuel and air flowrates.

In Figure 8, real exhaust gases temperature and the result of simulation are compared. Simulation results of oxygen excess and CO2 concentration are also included in Figure 8.

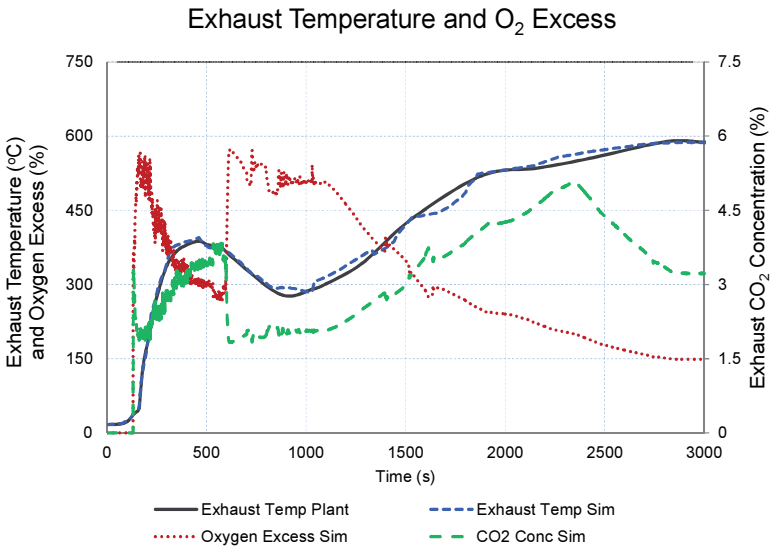

Figure 8. Automatic start-up exhaust temperatures and oxygen excess.

In Figure 9, simulated exhaust concentration of oxygen and nitrogen oxides are compared against real plant data.

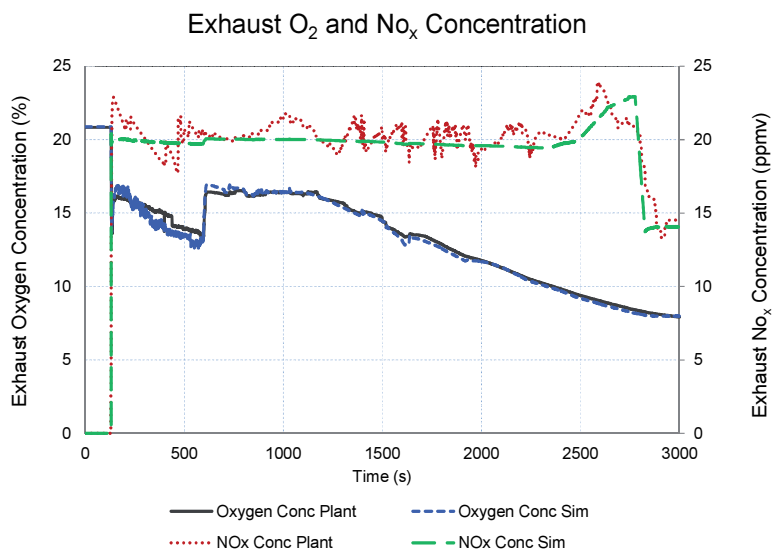

Figure 9. Automatic start-up exhaust oxygen and nitrogen oxides concentrations.

http://dx.doi.org/10.5772/59003

No SO_2 results exist because the natural gas considered in this simulator does not has any sulphur component.

All results are enough to satisfy the ANSI norm for fossil power plants simulators [19]. However, it clear, according Figure 9, that efficiencies should have an extra factor besides the oxygen excess to behave no that smooth as the curve presented by simulation results. This factor is an open issue to be studied.

No plant data are presently available for emission concentration during other transient, including malfunctions, but the qualitative simulation results are acceptable for training purposes.

7. Conclusion

7.1. Remarks

From the literature review, it may be concluded that few work on simple handled combustion models for training purposes has been reported. This work intends to cover the particular needs of the GSACS. A generic model of such a combustion process designed to work in any operators' training simulator has been presented.

Validation of the model has been intrinsically demonstrated with the inclusion of the model in a gas turbine and a combined cycle power plants simulators for operators' training. In the proper date, CENAC endorsed and accepted as correct the results of the tests in accordance with the testing acceptance procedures and the ANSI norm.

Some others off-line examples have been presented with the objective to explain the model principles and potential.

7.2. Future work

The combustion model is established and it is a relatively easy task to add new components to the possible set of reactions. Presence of other combustion sub-products such as free radicals or carbon should be studied and eventually considered.

There were mentioned different factors affecting the efficiency of reactions but not yet studied or included as part of the calculations like burner's tilt, ball fire position, gases recirculation, turbulent flow, bad mixing of reactants, level of pressure, kinetics, *etc*.

An automatized procedure should be devised to avoid the main withdrawal of this model, the manual adjustment of efficiencies. This process should include factors as oxygen excess, the *ul* values and some other factors influencing the efficiencies like the mentioned above.

8. Nomenclature

Indices

c- Mass or mole concentration	*P*- Pressure
Cp- Specific heat at constant pressure	*q*- Heat flowrate
f- Function sum of heat flowrates	*R*- Ideal gas constant
h- Enthalpy	*T*- Temperature
hA- Product of transfer area and heat transfer coefficient	*t*- Time
k- Constant	*ul*- Upper limit for sum of efficiencies
m- Mass or moles; Mole flowrate of products	*V*- Volume
n- Mole flowrate of reactants	*w*- Mole or mass flowrate
Oe- Oxygen excess	

Subscripts

a- air	*o*- output
com- combustion	*p*- products
con- convection	*r*- reactants
f- formation or flame	*rad*- radiation
fc- full combustion	*s*- sensible
fg- gas fuel	*sw*- surrounding walls
i - number of consecutive reaction	*Tf*- flame temperature
in- input	*w*- water
j - number of consecutive component	

Acronyms

ANSI- American National Standards Institute	IGV- Inlet Guide Vane
BMS- Burner Management System	IIE- Electrical Research Institute
CENAC- National Centre of Training Ixtapantongo	IPD - Interactive Process Diagrams
CFD- Computational Fluid Dynamics	MAS- Simulation Environment
CFE- Mexican National Utility Company	Oe- Oxygen Excess
EGTEI- Expert Group on Techo-Economic Issues	PDF- Probability Density Function
FLUPRE- Generic Model to Solve Flows and Pressures Networks	PID - Proportional-Integral-Derivative Controller
GSACS- Simulation and Advanced Training Systems Department	SAMA- Scientific Apparatus Makers Association
IC- Initial Condition	

Author details

Edgardo J. Roldán-Villasana* and Yadira Mendoza-Alegría

*Address all correspondence to: eroldan@iie.org.mx

Simulation and Advanced Training Systems Department, Electrical Research Institute, Mexico

References

[1] Sector Eléctrico Nacional. Subsecretaría de Electricidad. http://egob2.energia.gob.mx/portal/electricidad.html (accessed 30 July 2014).

[2] EPRI, Electric Power Research Institute. http://www.epri.com/abstracts/Pages/ProductAbstract.aspx?ProductId=TR-102690 (accessed 31 July 2014).

[3] EGTEI, Guidance document on control techniques for emissions of sulphur, NOx, OCs, dust (including PM10, PM2.5 and black carbon) from stationary sources. Convention on Long-Range Transboundary Air Pollution, 50th Working Group on Strategies and Review. 10-14 September 2012.

[4] Tabor G. Basics of Computational Combustion Modelling, University of Exeter. Fluid Flow: Course, Computational Modelling, https://projects.exeter.ac.uk/fluidflow/Courses/ComputationalModelling4029/combustionNew.pdf (accessed 7 July 2014).

[5] Ganesan V. Non-reacting and reacting flow analysis in an aero-engine gas turbine combustor using CFD. In: SAE International (eds.) SAE World Congress&Exhibition 2007: proceedings of SAE World Congress&Exhibition, 16-19 April 16, Detroit MI April 19, 2007

[6] Rathore P.S., Raj R., Thundil K. Numerical investigation of transverse jet in supersonic cross-flow using CFD techniques.In: American Society of Mechanical Engineers (eds.) ASME 2013: Gas Turbine India Conference: proceedings of ASME 2013 Gas Turbine India Conference, GTINDIA 2015, 5-6 December 2015,Bangalore, India. ASME; 2013.

[7] Rao P. S., Li X., Subbuswamy G. Numerical study of mist film cooling in combustor at operating conditions. In: American Society of Mechanical Engineers (eds.) ASME 2009 International Mechanical Engineering Congress and Exposition: proceedings of ASME International Mechanical Engineering Congress and Exposition IMECE2009 13-19 November 2009,New York, N.Y. ASME; 2010.

[8] Zeng Z. Wang Z. Song G. Numerical study of the effects of main parameters on micro-combustion for micro-gas turbine engine. In: IEEE Computer Society (eds.) APPEEC 2010: Asia-Pacific Power and Energy Engineering Conference: proceedings of

Asia-Pacific Power and Energy Engineering Conference, APPEEC 2010, 28-31 March 2010, State Grid of China. IEEE; 2010.

[9] Yang H. Zheng H. Li Z. Yang R. Zhang Z. Analysis of turbulence models in numerical simulation of combustion chamber. In: American Society of Mechanical Engineers (eds.) ASME 2013: Power Conference: proceedings of ASME 2013 Power Conference, Power Division 2015, July 29–August 1 2015, Boston MA USA. ASME; 2013.

[10] Vondál J. Hájek J. Swirling flow prediction in model combustor with axial guide vane swirler. Chemical Engineering Transactions 2012;29(1) 1069-1074.

[11] Reichling G. Noll B. Aigner M. Numerical simulation of the non-reactive and reactive flow in a swirled model gas turbine combustor. In: American Institute of Aeronautics and Astronautics (eds.) 2013 21st AIAA: Computational Fluid Dynamics Conference: proceedings of 2013 21st AIAA Computational Fluid Dynamics Conference, 24-27 June; San Diego CA. USA. AIAA; 2013.

[12] Bohorquez I. Barbosa J. Bastiaans J. De Goey P. Numerical simulation for the preliminary design of fuel flexible stationary gas turbine combustors using conventional and alternative fuels. In: American Society of Mechanical Engineers (eds.) ASME Turbo Expo 2012: proceedings of ASME Turbine Technical Conference and Exposition, GT 2012, 11-15 June 2012; Copenhagen Denmark. ASME; 2012.

[13] Jaber Q.M. Jaber J.O. Kawaldah M.A. Assessment of Power Augmentation from Gas Turbine Power Plants Using Different Inlet Air Cooling System. Jordan Journal of Mechanical and Industrial Engineering 2007;1(1) 7-17.

[14] Zhu Y. Frey H.C. Simplified Performance Model of Gas Turbine Combined Cycle Systems. Journal of Energy Engineering. 2007;133(2) 82-90.

[15] Chen L. Zhang W. Sun F. Performance Optimization for an Open-Cycle Gas Turbine Power Plant with a Refrigeration Cycle for Compressor Inlet Air Cooling Part I: Thermodynamic Modelling. Journal Power and Energy 2009;223(5) 505-513.

[16] Watanabe M. Y. Mitani Y. Iki H. Uriu Y. Urano Y. Developer of a dynamical model for customer´s gas turbine generator in industrial power systems. In: Institute of Electrical and Electronics Engineers (eds.) PECon 08: proceedings of IEEE International Conference on Power and Energy,PECON 08, 1-3 December 2008, Johor Baharu, Malaysia. IEEE;2010.

[17] Vieira L. Matt C. Guedes V. Cruz M. Castelloes F. Optimization of the operation of a complex combined-cycle cogeneration plant using a professional process simulator. In: American Society of Mechanical Engineers (eds.) IMECE2008: proceedings of International Mechanical Engineering Congress and Exposition, IMECE2008, October 31-November 6 2008, Boston, MA, USA. ASME; 2008.

[18] Bartells P.S. Gauthier J.S. AEgis Technologies. Technical Papers: Development of a Combination Boiler Simulator using General Purpose Simulation Tool. http://aegistg.com/technical_papers/isa2001finalpaper.pdf (accessed 30 March 2014).

[19] ANSI/ISA-77.20.01-2012 Fossil Fuel Power Plant Simulators: Functional Requirements, Instrumentation Systems, and Automation Society (ISA), 2012-2-9.

[20] Roldán-Villasana E., Cardoso M.J., Mendoza-Alegría Y. Modeling Methodology for Operator's Training Full Scope Simulators Applied on a Model of a Gas-Turbine Power Plant. In: (eds. Valderrama J.O., Rojas C.J.) Caip 2009: Modelado y Simulación de Procesos: proceedings of the Congreso Interamericano de Computación Aplicada a la Industria de Procesos, CAIP2009, 25-28 August 2009, Montevideo Uruguay.

[21] Mendoza Y., Roldán-Villasana E.J., Galindo I., Romero J. Methodology to Adapt the Feedwater and Condensate System, Using a Flow and Pressure Generic Model, for the Laguna Verde Nuclear Power Plant Simulator. In: (Bruzzone A.G.,Williams E. eds.) Scsc 2004: Lean Simulation Workshop: proceedings of Summer Computer Simulation Conference, The Society for Modeling and Simulation International, San Jose California, USA, July 2004.

[22] Pavri R. Moore GD. Gas Turbine Emissions and Control.GE Energy Services. Atlanta:GER-4211;2001. http://site.ge-energy.com/prod_serv/products/tech_docs/en/downloads/ger4211.pdf (accessed 27 June 2014).

[23] Reid R., Prausnitz J., Poling B. The properties of gases and liquids. New York: McGraw-Hill; 1987.

[24] Arnold E., Steam tables: thermodynamic properties of water and steam, viscosity of water and steam, thermal conductivity of water and steam. London: Electrical Research Association; 1967.

[25] Wikipedia the Free Encyclopedia. Atmosphere of Earth: http://en.wikipedia.org/wiki/Atmosphere_of_Earth (accessed 1 August 2014).

[26] Roldán-Villasana E.J. Mendoza-Alegría Y. Zorrilla-Arena J. Cardoso G. M. Cruz-Cruz R. Development of a Gas Turbine Full Scope Simulator For Operators' Training. International Journal of Simulation Systems, Science & Technology 2009;10(3) 8-23.

Edited by Gurrappa Injeti

This book presents current research in the area of gas turbines for different applications. It is a highly useful book providing a variety of topics ranging from basic understanding about the materials and coatings selection, designing and modeling of gas turbines to advanced technologies for their ever increasing efficiency, which is the need of the hour for modern gas turbine industries. The target audience for this book is material scientists, gas turbine engine design and maintenance engineers, manufacturers, mechanical engineers, undergraduate, post graduate students and academic researchers. The design and maintenance engineers in aerospace and gas turbine industry will benefit from the contents and discussions in this book.This book presents current research in the area of gas turbines for different applications. It is a highly useful book providing a variety of topics ranging from basic understanding about the materials and coatings selection, designing and modeling of gas turbines to advanced technologies for their ever increasing efficiency, which is the need of the hour for modern gas turbine industries. The target audience for this book is material scientists, gas turbine engine design and maintenance engineers, manufacturers, mechanical engineers, undergraduate, post graduate students and academic researchers. The design and maintenance engineers in aerospace and gas turbine industry will benefit from the contents and discussions in this book.

ISBN 978-953-51-6371-8

Photo by Petmal / iStock

IntechOpen